Theoretical and Experimental Investigations of Frustrated Pyrochlore Magnets

John Dickon Mathison Champion
University College London

Supervisor: Prof. S T Bramwell

A thesis submitted for the degree of Doctor of Philosophy in Chemistry

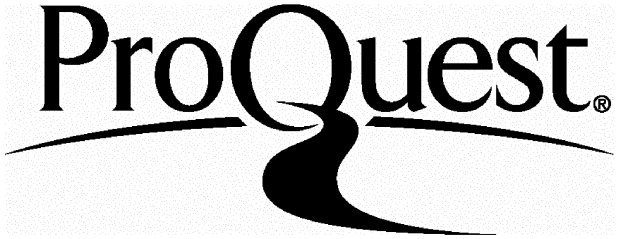

Abstract

This thesis describes the investigation of frustrated magnetic systems based on the pyrochlore lattice of corner-sharing tetrahedra.

Monte Carlo simulations and analytical calculations have been performed on a pyrochlore ferromagnet with local $\langle 111 \rangle$ easy-axis anisotropy related to the problem of 'spin ice'. The anisotropy-temperature-magnetic field phase diagram was determined. It contained a tricritical point as well as features related to some real ferroelectrics. A pyrochlore antiferromagnet with local $\langle 111 \rangle$ easy-plane anisotropy was studied by Monte Carlo simulation. A general expression for its degenerate ground states was discovered and normal-modes out of the ground states were calculated. Both systems are frustrated yet have a long-range ordered state at low temperature. The degeneracy lifting observed is discussed as well as the reasons for its presence.

The rare-earth titanate series $Ln_2Ti_2O_7$ (Ln = rare earth), crystallizes in the $Fd\bar{3}m$ space group, with the magnetic ions situated on the 16*c* sites which constitute the pyrochlore lattice. Crystal-field effects are known to play a significant role in the frustration observed in these compounds. Powder neutron diffraction was performed on gadolinium and erbium titanate. Both systems are frustrated antiferromagnets yet show long-range magnetic order at ~ 1 K and ~ 1.2 K respectively. The magnetic structures of both these compounds have been determined by powder neutron diffraction techniques and related to other theoretical results as well as the theoretical results of the author. Further neutron scattering experiments on the 'spin ice' materials $Ho_2Ti_2O_7$ and $Dy_2Ti_2O_7$ are also described.

Acknowledgements

I would like to thank my supervisor Professor Steven Bramwell, for his time, patience and understanding over the last four years. My 'petit chef', Professor Peter Holdsworth of the Ecole Normale Supérieure de Lyon, started me down the track of Monte Carlo simulation. I am greatly indebted to him for his 'Friday Night Lectures in Physics', which were invaluable to somebody with as little proper physics training as myself. Both men provided me with constant help and guidance. In the last year Andrew Wills has helped me considerably with the magnetic structures present in this work. Jason Gardner provided isotopic gadolinium oxide out of nowhere and Richard Down performed two sample changes of a dilution refrigerator on the POLARIS beamline. Mark Harris, Oleg Petrenko and Ron Smith also played no small part at ISIS.

I next have to thank my family for emotional, and more recently financial support. Particularly over the last few months as I have been writing up.

I need to thank the EPSRC, the Rutherford Appleton Laboratory and the Ecole Normale Supérieure de Lyon for funding me.

And now, in no particular order, alphabetical is too hard, I would like to thank all my friends at UCL Chemistry who have made the last four years so enjoyable. Starting from my office mates in G25 and working my way out in divergent concentric circles leaving behind UCL, reaching further and more exotic climes altogether: Maria-Rosa Russo, Katherine Brown, Linnea Forslund, Dirk Niemeyer, Aileen Gray, Emma O'Grady, Natalie Lambert, Simon Banks, Andrew Richardson, Sarah Brown, Louise Price, Sean McCormack, Mike Ewing, Helen Tsui, Joelle Le, Graeme Day, Jorge Lago, Steve Price, Shervin Moghaddam, Erasmo Buonomo,

Andrea Sella, Gisella Boendgen, Charles Willoughby, Anthony Meijer, Adam Farebrother, Mark Field, Marcia Saavedra, Daniel Morrison, Warren Cross, Catherine Lipton, Romano Giorgi, Anthony Birri, Shahbano Ali, Louise Affleck, Mark Roberts, Rob Campbell, Vicky Shorrock, Katie Jewell, Richard Stephenson, Mark Green, Christianna Zenonos, Martin Gilbert, Dina Shah, Yi-Ming Chan, Fiona Cowen, Emma Stevens, Jon Goff, Pascale Deen, Freddy Akeroyd, Joe Fletcher, Andrew Wildes, Jean-Yves Fortin, Baptiste Portelli, Mauro Sellito.....

Last, but not least, there are two special people who deserve a mention. Tom Fennell, the man with the driest wit of anyone I know, which has provided me with no end of amusement. If we ever lose contact I give you permission to shoot me. And lastly Alison Carruthers, who recently renewed my faith in something, I just haven't worked out what it is yet, but I know that it could be good!!

Contents

List of Figures

List of Tables

Chapter 1

Introduction

> 'The entropy of a pure condensed substance in internal thermodynamic equilibrium should be zero at the absolute zero.' [1]

Planck's formulation of the third law of thermodynamics suggests that at absolute zero there should be only one microscopic configuration of the system W, if the entropy S is defined:

$$S = k_B \ln(W). \tag{1.1}$$

This definition necessarily describes asymptotic behaviour of the system as the temperature $T \to 0$, since some systems, such as the 1-d Ising ferromagnet, do not order at any finite temperature but do exhibit long-range order at zero temperature [2]. This effectively implies that the ground state configuration is non-degenerate and unique in its arrangement as $T \to 0$.

Zero-point entropy of ice

The definition above does include the caveat for systems which have a zero-point entropy, but only with the hypothesis that they are not in internal thermodynamic equilibrium. A particularly simple example of such a system is in crystalline water ice. Giauque *et al.* determined the absolute entropy of water in the gas phase to

be 45.17 E.U (where 1 cal $\deg^{-1}$ mol^{-1} = 1 E.U) from spectroscopic measurements using the Sackur-Tetrode equation [3].

The absolute entropy of materials is often very difficult to measure and a common method is to measure the difference in entropy between two states, by integrating the specific heat C:

$$\Delta_b^a S = \int_{T_b}^{T_a} \frac{C}{T}\, dT. \tag{1.2}$$

If $S \to 0$ as $T \to 0$ then both types of measurement would be expected to give the same result. Accurate measurements of the specific heat to very low temperature by Simon [4] and Giauque *et al.* [5], when integrated, revealed a discrepancy in the entropy of 0.87 E.U [5]. This was larger than the errors of the calculations, and initially put down to the persistence of rotation of ortho water molecules ($\frac{3}{4}$ of the total) about their electric moment axes, giving an entropy of $\frac{3}{4}R\ln(2) = 1.03$ E.U [3].

Pauling proposed a different explanation for the zero-point entropy of ice. Ice crystallizes with oxygen atoms at the centres of corner-shared tetrahedra. The Bernal and Fowler 'ice-rules' stipulated that every oxygen must only have two short covalent oxygen-hydrogen bonds and two longer hydrogen bonds [6] (see Fig. 1.1). Pauling considered that for a system of N molecules of water there are a total of 2^{2N} configurations with hydrogen atoms between adjacent oxygen atoms (this allows molecules with more than two covalent oxygen-hydrogen bonds) [7]. There are $2^4 = 16$ possible arrangements of four hydrogen atoms around a given oxygen atom. Of these only six arrangements satisfy the ice-rules, all others have either too many or too few covalent oxygen-hydrogen bonds. The total number of configurations possible W is therefore:

$$W = 2^{2N}\left(\frac{6}{16}\right)^N = \left(\frac{3}{2}\right)^N \tag{1.3}$$

Thus $S(T \to 0) = R\ln\left(\frac{3}{2}\right) = 0.805$ E.U [7]. This value compares favourably with the measured discrepancy and is believed to be the true origin of the zero

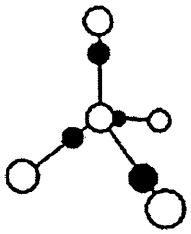

Figure 1.1: Every oxygen (○) has two hydrogen atoms (●) close to it (covalent bond) and two further away (hydrogen bond).

point entropy for ice. Ice is therefore disordered as $T \to 0$ with multiple random arrangements of the hydrogen atoms according to the ice-rules. Wollan *et al.* later confirmed this to be the structure using neutron diffraction methods [8]. However, it is widely believed (though not proven) that the disordered state is not the true equilibrium state as $T \to 0$.

1.1 Magnetic Systems with Residual Entropy

The implication of the third law to magnetic systems is simple. It predicts that all magnetic systems will be unique and ordered as $T \to 0$ with $S \to 0$. What happens if $S = O(N)$? This means that a system has many degenerate ground states, and is the start of an investigation into frustrated magnetism. This property has been observed in some real magnetic compounds.

There now follows a brief introduction to real compounds which have zero-point entropy.

1.1.1 Holmium Titanate

Holmium titanate, $Ho_2Ti_2O_7$, is a member of the family of compounds called the 'oxide pyrochlores' which belong to the $Fd\bar{3}m$ space group. They have a general chemical formula $A_2^{3+}B_2^{4+}O_7$ with A and/or B magnetic, with A often a rare-earth

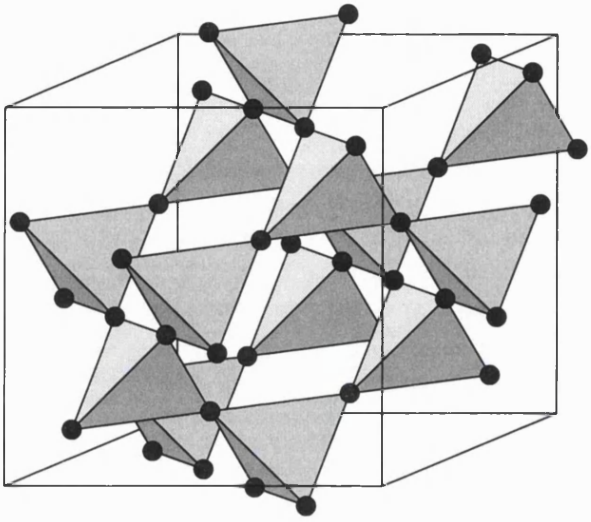

Figure 1.2: Rare earth sites in the pyrochlore structure.

ion. The A and B ions occupy the 16*c* and 16*d* sites respectively, which are each situated on their own pyrochlore lattice of corner-sharing tetrahedra, shown in Figure 1.2.

An oxide ion is situated at the centre of each tetrahedron of Ho^{3+} ions. The proximity of these ions along the $\langle 111 \rangle$ axes causes the ${}^5I_8$ free ion ground state term to be split, resulting in a low lying $M_J = \pm 8$ doublet ground state. Inelastic neutron scattering measurements have confirmed this splitting and shown the first excited state to be hundreds of Kelvin above the ground state [9].

The effect of the crystal electric field is therefore to restrict the Ho^{3+} ions to lie only on their local $\langle 111 \rangle$ axes, either pointing into or out of each tetrahedron. This effect is called single-ion anisotropy. It has been confirmed by bulk magnetization measurements, where, on application of a strong magnetic field, the saturated moment observed is only half that expected 10 μ_B [10].

When adjusted for crystal-shape dependent demagnetizing effects, susceptibility measurements showed the system to be ferromagnetic, with a Curie-Temperature $\theta_{CW} = 1.9 \pm 0.1$ K [11]. The material also seemed to have antiferromagnetic prop-

Figure 1.3: The ground state of a $\langle 111 \rangle$ Ising ferromagnet

erties as well, with a peak in the susceptibility at ~ 1 K [12].

Initial μSR and neutron scattering measurements on $Ho_2Ti_2O_7$ showed no signs of ordering in the compound down to 50 mK [13]. This was a remarkable observation since a naive assumption is that all simple ferromagnets must order at low temperature, and this was assumed to be the case for $Ho_2Ti_2O_7$. Two-state spins fixed along an axis are known as Ising spins (see section 1.2.2), and can only lie parallel or anti-parallel with the axis. In the case of $Ho_2Ti_2O_7$ the spins lie on the $\langle 111 \rangle$ or easy-axes of the tetrahedron which join the corners with its centre (see Fig. 1.3).

The ground state of an Ising pyrochlore ferromagnet is one with two spins pointing into the tetrahedron and two spins pointing out (see Fig. 1.3). There are six possible ways in which this ground state can be arranged on one tetrahedron, each one with the same energy. It is therefore possible to arrange the spins on the pyrochlore lattice in a ground state if and only if the configuration on *every* tetrahedron is 'two in – two out'. Over the whole lattice the spins can be quite disordered.

The pyrochlore lattice is the medial lattice (*i.e.* the lattice formed by the midpoints of the bonds) of the diamond-type oxide sublattice in cubic ice [14]. If the

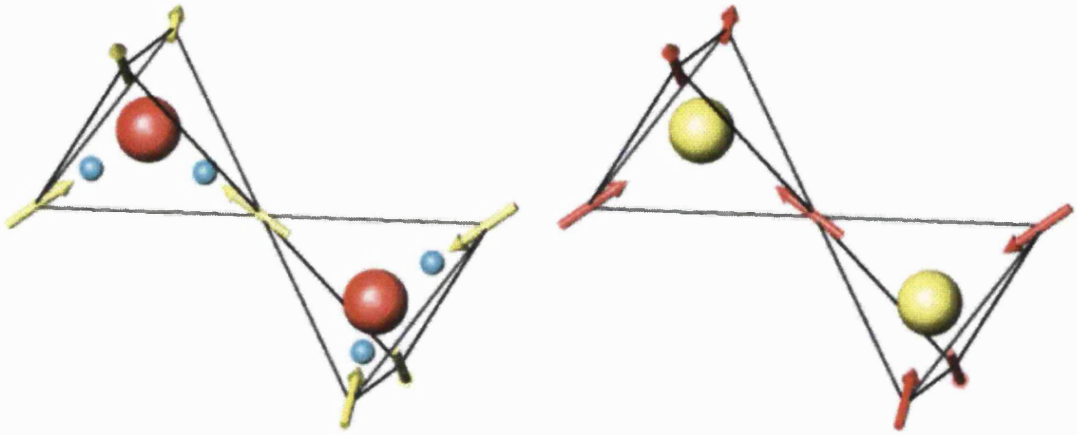

(a) Coordination of H_2O molecules in ice represented by proton displacement vectors.

(b) Spins in the spin ice model.

Figure 1.4: The spin ice mapping.

position of the proton is described by a displacement vector on the vertices of the lattice (see Fig. 1.4(a)), it is easy to see that the ground state condition of an Ising pyrochlore ferromagnet maps onto the ice-rules (see Fig. 1.4(b)). It follows from this that the ground states of the Ising pyrochlore ferromagnet are macroscopically degenerate [11, 15]. With this mapping in mind $Ho_2Ti_2O_7$ was called 'spin ice', to represent the remarkable similarity between the two different systems.

If the ground state condition of $Ho_2Ti_2O_7$ obeys the ice-rules, it must follow that $Ho_2Ti_2O_7$ also has a zero-point entropy. For a system of N two-state Ho atoms the total number of possible configurations at high temperature is simply $W = 2^N$. Every Ho atom is shared between two tetrahedra, so there are $\frac{N}{2}$ tetrahedra in the system. Using the same arguments as Pauling, the total number of spin ice ground states $W = \left(\frac{3}{2}\right)^{N/2}$ [7]. The expected entropy difference is thus:

$$\begin{aligned} S(T) - S(T \to 0) &= k_B \ln(2)^N - k_B \ln\left(\frac{3}{2}\right)^{\frac{N}{2}} \\ &= R\left(\ln(2) - \frac{1}{2}\ln\left(\frac{3}{2}\right)\right) \qquad \text{where} \quad R = Nk_B \end{aligned} \tag{1.4}$$

The existence of zero-point entropy in $Ho_2Ti_2O_7$ has been confirmed by integration of the measured specific heat from 0.3 – 20 K, once the nuclear Schottky contribution had been subtracted [16, 17].

$Ho_2Ti_2O_7$ cannot simultaneously satisfy all its near neighbour ferromagnetic interactions and its ground state is also macroscopically degenerate. It belongs to a class of magnets called 'frustrated magnets'. Frustrated magnets either order with $T_c \ll \theta_{CW}$ or they do not order at all. Recently frustrated magnetic systems have been a topic of much research [18, 19], and are the prime topic of this thesis.

1.1.2 Dysprosium Titanate

$Dy_2Ti_2O_7$ is another oxide pyrochlore with magnetic Dy^{3+} ions situated on the pyrochlore sites of the $Fd\bar{3}m$ space group. $Dy_2Ti_2O_7$ has a positive Curie-Temperature $\theta_{CW} \sim 0.5K$, suggesting that it has ferromagnetic interactions [20]. Similarly to $Ho_2Ti_2O_7$ it also shows no ordering down to 0.2 K, with no sign of a sharp peak in the measured specific heat [20].

There is no nuclear contribution to the specific heat in $Dy_2Ti_2O_7$ and measurement of the zero-point entropy is much more straightforward than for $Ho_2Ti_2O_7$. Ramirez *et al.* [20] measured the specific heat of $Dy_2Ti_2O_7$ from 0.2 – 12 K. Integration of the results provided the first ever direct experimental evidence for the spin ice theory. Figure 1.5 shows the entropy found by integrating the measured specific heat, with the discrepancy determined in Eqn. (1.4).

1.2 Frustration in Model Magnetic Systems

Frustration arises when a system cannot simultaneously minimise all its bond interactions. Consequently, this often leads to a degeneracy of the ground states. Often the frustration is caused by the geometry of the lattice and these systems are referred to as 'geometrically frustrated magnets' [18, 19]. This section explains

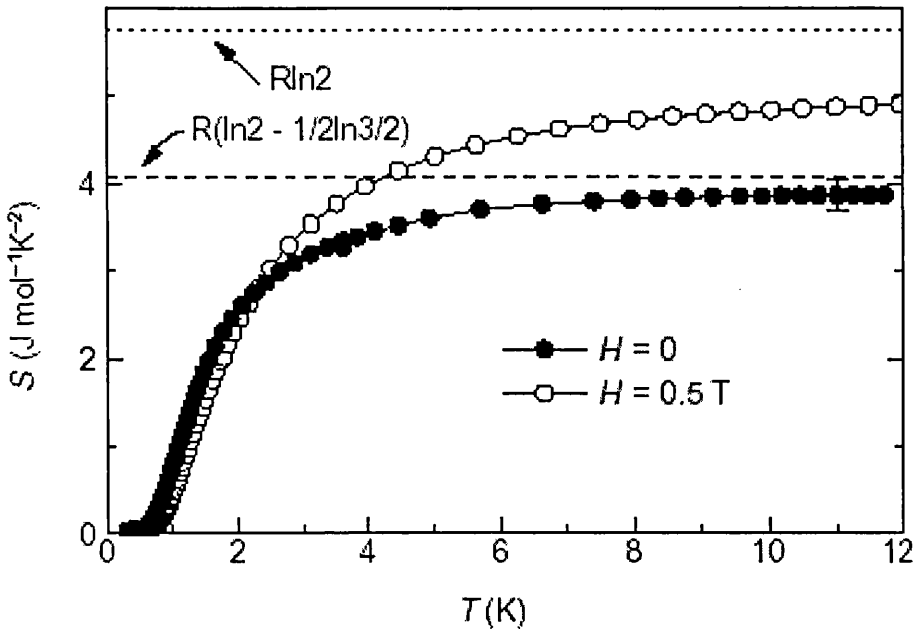

Figure 1.5: Entropy of $Dy_2Ti_2O_7$, after Ramirez *et al.* [20]

how and why these systems can become frustrated, as well as other properties of frustrated systems.

1.2.1 Types of Ordering in Magnetic Lattices

For ions that obey Russell-Saunders coupling, the magnetic moment μ of an ion is proportional to the total spin S and orbital L angular momentum present.

$$\mu = g_J\sqrt{J(J+1)} \qquad \text{with} \qquad g_J = \frac{3J(J+1)+S(S+1)-L(L+1)}{2J(J+1)}, \tag{1.5}$$

where g_J is the Landé g-factor and $J = |L| \pm |S|$ according to Hund's rules, for a many electron atom. In a crystalline lattice of magnetic ions, the moment or 'spin' is situated on the site of each magnetic ion, and its direction is represented by a vector. To a first approximation the magnetic energy of the system is determined by the interactions and relative orientations between nearest neighbour spins on

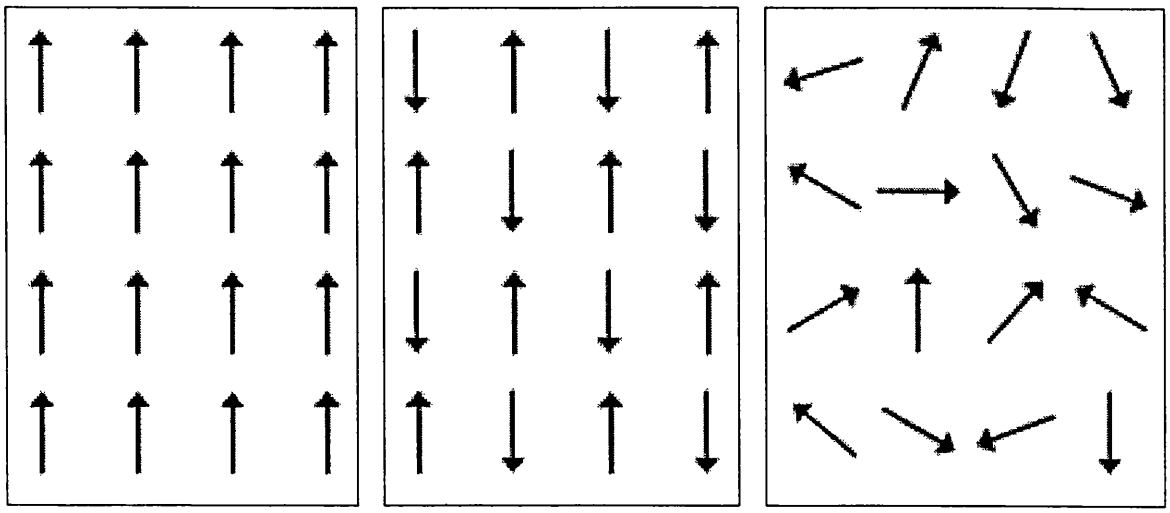

(a) Ferromagnetic (b) Antiferromagnetic (c) Paramagnetic

Figure 1.6: Different types of ordering for spins on a simple square lattice.

a lattice (nearest neighbour exchange). At low temperatures the system often seeks to order itself such that its magnetic energy is minimised. To all intents and purposes the magnetic energy can be considered as the internal energy U where the Gibbs free energy G is defined:

$$G = U - TS - Mh \tag{1.6}$$

If the system lowers its magnetic energy by orienting its near neighbour spins parallel with one another it is said to be **ferromagnetic** (see Fig. 1.6(a)). If the system lowers its magnetic energy by orienting its near neighbour spins anti-parallel with one another it is said to be **antiferromagnetic** (see Fig. 1.6(b)). At high temperatures the system is excited and randomly disordered (see Fig. 1.6(c)). A magnetic system is at equilibrium if its free energy is at a minimum. An *ordered* system at *low* temperature minimises the free energy by having a low internal energy. An ordered system has a low entropy ($W \rightarrow 1$) which makes little contribution to the Gibbs free energy. A paramagnetic system has a high internal energy, but is disordered and has a much higher entropy contribution to the free energy.

1.2.2 Magnetic Spin Models

There are three common magnetic spin models, in which a simple spin vector is defined as follows:

$$\mathbf{S} = S_x \underline{\mathbf{i}} + S_y \underline{\mathbf{j}} + S_z \underline{\mathbf{k}}. \tag{1.7}$$

where $\underline{\mathbf{i}}, \underline{\mathbf{j}}$ and $\underline{\mathbf{k}}$ are Cartesian unit vectors.

Ising spins

One-dimensional spin vectors simply point up or down with respect to a particular axis, such as the z direction. So $\mathbf{S} = \pm 1$ with for example $S_z = 1$ and $S_x = S_y = 0$. These are called **Ising** spins. In the case of the Ising pyrochlore system described in section 1.1, the spins point in or out of the tetrahedra with respect to the easy-axis of each tetrahedron.

XY spins

Two-dimensional spin vectors are fixed to lie in a plane. The simplest example is the XY plane where $S_x^2 + S_y^2 = 1$ and $S_z = 0$, and for this reason they are referred to as **XY Spins**. The spins can alternatively be fixed in planes where *all three* spin components take values, with $\mathbf{S} \cdot \mathbf{d}_i = 0$, where $\mathbf{d}_i$ is a local anisotropy axis. These cases are described in more detail in Chapter 4.

Heisenberg spins

Three-dimensional spins are able to point in all possible directions, and $S_x^2 + S_y^2 + S_z^2 = 1$. These are referred to as **Heisenberg Spins**.

Hamiltonian

The internal magnetic energy $U = E$ of a simple magnetic spin model is defined by minimising the Hamiltonian:

$$\mathbb{H} = -J \sum_{\langle i,j \rangle} \mathbf{S}_i \cdot \mathbf{S}_j \tag{1.8}$$

where J is the nearest neighbour exchange interaction and $\langle i, j \rangle$ denotes a sum over all nearest neighbour spins in the lattice (*i.e.* every bond in the lattice once). For a ferromagnetic system $J > 0$ and for an antiferromagnetic system $J < 0$. This expression is valid whatever the dimensionality of the spin variables of the system. Extra perturbations such as anisotropy or the application of a magnetic field can be added as extra terms in the Hamiltonian (see section 2.2.2).

1.2.3 A Simple Frustrated Model: The Triangular Antiferromagnet

The simplest example of a frustrated magnet comprises antiferromagnetic Ising spins on a triangle. The first two spins can easily be placed in an antiferromagnetic arrangement (see Fig. 1.7(a)). In order to lower the energy the system requires as many antiferromagnetic bonds as possible. The problem arises when the third spin needs to be positioned. Whichever way it is placed (up or down) there are two antiferromagnetic bonds and one ferromagnetic one (see Fig.1.7(b) and Fig.1.7(c)). Using Eqn. (1.8), both arrangements are degenerate with $E = -|J|$. If the triangle was repeated on a lattice, it is easy to see that the ground state has a macroscopic degeneracy. In fact, for a simple triangle, there are six configurations all with the same energy. The system is geometrically frustrated and cannot simultaneously minimise all its bond interactions.

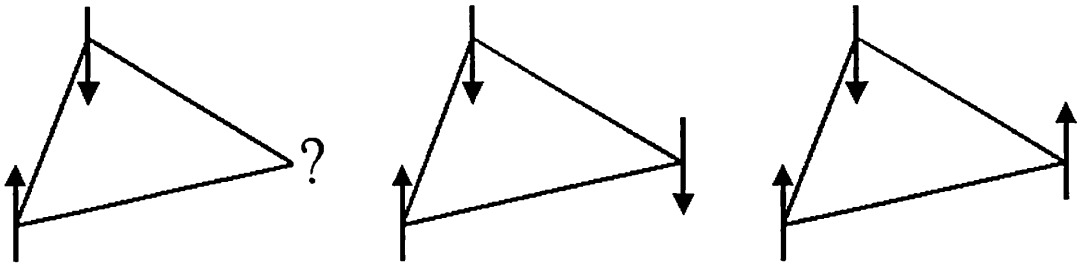

(a) (b) $E = -|J|$ (c) $E = -|J|$

Figure 1.7: Frustrated spins on a triangular unit.

1.2.4 The Ground State of a Geometrically Frustrated Antiferromagnet

Lattices are often considered in terms of the basic 'simplex' unit or plaquette of q interacting spins. If $q = 3$, the plaquette is a triangle, and if $q = 4$, it is a tetrahedron. As we have seen above, geometrically frustrated systems cannot minimise all their bond interactions. What is the ground state condition for a geometrically frustrated antiferromagnet? Initial insight to the problem was provided by Villain [21]. He reasoned that any state in which each individual plaquette has its energy minimised must also be a ground state for the whole system. This implies that only the local plaquettes are frustrated. When they are put together to form the lattice there is no increase in the local frustration. This is a particular property of geometrically frustrated systems. Disordered systems such as spin glasses do not necessarily have this property [22].

The proof of this condition is straightforward. We consider the energy on a single plaquette of q interacting Heisenberg spins, where the sum is over all bonds

twice, and therefore there is a factor of a half [23].

$$\begin{aligned}\mathbb{H} &= \frac{|J|}{2}\sum_{i,j=1}^{q}\mathbf{S}_i\cdot\mathbf{S}_j \\ &= \frac{|J|}{2}\left[\left(\sum_{i=1}^{q}\mathbf{S}_i\right)^2-\sum_{i=1}^{q}\mathbf{S}_i\cdot\mathbf{S}_i\right] \\ &= \frac{|J|}{2}\left[\left(\sum_{i=1}^{q}\mathbf{S}_i\right)^2-q\right] \end{aligned} \tag{1.9}$$

In Eqn. (1.9) the $-q$ term is constant and independent of the direction of the spins on the plaquette. Therefore in order to minimise the energy, the positive $\left(\sum_{i=1}^{q}\mathbf{S}_i\right)^2$ term must be zero. The only way for this to happen is if $\sum_{i=1}^{q}\mathbf{S}_i = 0$. Therefore the sum of the q interacting spins on a plaquette is zero. The argument can easily be extended to the whole lattice. For a lattice of corner-sharing units there are $2N/q$ separate units. Therefore the energy of the whole system can be described thus:

$$\mathbb{H} = \sum_{a=1}^{2N/q}\frac{|J|}{2}\left[\left(\sum_{i=1}^{q}{}^{a}\mathbf{S}_i\right)^2-q\right]. \tag{1.10}$$

For Eqn. (1.10) to be a minimum the same condition applies, and the total energy of the system $E_{tot} = 2N/q \times |J|/2 \times -q = -N|J|$.

1.2.5 The Effect of Constraints on the System

The ground state of any geometrically frustrated antiferromagnet (with continuous degrees of freedom), is one with the total magnetic moment of the q interacting spins on each plaquette equal to zero, as described in section 1.2.4. For Heisenberg spins this creates three different constraints:

$$\sum_{i=1}^{q}S_{ix}=0,\ \sum_{i=1}^{q}S_{iy}=0,\ \text{and}\ \sum_{i=1}^{q}S_{iz}=0,$$

For a one dimensional problem the Hamiltonian can be expanded in a Taylor expansion in the single phase space variable x about $x = x_o$, where the constraint

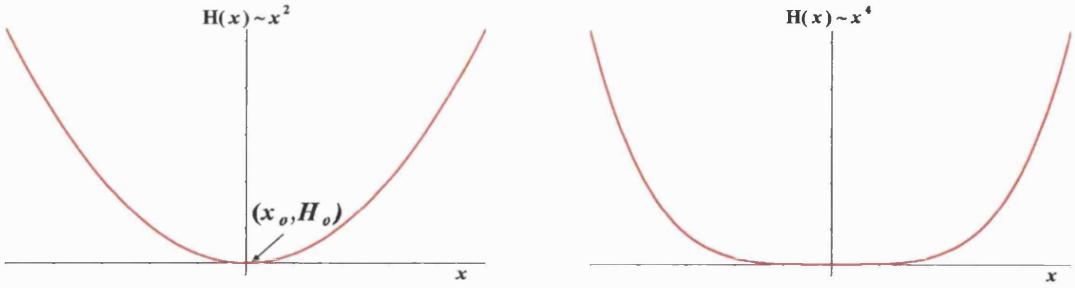

(a) Quadratic potential.

(b) Quartic potential.

Figure 1.8: Restoring forces for displacement away from $x = x_o$.

is satisfied and there is a minimum in energy $H_o = H(x_o)$. We can consider the energy of the system as a function of its position in phase space.

$$H(x) = H_o + \left.\frac{\partial H}{\partial x}\right|_{x=x_o} (x - x_o) + \frac{1}{2}\left.\frac{\partial^2 H}{\partial x^2}\right|_{x=x_o} (x - x_o)^2 + \ldots \tag{1.11}$$

The linear term in $(x - x_o)$ in this expansion is zero by definition, since otherwise there would not be a minimum. The constraint should give rise to an harmonic restoring force for displacement from $x = x_o$ (see Fig. 1.8(a)). The first term in the Taylor expansion should therefore be quadratic [24, 25].

From this argument, in the multi-dimensional problem considered here, each constraint should have an harmonic force associated with it and therefore a quadratic term in the Hamiltonian. By equipartition of energy, each quadratic term (which is called a quadratic mode) in the Hamiltonian contributes $\frac{k_B T}{2}$ to the specific heat. Therefore for a unit cell, the specific heat is equal to the number of constraints multiplied by $k_B T/2$. There are q spins in every unit cell, with two degrees of freedom per spin (for Heisenberg spins). When $q = 4$ (pyrochlore lattice) there will be eight degrees of freedom per unit cell, and eight modes. Associated with every unit cell in the pyrochlore lattice is an up tetrahedron and a down tetrahedron, even though there are only four sites in the unit cell (rhombohedral). The constraint applies to all tetrahedra in the lattice, and there are therefore six constraints per unit cell (three for each tetrahedron). This leaves two unconstrained degrees of

freedom for the unit cell, which contribute zero to the specific heat. These are true 'zero modes'. The specific heat per unit cell is thus:

$$C_h = 6 \times \frac{k_B T}{2} + 2 \times 0 = \frac{6 k_B T}{2}$$
$$\frac{C_h}{N k_B T} = \frac{3}{4},$$

where C_h/Nk_BT is the specific heat per spin.

Remarkably it is found that at some *special* points on the energy surface (if they exist), the constraints are imposed in a non-linear way. The leading term in Eqn. (1.11) is quartic. The cost in energy by making these fluctuations is zero in the harmonic approximation and they are sometimes called 'zero modes'. The cost in energy for displacement out of $x = x_o$ is quartic in x, which for small x is effectively zero. These 'soft modes' give a quartic restoring force to the energy surface (see Fig. 1.8(b)). The quartic terms in the Hamiltonian, or quartic modes, contribute $k_BT/4$ to the specific heat [24].

The specific heat then depends on the number of quadratic and quartic modes per unit cell.

$$\frac{C_h}{N k_B T} = \frac{(\#\,\text{of quadratic modes} \times \frac{1}{2}) + (\#\,\text{of quartic modes} \times \frac{1}{4})}{q} \tag{1.12}$$

The quartic modes are not true zero modes, but are the result of specific collective organisation of all the spins of the system, which leads to the quartic corrections. In order to determine if there are any quartic modes in the system, the normal modes of the system must be calculated, which are associated with different ground states (*i.e.* different parts of phase space) (see section 2.3).

1.2.6 The Effect of Quartic Modes on the Entropy and Order by Disorder

Quadratic modes contribute $O(T)^{1/2}$ to the partition function Z and quartic modes contribute $O(T)^{1/4}$ [24]. The partition function for the region of phase space

containing the ground states characterised by N_4 quartic modes and N_2 quadratic modes can be expressed [25]:

$$Z = A(T)^{\frac{N_4}{4}+\frac{N_2}{2}}, \qquad A = a^N, \tag{1.13}$$

with a a constant of order unity. The derivation of this expression is shown in Appendix B. The partial free energy $G = -T\ln(Z)$ for this area of phase space is thus [25]:

$$G = -TN\ln(a) - T\left(\frac{N_4}{4} + \frac{N_2}{2}\right)\ln(T). \tag{1.14}$$

The partition function defined in Eqn. (1.13) represents the probability of the system existing in that part of phase space. As $T \to 0$ the second term in Eqn. (1.14) is positive since $\ln(T \to 0) < 0$. In order to minimise the free energy, the system will choose to exist in a part of phase space with N_4 at a maximum, so that the positive term in Eqn. (1.14) is a minimum [25].

The entropy of the system can easily be defined in terms of the free energy in zero field:

$$S = \frac{U - G}{T}. \tag{1.15}$$

Clearly when the free energy is at a minimum the entropy will be at a maximum. This effect can be described in different way.

The curves in Figure 1.8 describe the limit of the allowed fluctuations in energy, as a function of temperature. For a fixed energy excitation, the system in a quartic potential can fluctuate further from the ground state. This is illustrated in Figure 1.9, where x_2 represents the maximum displacement in a quartic potential and x_1 represents the maximum displacement for a quadratic potential; clearly $x_2 > x_1$. If the system can fluctuate further out of the ground state it will have a higher entropy associated with it. The quartic fluctuations are 'soft fluctuations'.

The concept of 'order by disorder' was first suggested by Villain *et al.* [26] who considered a 'toy model' which showed long-range ferromagnetic order at finite temperature, but which was strictly disordered at T=0. In all of these ground

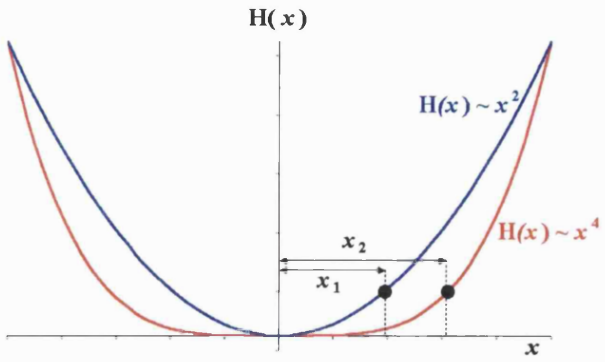

Figure 1.9: Different fluctuations out of the ground state.

states the internal energy U of the system is the same, and for $T = 0$ the system will have no order. The degeneracy of the ground states leads to a configurational entropy contribution to the free energy, since the system can explore all of the degenerate ground state manifold, unlike an ordered system which has only one configuration. However, anomalous soft fluctuations out of a particular ground state can sometimes occur, as described above. If there are many of these modes and they are sufficiently soft, the system will spend more time in this nearby part of phase space. If the entropy gained by making these soft fluctuations dominates that associated with exploring the ground state manifold, then the system will spend all of its time in these states [27]. The existence of these soft quartic modes is associated with collective behaviour of all the spins in the system. Often this leads to a form of long-range order. The order can be simply coplanarity of all the spins such as in the kagomé Heisenberg antiferromagnet [24] or the nematic order of the XY pyrochlore antiferromagnet [28] (see also section 4.1.1). The selection of these states can be associated with a phase transition, an 'order by disorder transition' [29].

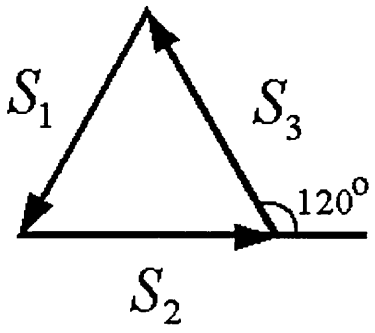

Figure 1.10: $S_1 + S_2 + S_3 = 0$ for three spins on a triangular plaquette, which necessarily lie in a plane.

1.2.7 Frustrated Antiferromagnets

This section introduces some examples of appropriate frustrated systems with $q = 3$ and $q = 4$ plaquettes.

$q = 3$: Heisenberg spins on the kagomé lattice

The kagomé lattice is one of corner-sharing triangles, and is a common structure for many real compounds [18] (see Fig. 1.11(a)). The lattice is described by the $12k$ sites of the $P6_3/mmc$ space group. Antiferromagnets on the kagomé lattice are frustrated for the same reasons described in section 1.2.3.

If there is zero moment on every triangle, this is a ground state (see section 1.2.5). For this to occur the three spins must necessarily lie in a plane, mutually oriented at 120° to one another (see Fig 1.10). There is a macroscopic degeneracy of ground states since there are many ways of fitting these planar units together [24].

There are two special points on the ground state manifold which correspond to long-range ordered states of the system: (i) the 'q=0'[a] ground state structure, where the arrangement of spins is the same on every triangular unit cell (see

[a]note that in this thesis 'q' and 'k' are both used as a label for a wave vector

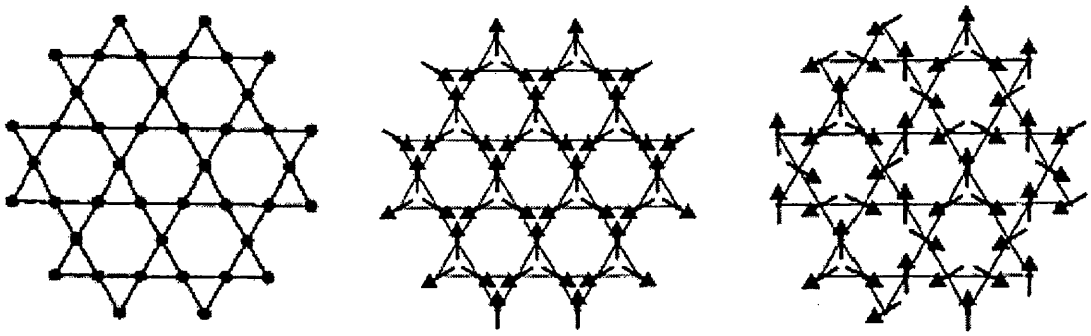

(a) Kagomé lattice of corner-sharing triangles (b) q=0 (c) $\sqrt{3} \times \sqrt{3}$

Figure 1.11: The Kagomé lattice and its ordered antiferromagnetic ground states, after Frunzke *et al.* [31].

Fig. 1.11(b)), (ii) the '$\sqrt{3} \times \sqrt{3}$' ground state structure, which has $q_{\sqrt{3}} = 2\pi(\frac{2}{3}, \frac{2}{3})$ (see Fig. 1.11(c) [30]). In both these ground states all the spins in the system are arranged in the same plane. However, there are also *many* coplanar ground states in which the spins are disordered [24].

In this system thermal fluctuations cause the spins to select ground states in which all the spins are coplanar. There are soft fluctuations out of these coplanar ground states. These are quartic modes (see section 1.2.6), and the energy cost of these fluctuations is zero in the harmonic approximation. Chalker *et al.* [24] determined that the most zero modes occurred out of these coplanar states. It was reasoned in section 1.2.6 that a system will select ground states with the most zero modes. This selection is therefore an example of an order by disorder mechanism.

As mentioned in section 1.2.5 the specific heat per spin is sensitive to the presence of quartic modes. A similar mode counting argument can been used to predict the low temperature specific heat of the system as follows. In the kagomé lattice the unit cell consists of three Heisenberg spins with six degrees of freedom. There are two triangles ('up' and 'down') in each unit cell, so there are six constraints. In the absence of any quartic modes the specific heat per spin

would simply be:

$$\frac{C_h}{Nk_BT} = \frac{6 \times \frac{1}{2}}{3} = 1. \tag{1.16}$$

Chalker *et al.* [24] determined the normal modes of the system out of a set of coplanar ground states and found that one quadratic mode becomes quartic. The specific heat per spin therefore becomes:

$$\frac{C_h}{Nk_BT} = \frac{\left(5 \times \frac{1}{2}\right) + \left(1 \times \frac{1}{4}\right)}{3} = \frac{11}{12}. \tag{1.17}$$

Monte Carlo simulations of the specific heat for the system confirmed this value [24]. The q=0 and $\sqrt{3} \times \sqrt{3}$ structures are special members of this set of coplanar ground states because they are characterised by a single wave vector. The precise nature of the nematically ordered states was a topic of considerable debate [32, 33, 30]. The most convincing results suggested that there were $\sqrt{3}\times\sqrt{3}$ correlations in the system, but as $N \to \infty$ the $\sqrt{3}\times\sqrt{3}$ moment tended to zero [30], and there is possibly no long-range order in the system at all.

A good example of an experimental kagomé system is the jarosite series $AB_3(SO_4)_2(OH)_6$ (where A=Na^+, K^+, H_3O^+; B= Fe^{3+}, Cr^{3+}, V^{3+}). When these systems order, they show q=0 structures in every case, in contradiction to theoretical predictions [31, 18]. These lattices are not 'perfect' kagomé systems and are made up of stacked kagomé layers. It has been suggested that the disagreement between experiment and theory is due to interplanar interactions having an effect on the intraplanar spin configurations [18].

$q = 4$: Heisenberg spins on the pyrochlore lattice

Determination of states satisfying the ground state condition for the Heisenberg pyrochlore is quite straightforward. Such states can be obtained by associating the four spins into two sets of anti-parallel paired spins (these are of course not the only possible ground states). This leads to an infinite number of possible ground states [21]. It has been shown that any particular ground state can be continuously

deformed into any other at no extra cost in energy [28]. The ground state manifold is said to be 'fully connected'. Monte Carlo simulations have shown there to be no order by disorder [27, 28]. No ordering or freezing of the spins is observed, and the system is never expected to show static Néel order even at $T = 0$ K [23, 34, 27].

In section 1.2.5 the modes of the system were discussed. In this case the number of constraints is less than the number of degrees of freedom. In the condensed state this is rare, and the Heisenberg pyrochlore system is said to be a classical spin liquid or a 'cooperative paramagnet' [21]. Calculations on a similar quantum system show no ordering either, and the system is said to be a 'quantum spin liquid' [35, 36].

$Gd_2Ti_2O_7$ has been proposed as a possible experimental realisation of a classical spin liquid, but the system shows ordering at a finite temperature [37]. This is discussed in more detail in Chapter 7, where new experimental results are discussed.

1.2.8 Frustrated Ferromagnets

Until very recently the *only* known frustrated ferromagnetic system was the $\langle 111 \rangle$ Ising pyrochlore already mentioned. In fact this system is one of the most frustrated of all. It is related to the problem of antiferromagnetic Ising spins on the same lattice. The ground state for such a system is one with two spins pointing up and two spins pointing down (see Fig. 1.12). Anderson related the up/down states of the spins to the positions of protons on the ice-lattice [14] (see also section 1.1). However, (a) Anderson's model is unphysical in that it breaks the cubic symmetry of the pyrochlore lattice; (b) there is no direct relationship between spin position and proton position. Harris *et al.* [11] made explicit the link between spin direction and proton position, the 'spin ice mapping' [15]. Thus all three systems are frustrated to the same degree. The problem is to a first approximation an experimental realisation of the 16-vertex model of statistical mechanics [38].

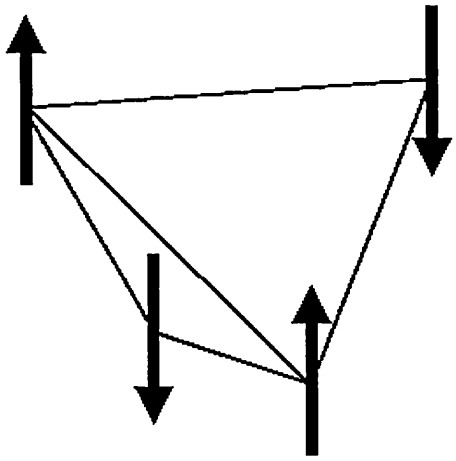

Figure 1.12: Ground state of the Ising Pyrochlore antiferromagnet

Recently, a kagomé analogue of spin ice was discovered [39]. This model system also consists of Ising spins and has a macroscopic ground state degeneracy. Integration of the specific heat confirmed it also had a zero-point entropy [39].

1.3 Degeneracy Lifting in Frustrated Systems: Perturbations of the Simple Model

In some special cases the degeneracy in frustrated systems can be lifted by adding extra perturbations into the Hamiltonian, or sometimes collective action of all the spins in the system causes order (see section 1.2.5).

1.3.1 Application of a Magnetic Field

When a magnetic field is applied to $Ho_2Ti_2O_7$ along the [110] direction, two classes of magnetic Bragg peaks are observed. The Bragg peaks are consistent with q=0 or q=X ordering in the system [11]. The q=0 structure is effectively the arrangement of spins in Figure 1.3 on *every* 'up' or 'down' tetrahedron in the lattice. Figure 1.13(a) illustrates how two spins on every tetrahedron are fixed to have

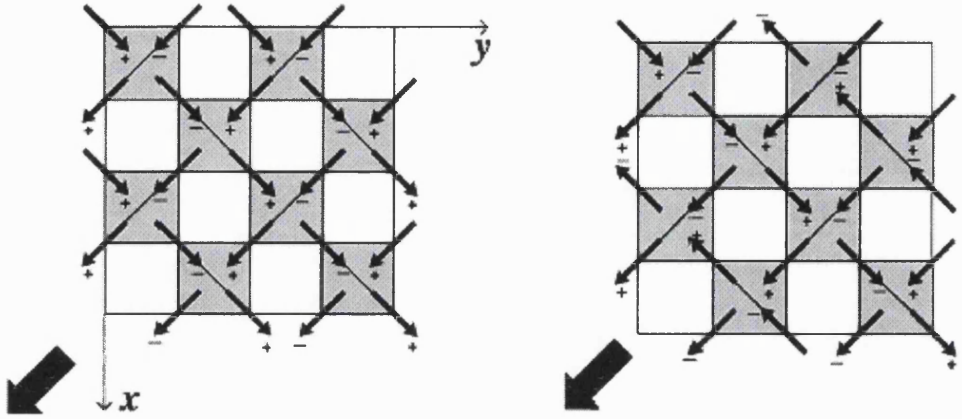

(a) The q=0 structure (b) The q=X structure

Figure 1.13: The magnetic structures observed in $Ho_2Ti_2O_7$, projected down the z-axis. The tetrahedra are shown as grey squares, with the '+' and '−' representing the sign of the S_z component of each spin. The bold arrow indicates the direction of the applied field, after Harris *et al.* [11].

components in the direction of the field, and so gain energy by coupling with it. In the simple model the other two spins on the tetrahedron are theoretically decoupled with respect to the field. One possibility is that they choose to arrange themselves so that the configuration of spins on every 'up' or 'down' tetrahedron is the same, the q=0 structure. Another possibility is that the decoupled spins adopt an antiferromagnetic arrangement, the q=X structure (see Figure 1.13(b)). This is a particularly interesting result since in the simple model they should not order as they are decoupled. This could be an effect of the dipolar interactions at work in the real material or even quantum fluctuations playing a role in the ordering processes.

Harris *et al.* [40] performed Monte Carlo simulations of the Ising pyrochlore ferromagnet in an applied magnetic field. When a field is applied to the system,

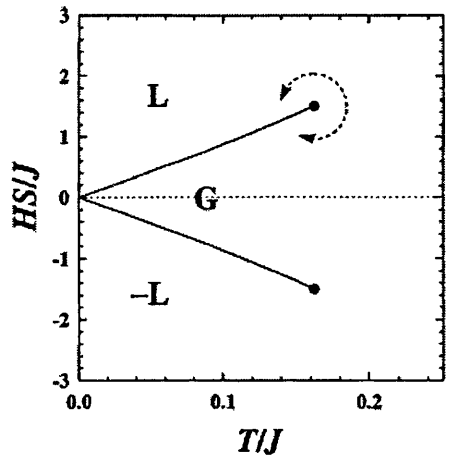

Figure 1.14: The phase diagram for the spin ice model with the magnetic field applied along the [100] direction, after Harris *et al.* [40].

an extra term is added to the Hamiltonian,

$$\mathbb{H} = -J \sum_{<i,j>} \mathbf{S}_i \cdot \mathbf{S}_j - \sum_{i=1}^{N} h \cdot \mathbf{S}_i, \tag{1.18}$$

where the vector h denotes the direction and strength of the applied magnetic field. In this case the field was applied along the [100], [110] and [111] directions. When the field was applied along the [100] direction the degeneracy was lifted due to the coupling of all of the spins with the field. The transition was first-order and occurred at a finite applied field [40]. There is also a critical temperature and field associated with the termination of the phase transition line (see Fig. 1.14). This line separates two phases with the same symmetry but different magnetization, and is considered to be like that of the liquid-gas transition in a fluid (see section 1.4).

When the field was applied along the [110] direction, two of the spins on every tetrahedron were coupled with the field. The spins perpendicular to the field remained truly independent and randomly ordered. There is ordered moment only from two of the spins in every tetrahedron and no phase transition is observed [40].

More complex behaviour is observed when the field is applied along the [111] direction. With the field along the [100] and [110] directions, the spins in each

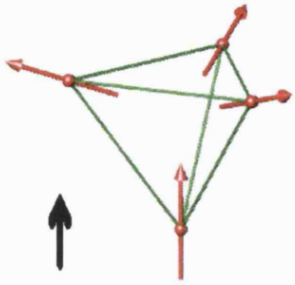

Figure 1.15: The configuration of spins with 1 in and three out when the magnetic field is applied along the [111] direction. The bold arrow represents the direction of the applied field.

case which *did* couple to the field, did so by the same amount. The ice-rules were preserved in both cases. With the field along the [111] direction one of the spins on every tetrahedron is parallel with the field and has coupling different from the other spins. The amount of coupling is dependent on the projection of the direction of the spin onto the direction of the field. So, in this case one of the spins has a full projection onto the field. It is locked instantly into alignment with the field and the rest of the spins arranged according to the satisfaction of the ice-rules. As the magnetic field increases it manages to break the ice-rules degeneracy to give a ground state with one spin pointing into the tetrahedron and three pointing out (see Fig. 1.15) [40, 16]. Magnetization curves for all three cases are shown in Figure 1.16.

Bulk magnetization experiments on a single crystal of $Ho_2Ti_2O_7$ showed qualitatively similar results to that of the theory with the field along the [100] and [111] directions [16]. The observed saturated moment along the [111] direction was 20 % higher than expected. With the field along the [110] direction more anomalous behaviour was observed with much slower saturation of the moment with respect to the other field directions. The value of the saturated moment was higher than that expected in the theory and put down to the effect of dipolar interactions in the

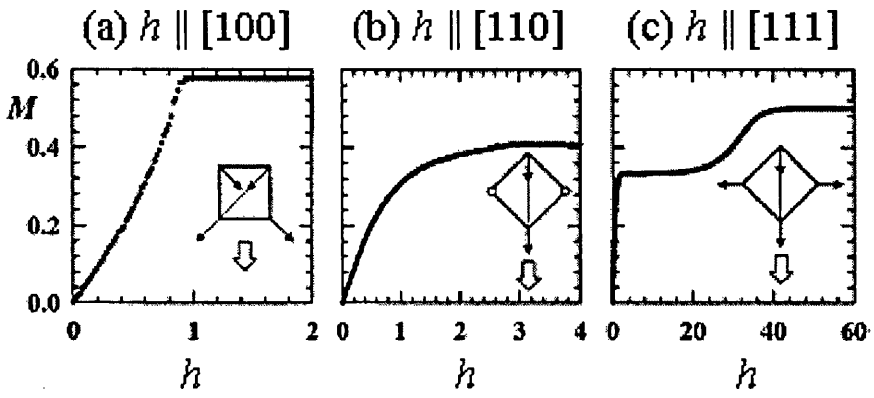

Figure 1.16: The magnetization, M, per spin for the spin ice model, calculated at a temperature of $T/J = 0.1$, with a magnetic field, H, applied along the three symmetry directions of the pyrochlore lattice: (a) [100], (b) [110], and (c) [111]. Beneath each magnetization curve is shown a view of a single tetrahedron of spins looking down its 4_1 axis, thus appearing as a square in projection. The black arrows represent the projections of spins ordered by the maximum field applied in each case, while the open circles represent spins unaffected by the field and thus disordered. The white arrows show the projections of the field directions, after Harris *et al.* [40].

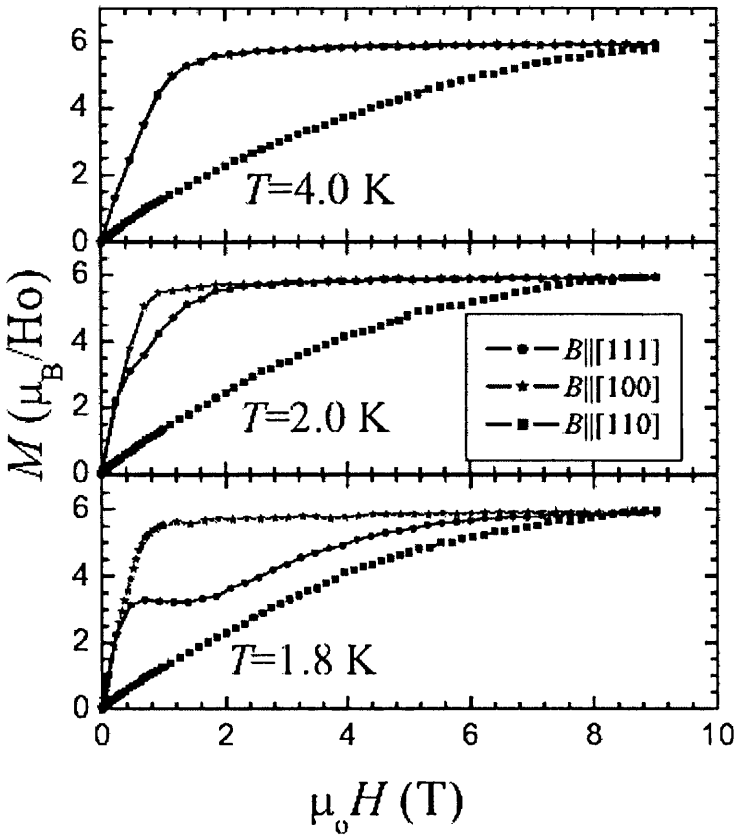

Figure 1.17: Magnetization as a function of applied magnetic field along the listed crystalline directions for $Ho_2Ti_2O_7$ at various temperatures, after Cornelius and Gardner [16].

material [16, 11, 40]. Conversely, recent magnetization measurements on a single crystal of $Dy_2Ti_2O_7$ showed excellent agreement with theoretical predictions [41].

Further investigations have been carried out on the system and are described in section 8.1.

1.3.2 Effect of Dipolar Interactions

In real materials there are often much longer interactions than nearest neighbour exchange. These are magnetic dipole-dipole electrostatic interactions, and their

strength depends on the size of the magnetic moment of the cation and the distance between the interacting moments ($1/r^3$). Rare earth cations have relatively large magnetic moments, and the dipole energy is not inconsiderable. The dipolar energy scale is typically O(1 K) (see Eqn. (1.20)). This is important since the exchange interaction J is typically of the same order.

The dipole energy is defined as an extra term in the Hamiltonian:

$$\begin{aligned} H &= -J\sum_{\langle ij\rangle} \mathbf{S}_i^{z_i}\cdot\mathbf{S}_j^{z_j} \\ &+ Dr_{\rm nn}^3\sum_{i>j}\frac{\mathbf{S}_i^{z_i}\cdot\mathbf{S}_j^{z_j}}{|\mathbf{r}_{ij}|^3} - \frac{3(\mathbf{S}_i^{z_i}\cdot\mathbf{r}_{ij})(\mathbf{S}_j^{z_j}\cdot\mathbf{r}_{ij})}{|\mathbf{r}_{ij}|^5}, \end{aligned} \tag{1.19}$$

where Ising spins $\mathbf{S}_i^{z_i}$ of unit length are constrained to their local $z_i = \langle 111\rangle$ axes; J is a near neighbour exchange coupling and D the dipolar coupling. Because of the local Ising axes the effective nearest neighbour energy scales are $J_{\rm nn} \equiv J/3$ and $D_{\rm nn} \equiv 5D/3$ [42, 43, 44]. This sum effectively defines interactions between every possible pair of spins on the lattice (*i.e.* 2$^{\rm nd}$ nearest neighbours, 3$^{\rm rd}$ nearest neighbours etc. across the whole lattice). There is some disagreement when to cut off the interactions. Some have chosen to stop at the 5$^{\rm th}$ or 12$^{\rm th}$ nearest neighbour interaction [45, 46], whereas another, possibly more accurate method, is to use the Ewald summation which considers an effective dipole-dipole interaction between *all* the spins in the system [47, 48]. The discussion here will only relate to the results from simulations using the Ewald summation technique, which gives results in agreement with experiment. For a particular cation the dipolar coupling $D_{\rm nn}$ is a constant value and can be defined:

$$D_{nn} = \frac{5}{3}\left(\frac{\mu_o}{4\pi}\right)\frac{\mu^2}{r_{\rm nn}^3} \approx +2.35{\rm K}, \tag{1.20}$$

where $r_{\rm nn} = 3.54$ Å for both $Ho_2Ti_2O_7$ and $Dy_2Ti_2O_7$. With both the nearest neighbour and dipolar interaction taken into account there is an *effective* nearest neighbour energy scale $J_{\rm eff}$, for (111) Ising spins:

$$J_{\rm eff} \equiv J_{\rm nn} + D_{\rm nn}. \tag{1.21}$$

Since for Ho and Dy, D_{nn} is fixed (see Eqn. (1.20)), the only variable in this equation is the nearest neighbour exchange J_{nn}. Simulations were performed by den Hertog and Gingras [42] for systems with various J_{nn}. The existence of spin ice properties were followed by numerical integration of the specific heat, such that the entropy was within a few percent of the Pauling value in Eqn. (1.4) [42]. For all $J_{nn} > 0$ spin ice behaviour was observed in the system [42]. This behaviour actually existed for $J_{nn} \gtrsim -0.91$. Values for the exchange in the real systems were fitted according to the shape and maximum of the experimental specific heat measurements. These values were negative for both $Ho_2Ti_2O_7$ ($J_{nn} \sim -0.52$K) [17] and $Dy_2Ti_2O_7$ ($J_{nn} \sim -1.24$K) [42]. This could go some way to explaining the anomalous antiferromagnetic characteristics observed in the susceptibility measurements of Cashion [12]. Both values give $J_{eff} > 0$ in agreement with the frustrated nearest neighbour spin ice model. For $J_{nn} < -0.91$ a second-order phase transition was observed to the non-degenerate FeF_3 structure with all spins either pointing into or out of every tetrahedron [49, 50]. In these single spin flip simulations the dipolar interactions have not lifted the degeneracy.

When the model is simulated with loop dynamics (loops of spins are flipped each step such that there is no increase in the exchange energy term of the Hamiltonian, the dipolar term does increase), the system undergoes a first-order phase transition to a q=X type ordered state [43].

1.3.3 Effect of Finite Anisotropy

For an Ising system the anisotropy of the spin is effectively infinite. It is also possible to apply a finite anisotropy to the system. In such cases this also lifts the degeneracy of the system allowing the spins to cant off their easy-axes. Further details of this investigation are discussed in Chapter 3.

1.4 Phase Transitions in a Fluid System

In nature three different phases of a material system are commonly observed: solid, liquid and gas. The existence of these three phases is governed by a functional relationship between the thermodynamic parameters pressure p, density ρ and temperature T, of the form $f(P, \rho, T) = 0$, known as the equation of state.

The Gibbs free energy is expressed naturally as a function of temperature and pressure $G(T, p)$ and is therefore the correct thermodynamic function to describe the experimental situation where T and p are the independent variables. In this situation volume (and entropy) are dependent variables and equilibrium corresponds to the minimum of G with respect to these variables. For a particular pressure and temperature the phase with the lowest Gibbs free energy will therefore be the most stable.

The solutions to the equation of state are therefore those with a minimum in the free energy. At certain points in the three-dimensional coordinate system of p, T and ρ there are singularities in the free energy, and it changes discontinuously (see section 1.4). When this occurs it defines a phase transition between two phases; these points are often joined together to form a 'phase boundary line'. On the phase boundary line the Gibbs free energy is the same for both phases. Both phases are equally stable and there is equilibrium between them [51]. The conditions on the Gibbs free energy apply equally to the chemical potential μ since it is the Gibbs free energy per particle $g(T, p)$.

The Gibbs free energy is related to the enthalpy H and entropy S of a system by Eqn. (1.22) and to chemical potential by Eqn. (1.23), where N is the number of particles in the system.

$$G = H - TS \quad G = Ng(T, p) \tag{1.22}$$

$$\mu = \left(\frac{\partial G}{\partial N}\right)_{p,T} = g(T, p) \tag{1.23}$$

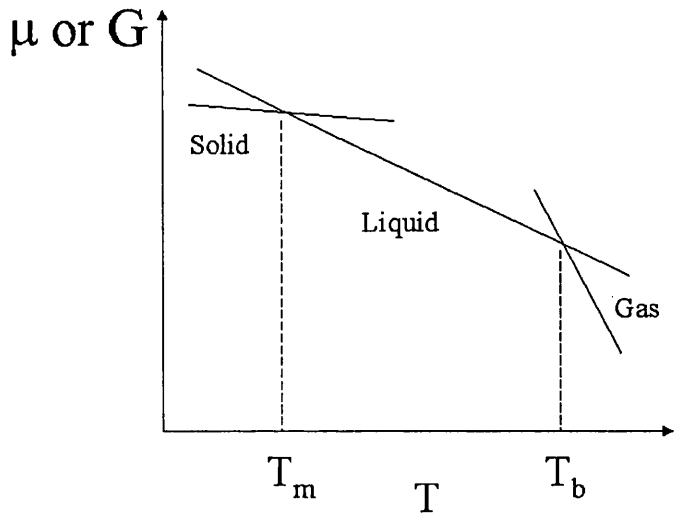

Figure 1.18: Chemical potential/Gibbs free energy versus temperature at constant pressure, for a pure substance.

In a plot of the chemical potential of a system versus temperature at a constant pressure (see Fig. 1.18), the selection of a phase is observed according to which one has the lowest chemical potential. At T_m, the melting point, the solid and liquid phases have the same μ, the phases coexist and the system is at equilibrium. This point corresponds to a particular point on the phase boundary line. The same applies to the boiling point T_b.

It is convenient to consider projections of the surface onto the pT, ρp and ρT planes. These are shown in Figures 1.19(a), 1.19(b) and 1.19(c) respectively. In Figure 1.19(a), the representation of separate regions of solid, liquid and gas is called the phase diagram. Each phase boundary line represents equilibrium between the respective phases (*i.e.* the vapour pressure curve between liquid and gas, the sublimation curve between solid and gas and the fusion curve between solid and liquid). The triple point, at which there is equilibrium between all three phases is also observed. The vapour pressure curve terminates at the so-called critical point, beyond which there is no observable difference between the

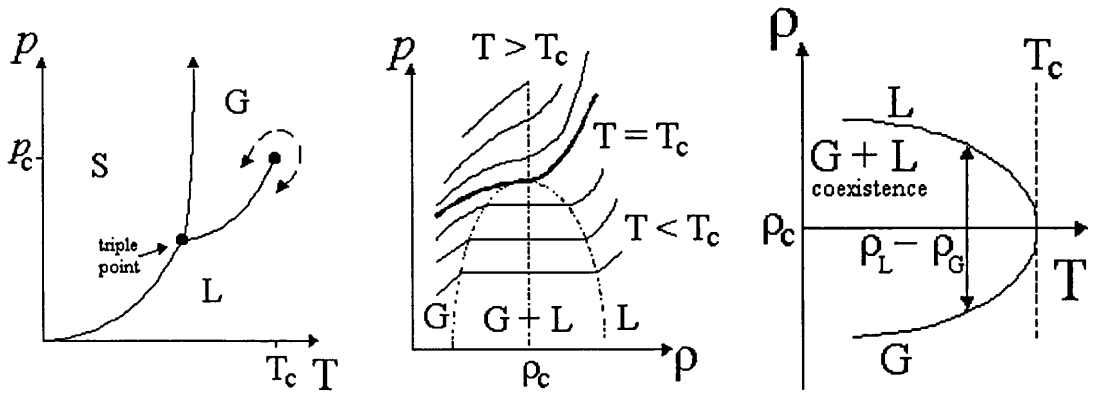

(a) pT plane (b) $p\rho$ plane (c) ρT plane

Figure 1.19: Projection of the surface onto different thermodynamic planes.

liquid and gaseous phases (*i.e.* $\rho_l = \rho_g$). The critical point has an associated temperature T_c, pressure p_c and density ρ_c. Figure 1.19(a) also shows that it is possible to convert a liquid to a gas without crossing the phase boundary line.

First-order phase transitions

The plot of chemical potential versus temperature is equivalent to that of Gibbs free energy versus temperature at constant pressure ($p < p_c$, see Fig. 1.18). For each phase G changes with temperature and at the equilibrium point the Gibbs free energy of the two phases is equal. Rewriting Eqn. (1.22) in terms of a change between two phases a and b:

$$\Delta_b^a G = \Delta_b^a H - T\Delta_b^a S \tag{1.24}$$
$$\Delta_b^a G = 0 \rightarrow \Delta_b^a H = T\Delta_b^a S$$

There is a change in entropy and enthalpy between the two phases, so there is a latent heat associated with the change from one phase to the other. If the entropy and volume are expressed as derivatives of the Gibbs free energy:

$$\left(\frac{\partial G}{\partial T}\right)_p = -S, \quad \left(\frac{\partial G}{\partial p}\right)_T = V, \tag{1.25}$$

the entropy of each phase corresponds to the slope of the line for each phase in Figure 1.18. At T_m and T_b the slope changes discontinuously. This is the main feature of a first-order phase transition. Therefore a **first-order phase transition** is defined as *that in which a discontinuity in one or more of the first derivatives of the free energy G occurs, such as the volume or the entropy.*

Second-order phase transitions

The next case to consider is what happens to the system when we travel along the liquid-gas phase boundary line. For $T > T_c$ the phases are not distinguishable as mentioned above. For $T < T_c$ there is coexistence of the liquid and gas phases, resulting in the observation of two separate densities. This is known as phase separation. The difference between the densities smoothly increases as the temperature is decreased, as shown in Figure 1.19(c). The parameter $\rho_L - \rho_G$ is known as the order parameter and at $T = T_c$ there is a critical phase transition. The order parameter has the property that it is non-zero below the phase transition, and zero above it. This is a general property of order parameters and is valid for all phase transitions.

For the change from a non-differentiable mixture to the coexistence of two phases, there is no discontinuity in the first derivatives of the Gibbs free energy, since the entropy is the same on both sides of the transition. If *all* the derivatives of the free energy are continuous at the transition, then this is referred to as a *continuous* or *critical* phase transition. In this case there is often a discontinuity observed in the second derivative of the Gibbs free energy, such as the specific heat C_p,

$$C_p = -T\left(\frac{\partial^2 G}{\partial T^2}\right)_p,$$

and the transition is referred to as a **second-order** phase transition. At a second-order phase transition there is a continuous change of the order parameter with respect to T, whereas in a first-order phase transition there is a discontinuity in

the order parameter.

It should be noted that thermodynamics only describes experimental observations of systems, it does not explain them.

1.5 Phase Transitions in a Magnetic System

This section deals with the properties of a simple ferromagnet. To study magnetic systems there are two important changes of variable. If pressure is applied to a fluid system the density increases, and if a magnetic field (h) is applied to a ferromagnetic system the magnetization (M) increases. Therefore the pressure is analogous to the field and the density to the magnetization. The magnetization is also the order parameter. The equation of state becomes a function of the magnetic field, magnetization and temperature. Substitution of the thermodynamic parameters also takes place [52].

$$V \to -M \quad \text{and} \quad p \to h$$

This results in the following thermodynamic relations:

$$G = A - Mh, \quad A = U - TS \quad \text{and} \quad H = U - Mh \tag{1.26}$$

$$\left(\frac{\partial G}{\partial h}\right)_T = -M \quad \text{or} \quad \left(\frac{\partial A}{\partial M}\right)_T = h, \tag{1.27}$$

$$\left(\frac{\partial G}{\partial T}\right)_h = -S \quad \text{or} \quad \left(\frac{\partial A}{\partial T}\right)_h = -S. \tag{1.28}$$

Similarly to the fluid system, if the temperature and magnetic field are imposed, there is a minimum in the magnetic Gibbs free energy, with respect to the magnetization (the dependent variable).

The projection of the thermodynamic surface onto the hT, Mh and MT planes is shown in Figures 1.20(a), 1.20(b) and 1.20(c). The projection onto the hT plane

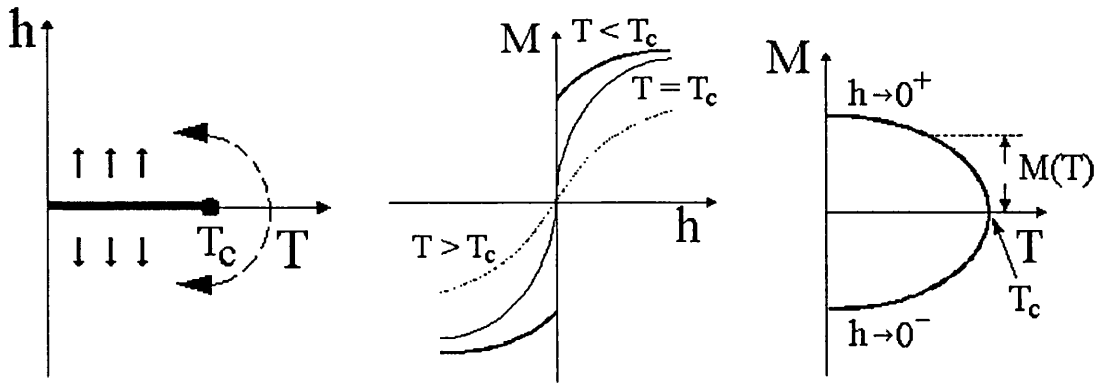

(a) hT plane (b) Mh plane (c) MT plane

Figure 1.20: Projection of the surface onto different thermodynamic planes.

is much simpler for a magnetic system and two distinct phases are observed: i) with predominantly all the spins up and ii) with predominantly all the spins down (see Fig 1.20(a)). The symmetry of the phase diagram is due to the symmetry of a ferromagnet under reversals of the magnetic field.

Figure 1.20(b) shows the projection of the surface onto the Mh plane for various values of temperature, where obvious parallels can be drawn between the shapes of the isotherms of the two systems. The simpler picture for the magnetic system is again due to the symmetry previously mentioned. Isotherms crossing the phase boundary ($T < T_c$) result in a first-order phase transition and a discontinuous change in the order parameter. This symmetry does not exist for the liquid-gas transition. There is a critical point at T_c and $h_c = 0$ which terminates the line of first-order phase transitions.

The isotherm for $T > T_c$ is continuous. This is not a continuous phase transition, but reflects a continuous change in the magnetization from one sign to the other as the direction of the field is switched. It also represents part of a curve in which the system can change from all the spins pointing up to all the spins pointing down without crossing the phase transition line, analogous to that of the fluid system.

For the projection on to the MT plane a similar diagram to the fluid system again exists (see Fig. 1.20(c)). In the ferromagnetic system for $T < T_c$ there are two possible minima in the free energy for the system to choose and the system *has* to pick a state with *either* the majority of spins up or with the majority of spins down. There is no coexistence and symmetry breaking occurs instead. As a paramagnetic system is cooled from high temperature, small pockets of parallel spins form amongst a sea of disordered spins. Gradually the pockets become larger and larger and the system makes its choice which minimum to pick (either all up or all down).

In reality this is slightly inaccurate since domains form and there is coexistence, which is due to the interaction of the dipole moments. This projection is along the $h = 0$ cross-section of the hMT surface and for $T > T_c$ $M = 0$. This part of the line represents a paramagnetic phase and at $T = T_c$ there is a second-order or continuous phase transition, since there is a continuous increase in the order parameter with respect to temperature. There is no discontinuity in the first derivative but there is a discontinuity in the specific heat C_h:

$$C_h = -T \left(\frac{\partial^2 G}{\partial T^2} \right)_h . \tag{1.29}$$

There is another discontinuity in the isothermal susceptibility χ_T which is another second derivative of the Gibbs free energy:

$$\chi_T = \left(\frac{\partial M}{\partial h} \right)_T = - \left(\frac{\partial^2 G}{\partial h^2} \right)_T . \tag{1.30}$$

The discontinuity in the susceptibility can be understood by considering the consequences of determining the gradient defined in Eqn. (1.30) on Figure 1.20(b). For all $T \leq T_c$ isotherms the gradient is infinite.

1.6 Critical Behaviour of Magnetic Systems

1.6.1 Critical Exponents

Section 1.5 stated that quantities such as the susceptibility and specific heat have discontinuities, or divergences close to the critical point. With the notion of universality (see section 1.6.2) it is important to understand the nature of these divergences, and the singular behaviour of the thermodynamic functions near the critical point.

More often than not, the divergence of these quantities follows a simple power law. For example, a measure of proximity to the critical temperature called the reduced temperature t is defined

$$t = \frac{T - T_c}{T_c}. \tag{1.31}$$

It has been observed that measurements of the isothermal susceptibility close to the critical point, in small fields, fit the law:

$$\chi_T = at^{-\gamma}, \tag{1.32}$$

where a and γ are constants. This relationship can be rearranged very easily and it is obvious that a plot of $\log \chi_T$ versus $\log t$ will have a slope of $-\gamma$. This is illustrated in Figure 1.21 which shows such a plot for iron alloyed with 0.5 % tungsten. The plot gives a value of 1.33 to the constant γ. The indices in the various power laws, such as γ, are called critical exponents. The numerical values of the critical exponents vary from substance to substance and property to property, but very often a power law fit is observed.

Critical exponents can be defined in a more general fashion. If a function $f(x)$ has critical exponent λ close to the critical point $x = 0$, as the critical point is approached from positive x,

$$f(x) \sim x^{\lambda} \quad \text{when} \quad x \to 0^{+}. \tag{1.33}$$

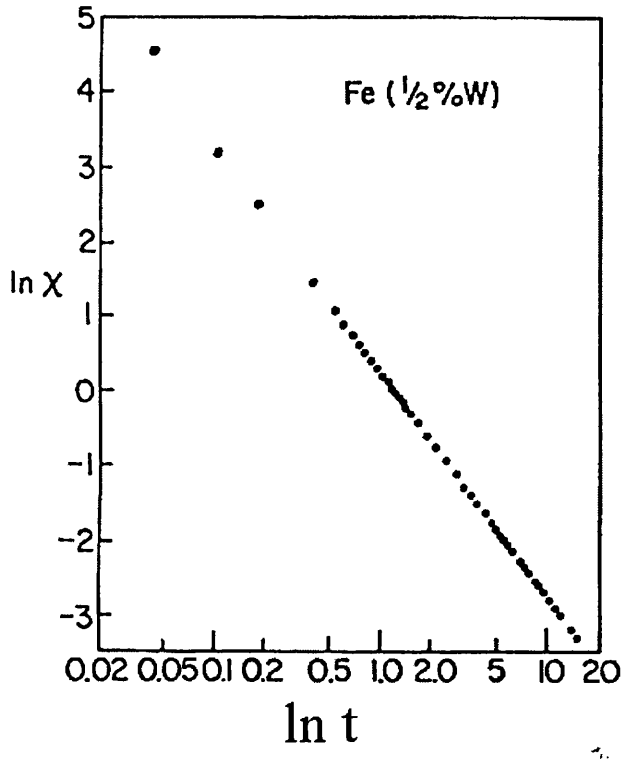

Figure 1.21: $\ln \chi$ vs $\ln t$ for a ferromagnet, after Noakes *et al.* [53]

Another way of expressing this is:

$$\lambda = \lim_{x \to 0^+} \frac{\ln f(x)}{\ln x}. \tag{1.34}$$

Analogous exponents λ' can be defined for $x \to 0^-$. Early Renormalisation Group theory showed that $\lambda = \lambda'$ [54].

λ has been defined by asymptotic behaviour close to the critical point, but further away in temperature the simple power law may not hold so well. Correction terms to this asymptotic law can be defined [55],

$$f(x) = Ax^{\lambda}(1 + a_y x^y + \ldots) \tag{1.35}$$

where $y > 0$ and the correction term dies away as the limit goes to zero.

A problem can occur in the plotting of graphs such as Figure 1.21, if there is uncertainty in the value of T_c. Errors in T_c can generate large variation in small x and small variations in large x. Often in plots such as Figure 1.21, T_c is a fitted parameter so that there is a straight line at small x. These discrepancies in T_c can therefore generate errors in the calculated critical exponents. These uncertainties are usually in the region of 0.01 – 0.02 because of the above difficulties. However, very accurate neutron diffraction studies on magnetic systems can determine the true value of T_c with sufficient accuracy to make this source of error negligible. Table 1.1 lists some common critical exponents of thermodynamic properties, their simple power law and conditions.

1.6.2 Universality

An analysis of all the data collected on critical exponents, either experimentally or from theoretical models, has revealed some systematic trends. These trends are generally known as the hypothesis of universality [55], which states that for a continuous phase transition the static critical exponents depend exclusively on the following three properties: (i) the dimensionality of the system, (ii) the dimensionality of the order parameter (or more precisely, the symmetry of the order

Property	Exponent	Power Law	Conditions	Ni
χ_T	γ	$t^{-\gamma}$	$T > T_c,\ h = 0$	1.33 ± 0.02
C_p	α	$t^{-\alpha}$	$T > T_c,\ h = 0$	0.04 ± 0.12
M	β	$(-t)^{\beta}$	$T > T_c,\ h = 0$	0.358 ± 0.003
M	δ	$h^{\frac{1}{\delta}}$	$T = T_c$	4.22

Table 1.1: Definitions of some common critical exponents with some experimental values observed for a Nickel ferromagnet (taken from Ref. [56, 52]).

parameter *i.e.* the number of dimensions in which the order parameter is free to vary.), (iii) whether the forces are of short or long-range. This is a profound generalisation, as it makes the assumption that the type of microscopic interaction is irrelevant, and only its range is important. Other interpretations are that the classical or quantum mechanical nature of the system is immaterial. In magnetic systems it predicts that the critical exponents will be the same whatever the crystal structure, as long as the systems are in the same universality class. Universality classes are the groups of systems which all have characteristic critical exponents. They are usually labeled by the simplest model systems belonging to them (eg. 2D-Ising, 3D-Heisenberg etc.). One of the most striking pieces of evidence in support of universality is the plot obtained by Guggenheim [57](see Fig. 1.22). This is a plot of the coexistence curves of eight different fluids, which when normalised lie more or less on the same line over a large range of densities.

1.7 Landau Theory of Phase Transitions

In magnetic systems the requirement for stability is that there is a minimum in the Gibbs free energy G (see section 1.5). In Landau theory [58], the basic assumption is that near to the critical point the thermodynamic energy functions may be expanded as a Taylor series. The thermodynamic function $\mathcal{L}$ is used, which is an

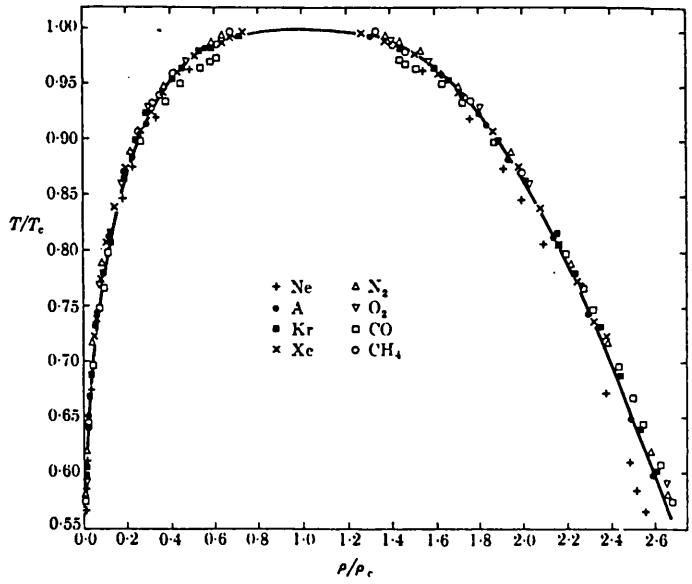

Figure 1.22: The coexistence curves of eight different fluids all with $\beta = \frac{1}{3}$ where $\rho - \rho_c \sim (-t)^\beta$, after Guggenheim [57].

approximation to the Gibbs free energy [55, 59]. It is assumed that state functions such as the specific heat can be derived from $\mathcal{L}$ as if it was the Gibbs free energy. In zero field $G = A$ since $G = A - hM$.

1.7.1 Second-order Phase Transitions

For a simple magnetic phase transition (paramagnetic $\rightarrow$ ferromagnetic) the Gibbs free energy is a function of the temperature and magnetization. For generality the order parameter M is written as η and $\mathcal{L}(T, \eta)$. Near the critical point the order parameter is small and $\mathcal{L}$ is expanded such that:

$$\mathcal{L}(T, \eta) = \mathcal{L}_o(T) + \alpha_2(T)\eta^2 + \alpha_4(T)\eta^4 + \ldots \tag{1.36}$$

There are no odd terms in the expansion due to the symmetry present. The free energy is the same under a reversal of field, that is, for a change in order parameter

$\eta \rightarrow -\eta$. For a given temperature the system will be in equilibrium when $\mathcal{L}(T,\eta)$ has a minimum value, and the derivatives in Eqn. (1.37) and Eqn. (1.38) apply.

$$\left(\frac{\partial \mathcal{L}}{\partial \eta}\right)_T = 0 \tag{1.37}$$

$$\left(\frac{\partial^2 \mathcal{L}}{\partial \eta^2}\right)_T > 0 \tag{1.38}$$

Application of Eqn. (1.37) and Eqn. (1.38) to Eqn. (1.36) gives.

$$\eta\alpha_2(T) + 2\eta^3\alpha_4(T) = 0 \tag{1.39}$$

$$\alpha_2(T) + 6\eta^2\alpha_4(T) > 0 \tag{1.40}$$

For $T > T_c$ $\eta = 0$, this implies from Eqn. (1.40)

$$\alpha_2(T) > 0 \quad \text{for } T > T_c. \tag{1.41}$$

For $T < T_c$ $\eta \neq 0$, which implies:

$$\alpha_2(T) = -2\eta^2\alpha_4(T) \quad \text{for } T < T_c \tag{1.42}$$

$$\therefore \alpha_2(T) < 0 \quad \text{if } \eta^2\alpha_4(\mathrm{T}) > 0 \quad \therefore \alpha_4(\mathrm{T}) > 0.$$

$\alpha_2(T)$ therefore changes sign at $T = T_c$ (*i.e.* $\alpha_2(T) = 0$ at $T = T_c$), and $\alpha_4(T)$ is always positive for this type of transition.

$\alpha_2(T)$ can be expanded about $T = T_c$ with the lowest non-zero terms retained.

$$\alpha_2(T) = (T - T_c)\alpha_o \tag{1.43}$$

By rearranging Eqn. (1.42) and substituting with Eqn. (1.43) we get:

$$\eta^2 = \frac{\alpha_o(T - T_c)}{2\alpha_4(T)} \quad \text{for } \mathrm{T} < \mathrm{T_c} \tag{1.44}$$

$$\therefore |\eta| \propto |-t|^{\frac{1}{2}} \qquad \therefore \beta = \frac{1}{2}$$

For this particular transition the critical exponent $\beta = \frac{1}{2}$ can be deduced. Figure 1.23 shows the plots of the $\mathcal{L}$ versus η for various isotherms. For $T > T_c$ there

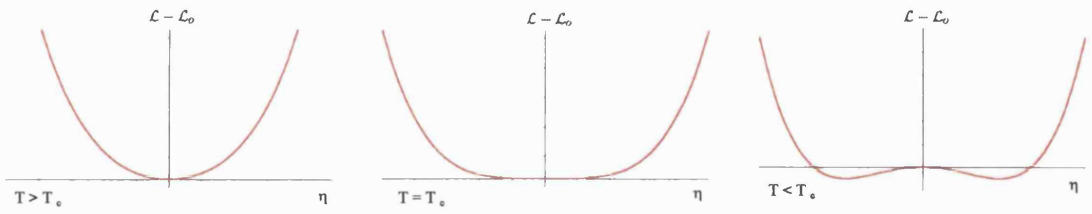

(a) $\alpha_2 > 0$ (b) $\alpha_2 = 0$ (c) $\alpha_2 < 0$

Figure 1.23: $\mathcal{L} - \mathcal{L}_o = \alpha_2\eta^2 + \alpha_4\eta^4$ for various values of α_2.

is only one minimum, $\eta = 0$ (see Fig. 1.23(a)). At $T = T_c$ there is a flattening of this curve as its splits into two minima for $T < T_c$ (see Fig. 1.23(b)), which continuously move away from the origin as T decreases below T_c. These two degenerate minima correspond to the two possible states formed due to the two possible field directions (see Fig. 1.23(c)). This is a continuous transition, since the minima of energy (and observed order parameter) change continuously with temperature [60]. Expressions can easily be derived for the specific heat C_h using Eqn. (1.29) and Eqn. (1.26), for small applied fields and substitution of Eqn. (1.44)

$$\begin{aligned} C_h &= -T\left(\frac{\partial^2 \mathcal{L}_o}{\partial T^2}\right)_h \quad \text{for } \mathrm{T} > \mathrm{T_c} \\ C_h &= -T\left(\left(\frac{\partial^2 \mathcal{L}_o}{\partial T^2}\right)_h + \frac{\alpha_o^2}{2\alpha_4}\right) \quad \text{for } \mathrm{T} < \mathrm{T_c} \end{aligned} \tag{1.45}$$

α_4 is assumed to be independent of temperature, and $h \to 0$. From Eqn. (1.45) C_h is predicted to have a downward discontinuity of $-T\alpha_o^2/2\alpha_4$ at $T = T_c$. This prediction illustrates a major failing of Landau theory, since there is a divergence in specific heat at the critical temperature, not a simple jump discontinuity. The other inadequacy of Landau theory is that it predicts critical exponents that do not agree with those experimentally observed. Experimentally $\beta \sim \frac{1}{3}$ not $\frac{1}{2}$. The main reason for these shortcomings is the fact that the initial assumption was incorrect. As mentioned above, the thermodynamic energy functions are *not* analytic at the critical point. However, the theory does hold well for systems with interactions of

infinitely long-range, such as ferroelectrics or type I superconductors [55, 61].

1.7.2 First-order Phase Transitions

Even though it has the failings discussed above, Landau theory is equally applicable to first-order transitions. Eqn. (1.36) is extended to include a further term $\alpha_6(T)$:

$$\mathcal{L}(T,\eta) = \mathcal{L}_o(T) + \alpha_2(T)\eta^2 + \alpha_4(T)\eta^4 + \alpha_6(T)\eta^6 + \ldots \tag{1.46}$$

The same conditions of equilibrium Eqn. (1.37) and Eqn. (1.38) apply to give:

$$2\eta(\alpha_2(T) + 2\eta^2\alpha_4(T) + 3\eta^4\alpha_6(T)) = 0 \tag{1.47}$$

$$2(\alpha_2(T) + 6\eta^2\alpha_4(T) + 15\eta^4\alpha_6(T)) > 0 \tag{1.48}$$

These equations lead to the same solutions as Eqn. (1.44) with $\beta = \frac{1}{2}$ if both $\alpha_4 > 0$ and $\alpha_6 > 0$.

If the free energy is also a function of other (non-ordering) fields g (such as anisotropy or a staggered field h'), T_c will also be a function of g, as will the parameters α_n. There will be a line of critical points in the $T - g$ plane. α_4 is assumed to depend analytically on g and α_2 on T [62].

Close to T_c η is small, therefore η^4 is small and can be approximated using Eqn. (1.44).

$$\eta^4 \approx \left(\frac{\alpha_o}{2\alpha_4}(T - T_c)\right)^2 \tag{1.49}$$

Eqn. (1.49) can be substituted into Eqn. (1.47) to give an expression for η^2.

$$\eta^2 \approx \frac{\alpha_o}{2\alpha_4}(T - T_c)\left(1 + \frac{3\alpha_o\alpha_6}{4\alpha_4^2}(T - T_c) + \ldots\right) \tag{1.50}$$

This expression can be seen as correction terms to power law behaviour, similar to Eqn. (1.35), (*i.e.* it determines the range of temperatures for which $\beta = \frac{1}{2}$ applies). As g is varied α_4 changes, and at a particular point it will be zero. When $\alpha_4 = 0$ Eqn. (1.47) can be simply solved to give Eqn. (1.51), where a new value for the

critical exponent can be deduced, $\beta = \frac{1}{4}$.

$$\eta = \left(\frac{\alpha_o(T - T_c)}{3\alpha_6(T)}\right)^{\frac{1}{4}} \tag{1.51}$$
$$\therefore |\eta| \propto |-t|^{\frac{1}{4}} \qquad \therefore \beta = \frac{1}{4}$$

This particular point is called a tricritical point [60, 63]. As $\alpha_4 \to 0$ the correction term in Eqn. (1.50) becomes larger and larger, and the range of temperatures for which $\beta = \frac{1}{2}$ becomes narrower and narrower. When $\alpha_4 = 0$ the correction term is infinite and Eqn. (1.50) becomes invalid. There is also a new critical exponent, $\beta = \frac{1}{4}$. This is called a tricritical exponent [64]. The region where $\beta = \frac{1}{2} \to \frac{1}{4}$ is called the tricritical region.

When $\alpha_4 < 0$, Eqn. (1.47) can be solved simply and has five solutions.

$$\eta = 0 \quad \text{and} \quad \eta^2 = \frac{-\alpha_4}{3\alpha_6}\left[1 \pm \left(1 - \frac{3\alpha_2\alpha_6}{\alpha_4^2}\right)^{\frac{1}{2}}\right] \tag{1.52}$$

These solutions correspond to three minima and two maxima of the Gibbs free energy. In Figure 1.24 $\mathcal{L}$ is plotted versus η for three different isotherms. For $T > T_o$ the lowest minimum is at $\eta = 0$, representing the paramagnetic state. The other minima represent metastable states in which the system is very unlikely to be, since they have a higher free energy. The energies of these states gradually decrease as $T \to T_o$, and at $T = T_o$ there are three degenerate minima. This is therefore a representation of coexistence between ordered ($\eta \neq 0$) and paramagnetic states ($\eta = 0$). When $T < T_o$ these ordered states decrease in energy below that of the paramagnetic state. Therefore the order parameter changes discontinuously, and a first-order phase transition occurs at $T = T_o$. The system changes discontinuously from a disordered state into an ordered state. A tricritical point therefore separates a line of continuous phase transitions from a first-order line in the $T - g$ or $\alpha_2 - \alpha_4$ plane. The line of first order transitions can be described in the $\alpha_2 - \alpha_4$ plane by the relationship in Eqn. (1.53) [55].

$$\alpha_2 = \frac{\alpha_4^2}{4\alpha_6} \tag{1.53}$$

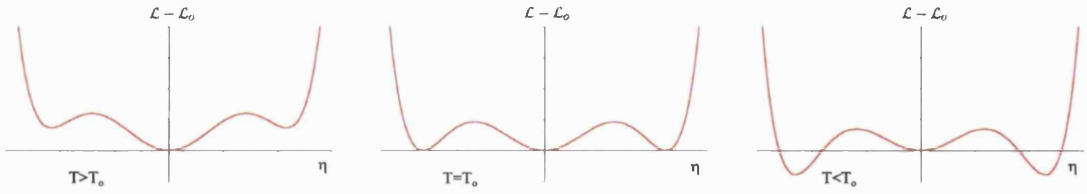

(a) $\alpha_2 > \frac{\alpha_4^2}{4\alpha_6}$ (b) $\alpha_2 = \frac{\alpha_4^2}{4\alpha_6}$ (c) $\alpha_2 < \frac{\alpha_4^2}{4\alpha_6}$

Figure 1.24: $\mathcal{L} - \mathcal{L}_o = \alpha_2\eta^2 - \alpha_4\eta^4 + \alpha_6\eta^6$ for various values of α_2.

Hysteresis in first-order phase transitions

Sometimes in first-order phase transitions a phenomenon occurs called hysteresis [65]. As described above, for $T > T_o$ metastable states exist. If these states are stable for small fluctuations, on heating through T_o the system may remain in these states for a little while longer, for T slightly greater than T_o (see Fig 1.24(a)). Therefore a non-zero order parameter will be observed for $T > T_o$. At higher temperatures more fluctuations force the system out of these metastable states and the first-order transition occurs. The transition is seen to occur at a higher temperature for heating than for cooling. This observation is known as hysteresis, and is a common characteristic of first-order phase transitions.

Chapter 2

Introduction to the Theoretical Techniques

This chapter gives a brief introduction to the theoretical techniques which have been used in this thesis. These range from Monte Carlo simulations to more analytical calculations.

The first sections describe the statistical mechanics underlying the Monte Carlo method, and discuss the way it has been applied to the simulation of magnetic systems.

The latter part of the chapter contains an example calculation of the normal modes of a one-dimensional lattice with a basis. This introduces the technique which is used in Chapter 4.

2.1 The Monte Carlo Method

Monte Carlo Simulations are an important tool in condensed matter physics. They can be used to probe the physical properties of model systems which cannot be analytically solved.

2.1.1 Statistical Mechanics

Monte Carlo simulations are founded on the ability of statistical mechanics to make predictions for the bulk thermodynamic properties of a system. Through knowledge of the microstates of a system, statistical mechanics is able to predict an expectation value of a thermodynamic property A (Eqn. (2.1)). The property A might be the internal energy or the density of a system.

$$\langle A \rangle = \sum_r P(A_r) A_r, \tag{2.1}$$

where the expression in Eqn. (2.1) is a sum over all the possible microstates of the system. A_r is the value of A in state r, with $P(A_r)$ the probability of the system existing in state r. The expectation value can be considered as the mean value of a sharply peaked probability distribution of A.

For a system in thermal equilibrium every microstate has a probability of existing, which is directly proportional to its Boltzmann factor.

$$P(E_r) \propto \exp(-\beta E_r) \qquad \beta = \frac{1}{k_B T} \tag{2.2}$$

E_r is the internal energy of a system in state r. The Gibbs probability for finding the system in state r is

$$P(E_r) = \frac{\exp(-\beta E_r)}{Z}, \tag{2.3}$$

where Z is the partition function, and used as a normalization factor,

$$Z = \sum_r \exp(-\beta E_r). \tag{2.4}$$

A final expression for the average internal energy of a system can be determined:

$$\langle E \rangle = \sum_r P(E_r) E_r = \frac{\sum_r E_r \exp(-\beta E_r)}{Z} = -\frac{\partial \ln Z}{\partial \beta}. \tag{2.5}$$

The fluctuations of thermodynamic properties with time in a system at equilibrium can also be calculated. Specifically this is related to the variance of the

thermodynamic property. The average internal energy is directly related to the enthalpy H of the system. This in turn can be used to create an expression for the fluctuations of the energy:

$$C_p = \left(\frac{\partial H}{\partial T}\right)_p = \left(\frac{\partial \langle E \rangle}{\partial T}\right)_p = \frac{\beta}{T}\left[\langle E^2 \rangle - \langle E \rangle^2\right]. \tag{2.6}$$

A full derivation is illustrated in section A.1.1.

2.1.2 Sampling and Markov processes

Simple numerical simulation of a system involves calculation of its partition function, and with it the thermodynamic properties. Implicit calculation of the partition function is very often not feasible for large systems. For an Ising system it is not difficult to see that the total number of possible microstates is 2^N, where N is the total number of spins in the system. This is a number which is very large, and direct numerical evaluation of the partition function is only feasible for $N \lesssim 40$. For low N the relative fluctuation is quite large ($N = 40, \frac{\Delta E}{\langle E \rangle} = 0.16$), better statistics require simulation of a larger system. Approximation to the thermodynamic limit requires a macroscopic system $N \sim 10^{23}$, and it is obvious that sampling of the system is required.

Every microstate of the system can be considered as a point in an abstract **phase space**, with its own Boltzmann factor (Eqn. (2.2)). At thermal equilibrium the system exists in a region of phase space where the Boltzmann factors are high (*i.e.* when the internal energy is low); this is the Boltzmann distribution. The vast majority of microstates have energies that are too high, and make a negligible contribution to the partition function.

Simple sampling

One type of sampling is called simple sampling. A number of microstates are generated at random, and their energies and other thermodynamic variables are

averaged. This would result in a Gaussian distribution of all the properties. For example in a magnetic system the probability distribution of magnetization per spin (m) is defined [66]:

$$P(m) \propto \exp\left(\frac{-m^2 N}{2}\right). \tag{2.7}$$

This distribution would have little overlap with that of a system at thermal equilibrium. These randomly picked microstates are not representative of the particular region of phase space associated with thermal equilibrium.

Importance sampling

It is necessary to use a sampling technique that will directly sample the important part of phase space in which the system sits at thermal equilibrium. An 'importance sampling' approach was developed by Metropolis *et al.* in 1953 [67]. This technique is known as the Monte Carlo method due to its use of random numbers.

It is assumed that phase space is discrete. Division of phase space into very small cells approximates to a continuous phase space such as in a Heisenberg system. The Hamiltonian must be known, and the energy of a microstate must be easy to calculate. If microstates are sampled according to their importance, then the average of a thermodynamic quantity will be:

$$\langle A \rangle_{MC} = \frac{1}{R} \sum_{r=1}^{r=R} A_r = \langle A \rangle + O\left(\frac{1}{\sqrt{R}}\right) \tag{2.8}$$

The quantity r can be thought of as a measure of time, and denotes a configuration sampled at a 'time' r. R is the number of microstates sampled and $\langle A \rangle$ is the true thermodynamic average of the system. A Markov process is used to generate a Markov chain of microstates. Over a period of time (akin to thermal equilibrium of a physical system), these states have the same probabilities as those given by the Boltzmann distribution. A Markov chain is a sequence of microstates, each of which depends on the preceding one. The transition from one state to another is described in the following way. A random configuration Ω_μ is chosen, and altered

using a random process to give a new configuration Ω_ν (for example a spin is picked at random and flipped). The probability that the system is allowed to move from $\mu \rightarrow \nu$ per unit time is denoted by $W(\mu \rightarrow \nu)$. The Markov system will converge on states relevant to the thermodynamic average if the system is ergodic (all states are eventually accessible), and the condition of detailed balance is obeyed [66].

$$P(\Omega_\mu)W(\Omega_\mu \rightarrow \Omega_\nu) = P(\Omega_\nu)W(\Omega_\nu \rightarrow \Omega_\mu) \tag{2.9}$$

$P(\Omega_r)$ is the probability that the system is in configuration Ω_r. The method of Metropolis *et al.* chooses a transition probability that obeys both conditions.

$$W(\mu \rightarrow \nu) \propto \begin{cases} \exp(-\beta\Delta E) & \text{if } E_\nu > E_\mu \\ 1 & \text{if } E_\nu \leqslant E_\mu \end{cases} \tag{2.10}$$

The choices defined above, called the Metropolis algorithm, are those used in Monte Carlo simulations.

2.1.3 The Metropolis Algorithm

Monte Carlo Simulation can easily be performed on a magnetic system according to the theory described in section 2.1.2. The procedure used in the computer program is illustrated in Figure 2.1.

At each temperature the thermodynamic average of a property, such as the magnetization, is calculated. In a Heisenberg system the magnetization vector can point in any direction as the system is isotropic.

$$M = \sqrt{\left(\frac{1}{N}\sum_{i=1}^{N} S_{xi}\right)^2 + \left(\frac{1}{N}\sum_{i=1}^{N} S_{yi}\right)^2 + \left(\frac{1}{N}\sum_{i=1}^{N} S_{zi}\right)^2} \tag{2.11}$$

Therefore a root mean square magnetization per spin is calculated, as defined in Eqn. (2.11), together with its square. The fluctuations of the magnetization can also be determined in the same way as the energy. When M is the magnetization

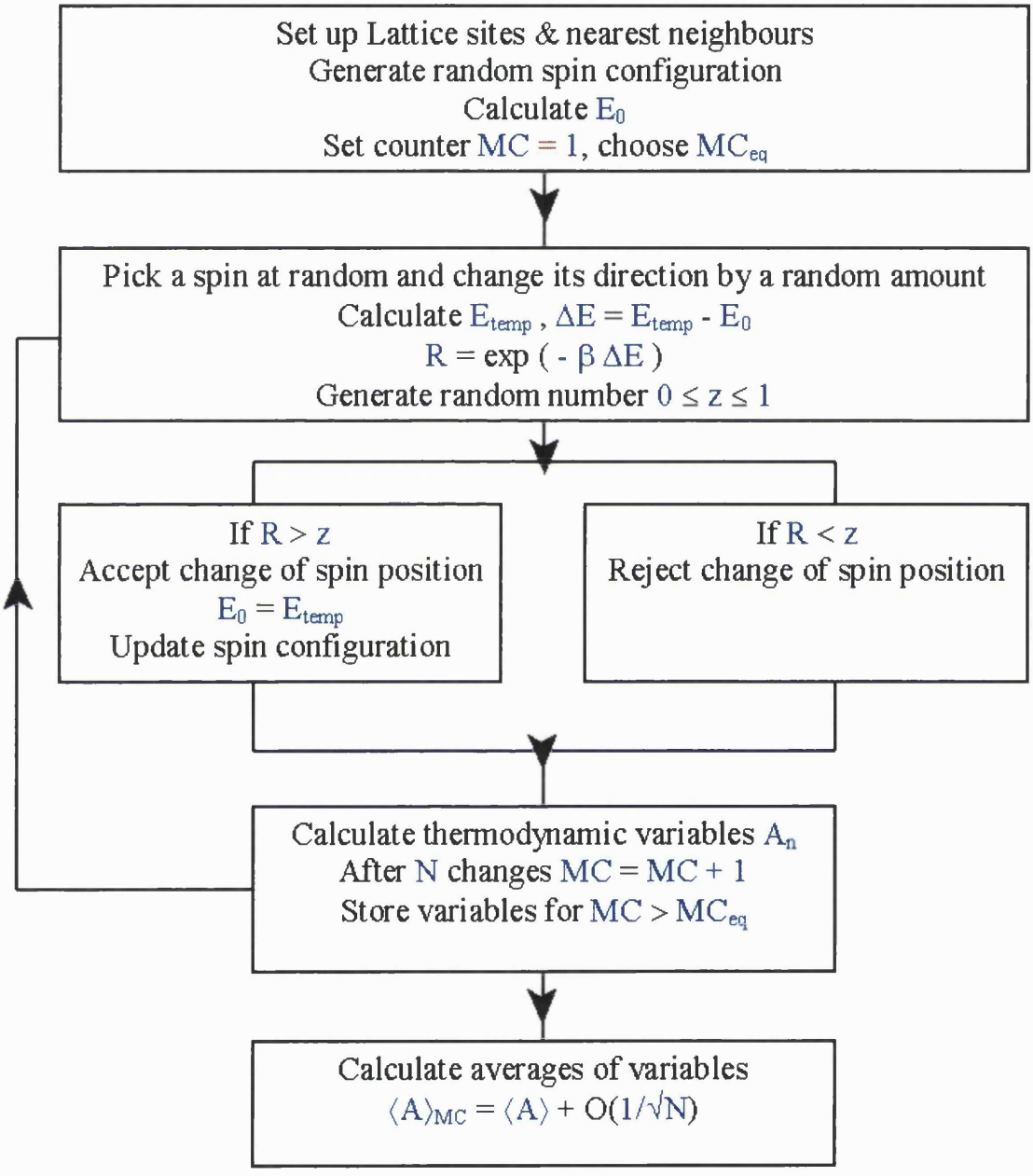

Figure 2.1: The Metropolis algorithm

per spin, χ_T is isothermal magnetic susceptibility per spin. A full derivation is illustrated in section A.1.2.

$$\chi_T = \left(\frac{\partial\langle M\rangle}{\partial h}\right)_T = \beta N\left[\langle M^2\rangle - \langle M\rangle^2\right] \tag{2.12}$$

In each Monte Carlo step only one spin is moved. There will be large correlations between two successive spin configurations in the Markov chain, if the spin move is accepted. Therefore not every single configuration is used to calculate the average. Configurations are averaged after every N Monte Carlo steps. This period is denoted 1 Monte Carlo Step per spin. The length of simulations are measured by their number of Monte Carlo steps per spin (MCS/S). As described in section 2.1.2 the Markov chain needs to equilibrate, so the first 30-40% of MCS/S are not included in the average. This is the quantity MC_{eq} described in the flowchart in Figure 2.1. The thermodynamic quantities measured are the magnetization (Eqn. (2.11)) and the energy (Eqn. (2.5)) of the system. The specific heat (Eqn. (2.6)) and magnetic susceptibility (Eqn. (2.12)) are calculated from the fluctuations of these variables over the course of the simulation.

A Monte Carlo run is made for a succession of decreasing temperatures. The first simulation is generally started from a random configuration. The final configuration is conserved and is used as the starting point for the next temperature.

2.2 Simulation of Pyrochlore Systems

This report is concerned with the simulation of magnetic systems on the pyrochlore lattice (see Fig. 1.2). A computer program has been written in FORTRAN 77, using the Metropolis algorithm to simulate a magnetic system. The procedure followed is based on the theory discussed in section 2.1.2. By a simple choice of input parameters different types of magnetic models can be studied. Ferromagnetic or antiferromagnetic systems can be investigated, as well as those with or without anisotropy or magnetic field applied.

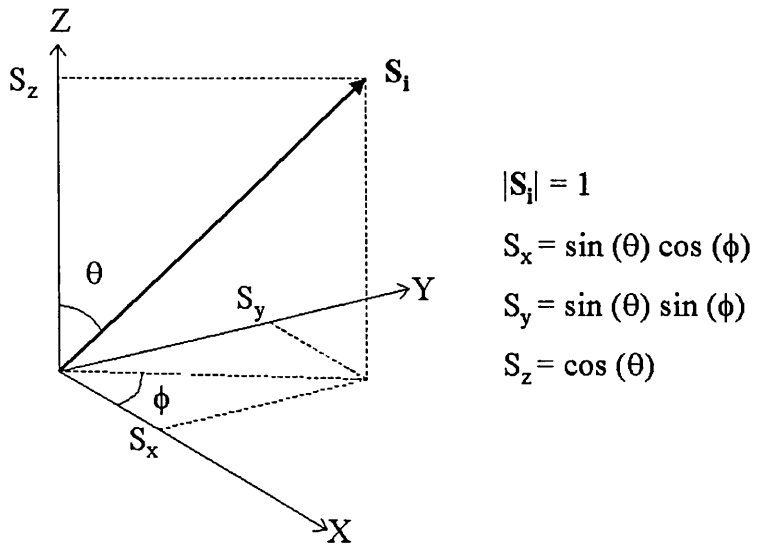

Figure 2.2: 3-d spin vector as polar coordinates

2.2.1 Definition of the Microscopic Variables

The direction of a magnetic spin $\mathbf{S}_i$ is described simply as a three dimensional vector (Eqn. (2.13)), where $\underline{\mathbf{i}}, \underline{\mathbf{j}}$ and $\underline{\mathbf{k}}$ are Cartesian unit vectors. The spin components are also expressed in terms of polar coordinates ϕ and θ (see Fig. 2.2).

$$\mathbf{S}_i = S_{xi}\,\underline{\mathbf{i}} + S_{yi}\,\underline{\mathbf{j}} + S_{zi}\,\underline{\mathbf{k}}. \tag{2.13}$$

The pyrochlore lattice is made up of four interpenetrating face-centred cubic lattices (see Fig. 1.2). The sites of the lattice form corner-sharing tetrahedra. In a cubic unit cell there are sixteen separate positions, each defined by a face-centering operation on a four site basis (see Table 2.2.1). A magnetic moment is situated on every site. The lattice is generated on an array of cubic unit cells. The number of cubic unit cells along one axis is denoted by L, therefore the total number of spins in a system $N = 16L^3$.

Position	δ_x	δ_y	δ_z
$(0,0,0)$ + FC	$\frac{1}{\sqrt{3}}$	$\frac{1}{\sqrt{3}}$	$\frac{1}{\sqrt{3}}$
$(\frac{1}{4},0,\frac{1}{4})$ + FC	$\frac{1}{\sqrt{3}}$	$-\frac{1}{\sqrt{3}}$	$\frac{1}{\sqrt{3}}$
$(0,\frac{1}{4},\frac{1}{4})$ + FC	$\frac{1}{\sqrt{3}}$	$-\frac{1}{\sqrt{3}}$	$-\frac{1}{\sqrt{3}}$
$(\frac{1}{4},\frac{1}{4},0)$ + FC	$\frac{1}{\sqrt{3}}$	$\frac{1}{\sqrt{3}}$	$-\frac{1}{\sqrt{3}}$

Table 2.1: Pyrochlore lattice positions for a cubic basis. FC denotes the face-centering operation $(0,0,0;\ 0,\frac{1}{2},\frac{1}{2};\ \frac{1}{2},0,\frac{1}{2};\ \frac{1}{2},\frac{1}{2},0)$

2.2.2 The Energy Hamiltonian

The internal energy of the system for a particular state is defined by the Hamiltonian in Eqn. (2.14). The first term is the exchange interaction between nearest neighbour spins over all the bonds in the system. In the pyrochlore lattice each spin has six nearest neighbours. At the boundaries of the system the spins do not have nearest neighbours, and an approximation is made. A spin on one cubic face of the lattice is assumed to interact with the spin in the corresponding position on the other side of the lattice. This is referred to as 'periodic boundary conditions'.

The constant J is an exchange energy. Positive J favours ferromagnetic ordering of the system, and negative J favours antiferromagnetic ordering (normally $J = \pm 1$). Each site in the lattice has its own anisotropy axis $\boldsymbol{\delta_i}$ associated with it. These are also listed in Table 2.2.1.

$$\mathbb{H} = -J \sum_{<i,j>} \mathbf{S}_i \cdot \mathbf{S}_j - D \sum_{i=1}^{N} (\boldsymbol{\delta}_i \cdot \mathbf{S}_i)^2 - \sum_{i=1}^{N} h \cdot \mathbf{S}_i \qquad (2.14)$$

The second term in the Hamiltonian is the anisotropy energy. The relative strength of the anisotropy is determined by the parameter D. It is often quoted relative to the constant J. The third term in the Hamiltonian represents the application of a magnetic field.

Local easy-axis anisotropy

If the variable D is positive, the system will lower its anisotropy energy if the spins point along the directions of the easy-axes (δ_i). The dot product is squared since the direction the spin takes along the axis is not important. This is known as local easy-axis anisotropy. If the value of D is infinity, then Ising spins are simulated. This is equivalent to spin ice if the interactions were ferromagnetic (see section 1.1).

Local easy-plane anisotropy

Since the anisotropy interaction is squared, all anisotropy contributions to the total energy are positive. Therefore if the variable D is negative, the lowest possible anisotropy term is zero, which will happen if the spins are perpendicular to the anisotropy axes. This is called local easy-plane anisotropy.

2.3 The Calculation of Normal Modes

Section 4.5 includes a calculation to determine the possible existence of soft modes in the easy-plane antiferromagnet on the pyrochlore lattice.

This calculation follows in principle the same calculation for a much simpler case: a one-dimensional lattice with a two-atom basis. The calculation for a simple lattice is instructive, since the answer is already known in advance. It is a good way to test the method for the more complicated system.

2.3.1 The Model and its Hamiltonian

The model is simply a linear chain of sites with N_{cell} unit cells, each ith unit cell contains two spins ${}^{a}\mathbf{S}_i$ and ${}^{b}\mathbf{S}_i$ (see Fig. 2.3). The primitive lattice vector is $\mathbf{a}$. There are two types of interaction in the Hamiltonian, the first within each

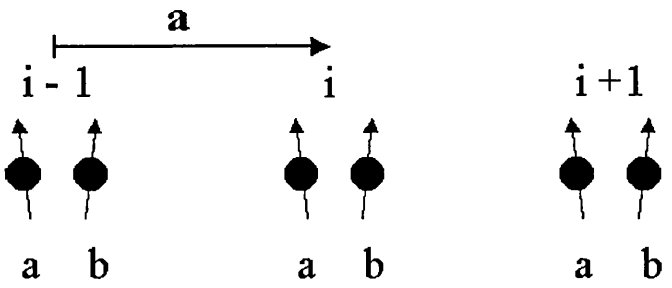

Figure 2.3: A one-dimensional linear chain of spins

unit cell with exchange constant $J_1 > 0$ and the second between unit cells with exchange constant $J_2 > 0$. The spins interact, with periodic boundary conditions, according to the Hamiltonian:

$$\mathbb{H} = -J_1 \sum_{i}^{N_{cell}} {}^{a}\mathbf{S}_i \cdot {}^{b}\mathbf{S}_i - J_2 \sum_{i}^{N_{cell}} {}^{b}\mathbf{S}_i \cdot {}^{a}\mathbf{S}_{i+1}. \tag{2.15}$$

The next step is to consider a small deviation out of a ferromagnetic ground state by an amount ${}^{m}\varepsilon_i$ for each spin, and its effect on the Hamiltonian.

$${}^{m}S_{ix} = {}^{m}\varepsilon_i, \; {}^{m}S_{iy} = \sqrt{1 - {}^{m}\varepsilon_i{}^2} \approx 1 - \frac{1}{2}{}^{m}\varepsilon_i{}^2 \quad \text{for } m = a, b \quad i = 1, N_{cell}$$

Both exchange interactions can be simplified in the following general argument for $m = a, b$, if the product ${}^{m}\varepsilon_i{}^2 \; {}^{n}\varepsilon_j{}^2$ is small.

$$\begin{aligned} {}^{m}\mathbf{S}_i \cdot {}^{n}\mathbf{S}_j &= {}^{m}\varepsilon_i {}^{n}\varepsilon_j + (1 - \frac{1}{2}{}^{m}\varepsilon_i{}^2)(1 - \frac{1}{2}{}^{n}\varepsilon_j{}^2) \\ &\approx {}^{m}\varepsilon_i {}^{n}\varepsilon_j + 1 - \frac{1}{2}({}^{m}\varepsilon_i{}^2 + {}^{n}\varepsilon_j{}^2) \\ &= 1 - \frac{1}{2}({}^{m}\varepsilon_i - {}^{n}\varepsilon_j)^2 \end{aligned}$$

Where H_o is the ground state component of the energy, the Hamiltonian becomes in terms of the excitation parameter ε:

$$\mathbb{H} - H_o = \mathbb{H} - N(J_1 + J_2) = -\frac{J_1}{2} \sum_{i}^{N_{cell}} [{}^{a}\varepsilon_i - {}^{b}\varepsilon_i]^2 - \frac{J_2}{2} \sum_{i}^{N_{cell}} [{}^{b}\varepsilon_i - {}^{a}\varepsilon_{i+1}]^2 \tag{2.16}$$

2.3.2 Determination of the Dynamical matrix $M_{ij}^{\alpha\beta}$

The next stage in the calculation is to rearrange Eqn. (2.16) in terms of the dynamical matrix such that:

$$\mathbb{H} - H_o = \frac{1}{2}\sum_{i}^{N_{cell}}\sum_{j}^{N_{cell}}\sum_{\alpha=a,\beta=a}^{\alpha=b,\beta=b} {}^{\alpha}\varepsilon_i \; M_{ij}^{\alpha\beta} \; {}^{\beta}\varepsilon_j \tag{2.17}$$

The '4th rank tensor' $M_{ij}^{\alpha\beta}$ is essentially made up of four different two-dimensional matrices: M_{ij}^{aa},M_{ij}^{ab},M_{ij}^{ba} and M_{ij}^{bb}. M_{ij}^{aa} and M_{ij}^{bb} contain only diagonal terms, whereas M_{ij}^{ab} and M_{ij}^{ba} contain off-diagonal terms due to the interactions between different spins ($\alpha \neq \beta$) in consecutive unit cells ($i \neq j$).

M_{ii}^{aa} and M_{ii}^{bb}: Diagonal terms

The elements of Eqn. (2.16) which contribute diagonal terms are considered first:

$$\sum_{i}^{N_{cell}} \frac{J_1}{2}({}^{a}\varepsilon_i{}^2 + {}^{b}\varepsilon_i{}^2) + \frac{J_2}{2}({}^{b}\varepsilon_i{}^2 + {}^{a}\varepsilon_{i+1}{}^2),$$

which is simplified by a change of variable $\left(\sum_{i+1}\varepsilon_{i+1}^2 = \sum_{i'}\varepsilon_{i'}^2 \text{ where } i+1=i'\right)$ to

$$\sum_{i}^{N_{cell}} \frac{1}{2}(J_1+J_2)({}^{a}\varepsilon_i{}^2 + {}^{b}\varepsilon_i{}^2) = \sum_{i}^{N_{cell}}\sum_{\alpha=a,\beta=a}^{\alpha=b,\beta=b} \frac{1}{2}(J_1+J_2)^{\alpha}\varepsilon_i{}^{\beta}\varepsilon_i\delta_{\alpha\beta}$$

where $\delta_{\alpha\beta} = 1$ for $\alpha = \beta$, and $\delta_{\alpha\beta} = 0$ for $\alpha \neq \beta$. This therefore leads to a simple diagonal matrix, since there are no other diagonal terms:

$$M_{ii}^{aa} = M_{ii}^{bb} = \begin{bmatrix} \ddots & & \\ & J_1+J_2 & \\ & & \ddots \end{bmatrix}. \tag{2.18}$$

M_{ij}^{ab} and M_{ij}^{ba}: Off-Diagonal terms

There are two separate elements of Eqn. (2.16) which contribute mixed terms. The first element defines interactions between spins in the same unit cell.

$$-J_1\sum_{i}^{N_{cell}} {}^{a}\varepsilon_i{}^{b}\varepsilon_i = -\frac{1}{2}J_1\sum_{i}^{N_{cell}}\sum_{\alpha=a,\beta=a}^{\alpha=b,\beta=b} {}^{\alpha}\varepsilon_i{}^{\beta}\varepsilon_i(1-\delta_{\alpha\beta}) \tag{2.19}$$

The same bond is counted twice to include elements in the M_{ij}^{ab} and M_{ij}^{ba} matrix. The total is then halved to cancel out the extra counting.

The second element contributing mixed terms defines interactions between spins in different unit cells:

$$\begin{aligned} -J_2 \sum_{i}^{N_{cell}} {}^{b}\varepsilon_i{}^{a}\varepsilon_{i+1} &= -\frac{1}{2}J_2 \sum_{i}^{N_{cell}} {}^{b}\varepsilon_i{}^{a}\varepsilon_{i+1} + {}^{a}\varepsilon_i{}^{b}\varepsilon_{i-1} \\ &= -\frac{1}{2}J_2 \sum_{i}^{N_{cell}} \sum_{\alpha=a,\beta=a}^{\alpha=b,\beta=b} \left({}^{\beta}\varepsilon_i{}^{\alpha}\varepsilon_{i+1} + {}^{\alpha}\varepsilon_i{}^{\beta}\varepsilon_{i-1}\right) \delta_{\alpha a}\delta_{\beta b}, \quad (2.20) \end{aligned}$$

where the same double counting argument is used. This leads to the two remaining component matrices of $M_{ij}^{\alpha\beta}$.

$$M_{ij}^{ab} = \begin{bmatrix} -J_1 & & & & -J_2 \\ & \ddots & & & \\ & -J_2 & -J_1 & & \\ & & & \ddots & \\ & & & -J_2 & -J_1 \end{bmatrix} \quad (2.21)$$

$$M_{ij}^{ba} = \begin{bmatrix} -J_1 & -J_2 & & & \\ & \ddots & & & \\ & & -J_1 & -J_2 & \\ & & & \ddots & \\ -J_2 & & & & -J_1 \end{bmatrix} \quad (2.22)$$

2.3.3 Treatment of the Dynamical Matrix

The elements of the dynamical matrix $M_{ij}^{\alpha\beta}$ depend on $\mathbf{R}_i - \mathbf{R}_j$ only, so will be diagonal in reciprocal space. So, defining $\mathbf{R}_{ij} = \mathbf{R}_i - \mathbf{R}_j$, $M^{\alpha\beta}(\mathbf{R}_{ij})$ is created, which can be Fourier transformed to give a matrix with elements

$$M^{\alpha\beta}(\mathbf{q}) = \frac{1}{N_{cell}} \sum_{\mathbf{R}_{ij}} M^{\alpha\beta}(\mathbf{R}_{ij}) \exp\left(i\mathbf{q}.\mathbf{R}_{ij}\right). \quad (2.23)$$

$\mathbf{R}_{ij}$ is simply the primitive lattice vector for interactions between two different unit cells. $\mathbf{R}_{ij} = 0$ for interactions within the same unit cell.

If the Fourier transform is applied to Eqn. (2.17) it is reduced to

$$\mathbb{H} - H_o = \frac{1}{2}\frac{1}{N_{cell}} \sum_{\mathbf{q}} \sum_{\alpha\beta} {}^{\alpha}\varepsilon_{\mathbf{q}}\, M^{\alpha\beta}(\mathbf{q})\, {}^{\beta}\varepsilon_{\mathbf{q}}, \tag{2.24}$$

where

$${}^{\alpha}\varepsilon_{\mathbf{q}} = \frac{1}{\sqrt{N_{cell}}} \sum_{\mathbf{R}_i} {}^{\alpha}\varepsilon_i \exp\left(-i\mathbf{q}.\mathbf{R}_i\right) \tag{2.25}$$

For example $M^{12}(\mathbf{R}_{ij} = 0) = -J_1$ and $M^{12}(\mathbf{R}_{ij} = -\mathbf{a}) = -J_2$ so:

$$M^{12}(\mathbf{q}) = -J_1(\exp\left(i\mathbf{q}.0\right)) - J_2(\exp\left(i\mathbf{q}.-\mathbf{a}\right)) = -J_1 - J_2\exp\left(-i\mathbf{q}.\mathbf{a}\right),$$

and all other elements can be constructed in the same way. The matrix $M^{\alpha\beta}(\mathbf{q})$ can thus be written:

$$M^{\alpha\beta}(\mathbf{q}) = \begin{bmatrix} J_1 + J_2 & -J_1 - J_2\exp\left(-i\mathbf{q}.\mathbf{a}\right) \\ -J_1 - J_2\exp\left(i\mathbf{q}.\mathbf{a}\right) & J_1 + J_2 \end{bmatrix} \tag{2.26}$$

Diagonalization of $M^{\alpha\beta}(\mathbf{q})$ and rewriting in terms of the eigenvectors of $M^{\alpha\beta}(\mathbf{q})$ the Hamiltonian reduces to a set of N independent harmonic oscillators, since there are a total of $2\,N_{cell} = N$ eigenvalue solutions which describe the normal modes of the system.

$$\mathbb{H} - H_o = \frac{1}{N} \sum_{mode=1}^{N} \lambda_{mode}\phi^2_{mode} \tag{2.27}$$

λ_{mode} and ϕ^2_{mode} are respectively the eigenvalues and eigenvectors of $M^{\alpha\beta}(\mathbf{q})$.

Determination of the eigenvalues of $M^{\alpha\beta}(\mathbf{q})$ gives two solutions, which are the acoustic and optical branches.

$$\lambda = J_1 + J_2 \pm \sqrt{{J_1}^2 + {J_2}^2 + 2J_1J_2\cos\left(\mathbf{q}.\mathbf{a}\right)} \tag{2.28}$$

This solution is analogous to the determination of phonons in a one-dimensional lattice with a two atom basis.

	J > 0	J < 0
D > 0	Easy-axis ferromagnet	Easy-axis antiferromagnet
D < 0	Easy-plane ferromagnet	Easy-plane antiferromagnet

Table 2.2: Combinations of local anisotropy D and exchange J for the $\langle 111 \rangle$ pyrochlore magnet

2.4 Summary: Aims of the Theoretical Work in this Thesis

By interchanging the signs of the two parameters J and D, four different permutations are possible using the same Hamiltonian (Eqn. (2.14)). These are described in Table 2.2. A systematic investigation has been made into the properties of each of these systems using primarily Monte Carlo simulation, as well as other theoretical techniques. Chapters 3 and 4 describe detailed investigation of the easy-axis ferromagnet and the easy-plane antiferromagnet respectively. The other two systems are not frustrated and have a singly degenerate ground state. They have also been investigated and the results are discussed in sections 9.4.1 and 9.4.2.

Chapter 3

Easy-Axis Ferromagnet

Monte Carlo simulations have recently been performed on the spin ice model, a ferromagnetic pyrochlore system with ⟨111⟩ Ising anisotropy [11, 40, 15]. These simulations corresponded to an easy-axis Heisenberg model with infinite anisotropy ($D = \infty$). This chapter is concerned with investigations of a ferromagnetic system with *finite* anisotropy. This is also referred to as the 'continuous spin ice model'. The first part deals with simulations of a system with zero applied field. The second part deals with simulations of a system with an applied field.

3.1 Initial Investigation of the Zero Field Ordering Processes

Monte Carlo simulations were performed for a system with the Hamiltonian defined in Eqn. (2.14). A survey was made of systems with anisotropy ranging from $D/J = 0.1 - 25.0$, on lattices ranging from $L = 3 - 9$. The runs were generally started in a random configuration at high temperature ($T/J \sim 2D$). The system was then slowly annealed with each successive temperature being 90-95% of that previously measured. The length of the simulations was generally 100,000 MCS/S with 30,000 equilibrium MCS/S. For each simulation thermodynamic averages were

taken of the energy (Eqn. (2.5)) and the magnetization (Eqn. (2.11)). The specific heat (Eqn. (2.6)) and magnetic susceptibility (Eqn. (2.12)) were determined from the fluctuations of the energy and magnetization respectively. Once the system had been cooled it was then heated up, in order to check for any hysteresis in the system.

Sublattice order parameter

As discussed in section 2.2.1 the pyrochlore lattice consists of 4 FCC sublattices. An extra property of the system which can be calculated is the sublattice order parameter M_{SL}.

$$M_{SL} = \frac{m_a + m_b + m_c + m_d}{4} \tag{3.1}$$

$$m_a = \sqrt{\left(\frac{4}{N}\sum_a S_x\right)^2 + \left(\frac{4}{N}\sum_a S_y\right)^2 + \left(\frac{4}{N}\sum_a S_z\right)^2}$$

The term m_a is equivalent to the magnetization per spin of the spins situated on sublattice a. If $M_{SL} = 1$, there is full q=0 order in the system, since the order has the periodicity of the lattice.

The fluctuations of M_{SL} can easily be determined, in an identical way to the isothermal magnetic susceptibility (Eqn. (2.12)).

$$\chi_{M_{SL}} = \beta N \left[\langle M_{SL}^2 \rangle - \langle M_{SL} \rangle^2\right] \tag{3.2}$$

3.1.1 Initial Results: Finite T Phase Transition

The primary result shown in Figure 3.1 is that for all values of D the system undergoes a phase transition to a long-range ordered state. That is, the infinite ground state degeneracy is lifted. The precise nature of the ordered state is however slightly different for each of the values of D/J, since the saturated magnetization is different for each case. The same result is observed for all lattice sizes

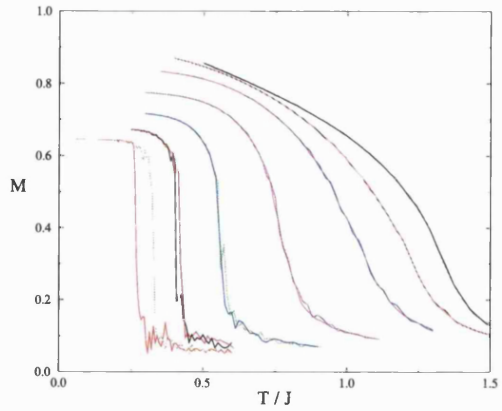

(a) L=4

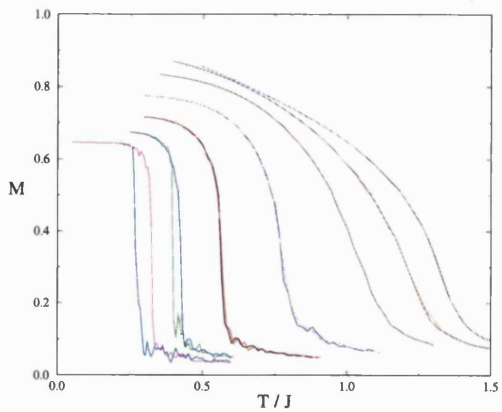

(b) L=5

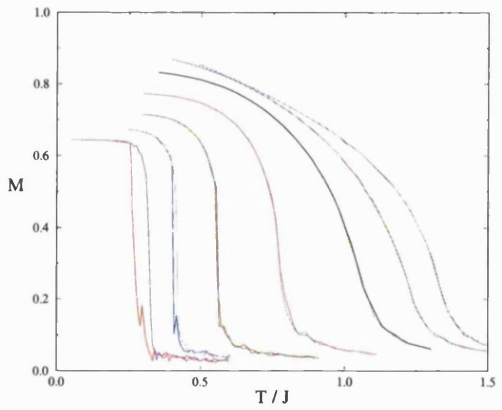

(c) L=6

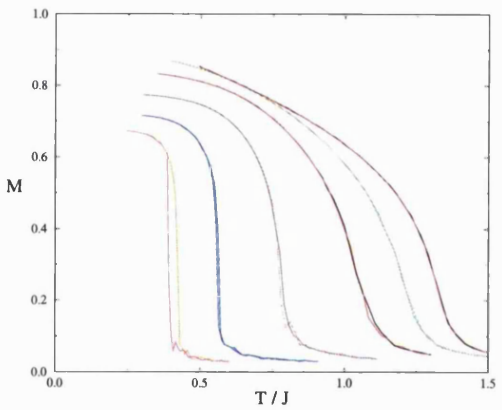

(d) L=7

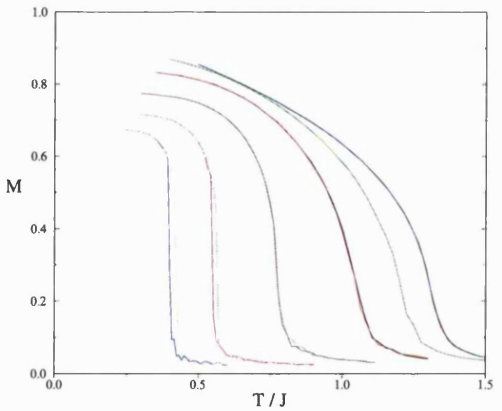

(e) L=8

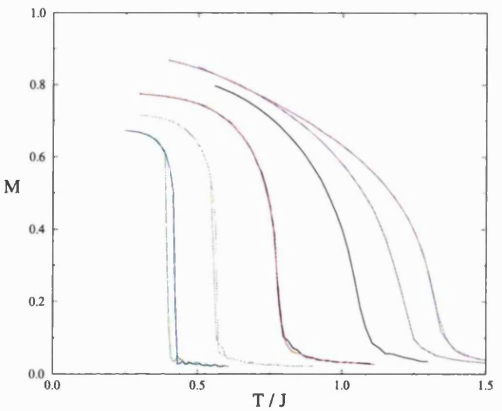

(f) L=9

Figure 3.1: Hysteresis curves for L=4–9. From right to left $D/J = 0.5, 3.24, 4.79, 7.08, 10.47, 15.49, 22.91$ ($L = 4, 5, 6$ only).

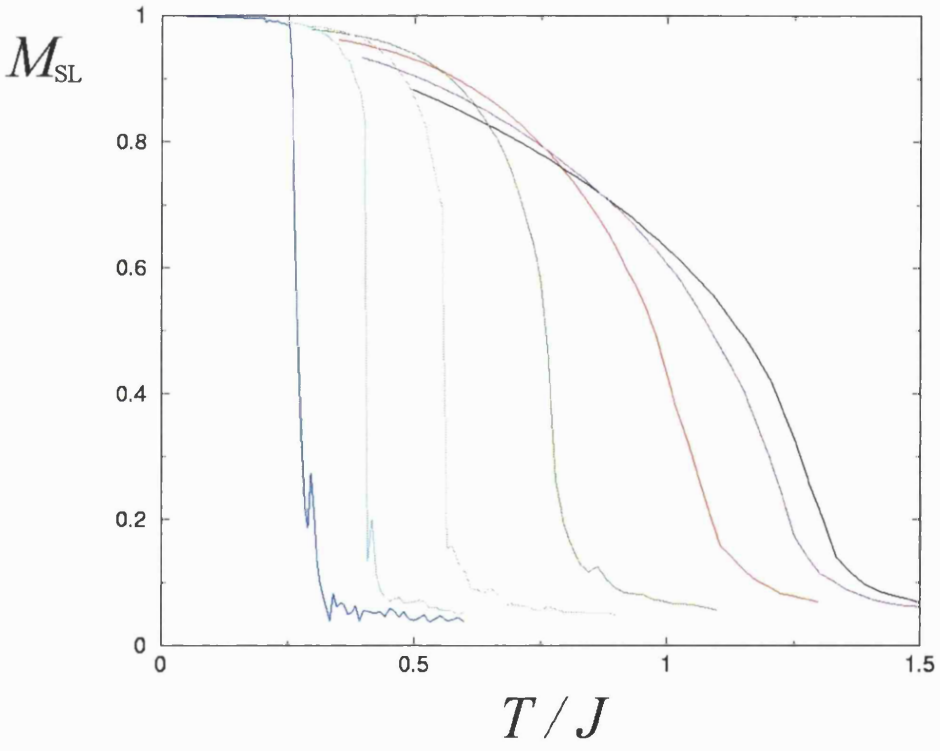

Figure 3.2: M_{SL} vs T/J for $D/J = 2.18 - 22.91$ with L=6.

For all values of anisotropy the system has full q=0 order. This is illustrated by the behaviour of the sublattice order parameter in Figure 3.2. For all values of D/J the sublattice order parameter has a saturation value of unity. In all cases the transition is marked by a maximum in specific heat and susceptibility (both χ and $\chi_{M_{SL}}$).

Order of the transition for small D

If the system had zero anisotropy ($D/J = 0$), then a simple Heisenberg ferromagnet would be modelled. In three dimensions this orders with a second-order phase transition, irrespective of the lattice (simple cubic, pyrochlore etc.), and has a simple ferromagnetically ordered state with magnetization per spin $M = 1$. It is no surprise therefore that for very low anisotropy systems the saturated magnetization per spin is very close to unity, and that the system seems to undergo a second-order transition. This type of behaviour does not seem to be exclusive to very small anisotropies. The continuous transition in the magnetization is mimicked by the sublattice order parameter.

Order of the transition for large D

As the anisotropy in the system is increased, the saturated magnetization per spin decreases. However, there is still long range q=0 order in the system. The transition observed seems to be first-order, as for the most part there is a discontinuous change in the magnetization and sublattice order parameter.

Preliminary interpretation of the results implies that there is a tricritical point in the temperature/anisotropy phase diagram.

3.1.2 Microscopic Animations of the Ordering Process

During the course of a simulation the microscopic positions of the spins are always declared. This facility can be used to visualize the magnetic state of the system

over 'Monte Carlo time'. The positions of the spins were recorded at three equally spaced intervals after equilibration. These 'snapshots' of the magnetic state of the system were taken at every temperature of the simulation. They were then joined together to form an animation of the simulation and the ensuing phase transition.

Construction of the animation

In order to preserve clarity of view only 16 tetrahedra were selected for the animation and the centre unit cell of an $L = 5$ lattice was selected to represent the system. Strictly this would have only 16 spins, but the associated tetrahedra on the centres of the faces and the corners of the cube are included. This amounts to 16 tetrahedra, with 56 different sites in all. Software was written to visualize the microscopic positions of the 56 spins in 3-d [68]. Animations were created for two different values of anisotropy ($D/J = 22.91$ and $D/J = 1.0$) and are included as animated .gif files on the enclosed CD-ROM. They are presented in the form of a webpage 'Spinice.htm'. In the bottom right-hand corner of each animation the current temperature is displayed in blue lettering.

Animation for $D/J = 1.0$

This animation starts at $T/J = 3.5$, a high temperature with respect to the transition temperature at $T/J \sim 1.3$. At this temperature the system has a significant amount of energy and the spins are in a random paramagnetic arrangement with no ordering. The paramagnetic regime holds until just above the transition, where short-range correlations begin to be visible. As the temperature decreases these correlations increase in length and a cooperative effect occurs. Between $T/J \sim 1.2$ and $T/J \sim 0.9$ the majority of the spins all seem to point in roughly the same direction, yet the direction they point in often changes. This cooperative movement is much like that of a shoal of fish, being a classic example of an infinite correlation length in a magnetic system. This is the type of behaviour that would be expected

in any second-order phase transition [52], such as in a simple ferromagnet.

The final ordered state is very much like one observed in a simple ferromagnet, with a magnetization very close to unity. This is no surprise since the anisotropy is very low.

Animation for $D/J = 22.91$

This animation starts at a high temperature ($T/J = 44.0$), and again the system is in a random paramagnetic state. The spins can point in all possible directions. This regime again persists for a long time. Between $T/J \sim 5$ and $T/J \sim 1.5$ the spins start to be restricted to the region around their easy-axes. Their position either changes by a very small amount or is equivalent to an Ising spin flip. The system is still randomly disordered. Below $T/J \sim 1.5$ the spins become confined even more to the region around their easy-axes. Single spin flip dynamics persist until the transition temperature at $T/J \sim 0.35$. At the transition temperature there is an abrupt ordering of the spins, which is a confirmation of a first-order phase transition. The movement of the spins is then restricted to a small precession around their positions.

The final ordered state is a 'q=0' type (as already confirmed in section 3.1.1), with the same arrangement of spins on every 'up' or 'down' tetrahedron. This arrangement is one with two spins pointing into the tetrahedron and two spins pointing out.

3.1.3 Thermal Hysteresis in the System

First-order transitions are often accompanied by a hysteresis, where the transition temperature on cooling the system is different from that of heating the system. This effect can be explained in terms of Landau theory (see section 1.7.2).

In order to investigate the first-order nature of some of the transitions, heating and cooling curves were measured for all lattices and anisotropies. These are shown

in Figure 3.1. The tricritical point, at which the transition changes from first to second order, might be determined by following the appearance of hysteresis with respect to D/J. This method has been used before to determine the position of a tricritical point [69, 70].

For the small lattices hysteresis is only observed for the larger anisotropies – $D/J = 15.49, 22.91$. As the lattice size increases it is observed for $D/J = 10.47$, but this is the lowest D/J at which it is observed, even when $L = 9$. It is difficult to determine *exactly* where the hysteresis stops appearing. In this case the method is not sensitive enough and only confirms the first-order nature of the transition for the large anisotropies.

3.1.4 The Probability Distribution of the Magnetization

Observation of a bimodal energy distribution during the phase transition is good evidence that the transition is first-order [71, 72]. Even if hysteresis is not evident by comparing heating and cooling curves, it shows that the system simultaneously exists in two different states. A bimodal magnetization distribution will also be observed in such a system. A second order phase transition will have a Gaussian distribution throughout all the simulation [71, 72].

Hysteresis was not obvious for some values of D/J whose phase transitions seemed to be first-order. Therefore, in order to confirm their nature, histograms were determined of the distribution of the energy and the magnetization. The systems were put in the ordered state below the transition temperature and gradually heated up. A probability distribution of the magnetization $P(M)$ (with M defined by Eqn. (2.11)) was created by binning the data after every MCS/S. Longer simulations were performed at these temperatures to improve the quality of statistics. Figure 3.3 shows an example of an observed bimodal distribution.

This method might also be used to determine the tricritical point of the system. The existence of bimodal distributions could be followed for changing anisotropy.

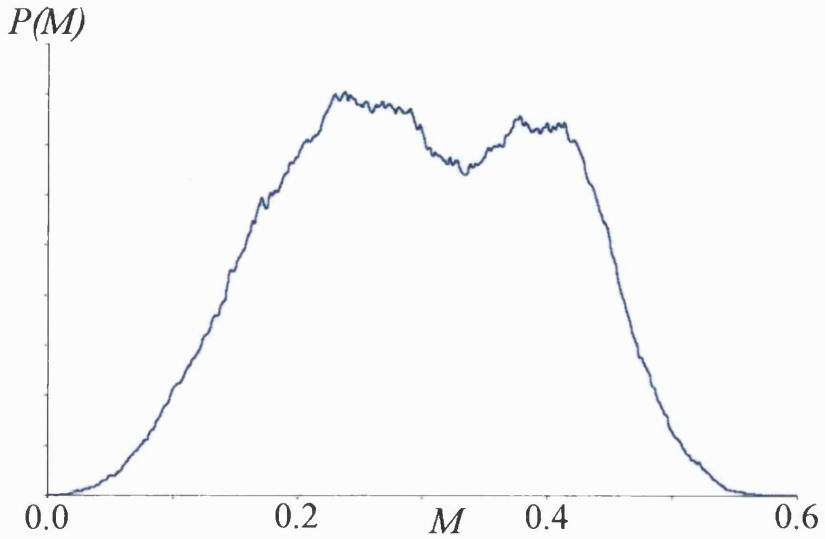

Figure 3.3: $P(M)$ for $D/J = 8.5$ at $T/J = 0.667$ with 2,500,000 MCS/S and 30,000 equilibration steps

The tricritical point would exist when the distributions became purely Gaussian. Further investigation into this possibility proved unsuccessful since it was only possible to determine *very* obvious bimodal distributions. The method is also not very sensitive since it is difficult to establish if the histogram is bimodal or not; it is only useful to confirm a first-order transition.

3.2 Second-order Transition: Finite-size Scaling Analysis

The obvious second-order nature of the transition for small anisotropy prompts calculation of critical exponents for the transition. In order to minimise the finite-size effects on the magnetization, the data collected from the largest system ($L = 9$) were analyzed.

D/J	0.1	0.5	1.0	2.18	3D-Ising	3D-Heis.
β	0.32±0.01	0.33±0.01	0.33±0.01	0.33±0.01	0.326	0.367
γ	1.20±0.01	1.23±0.01	1.22±0.01	1.25±0.01	1.2378	1.388

Table 3.1: Critical exponents determined from the data for $L = 9$, compared with the 3D-Ising and Heisenberg universality classes (from Ref. [55]).

3.2.1 Initial Critical Exponents

The exponents β and γ were determined for the following values of anisotropy: $D/J = 0.1$, 0.5, 1.0, 2.18. The results are shown in Table 3.1. An example of each one of the fits is shown in Figure 3.6. It proved much more difficult to fit the specific heat exponent α to any sensible value over any range of temperature.

The results in Table 3.1 suggest that the transition is in the 3D-Ising universality class. This is in itself an interesting result, since exponents for the 3D-Heisenberg class might be expected. The Ising-like γ reflects the broken rotational symmetry of the Hamiltonian for finite D/J.

3.2.2 Scaling of the Susceptibility

In the second-order regime the maximum of the magnetic susceptibility (χ_{max}) should scale as $L^{\gamma/\nu}$ [73], where γ and ν are the critical exponents describing the divergence of the susceptibility and correlation length. In the Ising universality class one has $\gamma/\nu = 1.969 \approx 2$ [56].

If $\frac{\chi_{max}(D)}{L^2}$ is plotted for each lattice size and one value of anisotropy then all values should collapse into a single point. If this is plotted over a range of anisotropic systems which are all in the same finite-size scaling regime, then a roughly horizontal line will be observed, provided they are all in the same universality class.

In first-order phase transitions the specific heat and magnetic susceptibility often scale with L^3 [74]. In these cases it is dependent on the correlation length

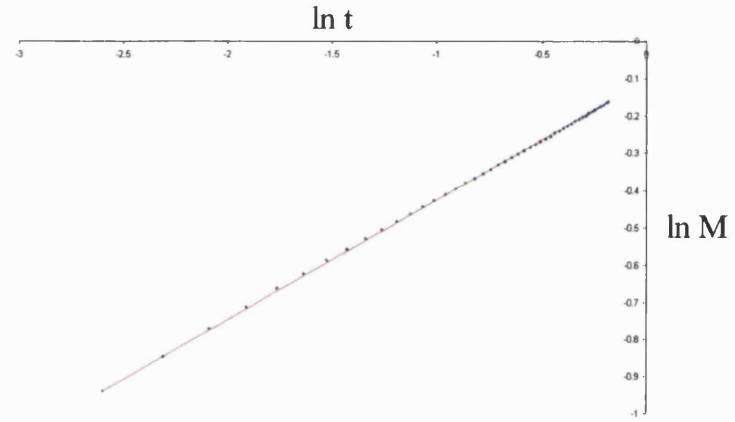

Figure 3.4: $\beta = 0.32 \pm 0.01$

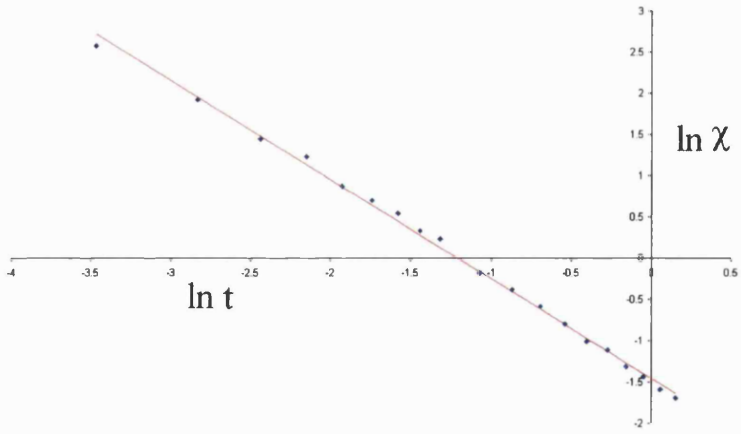

Figure 3.5: $\gamma = 1.20 \pm 0.01$

Figure 3.6: Critical exponent fits to data for $D/J = 0.1$, with $t = T - T_c$

being shorter than the lattice size. The existence of the second-order regime can therefore be followed as a function of anisotropy with respect to the L^2 scaling of χ_{max}. A rough position of the tricritical point will be indicated by the termination of data collapse.

The histograms generated in section 3.1.4 suggested that the tricritical point was somewhere between $D/J = 2.0 - 7.0$. Therefore $\chi_{\max}$ was determined for intermediate D/J from $2.0 - 7.0$ with $\Delta D/J = 0.2$. This was done for lattice sizes $L = 4 - 8$. The results of the scaling analysis are shown in Figure 3.7.

The simulations performed to generate the data in Figure 3.7 were heating runs out of the ordered state. These were the same length as those performed before, but with regular steps in temperature ($\Delta T/J = 0.01$).

As expected, good finite-size scaling is observed for low values of anisotropy. As the anisotropy increases the data gradually stop collapsing onto the same curve. When this happens the χ_{max} observed for larger lattices are systematically lower values than might be expected (*i.e.* they do not show proper scaling). It is often difficult to equilibrate systems with first-order transitions, since they often show hysteresis. Doubling the length of the simulation to $200,000$ MCS/S with $100,000$ equilibration steps did not always lead to any obvious improvement in the results. Time restrictions prevented checking of the anomalous results for the much larger lattices.

The breakdown of L^2 scaling in Figure 3.7 suggests that the tricritical point occurs at $D_{tc}/J = 5.0 \pm 0.5$. This is very much a qualitative result, owing to the difficulties mentioned above.

3.3 The Magnetic Structure of the Ordered State

Insight is gained into the ordered state through analysis of the microscopic positions of the spins at low temperature. Figure 3.8 shows the microscopic structure

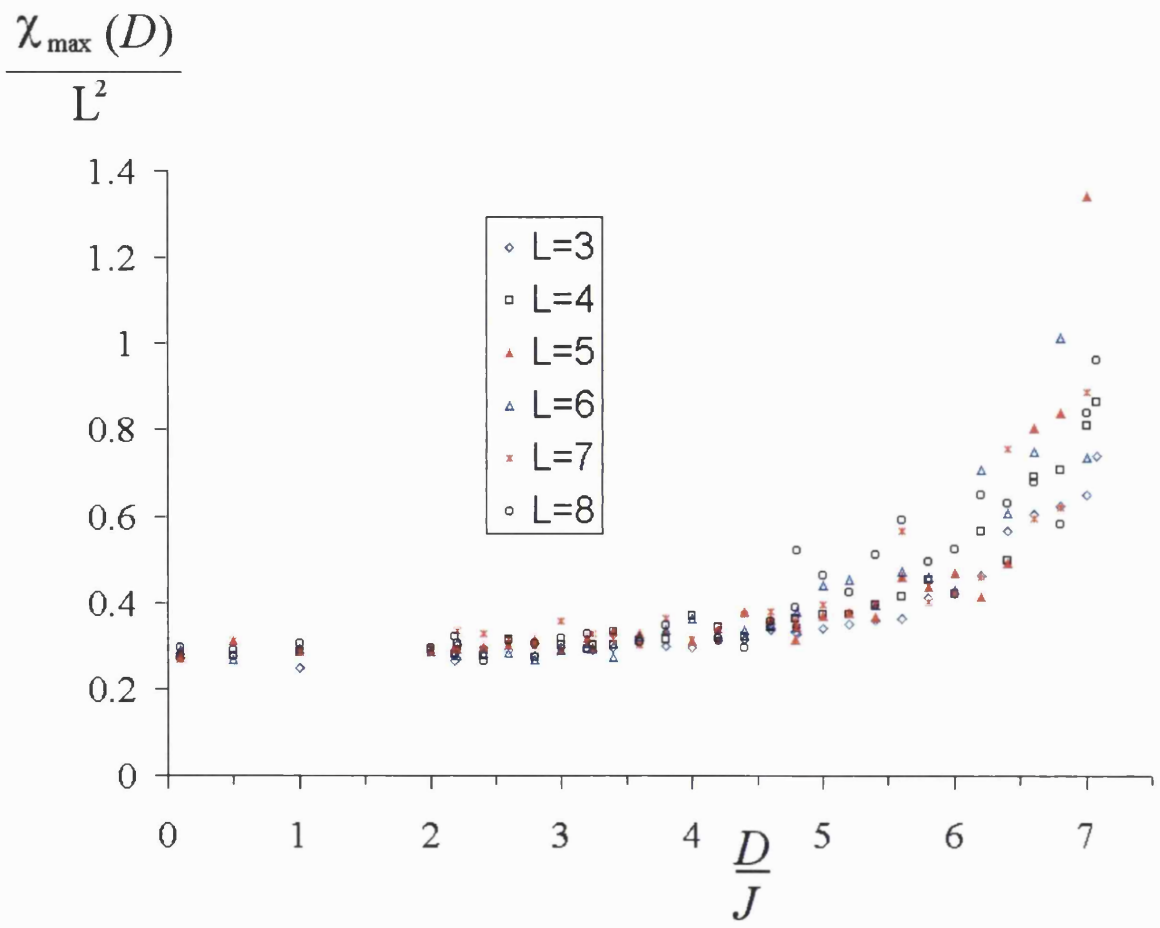

Figure 3.7: Plot of $\frac{\chi_{max}(D)}{L^2}$ versus D/J for different lattice sizes

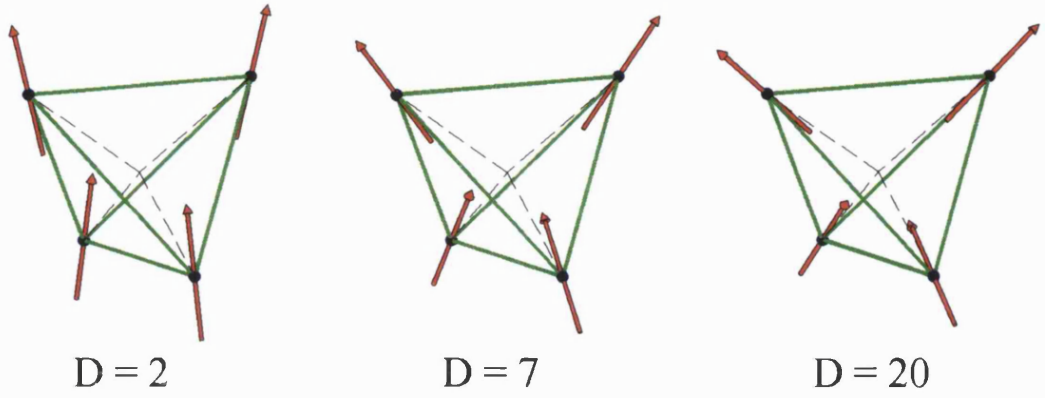

Figure 3.8: Ordered magnetic structure for a selection of anisotropies.

on one tetrahedron for $D/J = 2,\ 7,\ 20$.

As described in section 1.1, the ground state for a ferromagnetic Ising system is one with two spins pointing in and two spins pointing out. Figure 3.8 shows that for systems with large anisotropy the spins are, to a first approximation, fixed on the easy-axes. The spins have canted off the axes by a small amount and the magnetization of the system observed is slightly higher than that which is observed for a full Ising system ($M = \frac{1}{\sqrt{3}}$) [40].

As the anisotropy is decreased the spins gain more and more energy by canting off the axes, and the characteristics of the ordered state change. The spins become gradually more and more ferromagnetically ordered and the saturated magnetization increases (as $D/J \to 0,\ M \to 1$).

3.4 Analytical Expression for the Magnetization and Energy

In order to understand fully the results of Figures 3.1 and 3.8, the energy of the possible ordered states described in section 3.3 must first be considered, in particular the two limits $D/J \to 0$ and $D/J \to \infty$. The ordered state of each

of these limits is a q=0 state, with a magnetic unit cell consisting of a single tetrahedron, and therefore can be described by the positions of the four spins on one tetrahedron.

3.4.1 Limiting Expressions for the Energy

The energy is calculated using Eqn. (2.14) which is repeated below for convenience.

$$\mathbb{H} = -J \sum_{<i,j>} \mathbf{S}_i \cdot \mathbf{S}_j - D \sum_{i=1}^{N} (\boldsymbol{\delta}_i \cdot \mathbf{S}_i)^2 - h \sum_{i=1}^{N} \mathbf{S}_i$$

The four crystal field directions are as follows:

$$\begin{aligned} \boldsymbol{\delta}_1 &= 1/\sqrt{3}[1,1,1],\ \boldsymbol{\delta}_2 = 1/\sqrt{3}[1,-1,-1], \\ \boldsymbol{\delta}_3 &= 1/\sqrt{3}[1,-1,1],\ \boldsymbol{\delta}_4 = 1/\sqrt{3}[1,1,-1]. \end{aligned} \tag{3.3}$$

The particular sign of the crystal field is unimportant since the anisotropy term is squared.

$D/J \to 0$ Ground state energy

For $D/J \to 0$ the ground state is a perfect ferromagnet with all spins pointed along the [001] direction. It is termed the '[001]' state. All bonds are ferromagnetic and contribute $-J$ to the total exchange energy of $-3NJ$, since there are $3N$ bonds in the system. The total anisotropy energy is $-ND/3$ since every site contributes $-D/3$. The total energy is therefore

$$\frac{E}{N} = -3J - \frac{D}{3}. \tag{3.4}$$

$D/J \to \infty$ Ground state energy

For $D/J \to \infty$ the ground state is one with the spins directed along their local easy-axes in a two-in two-out fashion:

$$\begin{aligned} \mathbf{S}_1 &= 1/\sqrt{3}[1,1,1],\ \mathbf{S}_2 = 1/\sqrt{3}[-1,1,1], \\ \mathbf{S}_3 &= 1/\sqrt{3}[1,-1,1],\ \mathbf{S}_4 = 1/\sqrt{3}[-1,-1,1]. \end{aligned} \tag{3.5}$$

Here, this state is termed the '$\langle 111 \rangle$' state and has a magnetic moment along $\mathbf{z} = [001]$ of size $1/\sqrt{3}$. For each tetrahedron there are 4 bonds making an exchange contribution of $-J/3$ and two of $J/3$. There are $N/2$ tetrahedrons on the lattice each contributing $-2J/3$ to give a total of $-NJ/3$ for the exchange energy. The anisotropy term is simply $-D$ for every site and therefore the total energy for the state is

$$\frac{E}{N} = -\frac{J}{3} - D \tag{3.6}$$

3.4.2 Energy Expression for Finite Anisotropy

Neither of the ground states described above is valid for any finite values of D/J. They are for the limits only, but are a good starting point for a general state. An estimation can be made of the ground state spin orientation for large and small D/J by making the reasonable ansatz that the relaxation away from, or towards $\langle 111 \rangle$ is homogeneous for the four spins of the unit cell. This ansatz seems likely considering the intermediate ground states shown in Figure 3.8.

The extent of relaxation is defined by a deformation parameter ε. The energy is expanded as a function of ε and then minimised. This process produces an expression for the energy and magnetization in terms of anisotropy (in the form of a small parameter).

Small D/J expansion

For weak crystal field there is a deformation out of the [001] state towards the $\langle 111 \rangle$ state. Each spin is defined such that $|S_x| = \varepsilon$, $|S_y| = \varepsilon$, $|S_z| = \sqrt{1-2\varepsilon^2}$. The deformed spin directions then become:

$$\begin{aligned} \mathbf{S}_1 &= [\varepsilon, \varepsilon, \sqrt{1-2\varepsilon^2}],\ \mathbf{S}_2 = [-\varepsilon, \varepsilon, \sqrt{1-2\varepsilon^2}], \\ \mathbf{S}_3 &= [\varepsilon, -\varepsilon, \sqrt{1-2\varepsilon^2}],\ \mathbf{S}_4 = [-\varepsilon, -\varepsilon, \sqrt{1-2\varepsilon^2}]. \end{aligned} \tag{3.7}$$

The energy is now calculated using the same ideas illustrated in section 3.4.1. For each spin the dot product $\mathbf{S}_i.\boldsymbol{\delta}_i = \pm 1/\sqrt{3}(2\varepsilon + \sqrt{1-2\varepsilon^2})$. The scalar product exchange term takes on two possible values.

$$\begin{aligned} \mathbf{S}_1.\mathbf{S}_2 = \mathbf{S}_1.\mathbf{S}_3 = \mathbf{S}_2.\mathbf{S}_4 = \mathbf{S}_3.\mathbf{S}_4 &= 1 - 2\varepsilon^2 \\ \mathbf{S}_1.\mathbf{S}_4 = \mathbf{S}_2.\mathbf{S}_3 &= 1 - 4\varepsilon^2. \end{aligned} \tag{3.8}$$

As in section 3.4.1 the contribution from each bond in one tetrahedron is summed and then divided by two, to give a value for the energy per spin to the second order in ε.

$$\frac{E}{N} = \left(-\frac{D}{3} - 3J\right) - \frac{4D}{3}\varepsilon + \left(-\frac{2D}{3} + 8J\right)\varepsilon^2 + O\left(\varepsilon^3\right) \tag{3.9}$$

Eqn. (3.9) is minimised with respect to ε where we have defined the small parameter $\alpha = D/J$.

$$\frac{dE}{d\varepsilon} = 0 = -\frac{4\alpha J}{3} + \left(-\frac{4\alpha J}{3} + 16J\right)\varepsilon + O\left(\varepsilon^2\right) \tag{3.10}$$

This expression is solved to leading order in α to give:

$$\varepsilon = \frac{\alpha}{12} + O(\alpha^2). \tag{3.11}$$

Substituting this value back into Eqn. (3.9) and for $M = \sqrt{1-2\varepsilon^2}$ one finds:

$$\frac{E}{N} = J\left(-3 - \frac{\alpha}{3} - \frac{\alpha^2}{18}\right) \tag{3.12}$$

$$M = \sqrt{1 - \frac{\alpha^2}{72}}. \tag{3.13}$$

Large D/J expansion

For strong crystal field there is a deformation out of the $\langle 111 \rangle$ state towards the [001] state. Each spin is defined such that $S_z = 1/\sqrt{3} + \varepsilon$ and again imposing the

condition that $|S_x| = |S_y|$, which gives the deformed spin directions:

$$\begin{aligned}
\mathbf{S}_1 &= \left[\sqrt{\frac{1}{3}-\frac{\varepsilon}{\sqrt{3}}-\frac{\varepsilon^2}{2}}, \sqrt{\frac{1}{3}-\frac{\varepsilon}{\sqrt{3}}-\frac{\varepsilon^2}{2}}, \frac{1}{\sqrt{3}}+\varepsilon\right], \\
\mathbf{S}_2 &= \left[-\sqrt{\frac{1}{3}-\frac{\varepsilon}{\sqrt{3}}-\frac{\varepsilon^2}{2}}, \sqrt{\frac{1}{3}-\frac{\varepsilon}{\sqrt{3}}-\frac{\varepsilon^2}{2}}, \frac{1}{\sqrt{3}}+\varepsilon\right], \\
\mathbf{S}_3 &= \left[\sqrt{\frac{1}{3}-\frac{\varepsilon}{\sqrt{3}}-\frac{\varepsilon^2}{2}}, -\sqrt{\frac{1}{3}-\frac{\varepsilon}{\sqrt{3}}-\frac{\varepsilon^2}{2}}, \frac{1}{\sqrt{3}}+\varepsilon\right], \\
\mathbf{S}_4 &= \left[-\sqrt{\frac{1}{3}-\frac{\varepsilon}{\sqrt{3}}-\frac{\varepsilon^2}{2}}, -\sqrt{\frac{1}{3}-\frac{\varepsilon}{\sqrt{3}}-\frac{\varepsilon^2}{2}}, \frac{1}{\sqrt{3}}+\varepsilon\right]. \qquad (3.14)
\end{aligned}$$

Again the anisotropy term takes the same value for each spin, which is then approximated using a binomial expansion to the leading order in ε.

$$(\boldsymbol{\delta}_i.\mathbf{S}_i)^2 = \frac{1}{3}\left(2\sqrt{\frac{1}{3}-\frac{\varepsilon}{\sqrt{3}}-\frac{\varepsilon^2}{2}}+\frac{1}{\sqrt{3}}+\varepsilon\right)^2 \qquad (3.15)$$

$$\sqrt{\frac{1}{3}-\frac{\varepsilon}{\sqrt{3}}-\frac{\varepsilon^2}{2}} \approx \frac{1}{\sqrt{3}}-\frac{\varepsilon}{2}-\frac{9\varepsilon^2}{8\sqrt{3}}+\ldots \qquad (3.16)$$

$$(\boldsymbol{\delta}_i.\mathbf{S}_i)^2 \approx 1-\frac{3\varepsilon^2}{2}+\ldots \qquad (3.17)$$

For the exchange energy there are again two possible values for the scalar product.

$$\mathbf{S}_1.\mathbf{S}_2 = \left(\frac{1}{\sqrt{3}}+\varepsilon\right)^2 = \frac{1}{3}+\frac{2\varepsilon}{\sqrt{3}}+\varepsilon^2 \qquad (3.18)$$

$$\begin{aligned}
\mathbf{S}_1.\mathbf{S}_4 &= -2\left(\frac{1}{3}-\frac{\varepsilon}{\sqrt{3}}-\frac{\varepsilon^2}{2}\right)^2+\left(\frac{1}{\sqrt{3}}+\varepsilon\right)^2 \\
&= -\frac{1}{3}+\frac{4\varepsilon}{\sqrt{3}}+2\varepsilon^2 \qquad (3.19)
\end{aligned}$$

The energy per spin is determined again to the second order in ε by the same method:

$$\frac{E}{N} = \left(-D-\frac{J}{3}\right)-\frac{8J}{\sqrt{3}}\varepsilon+\left(\frac{3D}{2}-4J\right)\varepsilon^2+O\left(\varepsilon^3\right). \qquad (3.20)$$

Eqn. (3.20) is minimised with respect to ε:

$$\frac{dE}{d\varepsilon} = 0 = -\frac{8J}{\sqrt{3}}+(-8J+3D)\varepsilon+O\left(\varepsilon^2\right) \qquad (3.21)$$

This expression is solved to the leading order in the small parameter $\gamma = J/D$ to give:

$$\varepsilon = \frac{8\gamma}{3\sqrt{3}} + O(\gamma^2). \tag{3.22}$$

Substituting this value back into Eqn. (3.20) and for $M = \frac{1}{\sqrt{3}} + \varepsilon$ one finds:

$$\frac{E}{N} = D\left(-1 - \frac{\gamma}{3} - \frac{32\gamma^2}{9}\right) \tag{3.23}$$

$$M = \frac{1}{\sqrt{3}} + \frac{8\gamma}{3\sqrt{3}}. \tag{3.24}$$

3.4.3 Numerical Test of the Analytic Expression

To test the theoretical predictions, the magnetization was computed by performing zero temperature Monte Carlo simulations. This is a simple variant on the method described in section 2.1.2. In this case only spin moves which lower the energy are accepted [75]. In Fig. 3.9 these estimates are plotted versus the anisotropy D/J and compared with the small anisotropy result (Eqn. (3.13)) and the large anisotropy result (Eqn. (3.24)). The agreement is seen to be excellent in both cases, with each asymptotic equation breaking down near the tricritical point at $D_{tc}/J = 5$. It is therefore tempting to associate the change in order of the transition with a non-linear cross over from a regime that is nearly ferromagnetic, to one that is nearly q=0 spin ice.

3.5 Determination of the Magnetic Phase Diagram

Further insight into the nature of this cross over is gained by a consideration of the magnetic phase diagram. The behaviour of the continuous spin ice model is considered in an external magnetic field applied along the [100] direction which sustains the symmetry of the ordered state for all finite D/J. In Ref. [40] it was

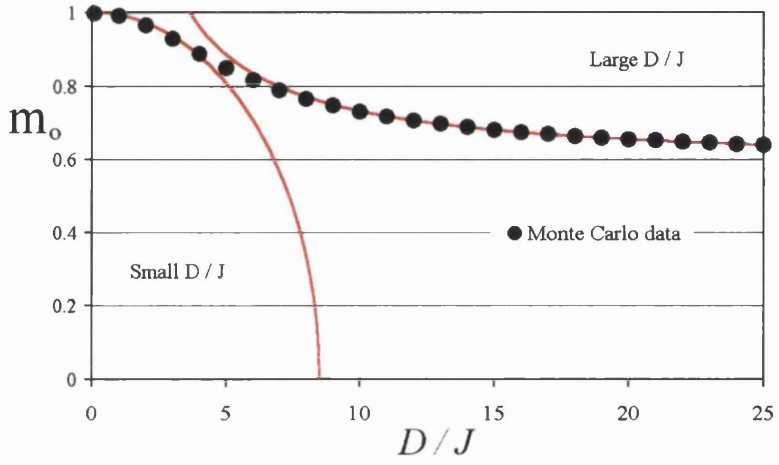

Figure 3.9: Comparison of the numerical zero temperature magnetization m_0, estimated by a zero-temperature Monte Carlo method, with that estimated by the analytical expressions Eqn. (3.13) (left hand line) and Eqn. (3.24) (right hand line). Both asymptotic expressions are seen to break down near the tricritical point $D_{tc}/J = 5.0 \pm 0.5$.

shown that the magnetic phase diagram of the near neighbour spin ice model with the field along [100] has two lines of first-order phase transitions that separate phases of different magnetization (see section 1.3.1). Both lines terminate in critical points. It was argued that the phase diagram can be considered analogous to that of a liquid-gas system, where a line of first-order transitions separates phases of different density. In this section the equivalent phase diagram for the continuous spin ice model has been mapped out.

3.5.1 Details of the Simulations

In this investigation it was decided to make simulations on only one size of system ($L = 5, N = 2000$). It was hoped that the system would be small enough to be at equilibrium after 30,000 MCS/S and large enough to give good statistical

results. Two types of measurement were made, as described below. All simulations were of the same length (100,000 MCS/S) with the same equilibration time (30,000 MCS/S). In each case the phase boundary was estimated from the maximum in the magnetic susceptibility (Eqn. (2.12)) and specific heat (Eqn. (2.6)).

Constant field

In this case the system was placed in the ordered state at a low temperature with a fixed applied magnetic field. The temperature was increased in small regular amounts $\Delta T = 0.005, 0.01$. This was then repeated for different fixed values of applied magnetic field.

Constant temperature

In this case the system was placed in the ordered state in a high applied magnetic field at a fixed temperature. The magnetic field was decreased in small regular amounts $\Delta h = 0.02$. This was then repeated for different fixed temperatures.

Anisotropy

The third axis on the magnetic phase diagram under investigation is the anisotropy. Three different anisotropic systems were simulated with $D/J = 20.0, 15.0, 10.0$.

3.5.2 Results: Description of the Phase Diagram

The results are shown in Figure 3.10a, and represented schematically in Figure 3.10b. It is seen that the two first-order lines of the spin ice phase diagram coalesce below the ordering temperature, which is therefore seen to be a triple point (see Fig. 3.10b). The triple point temperature increases with decreasing D/J and eventually the two 'wings' disappear and give way to a line of first-order transitions along the zero field axis, typical of a ferromagnet.

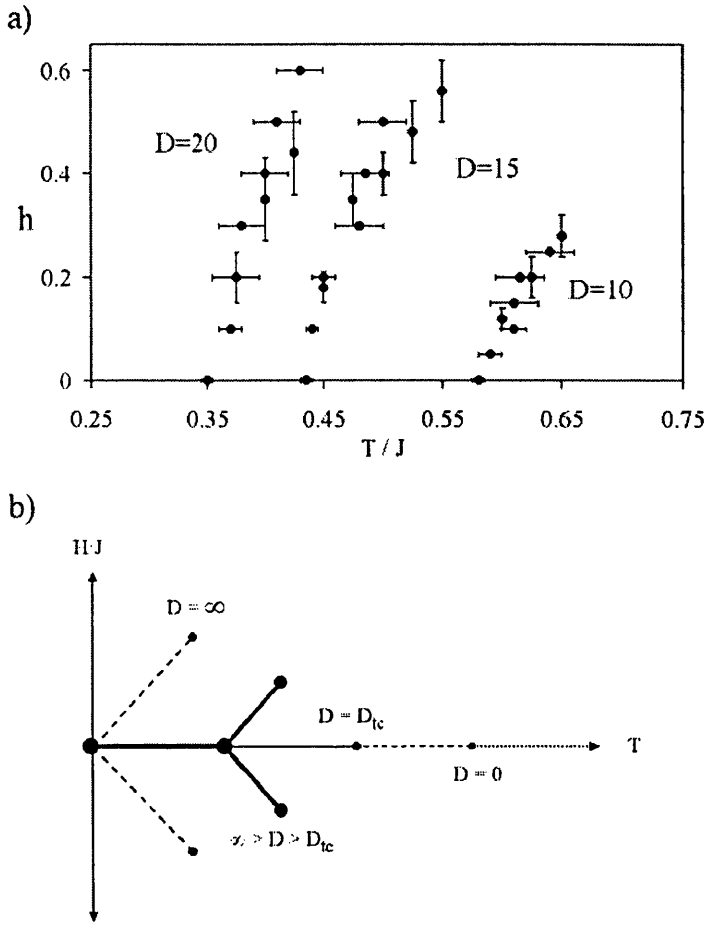

Figure 3.10: Magnetic phase diagram for the continuous spin ice model defined by Eqn. (2.14). (a) Phase diagram determined by Monte Carlo simulation on a system of $N = 2000$ spins. Points on the coexistence lines were determined from the maximum in the susceptibility in fixed temperature (vertical error bars) or fixed field (horizontal error bars) Monte Carlo runs. For ease of comparison with experiment and Ref. [40], the field h is defined as $h = H \times (\mu_B/k_B) = H/0.06717$, with μ_B and k_B the Bohr magneton and Boltzmann's constant respectively, and H defined in Eqn. (2.14). (b) Schematic phase diagram showing the case of $D/J = 0$ (short dashed line), $D/J = D_{tc}/J$ (thin line), $D/J > D_{tc}/J$ (thick line) and $D/J \to \infty$ (long dashed line)

3.6 Conclusions

This investigation has suggested the existence of a tricritical point in the system. Landau first looked at systems in which the order of transition changed and developed a theory to explain the phenomenon [58]. The term 'tricritical point' was first coined by Griffiths in his investigation of the superfluid transition in ^{3}He-^{4}He mixtures [63]. The term refers to a confluence of *three* lines of ordinary phase transitions, with a notion of three phases becoming identical at one point. It is relevant to briefly review some previous work on tricritical points in magnetic systems.

3.6.1 Tricritical Points in Metamagnets

Real examples of tricritical points in magnetic systems occur in metamagnets such as $FeCl_2$ [76, 77] and $Dy_3Al_5O_{12}$ [78]. In model systems as well as real metamagnets, there are often intra-sublattice antiferromagnetic interactions and inter-sublattice ferromagnetic interactions. The magnetic spins are often uniaxial Ising spins with a longitudinal magnetic field applied. In zero-field there is a continuous paramagnet to antiferromagnet phase transition. If a simple cubic lattice is considered, the antiferromagnetic phase is stabilised by both interactions present in the system. The phase diagram for a metamagnet is shown in Fig. 3.11. When a *disordering* magnetic field is applied to the system (with respect to the antiferromagnetic order), there is competition between the antiferromagnetic interactions of the spins, and the desire for the spins to align ferromagnetically with the field. At a certain critical field there is a phase transition to a ferromagnetically ordered state.

For $T_{tc} < T < T_N$ the application of the field does not affect the order of the transition and critical exponents are observed such as those in the zero-field case. At low temperatures the effect of the magnetic field is more evident, the phase transition is first-order and phase coexistence between the ordered and disordered

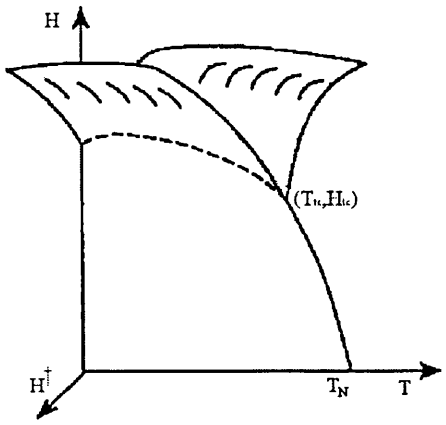

Figure 3.11: Schematic phase diagram of a metamagnet.

phases is observed (in a real system). At $T = T_{tc}$ there is a crossover in the nature of the phase transition. The transition is notionally second-order, but has particular 'tricritical' exponents associated with it [79, 77, 62].

A simple order parameter for the metamagnet under consideration is the magnetization of each ferromagnetically aligned sublattice, or 'staggered magnetization' $M^{\dagger}$. Therefore it is useful to consider the effect of applying a 'staggered' magnetic field $H^{\dagger}$, which couples directly to the staggered magnetization. This is of course impossible to apply to a real system. The third axis creates the possibility of 'up' and 'down' staggered magnetization separated by the phase coexistence surface at zero applied staggered field. The schematic phase diagram is shown in Fig. 3.11. The application of staggered field also creates a pair of coexistence surfaces which extend symmetrically into the $H^{\dagger} > 0$ and $H^{\dagger} < 0$ regions, separating the ordered and disordered phases. These two surfaces meet at the line of first-order phase transitions observed and are bounded by a line of critical points which meet at the tricritical point (T_{tc},H_{tc}). The properties of the critical behaviour change with respect to the ratio of the inter- to intra- sublattice interactions [80, 62].

All these metamagnetic properties have been observed in real [76, 77, 78] and

theoretical systems [81, 82, 62, 83].

3.6.2 Tricritical Point in Continuous Spin Ice

The continuous spin ice system under investigation in this chapter was shown to have a tricritical point. This system is also one of competing interactions, very similar to the metamagnets. In metamagnetic systems the antiferromagnetic exchange term in the Hamiltonian competes with the non-ordering magnetic field between the ordered and disordered phase. In continuous spin ice the ferromagnetic exchange term competes with the anisotropy *within* the ordered phase. In continuous spin ice the disordered phase is truly paramagnetic. The frustration of the exchange interaction (inherent in the spin ice model) is relieved by the finite nature of the anisotropy. The Heisenberg spins are allowed to cant off the easy-axes and gain some exchange energy at the cost of anisotropy energy (see section 3.3). This is the source of the degeneracy lifting in the system. Canting off the axes creates a non-degenerate ground state. The point at which the two properties are balanced is the tricritical point, where the system is neither spin ice-like nor ferromagnetic.

The anisotropy in the spin ice system has replaced the uniform field present in the metamagnet and the magnetic field along the [100] direction has replaced the effect of the staggered field. Consequently, application of the magnetic field creates two symmetrical coexistence surfaces separating areas of q=0 order and paramagnetic disorder. These 'wings' disappear precisely at the tricritical point determined above, $D_{tc}/J \approx 5$. This kind of phase diagram is exhibited by idealized ferroelectrics and also some real ones such as $BaTiO_3$ [61](see also section 9.1).

Chapter 4

Easy-Plane Antiferromagnet

In this chapter, the ordering and degeneracy of an easy-plane pyrochlore antiferromagnet are considered. While there is an infinite ground state degeneracy in the system, ordering still occurs. The nature of this ordering is discussed, as well as the reasons why it occurs.

The first part of the chapter deals with Monte Carlo investigations of the system and its possible ground states. The second part considers a theoretical calculation which sheds more light on the reasons for the ordering in the system.

4.1 Previous Studies of XY Pyrochlore Antiferromagnets

As discussed in section 1.2.4 the ground state of a frustrated pyrochlore antiferromagnet is one with all four spins on every tetrahedron summing to zero. The first XY pyrochlore antiferromagnet studied was by Bramwell *et al.* [84]. However, it is convenient to discuss first the simpler model studied by Moessner *et al.* [28]. Both examples discussed here are frustrated antiferromagnets.

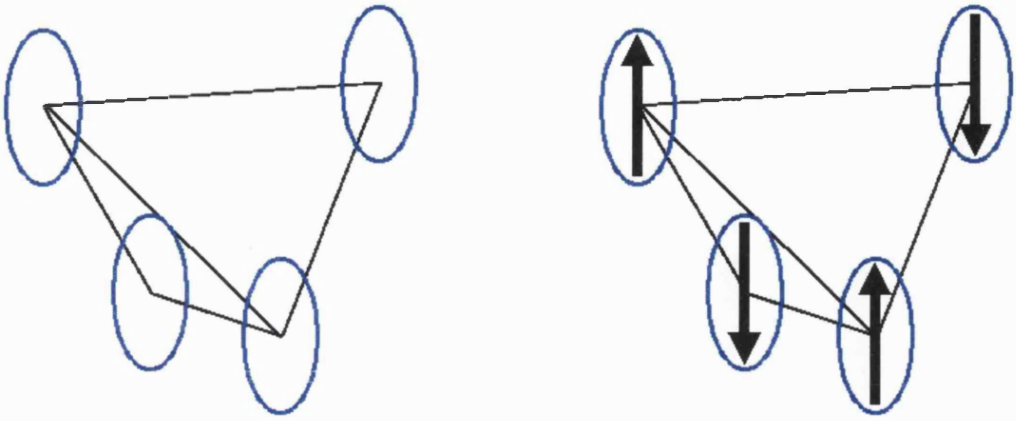

(a) XY planes (b) A ground state

Figure 4.1: Coplanar XY antiferromagnet

4.1.1 Coplanar XY Antiferromagnet

Moessner *et al.* studied a pyrochlore antiferromagnet which consisted of coplanar XY spins [28]. A diagram showing an example of the orientation of the planes is shown in Fig. 4.1(a). It should be noted that these planes do not have the symmetry of the pyrochlore lattice and are not comparable with any known experimental system.

It is often instructive to consider the ground states of a single tetrahedron. In such cases a simple ground state is one with two spins pointing up and two spins pointing down (see Fig. 4.1(b)). This is not the only ground state since the energy will be minimised by associating the four spins into two pairs of anti-parallel spins. This leads to an infinite number of possible ground states. The manifold is described as 'fully connected', since any particular ground state can be continuously deformed into any other at no extra cost [28]. This argument can be extended to cover the lattice as a whole and not just the single tetrahedron.

This is a 'smaller' degeneracy than that of the Heisenberg pyrochlore antiferromagnet, these ground states are simply a subset of coplanar states in the fully connected Heisenberg manifold.

Moessner *et al.* [28] calculated a probability distribution $W(\theta)$ for the angle θ between a pair of spins, integrating over all the four spins with a Boltzmann distribution and the Hamiltonian. They determined that the distribution in the limit $T \to 0$ is particularly concentrated near collinear spin arrangements ($\theta = 0$ and π). They found that there were soft modes out of the collinear states.

The specific heat of a system with order by disorder

Moessner *et* al. [28] determined how many soft modes per unit cell were present for a collinear state. The specific heat can be determined using the method described in section 1.2.5. There are four degrees of freedom with four constraints per unit cell (since there are only two component spins). In the absence of order all four modes are quadratic and $C_h/Nk_BT = 1/2$. The soft mode calculation in Ref. [28] showed that for a collinear state two of the quadratic modes become quartic. The specific heat per spin is thus $C_h/Nk_BT = 3/8$.

Monte Carlo simulations confirmed the reduction in specific heat [28]. This represents selection of these states by thermal fluctuations since there are soft modes out of the collinear states. This is an example of order by disorder (see section 1.2.6), where there is a concentration of statistical weight on a submanifold of ground states.

The order observed in the system has a nematic/collinear order, where two spins are pointing up and two spins are pointing down on every tetrahedron. But this arrangement is disordered over the whole lattice, in much the same way as spin ice, where two spins are pointing in and out of every tetrahedron, yet with no long range order.

Spin	Cartesian equation	Crystallographic form
1	$x+y+z=0$	$[1\ 1\ 1]$
2	$x-y+z=0$	$[1\ \bar{1}\ 1]$
3	$x-y-z=0$	$[1\ \bar{1}\ \bar{1}]$
4	$x+y-z=0$	$[1\ 1\ \bar{1}]$

Table 4.1: Cartesian and crystallographic description of the easy-planes.

4.1.2 Easy-Plane XY Antiferromagnet

Bramwell *et al.* studied a Heisenberg pyrochlore antiferromagnet with local easy-plane anisotropy [84]. The Hamiltonian used is shown below (Eqn. (2.14)).

$$\mathbb{H} = -J \sum_{<i,j>} \mathbf{S}_i \cdot \mathbf{S}_j - D \sum_{i=1}^{N} (\boldsymbol{\delta}_i \cdot \mathbf{S}_i)^2$$

This is a system with a variable anisotropy and allows out of plane fluctuations. The anisotropy may be set strong enough to consider the system as being effectively XY/easy-plane. A diagram of the easy-planes is shown in Fig. 4.2(a). The equation of each easy-plane is listed in Table 4.1 with its associated spin label in Figure 4.2(a).

Identification of the possible ground states for this system is more complex due to the non-coplanar nature of the easy-planes. It is again instructive to consider the possible ground states of a single tetrahedron. Bramwell *et al.* proposed a $T = 0$ ground state for the system that maximised the number of antiferromagnetic bonds. The arrangement of the spins is shown in Fig. 4.2(b) and from now on this will be referred to as 'state I'. In this coplanar arrangement there are two fully antiferromagnetic bonds and four bonds which make no contribution to the exchange energy (since the spin pairs are perpendicular). The anisotropy energy is trivially zero as the spins are fixed in the easy-planes. There are also two other arrangements related by symmetry, in which the spins are perpendicular to the two other coordinate axes [84].

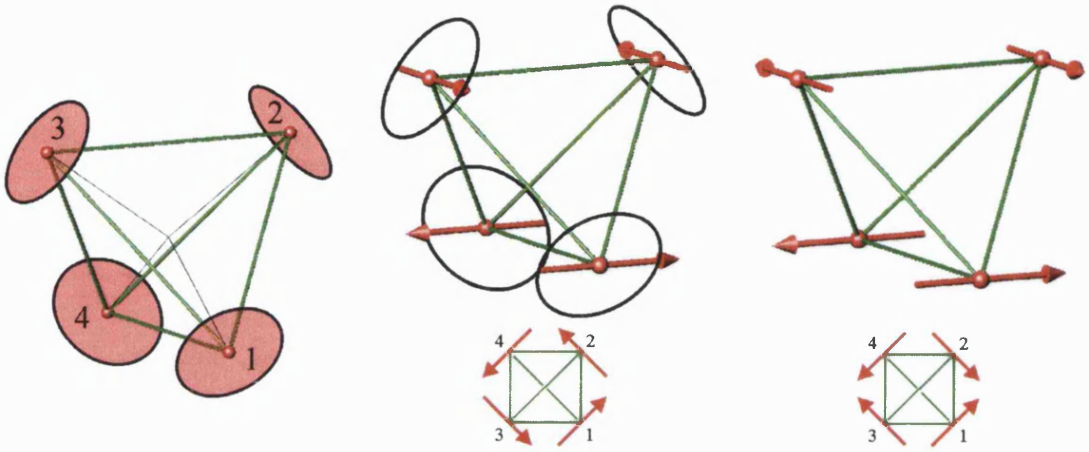

(a) (b) State **I** (c) State **II**

Figure 4.2: The easy-planes of a tetrahedron and two ground states.

Other related ground states are generated by flipping the pairs of spins, see for example Fig. 4.2(c) which will be referred to as 'state **II**'. When considering the lattice as a whole, the authors considered ground states consisting of rods of antiferromagnetically aligned spins. These are in fact the perpendicular bonds '1-4' and '2-3' in Fig. 4.2(b) on each tetrahedron, propagated over the whole lattice. If the system was in a q=0 ordered state, it could be disordered by flipping all the spins on different rods [84]. These disordered states of coplanar spins maintain zero spin on every tetrahedron, creating a macroscopic degeneracy of ground states. This manifold is rugged, since the proposed ground states cannot be continuously deformed into each other with no increase in the energy of the system.

Bramwell and co-workers performed Monte Carlo simulations of the system with $J = -1$ and $D/J = -5$. The system undergoes a first-order magnetic phase transition to a long-range ordered state. The authors concluded that the selection of the q=0 state must be caused by thermally-induced coupling between the spin rods. This type of ordering is another example of order by disorder [84].

No investigation was made into the low temperature specific heat or the microscopic nature of the ordered state. This chapter is concerned with a more detailed

investigation of the same system, albeit one with infinite easy-plane anisotropy, $D = \infty$. One of the main results presented here is that the ground state manifold proposed by Bramwell *et al.* is incomplete, as it does not contain all possible ground states (see section 4.3).

4.2 Monte Carlo Simulations of the Easy-Plane Antiferromagnet

Monte Carlo simulations were performed on a system with a simplified Hamiltonian with $D = \infty$ such that the spins are confined rigorously to the easy-planes, and any out of plane fluctuation is at infinite energy cost:

$$\mathbb{H} = -J \sum_{<i,j>} \mathbf{S}_i \cdot \mathbf{S}_j. \tag{4.1}$$

In this case, $J = -1$ and the spins are fixed in their easy-planes.

The runs were generally started in a random configuration at high temperature ($T/J \sim 1$). The system was then slowly annealed with each successive temperature being 90-95% of that previously measured. The length of the simulations was generally 400,000 MCS/S with 200,000 equilibrium MCS/S. A survey was made of systems with lattices ranging from $L = 3 - 6$.

For each simulation thermodynamic averages were taken of the energy and the sublattice order parameter defined in Eqn. (3.2). The specific heat was again determined from the fluctuations of the energy.

4.2.1 Initial Results

The sublattice order parameter is plotted versus temperature for different lattice sizes in Fig. 4.3. The main result from Ref. [84] is reproduced, with a strongly first-order phase transition at $T/J \approx 0.125$ to a q=0 long range-ordered state.

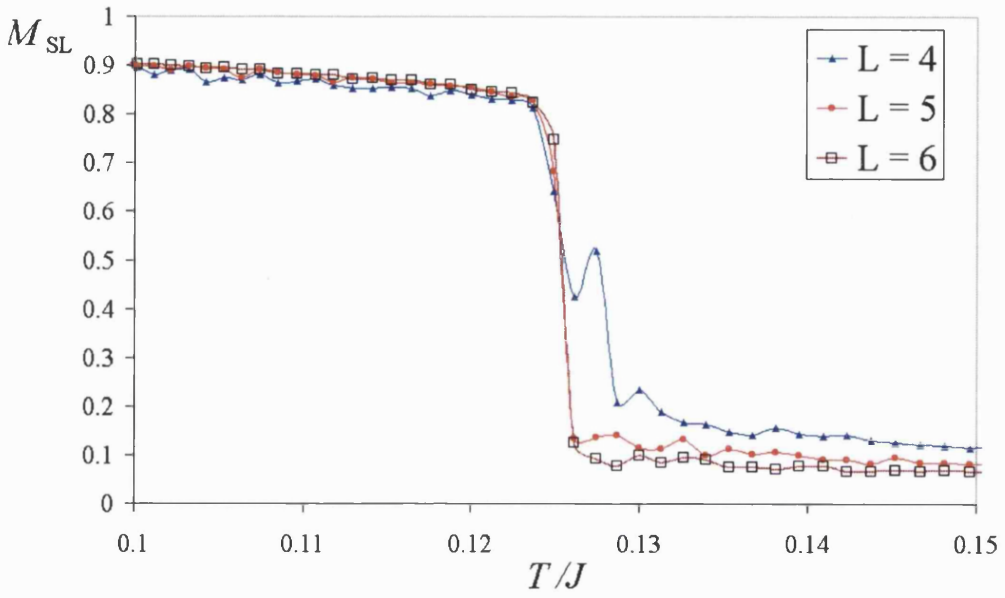

Figure 4.3: Transition to an ordered q=0 state.

Bramwell *et al.* observed scaling of the specific heat maxima with L^3 [84]. This occurs when the correlation length is shorter than the size of the lattice [74]. The results collected here did not seem to show such scaling, but the transition seems very strongly first-order. It may be that, in the case of infinite anisotropy, the correlation length is larger than the size of the lattice.

4.2.2 The Magnetic Structure of the Ordered State

As in section 3.3, insight is gained into the ordered state through analysis of the microscopic positions of the spins at low temperature. The system has q=0 long-range order and again it is only necessary to show the spin arrangement on one tetrahedron. The low temperature spin arrangement is shown in Figure 4.4(a) and will be referred to as 'state **III**'. This is a particularly interesting result, since the state **III** is spatially different from state **I**. State **III** has zero spin on every tetrahedron, and is another ground state for the system. It is evident that there are

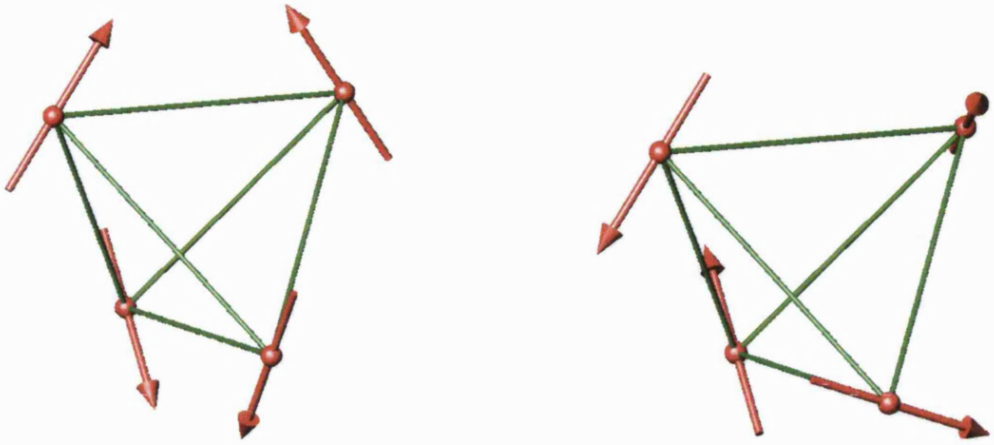

(a) State **III** (b) State **IV**

Figure 4.4: Ground states observed for the easy-plane tetrahedron.

many q=0 ordered states which satisfy the ground state criteria for the easy-plane antiferromagnet. These are discussed more fully in section 4.3.

As the system was cooled below the transition temperature there was sometimes a sharp dip in the order parameter (see Fig. 4.5). On further cooling, the system either recovered its full ordering, or stayed in a defected state down to very low temperatures. The dip in ordering can be explained by the existence of an infinite line defect of spins in the lattice. Figure 4.6 shows one such line of spins, which exist independently in a 'sea' of q=0 ordered spins. The red spins show the arrangement of q=0 spins, and the defect spins are superimposed as blue spins. It it interesting to note the arrangement of the spins on the tetrahedra which have bonds intersecting with the line defect (see Fig. 4.4(b)). Two spins are arranged in the manner of state **III**, and two of the spins are defected, (these are the blue spins in Figure 4.6). This state will be referred to as 'state **IV**', since it is also a ground state for a single tetrahedron and has a total spin of zero over the four spins.

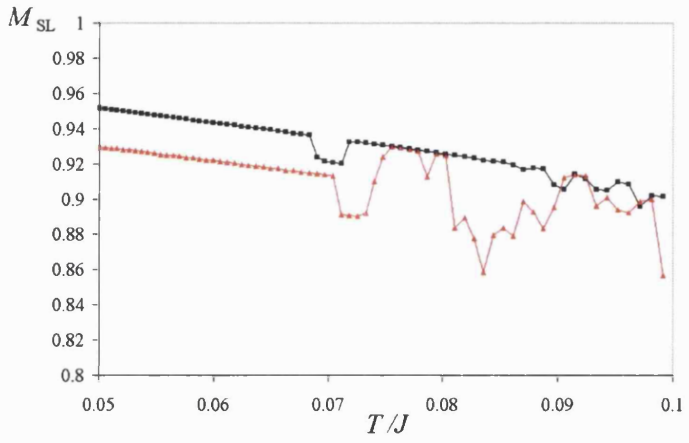

Figure 4.5: The effect of a defect on the sublattice order parameter for two different sized lattices. The black line shows a system which recovers q=0 order after experiencing a defect (L=5). The red line shows a system which does not recover q=0 order (L=4).

4.3 A General q=0 Ground state for the system

In section 4.2.2 some new ground states other than state **I** and state **II** were discussed. In order to determine a general solution of ground states, the constraints on the system must be stated in a consistent fashion. The ground states for a single tetrahedron are sufficient for the whole system.

4.3.1 Ground State Constraints

A spin at site i in the tetrahedron is defined

$$\mathbf{S}_i = S_{xi}\,\underline{\mathbf{i}} + S_{yi}\,\underline{\mathbf{j}} + S_{zi}\,\underline{\mathbf{k}}.$$

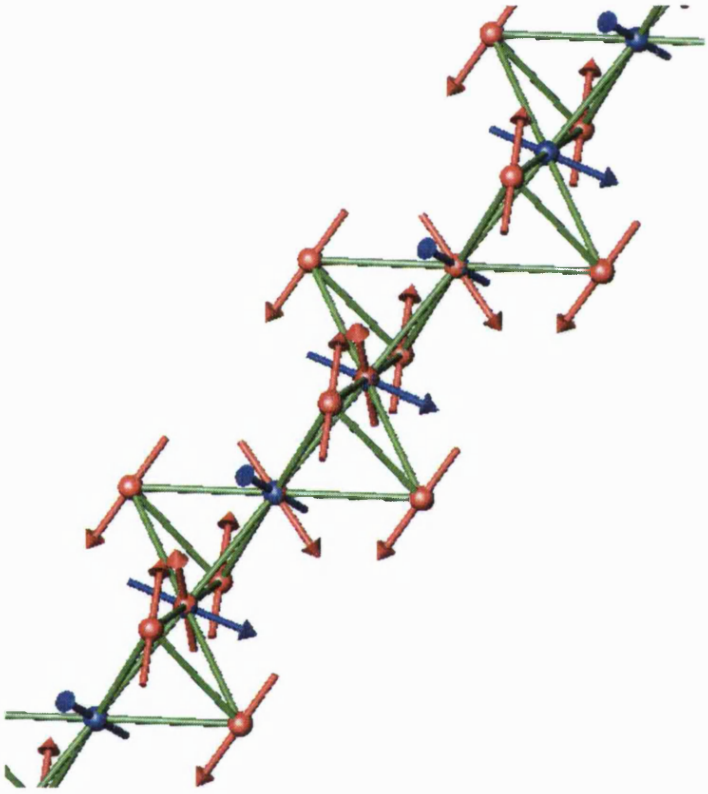

Figure 4.6: An infinite line defect in the lattice.

	State I			State II			State III			State IV		
i	S_x	S_y	S_z	S_x	S_y	S_z	S_x	S_y	S_z	S_x	S_y	S_z
1	$-\frac{1}{\sqrt{2}}$	$\frac{1}{\sqrt{2}}$	0	$\frac{1}{\sqrt{2}}$	$-\frac{1}{\sqrt{2}}$	0	$-\frac{1}{\sqrt{6}}$	$-\frac{1}{\sqrt{6}}$	$\frac{2}{\sqrt{6}}$	$-\frac{1}{\sqrt{6}}$	$-\frac{1}{\sqrt{6}}$	$\frac{2}{\sqrt{6}}$
2	$-\frac{1}{\sqrt{2}}$	$-\frac{1}{\sqrt{2}}$	0	$-\frac{1}{\sqrt{2}}$	$-\frac{1}{\sqrt{2}}$	0	$\frac{1}{\sqrt{6}}$	$-\frac{1}{\sqrt{6}}$	$-\frac{2}{\sqrt{6}}$	$\frac{1}{\sqrt{6}}$	$-\frac{1}{\sqrt{6}}$	$-\frac{2}{\sqrt{6}}$
3	$\frac{1}{\sqrt{2}}$	$\frac{1}{\sqrt{2}}$	0	$\frac{1}{\sqrt{2}}$	$\frac{1}{\sqrt{2}}$	0	$-\frac{1}{\sqrt{6}}$	$\frac{1}{\sqrt{6}}$	$-\frac{2}{\sqrt{6}}$	$\frac{2}{\sqrt{6}}$	$\frac{1}{\sqrt{6}}$	$\frac{1}{\sqrt{6}}$
4	$\frac{1}{\sqrt{2}}$	$-\frac{1}{\sqrt{2}}$	0	$-\frac{1}{\sqrt{2}}$	$\frac{1}{\sqrt{2}}$	0	$\frac{1}{\sqrt{6}}$	$\frac{1}{\sqrt{6}}$	$\frac{2}{\sqrt{6}}$	$-\frac{2}{\sqrt{6}}$	$\frac{1}{\sqrt{6}}$	$-\frac{1}{\sqrt{6}}$

Table 4.2: The spin orientations of different ground states of the system.

For $i = 1-4$ there are constraints on the spins such that they lie in the easy-planes of the tetrahedron:

$$S_{x1} + S_{y1} + S_{z1} = 0 \tag{4.2}$$

$$S_{x2} - S_{y2} + S_{z2} = 0 \tag{4.3}$$

$$S_{x3} - S_{y3} - S_{z3} = 0 \tag{4.4}$$

$$S_{x3} + S_{y4} - S_{z4} = 0. \tag{4.5}$$

The sum of the four spins on the tetrahedron must be zero:

$$S_{x1} + S_{x2} + S_{x3} + S_{x4} = 0 \tag{4.6}$$

$$S_{y1} + S_{y2} + S_{y3} + S_{y4} = 0 \tag{4.7}$$

$$S_{z1} + S_{z2} + S_{z3} + S_{z4} = 0. \tag{4.8}$$

The spins must all be of the same length:

$$|\mathbf{S}_1| = |\mathbf{S}_2| = |\mathbf{S}_3| = |\mathbf{S}_4| = 1. \tag{4.9}$$

Ground states **I**, **II**, **III** and **IV** are all valid solutions and their spin orientations are detailed in Table 4.2.

4.3.2 Solution of the Constraints

Linear equations (4.2) - (4.8) can be solved by row-echelon matrix reduction [85]. There are twelve variables and seven equations, so there will be seven dependent variables and five independent variables ($S_{z2}, S_{y3}, S_{z3}, S_{y4}, S_{z4}$), shown below:

$$
\begin{array}{lll}
S_{x1} = S_{z2} + S_{y4} & S_{y1} = S_{z3} - S_{y4} + S_{z4} & S_{z1} = -S_{z2} - S_{z3} - S_{z4} \\
S_{x2} = -S_{z2} - S_{y3} - S_{z3} - S_{z4} & S_{y2} = -S_{y3} - S_{z3} - S_{z4} & S_{z2} = S_{z2} \\
S_{x3} = S_{y3} + S_{z3} & S_{y3} = S_{y3} & S_{z3} = S_{z3} \\
S_{x4} = -S_{y4} + S_{z4} & S_{y4} = S_{y4} & S_{z4} = S_{z4}.
\end{array}
$$

The solutions above will include spins of different length. A subset of these general solutions which give spins of unit length is then required. Eqn. (4.9) must also be satisfied:

$$(S_{z2} + S_{y4})^2 + (S_{z3} - S_{y4} + S_{z4})^2 + (-S_{z2} - S_{z3} - S_{z4})^2 = 1 \tag{4.10}$$

$$(-S_{z2} - S_{y3} - S_{z3} - S_{z4})^2 + (-S_{y3} - S_{z3} - S_{z4})^2 + S_{z2}^2 = 1 \tag{4.11}$$

$$(S_{y3} + S_{z3})^2 + S_{y3}^2 + S_{z3}^2 = 1 \tag{4.12}$$

$$(-S_{y4} + S_{z4})^2 + S_{y4}^2 + S_{z4}^2 = 1 \tag{4.13}$$

We now have four equations in terms of five variables, so there will be one degree of freedom in the solutions. These equations have been solved analytically [86], but the proof is too complicated to explain briefly in this thesis. It is possible to use computer software to solve the equations for a given variable (where the variable must be a possible solution) [87].

For a given variable such as $S_{x1} = a$ there are eight possible solutions. Each solution can be considered as a linear combination of two specific basis vectors:

$${}^{s}\mathbf{S}_i = \alpha\, {}^{s}\boldsymbol{\nu}_i^{\alpha} + \beta\, {}^{s}\boldsymbol{\nu}_i^{\beta}, \quad \alpha^2 + \beta^2 = 1, \quad -1 \leqslant \alpha \leqslant 1 \tag{4.14}$$

where $i = 1 - 4$, s denotes each separate solution and both positive and negative values of β are used for each value of α. ${}^{s}\boldsymbol{\nu}_i$ are normalised basis vectors, specific

	Solution							
	1		2		3		4	
i	$\sqrt{6}\,\nu_i^\alpha$	$\sqrt{2}\,\nu_i^\beta$	$\sqrt{6}\,\nu_i^\alpha$	$\sqrt{2}\,\nu_i^\beta$	$\sqrt{6}\,\nu_i^\alpha$	$\sqrt{2}\,\nu_i^\beta$	$\sqrt{6}\,\nu_i^\alpha$	$\sqrt{2}\,\nu_i^\beta$
1	$\begin{pmatrix}1\\1\\-2\end{pmatrix}$	$\begin{pmatrix}1\\-1\\0\end{pmatrix}$	$\begin{pmatrix}1\\1\\-2\end{pmatrix}$	$\begin{pmatrix}1\\-1\\0\end{pmatrix}$	$\begin{pmatrix}1\\1\\-2\end{pmatrix}$	$\begin{pmatrix}1\\-1\\0\end{pmatrix}$	$\begin{pmatrix}1\\1\\-2\end{pmatrix}$	$\begin{pmatrix}1\\-1\\0\end{pmatrix}$
2	$\begin{pmatrix}-1\\1\\2\end{pmatrix}$	$\begin{pmatrix}-1\\-1\\0\end{pmatrix}$	$\begin{pmatrix}-1\\1\\2\end{pmatrix}$	$\begin{pmatrix}1\\1\\0\end{pmatrix}$	$\begin{pmatrix}-1\\-2\\-1\end{pmatrix}$	$\begin{pmatrix}-1\\0\\1\end{pmatrix}$	$\begin{pmatrix}-1\\1\\2\end{pmatrix}$	$\begin{pmatrix}-1\\-1\\0\end{pmatrix}$
3	$\begin{pmatrix}1\\-1\\2\end{pmatrix}$	$\begin{pmatrix}1\\1\\0\end{pmatrix}$	$\begin{pmatrix}1\\-1\\2\end{pmatrix}$	$\begin{pmatrix}-1\\-1\\0\end{pmatrix}$	$\begin{pmatrix}1\\-1\\2\end{pmatrix}$	$\begin{pmatrix}1\\1\\0\end{pmatrix}$	$\begin{pmatrix}-2\\-1\\-1\end{pmatrix}$	$\begin{pmatrix}0\\1\\-1\end{pmatrix}$
4	$\begin{pmatrix}-1\\-1\\-2\end{pmatrix}$	$\begin{pmatrix}-1\\1\\0\end{pmatrix}$	$\begin{pmatrix}-1\\-1\\-2\end{pmatrix}$	$\begin{pmatrix}-1\\1\\0\end{pmatrix}$	$\begin{pmatrix}-1\\2\\1\end{pmatrix}$	$\begin{pmatrix}-1\\0\\-1\end{pmatrix}$	$\begin{pmatrix}2\\-1\\1\end{pmatrix}$	$\begin{pmatrix}0\\1\\1\end{pmatrix}$

Table 4.3: Solutions 1 – 4

	Solution							
	5		6		7		8	
i	$\sqrt{6}\,\nu_i^\alpha$	$\sqrt{2}\,\nu_i^\beta$	$\sqrt{6}\,\nu_i^\alpha$	$\sqrt{2}\,\nu_i^\beta$	$\sqrt{6}\,\nu_i^\alpha$	$\sqrt{2}\,\nu_i^\beta$	$\sqrt{6}\,\nu_i^\alpha$	$\sqrt{2}\,\nu_i^\beta$
1	$\begin{pmatrix}1\\-2\\1\end{pmatrix}$	$\begin{pmatrix}1\\0\\-1\end{pmatrix}$	$\begin{pmatrix}1\\-2\\1\end{pmatrix}$	$\begin{pmatrix}1\\0\\-1\end{pmatrix}$	$\begin{pmatrix}1\\-2\\1\end{pmatrix}$	$\begin{pmatrix}1\\0\\-1\end{pmatrix}$	$\begin{pmatrix}1\\-2\\1\end{pmatrix}$	$\begin{pmatrix}1\\0\\-1\end{pmatrix}$
2	$\begin{pmatrix}-1\\-2\\-1\end{pmatrix}$	$\begin{pmatrix}-1\\0\\1\end{pmatrix}$	$\begin{pmatrix}2\\1\\-1\end{pmatrix}$	$\begin{pmatrix}0\\1\\1\end{pmatrix}$	$\begin{pmatrix}-1\\1\\2\end{pmatrix}$	$\begin{pmatrix}-1\\-1\\0\end{pmatrix}$	$\begin{pmatrix}-1\\-2\\-1\end{pmatrix}$	$\begin{pmatrix}-1\\0\\1\end{pmatrix}$
3	$\begin{pmatrix}1\\2\\-1\end{pmatrix}$	$\begin{pmatrix}1\\0\\1\end{pmatrix}$	$\begin{pmatrix}-2\\-1\\-1\end{pmatrix}$	$\begin{pmatrix}0\\-1\\1\end{pmatrix}$	$\begin{pmatrix}1\\2\\-1\end{pmatrix}$	$\begin{pmatrix}1\\0\\1\end{pmatrix}$	$\begin{pmatrix}1\\2\\-1\end{pmatrix}$	$\begin{pmatrix}-1\\0\\-1\end{pmatrix}$
4	$\begin{pmatrix}-1\\2\\1\end{pmatrix}$	$\begin{pmatrix}-1\\0\\-1\end{pmatrix}$	$\begin{pmatrix}-1\\2\\1\end{pmatrix}$	$\begin{pmatrix}-1\\0\\-1\end{pmatrix}$	$\begin{pmatrix}-1\\-1\\-2\end{pmatrix}$	$\begin{pmatrix}-1\\1\\0\end{pmatrix}$	$\begin{pmatrix}-1\\2\\1\end{pmatrix}$	$\begin{pmatrix}1\\0\\1\end{pmatrix}$

Table 4.4: Solutions 5 – 8

	Solution							
i	1	2	3	4	5	6	7	8
1	a b c	a b c	a b c	a b c	a c b	a c b	a c b	a c b
2	$-a$ b $-c$	$-b$ a $-c$	$-a$ c $-b$	$-a$ b $-c$	$-a$ c $-b$	$-c$ a $-b$	$-a$ b $-c$	$-a$ c $-b$
3	a $-b$ $-c$	b $-a$ $-c$	a $-b$ $-c$	c $-b$ $-a$	a $-c$ $-b$	c $-a$ $-b$	a $-c$ $-b$	b $-c$ $-a$
4	$-a$ $-b$ c	$-a$ $-b$ c	$-a$ $-c$ b	$-c$ $-b$ a	$-a$ $-c$ b	$-a$ $-c$ b	$-a$ $-b$ c	$-b$ $-c$ a

Table 4.5: General form of the solutions, where $a^2 + b^2 + c^2 = 1$.

to each spin for each different solution, taking the form:

$$ {}^s\boldsymbol{\nu}_i = \begin{pmatrix} {}^s x_i \\ {}^s y_i \\ {}^s z_i \end{pmatrix} . \qquad (4.15) $$

Tables 4.3 and 4.4 list the $\boldsymbol{\nu}$ for each spin i and solution s. The solutions *could* be expressed in terms of only one basis vector set, with specific relations between the coefficients α_s, β_s for $s = 1, 8$. However, these relations are elliptical and difficult to express clearly.

If the same α and β are used for each solution then the solutions can be directly compared. Table 4.5 shows the general form of each solution where this is the case. For a particular solution of one spin component $S_{x1} = a$ there are two possible

orientations of $\mathbf{S}_1$ with $S_{y1} = b, c$ and $S_{z1} = c, b$ respectively (where $a^2+b^2+c^2 = 1$).

It can be seen that there is a family of solutions for each orientation of $\mathbf{S}_1$. There is a symmetric solution where:

$$|S_{x1}| = |S_{x2}| = |S_{x3}| = |S_{x4}| = a$$
$$|S_{y1}| = |S_{y2}| = |S_{y3}| = |S_{y4}| = b \text{ or } c$$
$$|S_{z1}| = |S_{z2}| = |S_{z3}| = |S_{z4}| = c \text{ or } b.$$

There are three defect solutions with pairs of spins satisfying the following condition: $|S_{x1}| = |S_{xi}|$ and $|S_{y1}| = |S_{yi}|$ and $|S_{z1}| = |S_{zi}|$, where i is equal to either 2,3 or 4 in each case (for instance $i = 3$ for solutions 3 and 7 etc.). The components of the other spins take values such that the ground state conditions are satisfied (these values are taken specifically from $\{\pm a, \pm b, \pm c\}$). State **I** is a special example of a defect state since it satisfies the condition for both symmetric and defect states.

For $\alpha = \pm 0.5, \pm 1$ two defect solutions become coincident with each symmetric solution (see Table 4.6). So, for these special cases there are only six solutions. The symmetric solutions 1 and 5 in these cases are specific variants of state **III**.

4.3.3 Reduction of the Solutions

In principle the eight solutions described in Table 4.5 could be reduced to irreducible representations of the tetrahedral point group. This is not a trivial exercise and has not been attempted. Inspection of Table 4.5 shows that in a more general case the family of solutions 5 – 8 has the same 'shape' as solutions 1 – 4, by dint of a simple transposition of b with c.

However, inspection shows that there are basically two types of groups – defect and symmetric. States **II** and **III** are examples of symmetric solutions and states **I** and **IV** are examples of defect solutions.

α	Symmetric solution	Defect solution
1	1	2
	5	8
0.5	1	3
	5	7
-1	1	2
	5	8
-0.5	1	4
	5	6

Table 4.6: Coincident solutions for various values of α.

4.4 The Structure, Stability and Behaviour of the Ground States for $T < T_N$

In this section, the structure and dynamics of the system below the phase transition are discussed. The system can be placed in particular ground states, even though these are not the ones which the system orders in. Their stability can then be observed with respect to Monte Carlo time. A study of states **I, II, III** and **IV** in this way represents a complete investigation of the model.

4.4.1 The Distribution of Individual Bond Energies of the System

The Hamiltonian $\mathbb{H} = -J \sum_{<i,j>} \mathbf{S}_i \cdot \mathbf{S}_j$ is a sum over all bond interactions in the system. The bond interactions are simply inner products which can take values from -1 to 1. Therefore it is possible to calculate the distribution of individual bond energies of the system. A probability distribution $P(E_{ij})$ is created by simply binning all the bond energies of the system every MCS/S once the system is

equilibrated.

$P(E_{ij})$ is calculated for temperatures ranging from $T/J = 0.09 - 0.005$ for both state **III** and state **I** and the results for $L = 4$ are shown in Figures 4.7 to 4.14. The data have not been normalised but *are* directly comparable since the conditions were the same for each simulation.

Figure 4.3 shows that the system orders into a q=0 ordered state with $T_N \sim 0.0125$. If the system orders into a single state then there will only be small fluctuations about a clearly defined point. This behaviour will be represented in the bond energy distribution.

$P(E_{ij})$ for state I

In state **I** there are two bonds with $E_{ij} = -1$ and four bonds with $E_{ij} = 0$. $P(E_{ij})$ would therefore be expected to have a simple two peaked distribution. If the system is placed in state **I** at $T < T_N$ (see Fig. 4.8) the distribution is already bimodal around the two expected values of E_{ij}. As the temperature is decreased the distribution quickly becomes sharper around these values.

$P(E_{ij})$ for state III

In state **III** there are four bonds with $E_{ij} = -\frac{2}{3}$ and two bonds with $E_{ij} = \frac{1}{3}$. However unlike state **I**, $P(E_{ij})$ has a finite value over the whole range of energies: $E_{ij} = -1$ to $E_{ij} = \frac{1}{3}$ (see Fig. 4.7). This means that the system is not entering into a single ordered state, instead there is a phase transition onto a 'continuous manifold of q=0 ordered states'. This is a particularly interesting phenomenon to observe. As the temperature decreases the bond energy distribution does indeed become bimodal, but at a much slower rate than that of state **I**. It is also interesting to note that for the same number of bonds in each case the distribution in Figure 4.13 at $E_{ij} = -\frac{2}{3}$ is much more spread out than the corresponding distribution in Figure 4.14 at $E_{ij} = 0$. This shows that there is much more freedom for

State III

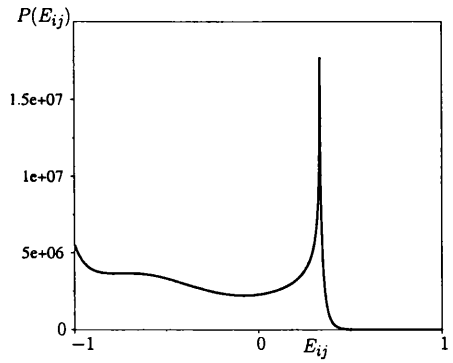

Figure 4.7: $T/J = 0.09 < T_N$

State I

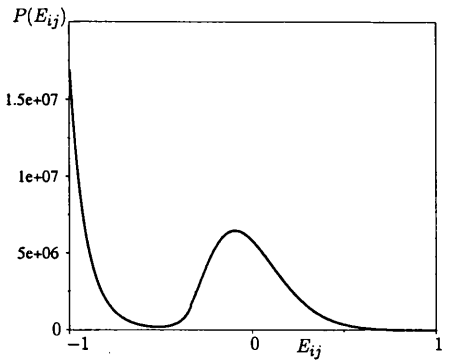

Figure 4.8: $T/J = 0.09 < T_N$

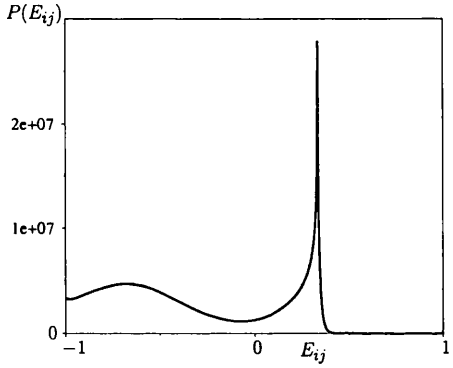

Figure 4.9: $T/J = 0.05$

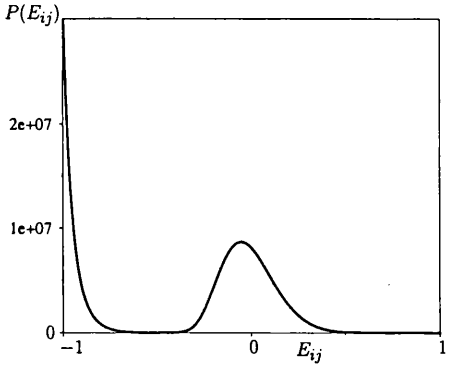

Figure 4.10: $T/J = 0.05$

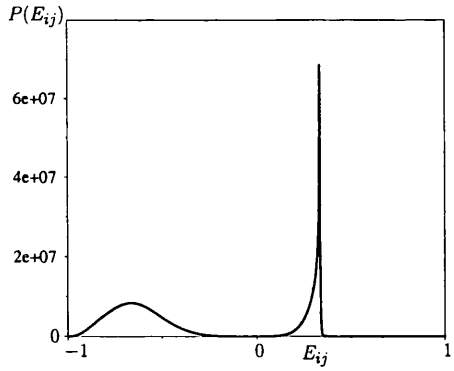

Figure 4.11: $T/J = 0.01$

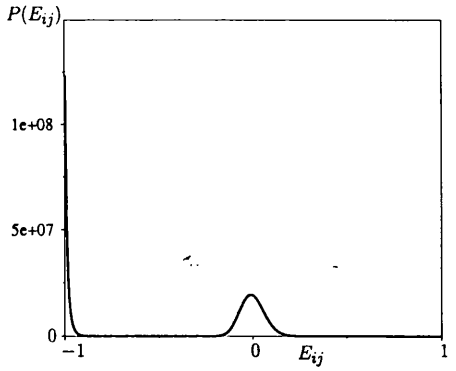

Figure 4.12: $T/J = 0.01$

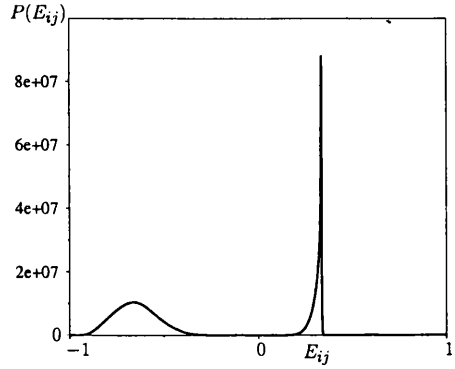

Figure 4.13: $T/J = 0.005 \ll T_N$

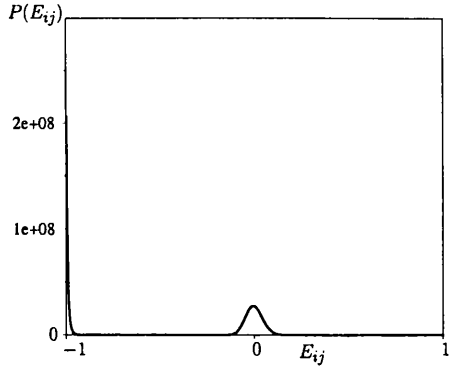

Figure 4.14: $T/J = 0.005 \ll T_N$

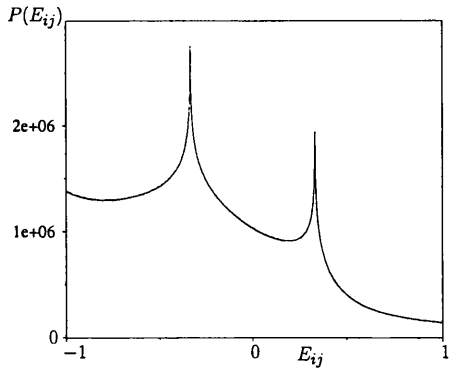

Figure 4.15: $T/J = 0.3 > T_N$

the spins to fluctuate in state **III** than state **I**, even at low temperature.

This evidence suggests selection of a single state at low temperature out of a degenerate manifold of states at $T/J < T_N$. This is consistent with an order by disorder mechanism.

For $T/J = 0.3 > T_N$ the energy distribution is also continuous. There is enough thermal energy in the system for the high energy bond interactions to be probable (see Fig. 4.15). It is particularly interesting to note the features at $E_{ij} = -\frac{1}{3}, \frac{1}{3}$, which is characteristic of the average bond energy interaction for two paramagnetic spins on two easy-planes [28].

4.4.2 Angular Distribution of the Spins on the Easy-Plane

It is possible to investigate in more detail the fluctuations of the spins referred to in section 4.4.1. The position of a spin can be described by its angle ($0 < \phi \leq 2\pi$) within its easy-plane. The distribution $P(\phi)$ for spins on a sublattice (since there is q=0 order in the system) can therefore be measured in the same way as in section 4.4.1.

The results are shown in Figure 4.16 for the same temperatures as section 4.4.1. The distribution of only one sublattice is shown for simplicity since the shapes are identical for each sublattice.

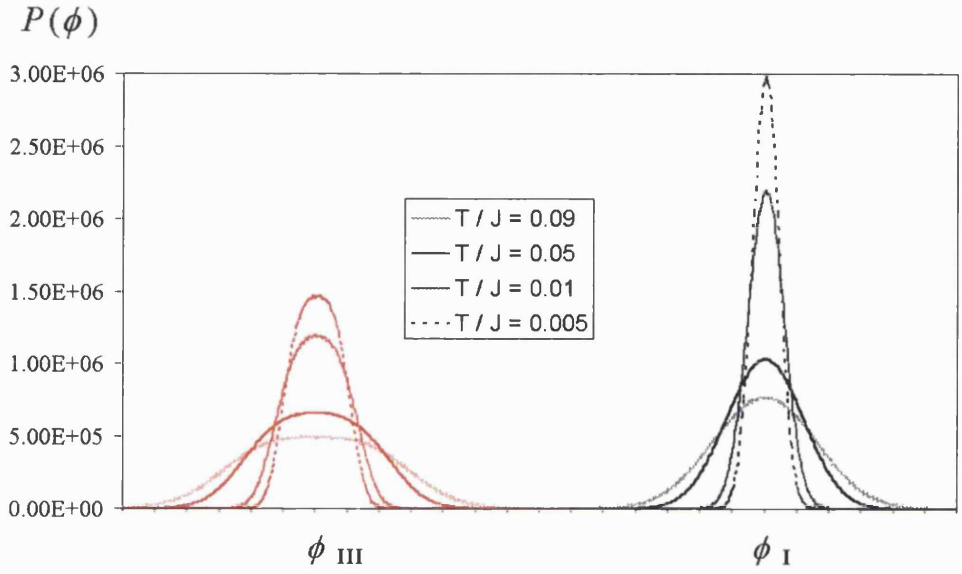

Figure 4.16: $P(\phi)$ for state **III** (red lines) and state **I** (black lines). One division is equal to 11.25°.

$P(\phi)$ for state I

The sublattice distributions for state **I** are much as expected and the spins have very small fluctuations around the ordered state with little spread.

$P(\phi)$ for state III

The sublattice distributions for state **III** showed the system to be fluctuating around the ordered spin directions. But when $T/J = 0.9$, $P(\phi = x \rightarrow x+\pi/5) \sim c$ and there is very little change in $P(\phi)$ over the range. The spins have a similar probability of existing over a small range of ϕ. This observation is still consistent with the system existing on a q=0 manifold.

For all temperatures the fluctuations are larger for state **III** than state **I**.

4.4.3 Stability of the Ground States for $T < T_N$

Results from sections 4.4.1 and 4.4.2 showed that if the system is placed in state **I** for $T < T_N$ it is rigidly confined to that state and does not leave it at all. It is therefore interesting to investigate the stability of another defect state such as state **IV** or another symmetric state such as state **II**. To achieve this, the angle ϕ of a q=0 ordered sublattice has been measured as a function of the length of the simulation. It shows collective q=0 movement of the spins on one sublattice from one state to another. Comparison of all the sublattice angles show any correlation of the spins on each sublattice which heretofore has not been discussed.

The data are collected by simply averaging over the ϕ of each sublattice spin after every N MCS/S.

The stability of state II

In Figure 4.17 an $L = 4$ system has been put into the symmetric q=0 state **II** at $MCS/S = 1$ with $T/J = 0.05$ and allowed to relax out of it. After only 500 MCS/S each sublattice has entirely left its initial configuration. In fact the spins have relaxed into state **III**. This is of particular interest and will be discussed in section 9.3.2.

It is important to observe the correlation of the spins between the sublattices. Figure 4.17 shows that in state **III** two pairs of sublattices of spins are highly correlated with each other. There is a very short response time between the correlations which can be ascribed to the sequential nature of the sampling method.

This is an important observation, since it shows that there are two independent pairs of sublattices which in themselves are highly correlated (i.e. if $\phi_{2,3} = x$ and $\phi_{1,4} = y$, then x is independent of y). There appears to be an internal degree of freedom in the system, which gives rise to bigger entropy fluctuations.

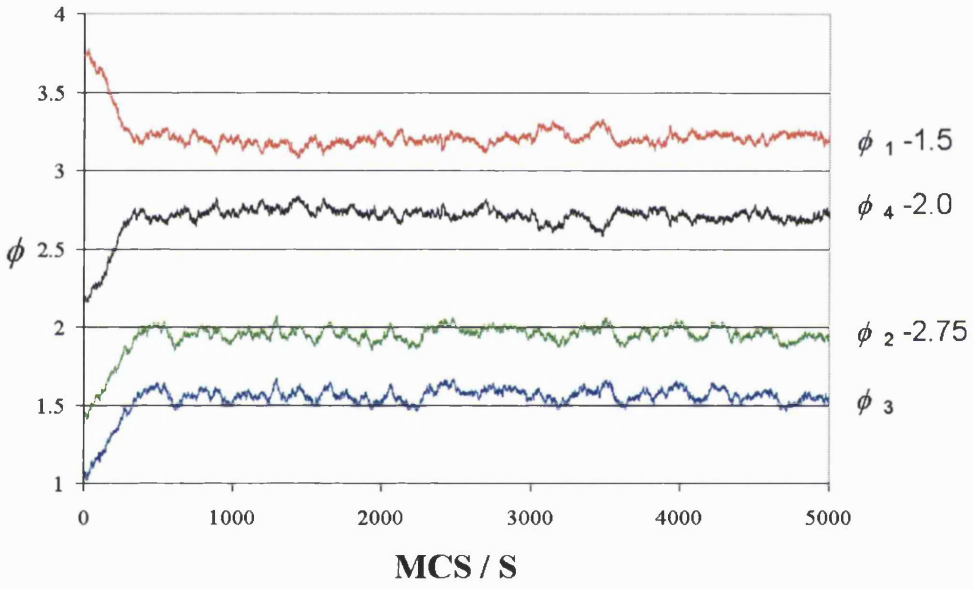

Figure 4.17: ϕ_s for each sublattice $s = 1 - 4$ for $T/J = 0.05$. Relaxation out of state **II** into state **III** as a function of Monte Carlo time.

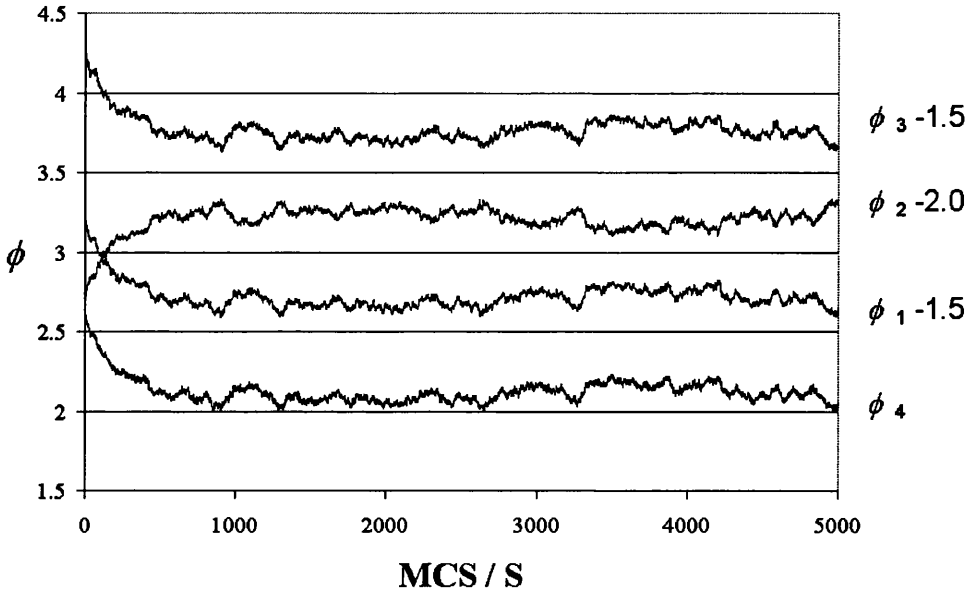

Figure 4.18: ϕ_s for each sublattice $s = 1 - 4$ for $T/J = 0.05$. Relaxation out of state **IV** into state **I** as a function of Monte Carlo time.

The stability of state IV

In Figure 4.18 an $L = 4$ system has been put into the defect q=0 state **IV** at $MCS/S = 1$ with $T/J = 0.05$ and allowed to relax out of it. After only 1000 MCS/S each sublattice has entirely left its initial configuration. In fact the spins have relaxed into state **I**. This is also of interest and the consequences will be discussed in section 9.3.2.

It is also important to observe the correlation of the spins between the sublattices. Figure 4.18 also shows that in state **I** all the sublattices of spins are highly correlated with each other. There is again a very short response time between the correlations. Not only are all the spins on each sublattice correlated (i.e. q=0 order), but the movement of spins on different sublattices is also correlated. The mutual dependence of the sublattices on each other restricts the total number of possible configurations W. The associated entropy will therefore be much lower

than that of state **III**, and confirms the idea of the system as being very 'rigid'.

The properties described in each case are valid for seemingly all $T < T_N$. As T gets smaller the amount of time it takes to reach state **I** increases. As $T \to T_N$ the amount of noise in the data increases, since the sublattice order parameter decreases (see Fig. 4.3).

4.5 State III: Calculation of the Normal Modes

The results from the Monte Carlo simulations and theoretical solution of the ground states show that there is a macroscopic set of degenerate solutions. There must be some sort of order by disorder in the system which makes the system choose type **III** ordered states. It therefore seems likely that 'soft' fluctuations exist out of state **III**. To determine whether these soft modes exist, the normal modes of the system have been calculated with respect to excitations out of ground state **III**.

In section 2.3 an example of a normal mode calculation was illustrated for a one-dimensional lattice with a two atom basis. The pyrochlore lattice is a three-dimensional lattice with a four atom basis. The pyrochlore calculation is slightly more complex, yet still follows the same principle of the earlier example.

4.5.1 The Unit Cell and its Nearest Neighbours

The pyrochlore lattice is a face-centred cubic Bravais lattice with a four-atom basis. The cubic unit cell contains sixteen atoms. However the simplest primitive unit cell is rhombohedral, again with a four-atom basis. The rhombohedral primitive

lattice vectors $\mathbf{a}, \mathbf{b}$ and $\mathbf{c}$ are as follows (in units of the cubic cell) [88]:

$$\begin{aligned} \mathbf{a} &= \left(\frac{1}{2}\,\frac{1}{2}\,0\right) \\ \mathbf{b} &= \left(\frac{1}{2}\,0\,\frac{1}{2}\right) \\ \mathbf{c} &= \left(0\,\frac{1}{2}\,\frac{1}{2}\right), \end{aligned}$$

with the four atom basis:

$$\begin{aligned} \mathbf{v}_1 &= 0\,0\,0 \\ \mathbf{v}_2 &= \frac{\mathbf{b}}{2} \\ \mathbf{v}_3 &= \frac{\mathbf{c}}{2} \\ \mathbf{v}_4 &= \frac{\mathbf{a}}{2}. \end{aligned}$$

respectively (see Fig. 4.19). The ith unit cell therefore has position:

$$\mathbf{R}_i = n_1\mathbf{a} + n_2\mathbf{b} + n_3\mathbf{c}, \tag{4.16}$$

where $n_m = 1, \ldots, n_{mo}$ for $m = 1, 2, 3$ and $N_{cell} = n_{1o}n_{2o}n_{3o}$. The system consists of $N = 4N_{cell}$ spins.

Nearest neighbours of atoms in the unit cell

In section 2.3 the nearest neighbours were simply defined. In the pyrochlore lattice each site has three neighbours in its unit cell (n_1, n_2, n_3) and three neighbours $(\bar{S},\ \bar{S} = 1, 2, 3 \text{ or } 4)$ in different unit cells. The four atoms in the ith unit cell therefore have general position:

$$\begin{aligned} \boldsymbol{\alpha}_1 &= \mathbf{R}_i + \mathbf{v}_1 \\ \boldsymbol{\alpha}_2 &= \mathbf{R}_i + \mathbf{v}_2 \\ \boldsymbol{\alpha}_3 &= \mathbf{R}_i + \mathbf{v}_3 \\ \boldsymbol{\alpha}_4 &= \mathbf{R}_i + \mathbf{v}_4. \end{aligned}$$

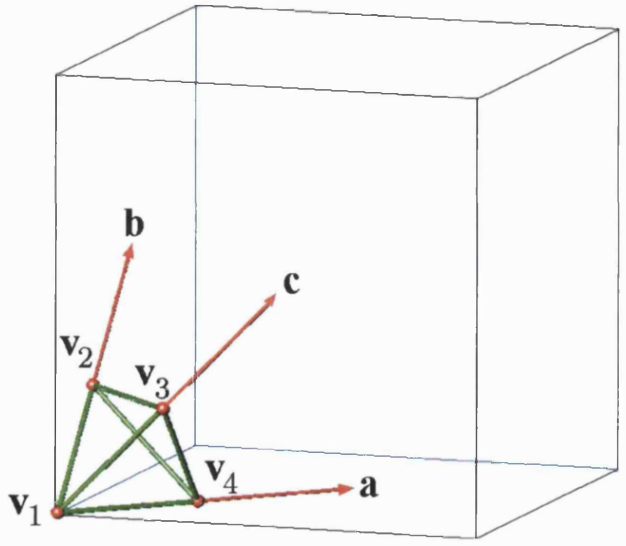

Figure 4.19: Rhombohedral axes with respect to the cubic unit cell.

The positions of the nearest neighbours in different unit cells are determined in the following way. Atom P has neighbours of type S and $\bar{S}$ at:

$$\begin{aligned} \boldsymbol{\beta}_S &= \boldsymbol{\alpha}_P + (-\mathbf{v}_P + \mathbf{v}_S) \\ \boldsymbol{\beta}_{\bar{S}} &= \boldsymbol{\alpha}_P - (-\mathbf{v}_P + \mathbf{v}_S)\,. \end{aligned}$$

For $P = 1$ and $S = 2$ the neighbours are determined thus:

$$\begin{aligned} \boldsymbol{\beta}_2 &= \boldsymbol{\alpha}_1 + (-\mathbf{v}_1 + \mathbf{v}_2) \\ &= n_1\mathbf{a} + n_2\mathbf{b} + n_3\mathbf{c} + \frac{\mathbf{b}}{2} \\ \boldsymbol{\beta}_{\bar{2}} &= \boldsymbol{\alpha}_1 - (-\mathbf{v}_1 + \mathbf{v}_2) \\ &= n_1\mathbf{a} + n_2\mathbf{b} + n_3\mathbf{c} - \frac{\mathbf{b}}{2} \\ &= n_1\mathbf{a} + (n_2 - 1)\mathbf{b} + n_3\mathbf{c} + \frac{\mathbf{b}}{2} \quad \text{since} \quad n_2\mathbf{b} - \frac{\mathbf{b}}{2} = (n_2 - 1)\mathbf{b} + \frac{\mathbf{b}}{2}. \end{aligned}$$

Neighbour 2 is therefore present in unit cell n_1, n_2, n_3 with neighbour $\bar{2}$ present in unit cell $n_1, n_2 - 1, n_3$. The same process can be used for $P = 1, 4$ and $S = 1, 4$ and the general positions of neighbours in other unit cells for each atom are listed in Table 4.7, with the associated unit cell of each neighbour.

Atom	Neighbour	Position	Unit Cell
1	$\bar{2}$	$n_1\mathbf{a} + (n_2 - 1)\mathbf{b} + n_3\mathbf{c} + \frac{\mathbf{b}}{2}$	$n_1, n_2 - 1, n_3$
	$\bar{3}$	$n_1\mathbf{a} + n_2\mathbf{b} + (n_3 - 1)\mathbf{c} + \frac{\mathbf{c}}{2}$	$n_1, n_2, n_3 - 1$
	$\bar{4}$	$(n_1 - 1)\mathbf{a} + n_2\mathbf{b} + n_3\mathbf{c} + \frac{\mathbf{a}}{2}$	$n_1 - 1, n_2, n_3$
2	$\bar{1}$	$n_1\mathbf{a} + (n_2 - 1)\mathbf{b} + n_3\mathbf{c}$	$n_1, n_2 - 1, n_3$
	$\bar{3}$	$n_1\mathbf{a} + (n_2 + 1)\mathbf{b} + (n_3 - 1)\mathbf{c} + \frac{\mathbf{c}}{2}$	$n_1, n_2 + 1, n_3 - 1$
	$\bar{4}$	$(n_1 - 1)\mathbf{a} + (n_2 + 1)\mathbf{b} + n_3\mathbf{c} + \frac{\mathbf{a}}{2}$	$n_1 - 1, n_2 + 1, n_3$
3	$\bar{1}$	$n_1\mathbf{a} + n_2\mathbf{b} + (n_3 + 1)\mathbf{c}$	$n_1, n_2, n_3 + 1$
	$\bar{2}$	$n_1\mathbf{a} + (n_2 - 1)\mathbf{b} + (n_3 + 1)\mathbf{c} + \frac{\mathbf{b}}{2}$	$n_1, n_2 - 1, n_3 + 1$
	$\bar{4}$	$(n_1 - 1)\mathbf{a} + n_2\mathbf{b} + (n_3 + 1)\mathbf{c} + \frac{\mathbf{a}}{2}$	$n_1 - 1, n_2, n_3 + 1$
4	$\bar{1}$	$(n_1 + 1)\mathbf{a} + n_2\mathbf{b} + n_3\mathbf{c}$	$n_1 + 1, n_2, n_3$
	$\bar{2}$	$(n_1 + 1)\mathbf{a} + (n_2 - 1)\mathbf{b} + n_3\mathbf{c} + \frac{\mathbf{b}}{2}$	$n_1 + 1, n_2 - 1, n_3$
	$\bar{3}$	$(n_1 + 1)\mathbf{a} + n_2\mathbf{b} + (n_3 - 1)\mathbf{c} + \frac{\mathbf{c}}{2}$	$n_1 + 1, n_2, n_3 - 1$

Table 4.7: Nearest neighbours of sites in other unit cells.

The reciprocal lattice vectors

The reciprocal lattice vectors α, β and γ are defined:

$$\alpha = \frac{2\pi \mathbf{b} \times \mathbf{c}}{\mathbf{a}.(\mathbf{b} \times \mathbf{c})} = 2\pi(-1,1,1) \tag{4.17}$$

$$\beta = \frac{2\pi \mathbf{c} \times \mathbf{a}}{\mathbf{a}.(\mathbf{b} \times \mathbf{c})} = 2\pi(1,-1,1) \tag{4.18}$$

$$\gamma = \frac{2\pi \mathbf{a} \times \mathbf{b}}{\mathbf{a}.(\mathbf{b} \times \mathbf{c})} = 2\pi(1,1,-1) \tag{4.19}$$

4.5.2 The Symmetrised Harmonic Hamiltonian

The Hamiltonian

$$\mathbb{H} = J \sum_{<i,j>} \mathbf{S}_i \cdot \mathbf{S}_j,$$

is rearranged such that there is a sum over all β nearest neighbours of each spin ${}^{\alpha}\mathbf{S}_i$ on every ith unit cell.

$$\sum_{<i,j>} = \frac{1}{2} \sum_{i=1}^{N_{cell}} \sum_{\alpha=1}^{\alpha=4} \sum_{\beta=1}^{\beta=6}$$

and

$$\sum_{i=1}^{N_{cell}} = \sum_{n_1=1}^{n_{1o}} \sum_{n_2=1}^{n_{2o}} \sum_{n_3=1}^{n_{3o}}$$

The total is divided by two since all bonds are counted twice.

To simplify the notation, the spin ${}^{\alpha}\mathbf{S}_i$ in unit cell $i = n_1, n_2, n_3$, is denoted ${}^{\alpha}\mathbf{S}_0$. In unit cell $i = n_1 \pm 1, n_2, n_3$ a spin is denoted ${}^{\alpha}\mathbf{S}_{\pm 100}$ and for $n_2 \pm 1$ and $n_3 \pm 1$ respectively. The Hamiltonian is written out in full:

$$\begin{aligned}
\mathbb{H} = \frac{J}{2} \sum_{n_1,n_2,n_3} & {}^1\mathbf{S}_0 \cdot ({}^2\mathbf{S}_0 + {}^2\mathbf{S}_{0-10} + {}^3\mathbf{S}_0 + {}^3\mathbf{S}_{00-1} + {}^4\mathbf{S}_0 + {}^4\mathbf{S}_{-100}) \\
& + {}^2\mathbf{S}_0 \cdot ({}^1\mathbf{S}_0 + {}^1\mathbf{S}_{010} + {}^3\mathbf{S}_0 + {}^3\mathbf{S}_{01-1} + {}^4\mathbf{S}_0 + {}^4\mathbf{S}_{-110}) \\
& + {}^3\mathbf{S}_0 \cdot ({}^1\mathbf{S}_0 + {}^1\mathbf{S}_{001} + {}^2\mathbf{S}_0 + {}^2\mathbf{S}_{0-11} + {}^4\mathbf{S}_0 + {}^4\mathbf{S}_{-101}) \\
& + {}^4\mathbf{S}_0 \cdot ({}^1\mathbf{S}_0 + {}^1\mathbf{S}_{100} + {}^2\mathbf{S}_0 + {}^2\mathbf{S}_{1-10} + {}^3\mathbf{S}_0 + {}^3\mathbf{S}_{10-1})
\end{aligned} \tag{4.20}$$

α	Plane	${}^{\alpha}f({}^{\alpha}\varepsilon)$	${}^{\alpha}f'({}^{\alpha}\varepsilon)$
1	$x+y+z=0$	$\frac{\sqrt{6}}{4}-\frac{{}^{\alpha}\varepsilon}{2}\pm\frac{1}{4}\sqrt{6+4\sqrt{6}{}^{\alpha}\varepsilon-12{}^{\alpha}\varepsilon^2}$	$-{}^{\alpha}f({}^{\alpha}\varepsilon)-{}^{\alpha}\varepsilon$
2	$x-y+z=0$	$\frac{\sqrt{6}}{4}+\frac{{}^{\alpha}\varepsilon}{2}\pm\frac{1}{4}\sqrt{6-4\sqrt{6}{}^{\alpha}\varepsilon-12{}^{\alpha}\varepsilon^2}$	${}^{\alpha}f({}^{\alpha}\varepsilon)-{}^{\alpha}\varepsilon$
3	$x-y-z=0$	$-\frac{\sqrt{6}}{4}+\frac{{}^{\alpha}\varepsilon}{2}\pm\frac{1}{4}\sqrt{6+4\sqrt{6}{}^{\alpha}\varepsilon-12{}^{\alpha}\varepsilon^2}$	$-{}^{\alpha}f({}^{\alpha}\varepsilon)+{}^{\alpha}\varepsilon$
4	$x+y-z=0$	$-\frac{\sqrt{6}}{4}-\frac{{}^{\alpha}\varepsilon}{2}\pm\frac{1}{4}\sqrt{6-4\sqrt{6}{}^{\alpha}\varepsilon-12{}^{\alpha}\varepsilon^2}$	${}^{\alpha}f({}^{\alpha}\varepsilon)+{}^{\alpha}\varepsilon$

Table 4.8: State **III**: The solution of the excitation terms.

4.5.3 Excitations Out of the Ground State: ${}^{\alpha}S = {}^{\alpha}S_o + {}^{\alpha}\varepsilon$

The next step in the calculation is to determine a general expression for the excited spin variable. Each excited spin variable is expressed as ${}^{\alpha}S = {}^{\alpha}S_o + {}^{\alpha}\varepsilon$ for each spin in the tetrahedron ($\alpha = 1, 4$), where S_o is the ground state term and ε is a small displacement parameter. It is constructive to consider the spin in its component form:

$$
\begin{aligned}
{}^{\alpha}S_x &= {}^{\alpha}S_{xo} + {}^{\alpha}\varepsilon && (4.21)\\
{}^{\alpha}S_y &= {}^{\alpha}S_{yo} + {}^{\alpha}f({}^{\alpha}\varepsilon) && (4.22)\\
{}^{\alpha}S_z &= {}^{\alpha}S_{zo} + {}^{\alpha}f'({}^{\alpha}\varepsilon). && (4.23)
\end{aligned}
$$

The y and z parameters are related to that of the x by the functions f and f' since each spin satisfies the condition of lying in its plane. The normalization condition must also be applied to ${}^{\alpha}S$ and the following equation must be solved to find the functions f and f':

$$
[{}^{\alpha}S_{xo} + {}^{\alpha}\varepsilon]^2 + [{}^{\alpha}S_{yo} + {}^{\alpha}f({}^{\alpha}\varepsilon)]^2 + [{}^{\alpha}S_{zo} + {}^{\alpha}f'({}^{\alpha}\varepsilon)]^2 = 1. \qquad (4.24)
$$

This equation is solved for $\alpha = 1, 4$ quite easily using the XMAPLE commercial software package [87]. Table 4.8 lists the equation of the easy-plane and the f and f' solutions for each spin. The ${}^{\alpha}S_o$ values for each spin are those elucidated already in Table 4.2 for state **III**.

α	${}^{\alpha}\varepsilon$	${}^{\alpha}f({}^{\alpha}\varepsilon)$	${}^{\alpha}f'({}^{\alpha}\varepsilon)$
1	${}^{1}\varepsilon$	$-{}^{1}\varepsilon + \frac{\sqrt{6}}{3}\,{}^{1}\varepsilon^{2}$	$-\frac{\sqrt{6}}{3}\,{}^{1}\varepsilon^{2}$
2	${}^{2}\varepsilon$	${}^{2}\varepsilon + \frac{\sqrt{6}}{3}\,{}^{2}\varepsilon^{2}$	$\frac{\sqrt{6}}{3}\,{}^{2}\varepsilon^{2}$
3	${}^{3}\varepsilon$	${}^{3}\varepsilon - \frac{\sqrt{6}}{3}\,{}^{3}\varepsilon^{2}$	$\frac{\sqrt{6}}{3}\,{}^{3}\varepsilon^{2}$
4	${}^{4}\varepsilon$	$-{}^{4}\varepsilon - \frac{\sqrt{6}}{3}\,{}^{4}\varepsilon^{2}$	$-\frac{\sqrt{6}}{3}\,{}^{4}\varepsilon^{2}$

Table 4.9: State **III**: Expansions of the excitation terms.

There are two sets of solutions for ${}^{\alpha}f$. ${}^{\alpha}f$ was evaluated for both solutions with ${}^{\alpha}\varepsilon = 0.1$. The solution which returned the lowest value was used since an excitant $f(\varepsilon \to 0) = 0$ is required. ${}^{\alpha}f({}^{\alpha}\varepsilon)$ was expanded to the second order term in ${}^{\alpha}\varepsilon$. The expansions for each spin are listed in Table 4.9.

4.5.4 The Separation of H_o from $H(\varepsilon)$

If ${}^{\alpha}S = {}^{\alpha}S_o + {}^{\alpha}\varepsilon$ then any dot product in Eqn. (4.20) can be expressed in the following way.

$$ {}^{\alpha}S \cdot {}^{\beta}S = {}^{\alpha}S_o \cdot {}^{\beta}S_o + g({}^{\alpha}\varepsilon, {}^{\beta}\varepsilon) \tag{4.25} $$

In this case the ground state term in the Hamiltonian $H_o = {}^{\alpha}S_o \cdot {}^{\beta}S_o$. The expression $g({}^{\alpha}\varepsilon, {}^{\beta}\varepsilon)$ can be expanded to the second order in ${}^{\alpha}\varepsilon$ and ${}^{\beta}\varepsilon$. These expansions are shown for each combination of α and β in Table 4.10.

It is interesting to note that there are linear terms in $g({}^{\alpha}\varepsilon, {}^{\beta}\varepsilon)$ for some of the bonds. This shows that the bond is not in its ground state configuration and that any small deviation of either spin in the right direction will lower its energy. However, when all the bond interactions are summed together the linear terms are all cancelled out. This shows that the system is globally in a ground state, but not every single bond. This is a result of the system being frustrated: by definition the spins cannot fully satisfy all the antiferromagnetic interactions at once. It is for this reason that the linear terms may be ignored when the Hamiltonian is

α	β	$g({}^{\alpha}\varepsilon, {}^{\beta}\varepsilon)$
1	2	$\frac{\sqrt{6}}{3}({}^{1}\varepsilon - {}^{2}\varepsilon) + \frac{1}{3}({}^{1}\varepsilon^{2} + {}^{2}\varepsilon^{2})$
1	3	$-\frac{\sqrt{6}}{3}({}^{1}\varepsilon + {}^{3}\varepsilon) + {}^{1}\varepsilon^{2} + {}^{3}\varepsilon^{2}$
1	4	$2{}^{1}\varepsilon{}^{4}\varepsilon - \frac{1}{3}({}^{1}\varepsilon^{2} + {}^{4}\varepsilon^{2})$
2	3	$2{}^{2}\varepsilon{}^{3}\varepsilon - \frac{1}{3}({}^{2}\varepsilon^{2} + {}^{3}\varepsilon^{2})$
2	4	$\frac{\sqrt{6}}{3}({}^{2}\varepsilon + {}^{4}\varepsilon) + {}^{2}\varepsilon^{2} + {}^{4}\varepsilon^{2}$
3	4	$\frac{\sqrt{6}}{3}({}^{3}\varepsilon - {}^{4}\varepsilon) + \frac{1}{3}({}^{3}\varepsilon^{2} + {}^{4}\varepsilon^{2})$

Table 4.10: State **III**: Expansions of the function $g({}^{\alpha}\varepsilon, {}^{\beta}\varepsilon)$ for each bond in the tetrahedron.

evaluated according to Eqn. (4.20) – expressed as a function of ε as follows:

$$\begin{aligned}
\mathbb{H} - H_o &= H(\varepsilon) \\
H(\varepsilon) &= \frac{J}{2}\sum_{n_1 n_2 n_3}^{N_{cell}} 4({}^{1}\varepsilon_0{}^{2} + {}^{2}\varepsilon_0{}^{2} + {}^{3}\varepsilon_0{}^{2} + {}^{4}\varepsilon_0{}^{2}) \\
&\quad + 4{}^{1}\varepsilon_0{}^{4}\varepsilon_0 + 2({}^{1}\varepsilon_0{}^{4}\varepsilon_{-100} + {}^{4}\varepsilon_0{}^{1}\varepsilon_{100}) \\
&\quad + 4{}^{2}\varepsilon_0{}^{3}\varepsilon_0 + 2({}^{2}\varepsilon_0{}^{3}\varepsilon_{01-1} + {}^{3}\varepsilon_0{}^{2}\varepsilon_{0-1-1}).
\end{aligned} \tag{4.26}$$

Eqn. (4.26) is then used to create the dynamical matrix of the system.

4.5.5 Determination of the Dynamical matrix $M_{ij}^{\alpha\beta}$

The determination of the dynamical matrix follows the same route described in section 2.3, except this time there are more combinations of α and β to consider, since there is a four atom basis.

Eqn. (4.26) is broken down quite easily into diagonal and off-diagonal terms. There are also off-diagonal interactions between spins in the same unit cell. It is clearer to summarise the different elements of $M^{\alpha\beta}(\mathbf{R}_{ij})$ in a Table 4.11 with each element's associated $\mathbf{R}_{ij} = \mathbf{R}_i - \mathbf{R}_j$ (where $\mathbf{R}_i$ is defined in Eqn. (4.16)). The

	$M_{ij}^{\alpha\beta}$	α	β	$M^{\alpha\beta}(\mathbf{R}_{ij})$	$\mathbf{R}_{ij}$
Diagonal Terms	$M_{ii}^{\alpha\alpha}$	1	1	$4J$	0
		2	2	4J	0
		3	3	4J	0
		4	4	4J	0
Off-Diagonal Terms	$M_{ii}^{\alpha\beta}$	1	4	$2J$	0
		4	1	$2J$	0
		2	3	$2J$	0
		3	2	$2J$	0
	$M_{ij}^{\alpha\beta}$	1	4	$2J$	**a**
		4	1	$2J$	$-\mathbf{a}$
		2	3	$2J$	$-\mathbf{b}+\mathbf{c}$
		3	2	$2J$	$\mathbf{b}-\mathbf{c}$

Table 4.11: State **III**: Diagonal and off-diagonal terms of $M^{\alpha\beta}(\mathbf{R}_{ij})$

same double counting argument as used in section 2.3 has been used for the $M_{ii}^{\alpha\beta}$ entries, all other terms in the matrix being zero.

4.5.6 Treatment of the Dynamical Matrix

$M^{\alpha\beta}(\mathbf{R}_{ij})$ is Fourier transformed in the same way as in section 2.3 such that:

$$M^{\alpha\beta}(\mathbf{q}) = \frac{1}{N_{cell}} \sum_{\mathbf{R}_{ij}} M^{\alpha\beta}(\mathbf{R}_{ij}) \exp\left(i\mathbf{q}.\mathbf{R}_{ij}\right). \tag{4.27}$$

and Eqn. (4.26) is reduced to

$$\mathbb{H} - H_o = \frac{1}{2}\frac{1}{N_{cell}} \sum_{\mathbf{q}} \sum_{\alpha\beta} {}^{\alpha}\varepsilon_{\mathbf{q}}\, M^{\alpha\beta}(\mathbf{q})\, {}^{\beta}\varepsilon_{\mathbf{q}}, \tag{4.28}$$

where

$${}^{\alpha}\varepsilon_{\mathbf{q}} = \frac{1}{\sqrt{N_{cell}}} \sum_{\mathbf{R}_i} {}^{\alpha}\varepsilon_i \exp\left(-i\mathbf{q}.\mathbf{R}_i\right). \tag{4.29}$$

The elements of $M^{\alpha\beta}(\mathbf{q})$ are then calculated, for example:

$$M^{14}(\mathbf{R}_{ij} = 0) = 2J$$
$$M^{14}(\mathbf{R}_{ij} = \mathbf{a}) = 2J$$
$$M^{14}(\mathbf{q}) = 2J(\exp(i\mathbf{q}.0) + \exp(i\mathbf{q}.\mathbf{a})) = 2J(1 + \exp(i\mathbf{q}.\mathbf{a})),$$

and so on for all elements in $M^{\alpha\beta}(\mathbf{q})$, to give Eqn. (4.12).

Points in the Brillouin zone

The system is made up of $N_{cell} = n_{1o}n_{2o}n_{3o}$ cells. If $n_{1o} = n_{2o} = n_{3o} = n_o$ there are n_o^3 cells. The points in the Brillouin zone are described in terms of the reciprocal lattice vectors such that

$$\begin{aligned}
\mathbf{q}(q_x, q_y, q_z) &= \boldsymbol{\alpha}\left(\frac{m_1}{n_o}\right) + \boldsymbol{\beta}\left(\frac{m_2}{n_o}\right) + \boldsymbol{\gamma}\left(\frac{m_3}{n_o}\right) \\
&= \frac{1}{n_o}(\boldsymbol{\alpha}\, m_1 + \boldsymbol{\beta}\, m_2 + \boldsymbol{\gamma}\, m_3) \\
\mathbf{q}(q_x, q_y, q_z) &= \frac{2\pi}{n_o}[(-m_1 + m_2 + m_3), (m_1 - m_2 + m_3), (m_1 + m_2 - m_3)]
\end{aligned}$$

for $m_i = 0, (n_o - 1)$.

4.5.7 Diagonalisation of $M^{\alpha\beta}(\mathbf{q})$

The branches of the normal modes are described by the eigenvalues $\lambda(\mathbf{q})$ of matrix 4.12. They are found by solving

$$\left|M^{\alpha\beta}(\mathbf{q}) - \lambda(\mathbf{q})\mathbf{I}\right| = 0,$$

which reduces to the solution of the following quartic equation in λ.

$$\left((G - \lambda)^2 - \frac{1}{2}G^2A\right)\left((G - \lambda)^2 - \frac{1}{2}G^2B\right) = 0 \qquad (4.30)$$

where $G = 4J$, $A = 1 + \cos(\mathbf{q}.\mathbf{a})$ and $B = 1 + \cos(\mathbf{q}.(\mathbf{c} - \mathbf{b}))$. If the substitution $1 + \cos(x) = 2\cos^2(\frac{x}{2})$ is made for A and B, the solutions of Eqn. (4.30) $\lambda(\mathbf{q})$ are

$$M^{\alpha\beta}(\mathbf{q}) = \begin{bmatrix} 4J & 0 & 0 & 2J\left(1+\exp\left(i\mathbf{q}.\mathbf{a}\right)\right) \\ 0 & 4J & 2J\left(1+\exp\left(i\mathbf{q}.\left(\mathbf{c}-\mathbf{b}\right)\right)\right) & 0 \\ 0 & 2J\left(1+\exp\left(-i\mathbf{q}.\left(\mathbf{c}-\mathbf{b}\right)\right)\right) & 4J & 0 \\ 2J\left(1+\exp\left(-i\mathbf{q}.\mathbf{a}\right)\right) & 0 & 0 & 4J \end{bmatrix}$$

(4.12)

elucidated.

$$\lambda(\mathbf{q})_{\pm} = 4J\left(1 \pm \cos\left(\frac{\mathbf{q}.\mathbf{a}}{2}\right)\right) \tag{4.31}$$

$$\lambda(\mathbf{q})_{\pm} = 4J\left(1 \pm \cos\left(\frac{\mathbf{q}.(\mathbf{c}-\mathbf{b})}{2}\right)\right) \tag{4.32}$$

4.5.8 Zero Modes Out of the Ground State

If $\lambda(\mathbf{q}) = 0$ for any values of $\mathbf{q}$ then it is a zero mode in the harmonic approximation and will be able to travel out of its ground state at a zero energy cost. These particular wave vectors might be singular points in reciprocal space, lines of points or even planes of points. These displacements are the soft modes mentioned in section 1.2.5.

Eqns. (4.31) and (4.32) will be zero when either $\mathbf{q}.\mathbf{a} = 0$, or $\mathbf{q}.(\mathbf{c}-\mathbf{b}) = 0$ respectively. This will only happen if $\mathbf{q}$ is perpendicular to either $\mathbf{a} = \left(\frac{1}{2}, \frac{1}{2}, 0\right)$ or $\mathbf{c}-\mathbf{b} = \left(-\frac{1}{2}, \frac{1}{2}, 0\right)$. Wave vectors which satisfy these conditions make up planes in reciprocal space. It is presumed that there are quartic corrections and there are two planes of zero modes which contribute $k_B T/4$ to the specific heat.

Figures 4.20-4.26 show plots of the eigenvalues $\lambda(\mathbf{q})$ versus $\mathbf{q}$ along different axes in the Brillouin zone. It is clear from the Figure 4.22 that wave vector $\mathbf{q} = (0, 0, q)$ is perpendicular to both $\mathbf{a}$ and $\mathbf{c}-\mathbf{b}$, since there are two superimposed branches at $\lambda(\mathbf{q}) = 0$. Wave vectors $\mathbf{q} = (q, q, 0)$ and $\mathbf{q} = (q, q, q)$ are only perpendicular to $\mathbf{c} - \mathbf{b}$, so there is only one branch at $\lambda(\mathbf{q}) = 0$ for those wave vectors (see Figures 4.23 and 4.26 respectively). There are no zero branches for any of the other wave vector directions other than $\mathbf{q} = (0, 0, 0)$.

4.5.9 The Implications for the Specific Heat

The specific heat for an XY pyrochlore system with no order by disorder was discussed in section 4.1.1. There are four degrees of freedom per unit cell and four constraints with $C_h/N = 1/2$. The same is true of the easy-plane pyrochlore.

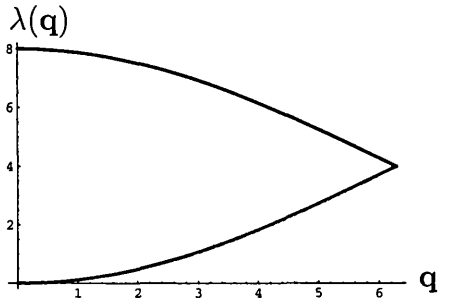

Figure 4.20: $\mathbf{q} = (q, 0, 0)$

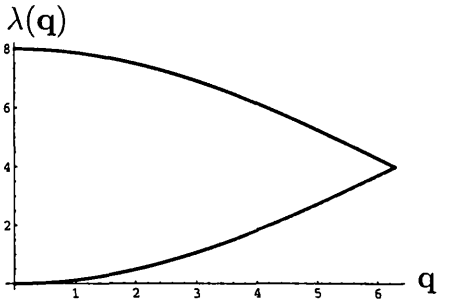

Figure 4.21: $\mathbf{q} = (0, q, 0)$

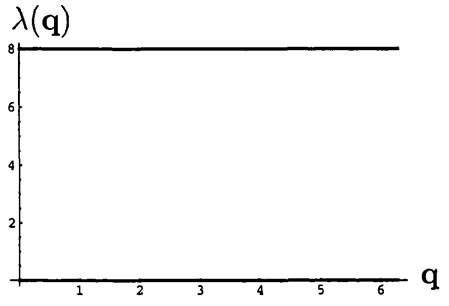

Figure 4.22: $\mathbf{q} = (0, 0, q)$

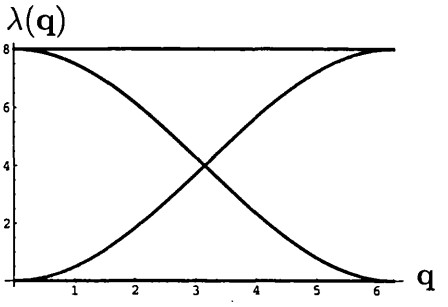

Figure 4.23: $\mathbf{q} = (q, q, 0)$

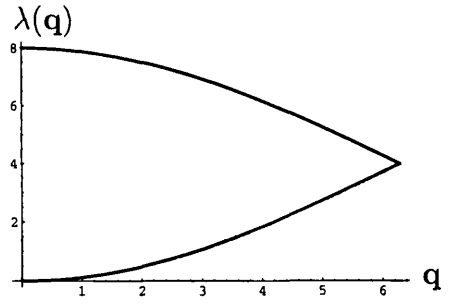

Figure 4.24: $\mathbf{q} = (q, 0, q)$

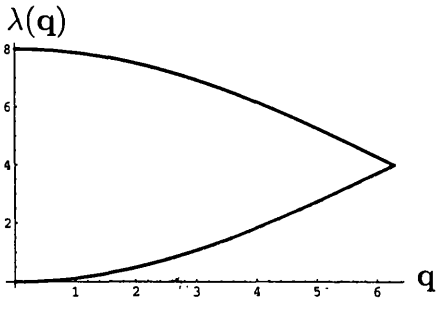

Figure 4.25: $\mathbf{q} = (0, q, q)$

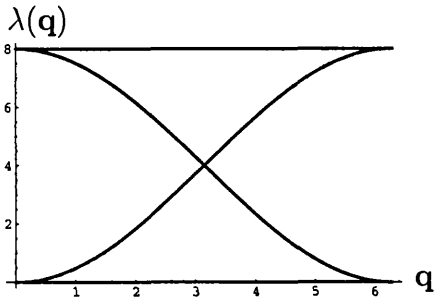

Figure 4.26: $\mathbf{q} = (q, q, q)$

The precise number of quartic modes per unit cell was known for the coplanar system [28], but it is more complicated for the local easy-plane situation studied here.

One plane in reciprocal space contains $N_{cell}^{2/3}$ zero modes. Therefore the number of zero modes per unit cell is $2N_{cell}^{1/3}$, since there are two planes. Using the method described in section 1.2.5 the specific heat per spin is thus:

$$\begin{aligned}
\frac{C_h}{Nk_BT} &= \frac{1}{4}\left[\left(4-2N_{cell}^{-1/3}\right)\frac{1}{2}+2N_{cell}^{-1/3}\frac{1}{4}\right] \\
&= \frac{1}{2}-\frac{1}{8}\frac{1}{N_{cell}^{1/3}} \\
&= \frac{1}{2}-\frac{1}{2^{11/3}}\frac{1}{L} \\
\frac{C_h}{Nk_BT} &= \frac{1}{2}-C\frac{1}{L}
\end{aligned} \tag{4.33}$$

where $N_{cell}=4L^3$ and C is a constant. Therefore if $\frac{1}{2}-\frac{C_h}{N}$ is plotted versus $\frac{1}{L}$, a straight line graph should result. This figure has been determined using data from Monte Carlo Simulation (see Fig. 4.27). Data were collected for $L=1-7$ at a temperature of $T/J=0.0001$ with $1,000,000$ MCS/S and $500,000$ equilibration steps, with five separate simulations averaged for each lattice point. The agreement with prediction is remarkable, confirming that there is order by disorder in the system. The precise gradient of the line is of the same order of magnitude as that predicted, 0.063 as opposed to 0.0787. However, it is *not* the value predicted, at present it has not been possible to explain the discrepancy in the slope.

4.6 State I: Calculation of the Normal Modes

In order to confirm that the only soft fluctuations are out of state **III**, another identical calculation can be performed for defect state **I**. This will constitute a full investigation of the ground states of the system. The method is exactly the same, except that the functions f and g are different. The ground state spin directions

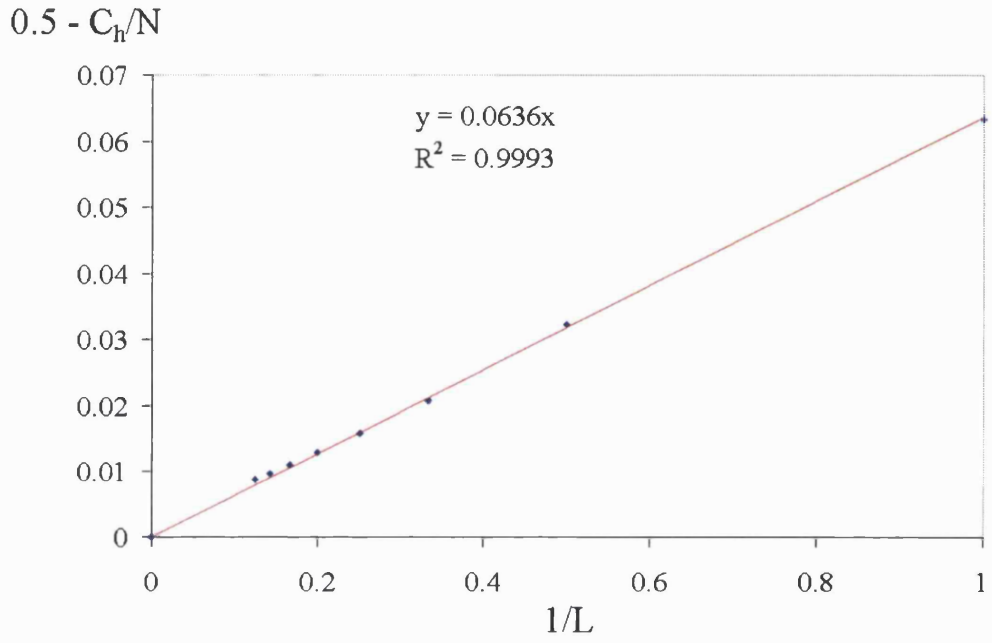

Figure 4.27: $\frac{1}{2} - \frac{C_h}{N}$ vs $\frac{1}{L}$ for State **III**.

S_o are also different.

4.6.1 Excitations Out of the Ground State: ${}^{\alpha}S = {}^{\alpha}S_o + {}^{\alpha}\varepsilon$

The functions f, f' and g associated with the position of the spin under a general displacement are listed in Tables 4.13 and 4.14.

It is again interesting to note the absence of linear terms in the $1-4$ and $2-3$

α	Plane	${}^{\alpha}f({}^{\alpha}\varepsilon)$	${}^{\alpha}f'({}^{\alpha}\varepsilon)$
1	$x+y+z=0$	$-\frac{\sqrt{2}}{4} - \frac{{}^{\alpha}\varepsilon}{2} \pm \frac{1}{4}\sqrt{2+12\sqrt{2}{}^{\alpha}\varepsilon - 12{}^{\alpha}\varepsilon^2}$	$-{}^{\alpha}f({}^{\alpha}\varepsilon) - {}^{\alpha}\varepsilon$
2	$x-y+z=0$	$\frac{\sqrt{2}}{4} + \frac{{}^{\alpha}\varepsilon}{2} \pm \frac{1}{4}\sqrt{2+12\sqrt{2}{}^{\alpha}\varepsilon - 12{}^{\alpha}\varepsilon^2}$	${}^{\alpha}f({}^{\alpha}\varepsilon) - {}^{\alpha}\varepsilon$
3	$x-y-z=0$	$-\frac{\sqrt{2}}{4} + \frac{{}^{\alpha}\varepsilon}{2} \pm \frac{1}{4}\sqrt{2+12\sqrt{2}{}^{\alpha}\varepsilon - 12{}^{\alpha}\varepsilon^2}$	$-{}^{\alpha}f({}^{\alpha}\varepsilon) + {}^{\alpha}\varepsilon$
4	$x+y-z=0$	$\frac{\sqrt{2}}{4} - \frac{{}^{\alpha}\varepsilon}{2} \pm \frac{1}{4}\sqrt{2+12\sqrt{2}{}^{\alpha}\varepsilon - 12{}^{\alpha}\varepsilon^2}$	${}^{\alpha}f({}^{\alpha}\varepsilon) + {}^{\alpha}\varepsilon$

Table 4.13: State **I**: The solution of the excitation terms.

α	β	$g({}^{\alpha}\varepsilon, {}^{\beta}\varepsilon)$
1	2	$-\sqrt{2}({}^{1}\varepsilon + {}^{2}\varepsilon) + 4{}^{1}\varepsilon^{2}\varepsilon + 3({}^{1}\varepsilon^{2} + {}^{2}\varepsilon^{2})$
1	3	$\sqrt{2}({}^{1}\varepsilon - {}^{3}\varepsilon) - 4{}^{1}\varepsilon^{3}\varepsilon - 3({}^{1}\varepsilon^{2} + {}^{3}\varepsilon^{2})$
1	4	$-2{}^{1}\varepsilon^{4}\varepsilon + 3({}^{1}\varepsilon^{2} + {}^{4}\varepsilon^{2})$
2	3	$-2{}^{2}\varepsilon^{3}\varepsilon + 3({}^{2}\varepsilon^{2} + {}^{3}\varepsilon^{2})$
2	4	$\sqrt{2}({}^{2}\varepsilon - {}^{4}\varepsilon) - 4{}^{2}\varepsilon^{4}\varepsilon - 3({}^{2}\varepsilon^{2} + {}^{4}\varepsilon^{2})$
3	4	$\sqrt{2}({}^{3}\varepsilon + {}^{4}\varepsilon) + 4{}^{3}\varepsilon^{4}\varepsilon + 3({}^{3}\varepsilon^{2} + {}^{4}\varepsilon^{2})$

Table 4.14: State **I**: Expansions of the function $g({}^{\alpha}\varepsilon, {}^{\beta}\varepsilon)$ for each bond in the tetrahedron.

bonds. This is because they are full antiferromagnetic bonds, and therefore the bonds are in a ground state. There are linear terms in the other bond interactions for the same reason stated in section 4.5.4.

4.6.2 The Separation of H_o from $H(\varepsilon)$

Application of the expressions for f and g to Eqn. (4.20) creates the following expression for the Hamiltonian in terms of the displacement parameter ε.

$$
\begin{aligned}
\mathbb{H} - H_o &= H(\varepsilon) \\
H(\varepsilon) &= \frac{J}{2}\sum_{n_1 n_2 n_3}^{N_{cell}} 12({}^{1}\varepsilon_0{}^{2} + {}^{2}\varepsilon_0{}^{2} + {}^{3}\varepsilon_0{}^{2} + {}^{4}\varepsilon_0{}^{2}) \\
&\quad +8{}^{1}\varepsilon_0{}^{2}\varepsilon_0 + 4({}^{1}\varepsilon_0{}^{2}\varepsilon_{0-10} + {}^{2}\varepsilon_0{}^{1}\varepsilon_{010}) \\
&\quad -8{}^{1}\varepsilon_0{}^{3}\varepsilon_0 - 4({}^{1}\varepsilon_0{}^{3}\varepsilon_{00-1} + {}^{3}\varepsilon_0{}^{1}\varepsilon_{001}) \\
&\quad -4{}^{1}\varepsilon_0{}^{4}\varepsilon_0 - 2({}^{1}\varepsilon_0{}^{4}\varepsilon_{-100} + {}^{4}\varepsilon_0{}^{1}\varepsilon_{100}) \\
&\quad -4{}^{2}\varepsilon_0{}^{3}\varepsilon_0 - 2({}^{2}\varepsilon_0{}^{3}\varepsilon_{01-1} + {}^{3}\varepsilon_0{}^{2}\varepsilon_{0-11}) \\
&\quad -8{}^{2}\varepsilon_0{}^{4}\varepsilon_0 - 4({}^{2}\varepsilon_0{}^{4}\varepsilon_{-110} + {}^{4}\varepsilon_0{}^{2}\varepsilon_{1-10}) \\
&\quad +8{}^{3}\varepsilon_0{}^{4}\varepsilon_0 + 4({}^{3}\varepsilon_0{}^{4}\varepsilon_{-101} + {}^{4}\varepsilon_0{}^{3}\varepsilon_{10-1})
\end{aligned}
\tag{4.34}
$$

$M_{ij}^{\alpha\beta}$	α	β	$M^{\alpha\beta}(\mathbf{R}_{ij})$	$\mathbf{R}_{ij}$
$M_{ii}^{\alpha\alpha}$	1	1	$12J$	0
	2	2	12J	0
	3	3	12J	0
	4	4	12J	0

Table 4.15: State I: Diagonal terms of $M^{\alpha\beta}(\mathbf{R}_{ij})$.

4.6.3 Determination of the Dynamical Matrix $M_{ij}^{\alpha\beta}$

Eqn. (4.34) is again broken down into diagonal and off-diagonal terms. The diagonal elements are listed in Table 4.15. In this case there are many more off-diagonal terms, with a greater variety of different $\mathbf{R}_{ij}$; they are listed in Table 4.16. The double counting argument has been used again for the $M_{ii}^{\alpha\beta}$ entries.

4.6.4 Treatment of the Dynamical Matrix

$M^{\alpha\beta}(\mathbf{R}_{ij})$ is Fourier transformed in the same way as before to give $M^{\alpha\beta}(\mathbf{q})$, detailed in Eqn. (4.17).

4.6.5 Diagonalisation of $M^{\alpha\beta}(\mathbf{q})$

The branches of the normal modes are described by the eigenvalues $\lambda(\mathbf{q})$ of matrix 4.17. They are found by solving

$$\left| M^{\alpha\beta}(\mathbf{q}) - \lambda(\mathbf{q})\mathbf{I} \right| = 0. \tag{4.35}$$

It has not been possible to solve Eqn. (4.35) analytically. However, it can be solved numerically for particular values of $\mathbf{q}$ [89]. Figures 4.28-4.34 show plots of the eigenvalues $\lambda(\mathbf{q})$ versus $\mathbf{q}$ along different axes in the Brillouin zone. The most important result to note is that there are no zero modes in any direction in the Brillouin zone, other than at $\mathbf{q} = (0, 0, 0)$.

$M_{ij}^{\alpha\beta}$	α	β	$M^{\alpha\beta}(\mathbf{R}_{ij})$	$\mathbf{R}_{ij}$	$M_{ij}^{\alpha\beta}$	α	β	$M^{\alpha\beta}(\mathbf{R}_{ij})$	$\mathbf{R}_{ij}$
$M_{ii}^{\alpha\beta}$	1	2	$4J$	0	$M_{ij}^{\alpha\beta}$	1	2	$4J$	b
	1	3	$-4J$	0		1	3	$-4J$	c
	1	4	$-2J$	0		1	4	$-2J$	a
	2	1	$4J$	0		2	1	$4J$	$-$b
	2	3	$-2J$	0		2	3	$-2J$	c $-$ b
	2	4	$-4J$	0		2	4	$-4J$	a $-$ b
	3	1	$-4J$	0		3	1	$-4J$	$-$c
	3	2	$-2J$	0		3	2	$-2J$	$-$(c $-$ b)
	3	4	$4J$	0		3	4	$4J$	a $-$ c
	4	1	$-2J$	0		4	1	$-2J$	$-$a
	4	2	$-4J$	0		4	2	$-4J$	$-$(a $-$ b)
	4	3	$4J$	0		4	3	$4J$	$-$(a $-$ c)

Table 4.16: State I: Off-diagonal terms of $M^{\alpha\beta}(\mathbf{R}_{ij})$.

$$M^{\alpha\beta}(\mathbf{q}) =$$

$$\begin{bmatrix} 12J & 4J\left(1+\exp\left(i\mathbf{q}.\mathbf{b}\right)\right) & -4J\left(1+\exp\left(i\mathbf{q}.\mathbf{c}\right)\right) & -2J\left(1+\exp\left(i\mathbf{q}.\mathbf{a}\right)\right) \\ 4J\left(1+\exp\left(-i\mathbf{q}.\mathbf{b}\right)\right) & 12J & -2J\left(1+\exp\left(i\mathbf{q}.\left(\mathbf{c}-\mathbf{b}\right)\right)\right) & -4J\left(1+\exp\left(i\mathbf{q}.\left(\mathbf{a}-\mathbf{b}\right)\right)\right) \\ -4J\left(1+\exp\left(-i\mathbf{q}.\mathbf{c}\right)\right) & -2J\left(1+\exp\left(-i\mathbf{q}.\left(\mathbf{c}-\mathbf{b}\right)\right)\right) & 12J & 4J\left(1+\exp\left(i\mathbf{q}.\left(\mathbf{a}-\mathbf{c}\right)\right)\right) \\ -2J\left(1+\exp\left(-i\mathbf{q}.\mathbf{a}\right)\right) & -4J\left(1+\exp\left(-i\mathbf{q}.\left(\mathbf{a}-\mathbf{b}\right)\right)\right) & 4J\left(1+\exp\left(-i\mathbf{q}.\left(\mathbf{a}-\mathbf{c}\right)\right)\right) & 12J \end{bmatrix}$$

(4.17)

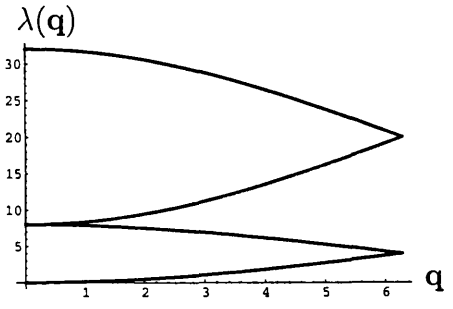

Figure 4.28: $\mathbf{q} = (q, 0, 0)$

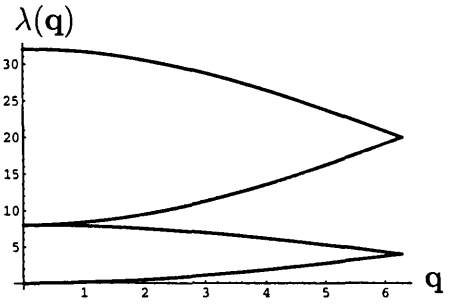

Figure 4.29: $\mathbf{q} = (0, q, 0)$

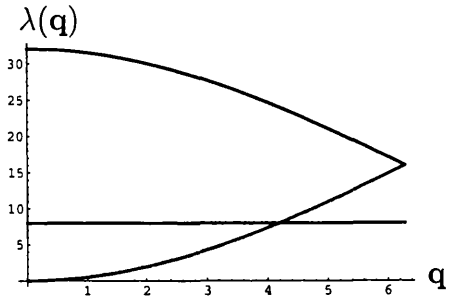

Figure 4.30: $\mathbf{q} = (0, 0, q)$

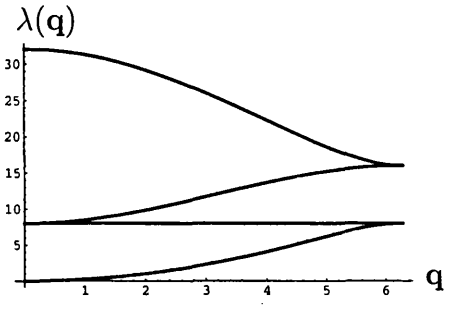

Figure 4.31: $\mathbf{q} = (q, q, 0)$

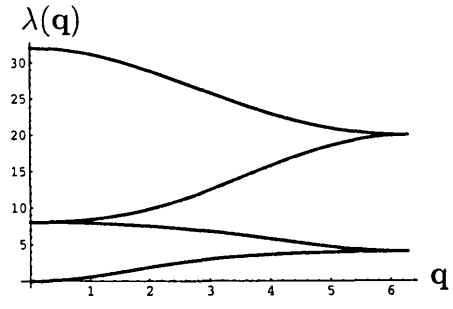

Figure 4.32: $\mathbf{q} = (q, 0, q)$

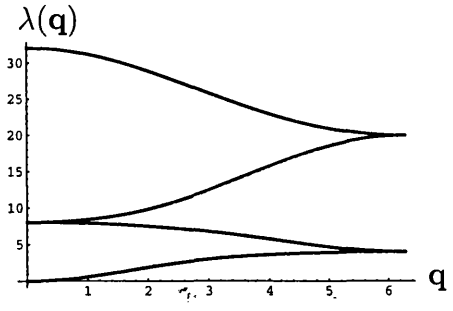

Figure 4.33: $\mathbf{q} = (0, q, q)$

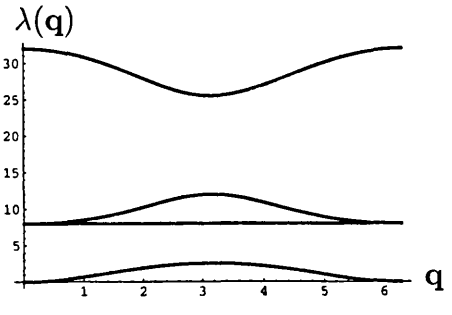

Figure 4.34: $\mathbf{q} = (q, q, q)$

4.7 Conclusions

This chapter has provided an insight into the ordering processes involved in the frustrated easy-plane pyrochlore antiferromagnet. The following section summarises the main results.

4.7.1 Degeneracy of Ground States

The results in this chapter have shown that the ground state degeneracy in the easy-plane antiferromagnet is much greater than first thought [84]. The q=0 ground states are fully connected and explicitly described by the linear combination of eight separate pairs of basis vectors. The key difference with the analysis of Ref. [84] is the identification of state **III**, which turns out to be the true ground state of the model. It is also possible to observe disordered ground states, consisting of infinite line defects existing in a 'sea' of q=0 order. These defects are observed less as the lattice size is increased. There are $O(L^2)$ independent rods which support the existence of these defects.

4.7.2 Order by Disorder

The observed ordered state for the model was shown to be state **III**, which was not discussed in Ref. [84]. A normal mode calculation was performed to determine the fluctuations out of state **III**. There are $O(L^2)$ zero modes (in the harmonic approximation) in the spin wave spectrum. These results provide an explicit mechanism for the order by disorder transition in the system: since long-range order is observed for finite temperature and at $T = 0$ the degeneracy strictly prevents ordering [26].

The same calculation was repeated for the defect state **I**. No zero modes were determined, other than at $\mathbf{q} = (0, 0, 0)$. It is presumed that the zero modes are strictly a property of state **III**, since they are also not observed for the symmetric

state **II** [90].

4.7.3 Relation of these Results to $Er_2Ti_2O_7$

The results of this chapter have a direct relation to those presented in Chapter 6, in which $Er_2Ti_2O_7$ is described as a realisation of the local easy-plane pyrochlore antiferromagnet. A precise comparison between the theoretical results presented in this chapter, and the powder neutron diffraction data in Chapter 6, is made in the conclusion (see section 9.3.3).

Chapter 5

Introduction to Neutron Scattering Techniques

This thesis contains experimental results from the neutron diffraction of both powder and single crystals. This chapter aims to introduce the very basic elements of neutron scattering theory [91]. The analysis of powder neutron diffraction data is then discussed, with respect to the determination of magnetic structures. The neutron scattering instruments which have been used are described very briefly, followed by the aims of the experimental work which has been carried out.

5.1 Basic Neutron Scattering Theory

For the purposes of neutron scattering, neutrons are considered as particles with a de Broglie momentum p and kinetic energy E:

$$p = \frac{h}{\lambda}, \quad E = \frac{h^2}{2m\lambda^2}, \tag{5.1}$$

with h Planck's constant, m mass of the neutron and λ the wavelength. $E = 25$ meV corresponds to $\lambda = 1.8$ Å, which is of the same order of magnitude as the interatomic distances in a crystalline solid. Neutrons have a magnetic spin $S = \frac{1}{2}$ and

interact with the magnetic fields from unpaired electrons (magnetic scattering) as well as atomic nuclei (nuclear scattering).

The neutron-matter interaction is very weak as most neutrons miss the nuclei. The consequences of this are that neutrons probe the bulk of the sample (they penetrate ~ 1 cm), but they cause no damage to the sample. The linear response of the system can be quantified well by theory allowing for excellent interpretation of neutron scattering results.

5.1.1 Scattering from a Nucleus and a Crystalline Lattice

The incoming neutron wave function ψ_{inc} is described by a plane wave and the scattered wave function ψ_{sc} is a spherical wave.

$$\psi_{inc} = \exp(i\mathbf{k}_i z)$$
$$\psi_{sc} = -\frac{b}{r}\exp(i\mathbf{k}_f r) \qquad k = \frac{2\pi}{\lambda}$$

where z is the direction of the incoming plane wave, r the radius of the scattered sphere and $\mathbf{k}_{i/f}$ the incident and final wave vectors. b is the amplitude of the scattered wave, and is sometimes called the scattering length. b varies with isotope and with nuclear spin orientation.

When neutrons are scattered from the planes of a lattice, each atom scatters with a spherical wave, but the diffracted patterns can interfere constructively to give another plane wave. The neutrons need to travel an integral number of wavelengths for scattering to be constructive and the wavelengths to be the same. This will only occur when the diffraction condition is satisfied:

$$n\lambda = 2d\sin\theta, \tag{5.2}$$

where d is the spacing between planes and θ is half the scattering angle, Eqn. (5.2) is known as Bragg's law.

A neutron scattering instrument measures the intensity of the scattered neutrons from the different planes of a crystalline lattice. The intensity of the scattered neutrons from nuclei I_N is dependent on the nuclear structure factor F_N:

$$I_N \propto |F_N|^2 \tag{5.3}$$

$$F_N = \sum_n b_n \exp(i\mathbf{Q} \cdot \mathbf{r}_n) \qquad \mathbf{Q} = \mathbf{k}_i - \mathbf{k}_f. \tag{5.4}$$

This is a sum over all the atoms in the unit cell, where b_n is an average over all isotopes present in the crystal.

As mentioned above neutrons are scattered by magnetic moments. Magnetic Bragg scattering occurs, which has an associated scattering intensity I_M and structure factor F_M:

$$I_M \propto \sin^2\theta |F_M|^2 \tag{5.5}$$

$$F_M = f(Q) \sum_n \mu_n \exp(i\mathbf{Q} \cdot \mathbf{r}_n) \tag{5.6}$$

where $f(Q)$ is the magnetic form factor and θ is the angle between the magnetic moment μ and $\mathbf{Q}$. The magnetic form factor reduces the intensity of the scattering for larger $|\mathbf{Q}|$, since at larger angles the phase difference between waves scattered from different parts of the atom (since scattering from electrons) increases with angle. The total observed scattering intensity $I = I_N + I_M$.

5.1.2 Time of Flight Crystallography

The neutron source at ISIS is a pulsed spallation source, and a time of flight technique is used to obtain the diffraction patterns of the crystalline samples. Relating Eqn. (5.1) and Eqn. (5.2), one can write:

$$\lambda_{hkl} = 2d_{hkl} \sin\theta = \frac{h}{(2mE)^{1/2}} = \frac{h}{m\nu} \tag{5.7}$$

In time of flight neutron diffraction, λ_{hkl} is determined by measuring the time of fight t_{hkl} of the neutrons over a known path length L from the source to the detec-

tor, passing through the sample. The velocity v of the neutron can be calculated as $v = L/t_{hkl}$. Substituting ν into Eqn. (5.7) and rearranging for t_{hkl} gives:

$$t_{hkl} = 2d_{hkl}L\left(\frac{m}{h}\right)\sin\theta \tag{5.8}$$

5.2 Rietveld Refinement

Rietveld refinement is a method for fitting experimental powder diffraction measurements to a calculated structural model. The method aims to match the entire experimental profile by taking account of a model for the crystal structure and also the instrumental parameters [92]. The essential feature is that the whole pattern is matched, rather than decomposed into separate Bragg peaks as in other structure refinement methods. During the refinement the models are improved to obtain the best possible fit of the calculated and observed profile.

The pattern is digitized as a series of intensities y^i, with a least squares fit made to all the calculated intensities simultaneously. The quantity minimised is

$$S_y = \sum_i w_i(y^i_{obs} - y^i_c)^2, \tag{5.9}$$

where $w_i = 1/y^i_{obs}$, y^i_{obs} is the observed intensity for the ith step and y^i_c is the calculated intensity for the ith step.

The intensity at the ith point is calculated primarily using the structure factor for the model. y^i_c is defined:

$$y^i_c = y^i_b + s\sum_k L_k|F_k|^2\phi(2\theta_i - 2\theta_k)P_kA, \tag{5.10}$$

where y_b is the background intensity, s is the scale factor, L_k includes Lorentz polarisation and multiplicity factors, ϕ represents a peak profile function, A is the absorption factor and F_k is the structure factor of the k^{th} Bragg reflection.

Since the pattern is not decomposed a contribution from neighbouring peaks within a suitable range is summed. The contributions from the background and

the instrumental effects are also included. The intensity is calculated and then the residuals are obtained iteratively. These are used to calculate shifts that are applied to the initial parameters to improve the model. The process is then repeated. This is implemented by computer, several programs exist and in this work all refinements are carried out using the GSAS software of Larson and Von Dreele [93].

The Rietveld method is not designed to solve a structure *ab initio*. If a stable refinement that reaches the global minimum is to be obtained, it requires a reasonably good starting model. Often a sufficient start can be obtained using the atom positions of an isostructural compound and adjusting the lattice parameters manually.

Whilst the best guide to the progress of a refinement is usually the difference curve, it is essential to be able to quantify the goodness of the fit. The refinement program minimises the residual and then calculates several R-factors. These are

$$R_F = \frac{\sum |(I_k(obs))^{\frac{1}{2}} - (I_k(c)^{\frac{1}{2}})|}{\sum (I_k(obs))^{\frac{1}{2}}} \tag{5.11}$$

$$R_B = \frac{\sum |I_k(obs) - I_k(c)|}{\sum I_k(obs)} \tag{5.12}$$

$$R_p = \frac{\sum |y^i_{obs} - y^i_c|}{\sum y^i_{obs}} \tag{5.13}$$

$$R_{wp} = \left\{ \frac{\sum w_i (y^i_{obs} - y^i_c)^2}{\sum w_i (y^i_{obs})^2} \right\}^{\frac{1}{2}} \tag{5.14}$$

where I_k is the intensity assigned to the k^{th} Bragg reflection at the end of the refinement cycle. I_k is rarely observed and is obtained from programmatic allocation of the total observed intensity in a collection of overlapping peaks to the individual reflections according to calculated reflection intensity.

These R-factors provide a guide to the adequacy of the model. R_{wp} is the most meaningful as it actually includes the residual being minimised. Because R_F and R_B include the I_k intensities which are not actually observed but are deduced using the model, these R- factors favour the model being used. However, it is not

sufficient to obtain a small R_{wp}; for example, a high and well fitted background may lead to a low R_{wp} as the slowly varying background is relatively easily fitted.

The associated χ^2 of the least squares fit is also determined:

$$\chi^2 = \frac{\sum w(I_{obs} - I_c)^2}{N_{obs} - N_{var}}, \tag{5.15}$$

where N_{obs} and N_{var} are the number of experimental and varying points respectively.

5.3 The Application of Group Theory to Magnetic ordering

In Chapters 6 and 7 Representational Analysis has been used to help determine the magnetic structure of $Er_2Ti_2O_7$ and $Gd_2Ti_2O_7$. This section gives a brief introduction to the method.

5.3.1 The Ordering Wave Vector

The ordering wave vector has already been mentioned with respect to two ground state structures in the kagomé antiferromagnet and the pyrochlore ferromagnet in a field (see sections 1.2.7 and 1.3.1). The magnetic structure is a periodic property of the crystal, but need not necessarily have the same period as the atomic structure.

If the magnetic ordering is considered to be a distribution of moments $\mathbf{m}_{lj}$ associated with the Bravais sublattice j of the nuclear unit cell, they can be Fourier expanded as

$$\mathbf{m}_{lj} = \sum_{\mathbf{k}} \mathbf{m}_{\mathbf{k},j} \exp\left(-i\mathbf{k}.\mathbf{R}_l\right) \tag{5.16}$$

where $\mathbf{R}_l$ is the position of the lth unit cell [94]. The wave vector $\mathbf{k}$ is of central importance in the determination and description of the magnetic structure. It is a propagation vector describing the relation between the nuclear basis and the

magnetic superlattice. The wave vector $\mathbf{k}$ is one member of a set of equivalent wave vectors $\mathbf{k}_p$ called the star of $\mathbf{k}$. The other wave vectors in the star are obtained by applying the symmetry operations of the paramagnetic group to $\mathbf{k}$. A magnetic structure may be characterized by more than one wave vector giving single-$\mathbf{k}$ or multi-$\mathbf{k}$ structures. The magnetic structure belongs to a magnetic symmetry group. These contain the information of the crystallographic space group, and also additional symmetry operations to take account of the magnetic moment at each site [95]. Many ordered structures are possible since there are 1421 magnetic symmetry groups. The structure may be collinear, non-collinear, or helical. The essential feature of all magnetic structures is that the order is invariant under arbitrary lattice translations (with consideration of the propagation vector), and that the magnetic energy is minimised.

5.3.2 Symmetry-allowed Magnetic Structures

The calculations of Representational Analysis [96, 95, 97] allow the determination of the different symmetry-allowed magnetic structures given only the crystal structure before the magnetic ordering transition and the propagation vector of the magnetic structure, again with respect to the nuclear cell before the transition. They involve first the determination of the space group symmetry elements, g, that leave the propagation vector $\mathbf{k}$ invariant: these form the little group $G_{\mathbf{k}}$. The magnetic representation, Γ_R, of an atomic site R, can be decomposed in terms of the Irreducible Representations (IRs) of $G_{\mathbf{k}}$:

$$\Gamma_R = \sum_{\nu} n_\nu \Gamma_\nu \tag{5.17}$$

where the number of times, n_ν, that the IR Γ_ν appears in the magnetic representation Γ is given by:

$$n_\nu = \frac{1}{|G_{\mathbf{k}}|} \sum_{g \in G_{\mathbf{k}}} \chi(g)\chi_\nu^*(g) \tag{5.18}$$

Here, χ is the character of the magnetic representation Γ, and χ_ν is the character of the IR with index ν.

The unique basis vectors, ψ_ν, that transform according to the μ dimensional IR $\Gamma_\nu^{(\mu)}$ are projected from of the representation matrix D_ν using the general projection operator formula:

$$\psi_\nu^{i\lambda} = \sum_{g \in G_\mathbf{k}} D_{(\nu)}^{\lambda *} \sum_i \delta_{i,gi} \delta_h R^h \psi^\alpha, \tag{5.19}$$

where δ_h represents the determinant of the rotational part of g and the summation is over the symmetry elements of the little group $G_\mathbf{k}$. ψ^i is the column matrix of the spin component projected from the test function ψ^α. The index i labels the Bravais-sublattice.

5.4 Practical Implementation of Representational Analysis

The determination of specific symmetry-allowed basis vectors described above is necessarily complicated. Fortunately the relevant calculations can be performed automatically using a computer program. The software used in this thesis was the 'SARA*h*-2K Representational Analysis' written by Andrew Wills [98].

5.4.1 Sara*h* Representational Analysis

The SARA*h* program performs the symmetry calculations mentioned in section 5.3. Given only the crystallographic space group, the positions of the magnetic atoms and the propagation vector before the magnetic transition. The program produces a set of symmetry-allowed basis vectors for the system. A particular advantage of the software is that no knowledge of theoretical exchange Hamiltonian or crystal electric field are required.

The program has been integrated with the standard software package GSAS [93],

so that refinement of the magnetic structure is simple and straightforward. The method of refinement follows a simple path. The atomic spin on a particular atom S^i is most generally given by the sum of the symmetry-allowed basis vectors for a particular irreducible representation

$$S^i = \sum_\nu C^i_\nu \psi^i_\nu, \tag{5.20}$$

where C^i_ν is the mixing coefficient for atom i of the basis vector ν. The refinement of the orientation of an atomic moment is in effect the refinement of the mixing coefficients C^i_ν of the basis vectors within the irreducible representation being examined. SARA*h* creates the appropriate magnetic structures and enters them into the GSAS '.EXP' file. GSAS then calculates the appropriate magnetic structure factors and performs a least-squares fit to the data, by refining the length of the magnetic moment. The number of variables in the refinement is simply the number of unique basis vectors that transform according to a particular representation [98].

5.5 Neutron Scattering Instruments

Both single crystal and powder neutron scattering results are discussed in this thesis. Two instruments in particular were used, both are based at the ISIS neutron facility of the Rutherford Appleton Laboratory. These instruments are very briefly discussed in this section.

5.5.1 POLARIS

The Polaris high-intensity diffractometer, is a medium resolution instrument situated on the N7 beamline at the Rutherford Appleton Laboratory's ISIS Facility. Due to its high intensity it has the ability to characterize condensed matter structures rapidly, with only a small amount of sample material.

Sample environment

The sample is placed 12 metres from the ambient temperature water moderator, where it receives a polychromatic 'white beam' of incident neutrons. The beam is collimated to be 40 mm high by 20 mm wide, which can be reduced to match the sample size, if required. A dilution refrigerator with vanadium tails can be placed on the beamline to provide very low temperature conditions.

Detector banks

Figure 5.1 shows the detector arrangement setup of the POLARIS instrument. The highest resolution ($\Delta d/d \approx 5 \times 10^{-3}$) detector bank is the backscattering or C bank which is made up of two pairs of 29 ^{3}He detectors. It has a d-range of 0.2 Å– 3.2 Å, with $130° < 2\theta < 160°$.

Due to the magnetic form factor, magnetic Bragg peaks generally have more intensity at longer d-spacing. For this reason the low-angle or A bank can be used as well. This has two pairs of 40 ^{3}He detectors, but due to the lower angle of scattering the resolution is lower ($\Delta d/d \approx 1 \times 10^{-2}$). It has a much longer d-range of 0.5 Å – 8.3 Å, with $28° < 2\theta < 42°$.

The POLARIS instrument provides good structural and magnetic data which can be easily analysed by Rietveld Refinement with the GSAS package [93].

5.5.2 PRISMA

The PRISMA instrument at ISIS is an inelastic spectrometer which can also be used as a high resolution, low background diffractometer. It receives a polychromatic beam of thermally moderated neutrons. The moderator used is liquid methane at 100 K.

In diffraction mode there are sixteen ^{3}He tube detectors which are separated by 1°. They can be used simultaneously to map out a large area of reciprocal space

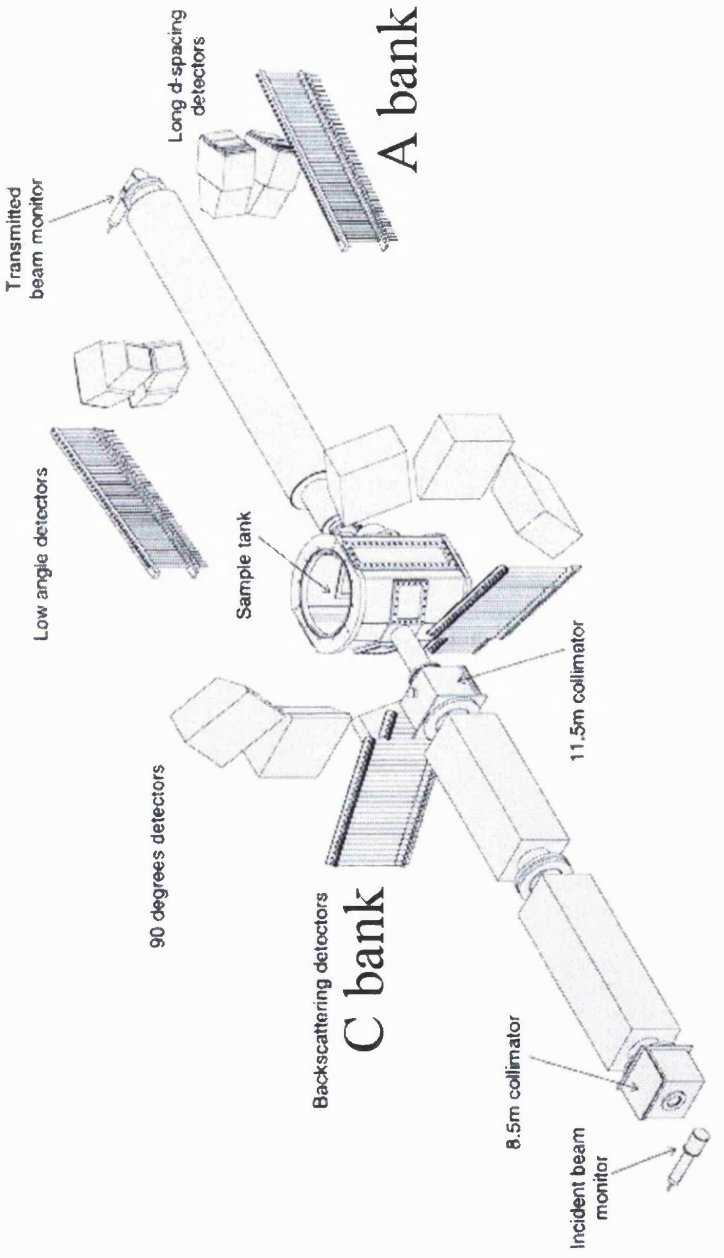

Figure 5.1: Detector arrangement of the POLARIS instrument.

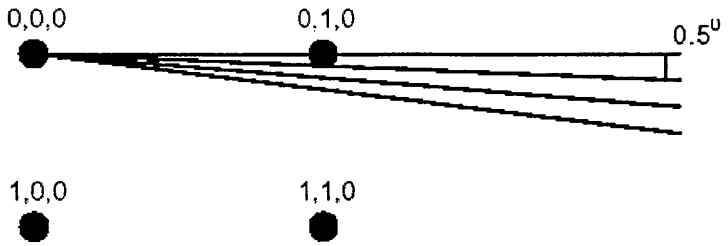

Figure 5.2: Mapping out reciprocal space.

very rapidly. For a single setting of the spectrometer, each detector measures a radial scan in reciprocal space so that a set of detectors covers a fan-shaped area. Figure 5.2 shows a schematic view of reciprocal space for a crystal, with the fan corresponding to radial scans from 4 detectors. Further details of the instrument can be found in Ref. [99].

PRISMA provides an excellent tool for investigating the diffuse magnetic scattering of single crystals. A dilution refrigerator or a sorption cryostat can be placed on the beamline to provide low temperature conditions. The scattering of the sample can also be measured in a magnetic field with the use of a cryomagnet.

5.6 Summary: Aims of the Experimental work in this Thesis

The main aim of the experimental work carried out in this thesis was to determine the magnetic structures of $Er_2Ti_2O_7$ and $Gd_2Ti_2O_7$. The technique of powder neutron diffraction was used in both cases. Both these systems are frustrated yet show an ordering transition. The results of the work on $Er_2Ti_2O_7$ are presented in Chapter 6. The magnetic structure observed is specifically relevant to the theoretical results obtained in Chapter 4, since $Er_2Ti_2O_7$ is believed to be an antiferromagnet with local easy-plane anisotropy [13]. The results of the work

on $Gd_2Ti_2O_7$ are presented in Chapter 7. The work follows on from the specific heat measurements of Raju *et al.* [37] which reported ordering in the system. The observed magnetic structure is then compared with that predicted by Palmer *et al.* [100].

Further experiments have been made on the spin ice materials $Ho_2Ti_2O_7$ and $Dy_2Ti_2O_7$. The understanding of these systems has been improved by further comparison with the dipolar spin ice model. These results are presented in Chapter 8.

Chapter 6

Magnetic Structure of $Er_2Ti_2O_7$

$Er_2Ti_2O_7$ is a pyrochlore antiferromagnet which has a magnetic ordering transition at $\sim 1.2K$ [13]. It is a system which will have strong crystal field effects and it has been suggested to have easy-plane anisotropy [13]. The aim of the work described in this chapter was to test this conjecture, by determining the magnetic structure of the ordered state

Group theory has been used to calculate the different symmetry allowed magnetic structures with the $\mathbf{k} = 000$ ordering wave vector, which is observed in $Er_2Ti_2O_7$ (see Fig. 6.3). The possible structures have been tested against new powder neutron diffraction results of $Er_2Ti_2O_7$.

6.1 Previous Work on $Er_2Ti_2O_7$

$Er_2Ti_2O_7$ was first determined to be a cubic pyrochlore ($Fd\bar{3}m$) by Knop *et al.* in 1965 [101]. Nuclear structure factors were calculated and compared with those observed in neutron and x-ray diffraction as well as the spectra from other rare-earth titanates. In 1966 Van Geuns demonstrated by susceptibility and demagnetization experiments that the compound was antiferromagnetic in nature with a very large Curie-Weiss temperature $\theta_{CW} = -22$ K [102]. Blöte *et al.* performed specific heat

measurements and observed a magnetic ordering transition with T_N=1.25 K [102]. They postulated that the large θ observed could be rationalised by crystal field effects, since it was too large to be due solely to antiferromagnetic exchange interactions. They suggested that there might be a low-lying crystal field excitation about 1 meV above the ground state Kramers doublet of Er^{3+}. However, this level was not observed by neutron scattering: rather, two low-lying excitations are present at 6-8 meV above the ground state level [10]. It seems unlikely that these excitations can fully account for the large Curie-Weiss temperature.

The $4f^{11}$ electronic configuration of Er^{3+} gives rise to a free ion magnetic moment of $9.59\mu_B$ ($L = 6$, $S = 3/2$) with a $^4I_{15/2}$ ground state term. The large value of L suggests a significant amount of anisotropy in the system but does not give an idea of the type, uniaxial or planar. Transitions are observed in real [49] and theoretical (see Chapter 4 and section 9.4.2) antiferromagnetic systems with both types of anisotropy. Preliminary single crystal neutron scattering showed there to be magnetic ordering with the periodicity of the lattice. The magnetic Bragg peaks observed are coincident with the structural Bragg peaks, indicating an ordering wave vector **k**=000. A system ordering with this wave vector will have the same arrangement of spins on every 'up' or 'down' tetrahedron. The antiferromagnetic fluoride pyrochlore FeF_3 has $\langle 111 \rangle$ easy-axis anisotropy similar (though much weaker) to that of $Ho_2Ti_2O_7$. The ground state for this system is non-degenerate and has **k**=000 ordering, where all the spins point into the centre (or away from the centre) of every tetrahedron. This consequence of such ordering is that the (1,1,1) magnetic Bragg peak is absent [49], whereas in $Er_2Ti_2O_7$ it is present [13]. This suggests that the dominant anisotropy in the system might be planar [13]. This speculation was supported by direct measurements of the crystal field interaction by Rosenkranz *et al.* [9, 45].

6.2 Powder Neutron Diffraction Experiment

Powder neutron diffraction data were collected using the POLARIS high intensity diffractometer at the ISIS pulsed neutron facility (see section 5.5.1). The sample was contained in a vanadium can with a small amount of ^{4}He exchange gas. The can was mounted in an Oxford Instruments dilution refrigerator, and then placed in a cryostat. ^{3}He exchange gas was introduced into the Inner Vacuum Chamber (IVC) of the cryostat to maintain stability of the dilution refrigerator.

Data were collected for $\sim$ 12 hours above and below the ordering transition ($T_N \sim 1.2$ K) at 4.85 K and 50 mK.

6.2.1 Analysis of the 4.85 K data

Refinement of the data collected at 4.85 K was performed using the GENLES routine of the GSAS Suite [93]. The optimum refined profile is shown in Fig. 6.1. The sample was proved to be phase pure and the structural data could be easily refined. Details of the refinement parameters are shown in Table 6.1. These results are within 3 e.s.d of the room temperature results of Knop *et al.* ($x(O_2) = 0.4200(10)$) [101].

6.2.2 Representational Analysis

As previously reported [13] and confirmed below, the magnetic diffraction peaks of $Er_2Ti_2O_7$ could be indexed on a $\mathbf{k} = 000$ propagation vector. In section 5.3 the theoretical basis of group theory applied to magnetic structures was outlined. In this section it is applied to the case of $\mathbf{k} = 000$ propagation vector, for the spins on the 16*c* sites of the $Fd\bar{3}m$ space group.

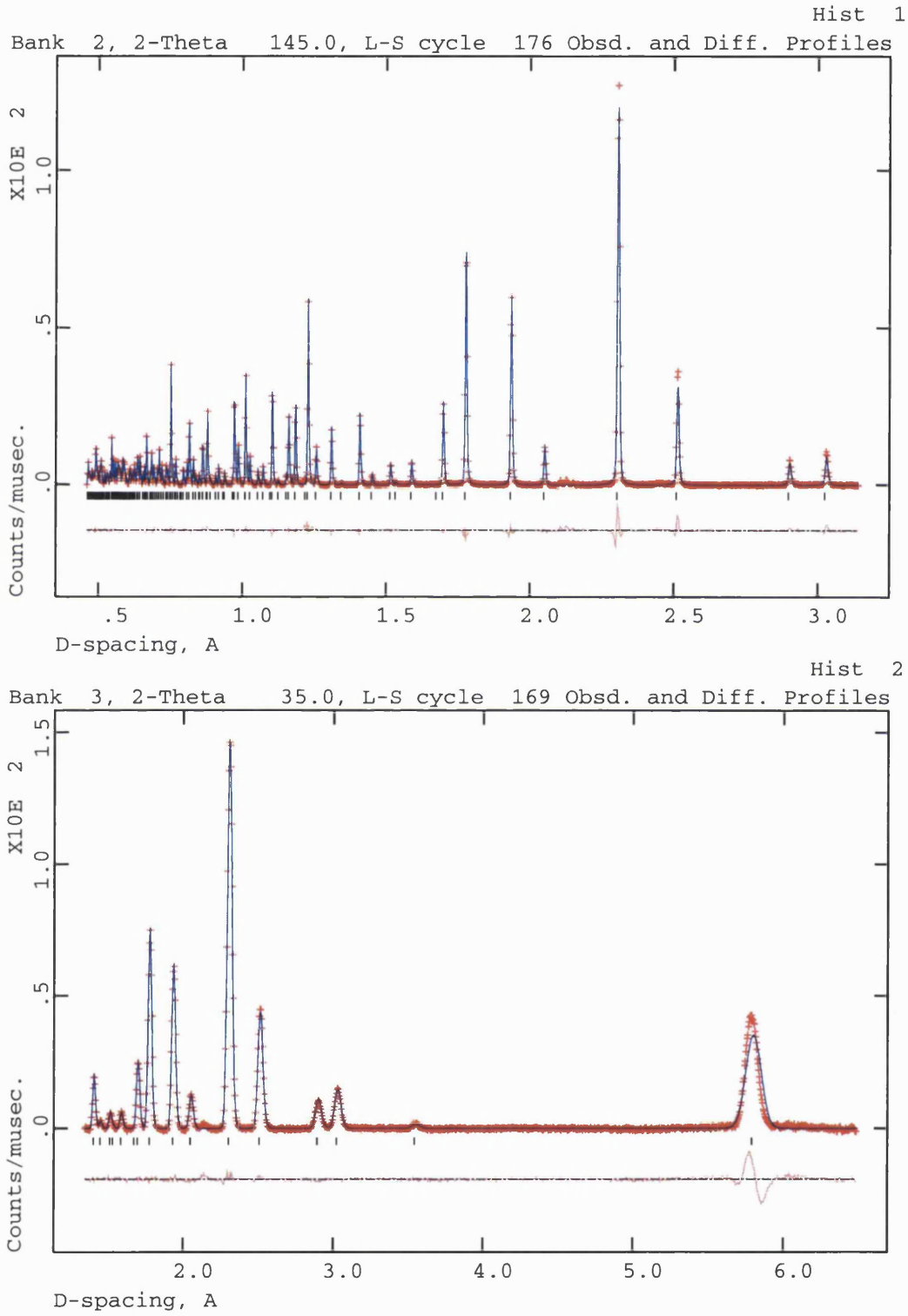

Figure 6.1: Refined profile for data collected from the C and A detector banks of the POLARIS instrument from $Er_2Ti_2O_7$ at 4.85 K

	A Bank	C Bank
a_o	10.03740(8)	10.04758(7)
$x(O_2)$	0.419326(54)	0.419820(34)
U_{iso}(Er)	0.01346(31)	0.00164(4)
U_{iso}(Ti)	0.00973(52)	0.00152(10)
U_{iso}(O)	0.01155(32)	0.00279(3)
Abs. Coeff.	0.36031(631)	0.32682(77)
R_{wp}	0.0136	0.0123
χ^2	3.735	24.81

Table 6.1: Refinement parameters of $Er_2Ti_2O_7$ at 4.85 K. A linear absorption correction was used [93] and the thermal parameters of the oxygen atoms were restricted to be the same. For the structural parameters see Appendix C.

6.2.3 Decomposition of the Magnetic Representation

$G_{\mathbf{k}}$ is defined as the little group of symmetry elements that leave the propagation vector $\mathbf{k}$ invariant. The magnetic representation, Γ_{Er}, of the Er site ($16c$ in $Fd\bar{3}m$, this is common for the majority of rare-earth titanates), can be decomposed in terms of the irreducible representations (IRs) of $G_{\mathbf{k}}$. These are listed in Table 6.2 along with their associated basis vectors. The application of $G_{\mathbf{k}}$ to the four Er positions of the tetrahedron of the asymmetric unit results in a single orbit. For these sites the decomposition of the magnetic representation Γ_{Er} is:

$$\Gamma_{Er} = 0\Gamma_1^{(1)} + 0\Gamma_2^{(1)} + 1\Gamma_3^{(1)} + 0\Gamma_4^{(1)} + 1\Gamma_5^{(2)} + 0\Gamma_6^{(2)} + 1\Gamma_7^{(3)} + 0\Gamma_8^{(3)} + 2\Gamma_9^{(3)} + 0\Gamma_{10}^{(3)}. \quad (6.1)$$

The basis vectors

Landau theory requires that only one representation can be involved in a critical transition, so with this constraint there are four possible magnetic structures in

IR	Basis Vector	Atom1			Atom 2			Atom 3			Atom 4		
		m_x	m_y	m_z	m_x	m_y	m_z	m_x	m_y	m_z	m_x	m_y	m_z
Γ_3	ψ_1	1	1	1	-1	-1	1	-1	1	-1	1	-1	-1
Γ_5	ψ_2	1	-1	0	-1	1	0	-1	-1	0	1	1	0
	ψ_3	1	1	-2	-1	-1	2	-1	1	2	1	-1	2
Γ_7	ψ_4	0	1	-1	0	1	1	0	-1	-1	0	-1	1
	ψ_5	-1	0	1	-1	0	-1	1	0	-1	1	0	1
	ψ_6	1	-1	0	-1	1	0	1	1	0	-1	-1	0
Γ_9	ψ_7	1	0	0	1	0	0	1	0	0	1	0	0
	ψ_8	0	1	1	0	1	-1	0	-1	1	0	-1	-1
	ψ_9	0	1	0	0	1	0	0	1	0	0	1	0
	ψ_{10}	1	0	1	1	0	-1	-1	0	-1	-1	0	1
	ψ_{11}	0	0	1	0	0	1	0	0	1	0	0	1
	ψ_{12}	1	1	0	-1	-1	0	1	-1	0	-1	1	0

Table 6.2: Non-zero IRs and associated basis vectors ψ_ν for the space group $Fd\bar{3}m$ with $\mathbf{k} = 0$ calculated using the program SARA*h*-Representational Analysis. [98, 97]. The labelling of the propagation vectors and the IRs follows the scheme of Kovalev [103].

which the system can order. These are discussed below with reference to visual representations of the most characteristic basis vectors (see Fig. 6.2).

Representation Γ_3 is one-dimensional, and corresponds directly to the FeF_3 ordered magnetic structure with all spins pointing into or out of the tetrahedron, along the easy-axes.

Representation Γ_5 is two dimensional and therefore the possible directions for one particular site will all be in a plane. In fact, linear combinations of ψ_2 and ψ_3 map out arrangements in which the spins are situated in the $\langle 111 \rangle$ planes of the tetrahedron. These are the easy-planes in the XY model that is expected to apply to $Er_2Ti_2O_7$.

Representation Γ_7 is three dimensional, and has associated with it three non-orthogonal basis vectors. Consequentially, linear combinations that involve non-zero contributions from more than one basis vector will describe configurations of spins with differing lengths. Therefore, given the assumption that all the moments of a given crystallographic site have equal length, as is typical for an insulator, only linear combinations which involve single basis vectors are of interest, *i.e.* ψ_4, ψ_5 or ψ_6. The moments associated with each of these basis vectors again lie in the $\langle 111 \rangle$ easy-planes of the XY-model. Each basis vector has been refined individually.

Representation Γ_9 is much more complicated. As in the case of Γ_7, the six basis vectors are not all orthogonal to one another. To simplify the refinement only orthogonal sets of basis vectors have been tested. There are three pairs of orthogonal vectors: ψ_7 ψ_8, ψ_9 ψ_{10} and ψ_{11} ψ_{12}. There is also one orthogonal triplet: ψ_7 ψ_9 ψ_{11}.

6.2.4 Analysis of the 50 mK data

As expected, new reflections were discovered below the transition temperature (1.2 K). The new magnetic Bragg reflections confirmed the suspicion that the ordering was of the **k**=000 type. A difference plot for the A Bank is shown in

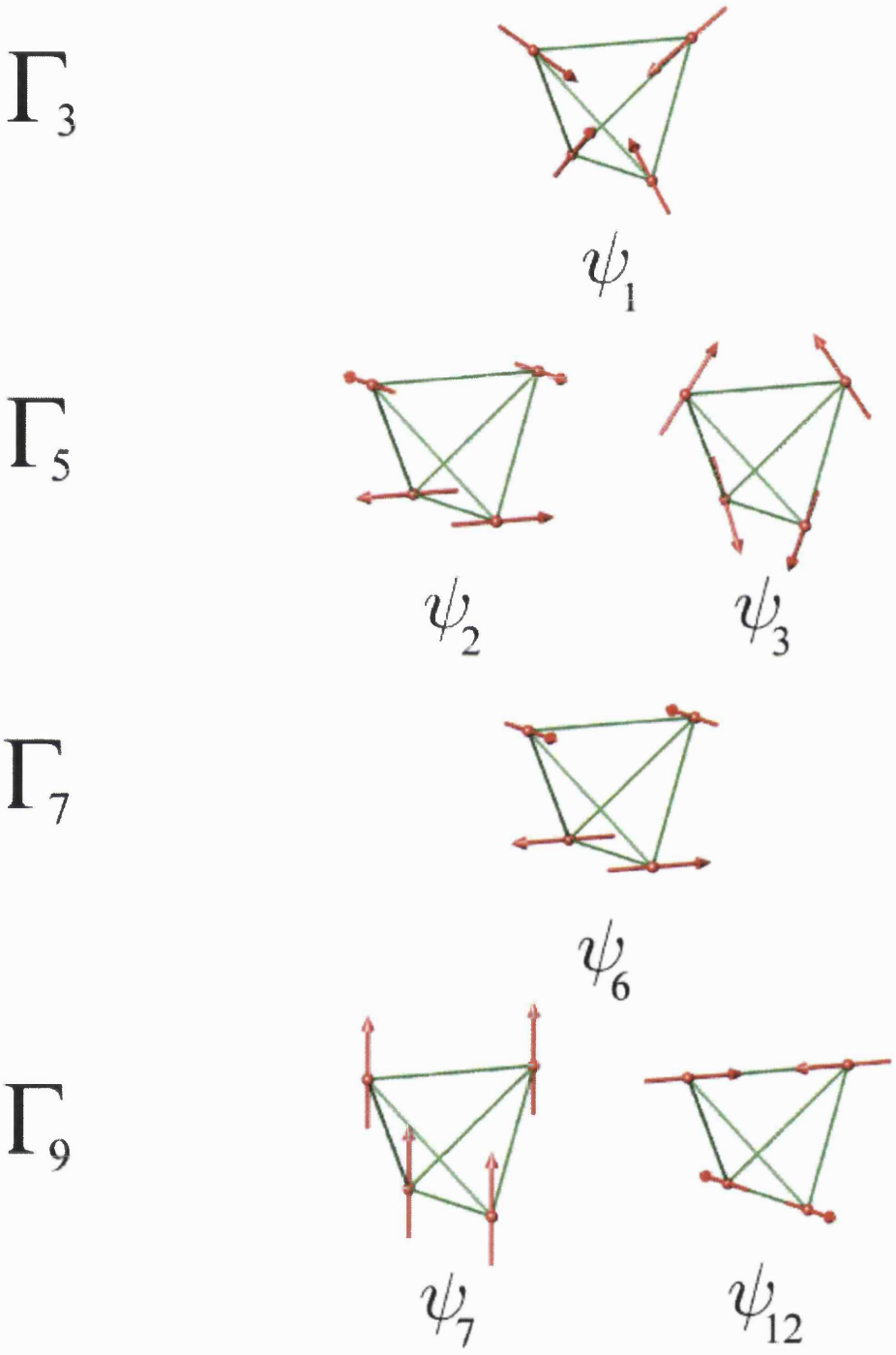

Figure 6.2: Graphical representation of the basis vectors listed in Table 6.2. The ψ_n not shown in the figure are identical arrangements, but are aligned along different axes.

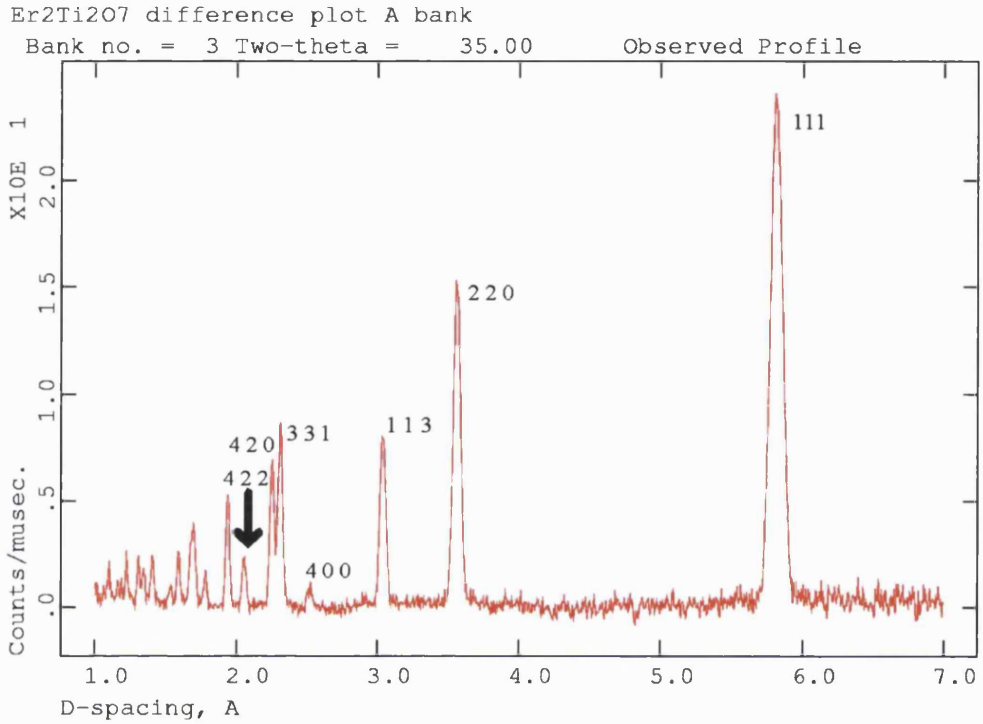

Figure 6.3: Magnetic diffraction pattern of $Er_2Ti_2O_7$, obtained by subtracting the high temperature scan (4.85 K) from the low temperature scan (50 mK). The low multiplicity magnetic Bragg peaks are indexed accordingly.

Fig. 6.3 to illustrate the new magnetic peaks observed. The strongest magnetic peaks are present in this part of the spectrum.

The refinement of the 4.85 K data was used as a starting point for the 50 mK data. Only the lattice and background parameters were varied for the system at lower temperature.

Magnetic structure factors were calculated using the GENLES routine of the GSAS suite [93], while the orientations of the magnetic moments were controlled and refined separately by the simulated annealing-based program SARA*h*–Refine for GSAS [98].

The basis vectors enumerated in section 6.2.2 were refined sequentially and the

		A Bank		C Bank	
IR	ψ_ν	χ^2	R_{wp}	χ^2	R_{wp}
Γ_3	ψ_1	13.07	0.0271	11.68	0.0424
Γ_5	ψ_2 ψ_3	4.462	0.0158	2.720	0.0205
Γ_7	ψ_4	24.30	0.0369	19.99	0.0116
	ψ_5	24.30	0.0369	19.99	0.0116
	ψ_6	24.30	0.0369	19.99	0.0116
Γ_9	$\psi_7\psi_8$	24.21	0.0369	20.56	0.0117
	ψ_9 ψ_{10}	24.21	0.0369	20.56	0.0117
	ψ_{11} ψ_{12}	24.21	0.0369	20.56	0.0117
	ψ_7 ψ_9 ψ_{11}	41.95	0.0485	32.75	0.0148

Table 6.3: Goodness of fit parameters χ^2 and R_{wp} for each of the possible combinations of IRs, for the data measured on the A and C detector banks of POLARIS.

χ^2 and R_{wp} values for each refinement are shown in Table 6.3. In the case of Γ_7 and Γ_9 the particular basis vector combinations are identified.

6.3 Conclusions

6.3.1 The Ordered Magnetic Structure

It is clear from the χ^2 values listed in Table 6.3 that Γ_5 is the only serious candidate for the magnetic structure of $Er_2Ti_2O_7$. It is noted that scattering was again observed at the [111] magnetic Bragg peak. This observation ruled out the second best structure, Γ_3, which has no such scattering [13]. The final refined profile is shown in Figure 6.4.

The system orders within representation Γ_5. It was found that every linear combination of ψ_2 and ψ_3 has the same value of χ^2, suggesting that the magnetic

scattering intensity is the same for all linear combinations of the basis vectors.

Powder neutron diffraction gives the average scattering over all crystallites in the sample. For a particular Bragg peak the magnetic structure factor

$$F_{magn}^{hkl} = -\frac{e^2\gamma}{mc^2}\sum_n S^{\perp} f_n \exp\{2\pi i\,(hx_n/a + ky_n/b + lz_n/c)\}, \qquad (6.2)$$

can be calculated, where $S^{\perp}$ is the resolved component of the spin vector on to the reflection plane [hkl] and f_n is the magnetic form factor. If F_{magn}^{hkl} is calculated for each magnetic Bragg peak and averaged over all magnetic domains (of a single crystal), the values remain constant for all linear combinations of ψ_2 and ψ_3. This confirms the refinement result observed.

6.3.2 The Ordered Magnetic Moment

At low temperatures the maximum observed magnetic moment by neutron diffraction is $g_J J$ [104]. For Er^{3+} this moment is $9\,\mu_B$. The refined value of the ordered moment of $Er_2Ti_2O_7$ is $3.01 \pm 0.05\,\mu_B$. This is only a third of the expected value.

In antiferromagnetic systems a reduced moment is often observed. This is due to zero-point quantum fluctuations, which are a general property of antiferromagnets [105, 106]. There is normally only a very small deviation from the expected value, as in the case of $Gd_2Ti_2O_7$ (see section 7.4). The large deviation observed in $Er_2Ti_2O_7$ is quite a remarkable observation and cannot be easily explained. Quantum fluctuations, exacerbated by frustration, might be playing a role in the system.

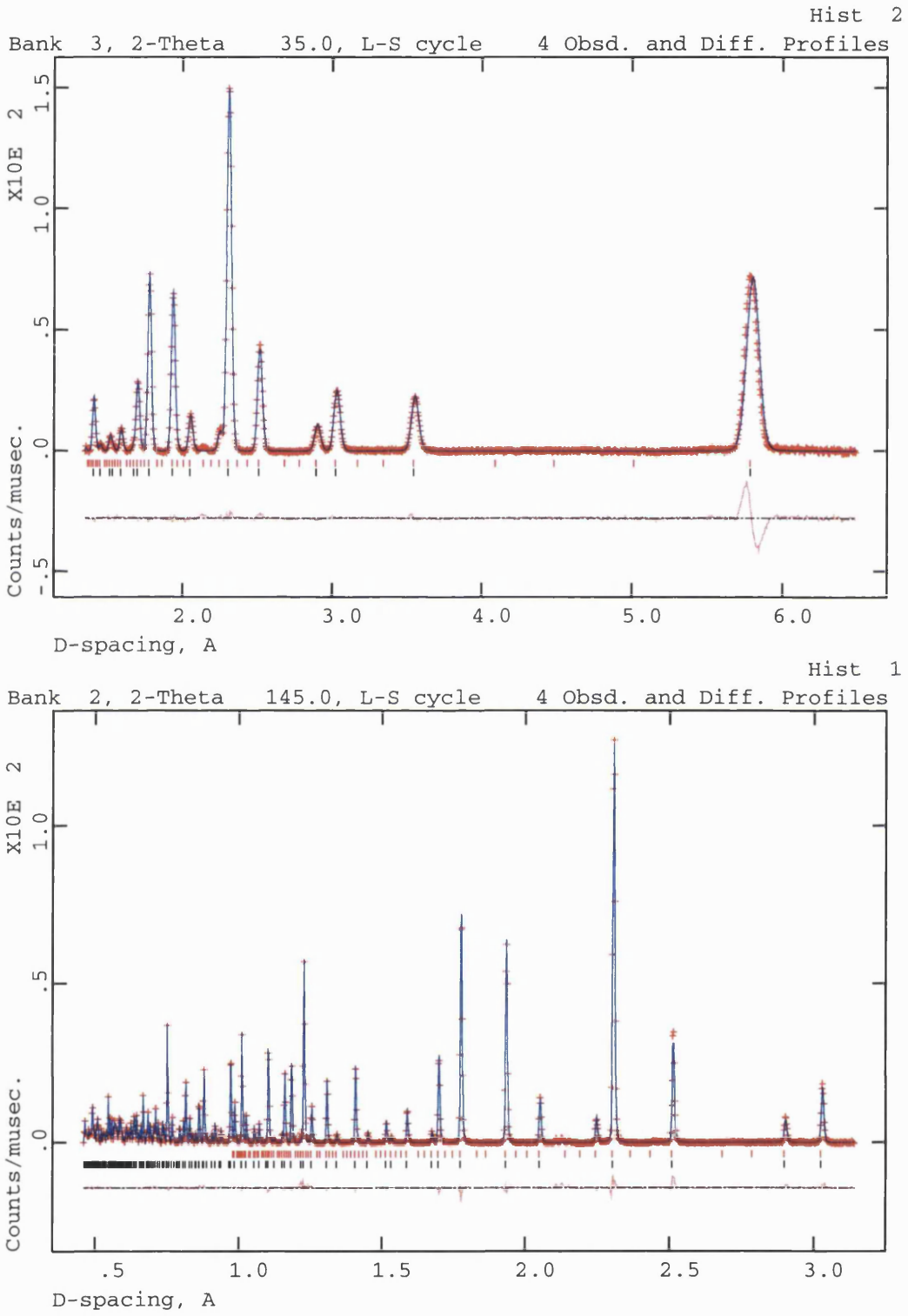

Figure 6.4: The final refined magnetic profiles for data collected from the A and C detector banks of the POLARIS instrument from $Er_2Ti_2O_7$ at 50 mK (nuclear reflections are marked by the lower line of ticks)

Chapter 7

Magnetic Structure of $Gd_2Ti_2O_7$

In this chapter, the low temperature properties of $Gd_2Ti_2O_7$ are discussed. This material is of great interest as it was expected to be an ideal first example of an Heisenberg pyrochlore antiferromagnet (see section 1.2.7). However, specific heat measurements disproved this supposition by showing a transition to an ordered state [37]. The aim of this work was to determine the magnetic structure of the ordered state.

Powder neutron diffraction experiments were performed on isotopically enriched $^{160}Gd_2Ti_2O_7$. In the first experiment, the sample showed signs of long-range magnetic order, but proved to be impure (see section 7.2). Therefore, the sample was re-annealed and the full magnetic structure was determined after a second experiment. Group theory was used to facilitate determination of the magnetic structure (see section 5.3).

The results presented in this chapter have been published in Ref. [107], the title of which lists the collaborators with whom this work was performed.

7.1 Previous Work on $Gd_2Ti_2O_7$

In section 1.2.7 various models of geometrically frustrated antiferromagnetism were introduced. The Heisenberg pyrochlore antiferromagnet was described as having a spin liquid ground state with an absence of order at $T = 0\ K$ [27, 35]. It also has an absence of any kind of order by disorder, unlike the Heisenberg kagomé antiferromagnet [24].

Experimental realisations of pyrochlore magnets have been found in the rare earth pyrochlore oxides, particularly the titanates, which have the general formula $Ln_2Ti_2O_7$ (see section 1.1). These systems have been of particular interest due to their well defined single-ion anisotropies e.g. $\langle 111 \rangle$ Ising ferromagnets (Ln = Ho or Dy) (see Chapter 8) and the $\langle 111 \rangle$ XY-antiferromagnet (Ln = Er) (see Chapter 6). In these materials, the anisotropies result from the very strong axial crystal electric field generated by the oxide environment of the rare earth site. Due to these crystal field effects, previous work on the isotropic pyrochlore antiferromagnet has focused on another crystal system, the fluoride pyrochlore $CsNiCrF_6$ [108]. Good comparisons were found between Monte Carlo simulation and single crystal neutron diffraction results. However, the use of $CsNiCrF_6$ as a model system is limited by the presence of a disorder on the (Ni, Cr) site.

$Gd_2Ti_2O_7$ has therefore attracted much interest from both experimentalists and theorists as a possible model Heisenberg antiferromagnet on the pyrochlore lattice because in this material the isotropic nature of the Gd^{3+} ion ($4f^7$, $L = 0$) prevents the crystal electric field from being important.

Confounding expectations, $Gd_2Ti_2O_7$ was found to have an ordering transition at 0.97 K, a temperature smaller than the Curie-Weiss temperature of 9.6 K [37], but not as small as in some frustrated systems. The transition was evinced by a peak in the specific heat, as shown in Figure 7.1. To understand this transition, two recent theoretical studies are particularly important, both of which developed the mean field theory approach of Reimers *et al.* [23]. The first, by Raju *et al.* [37],

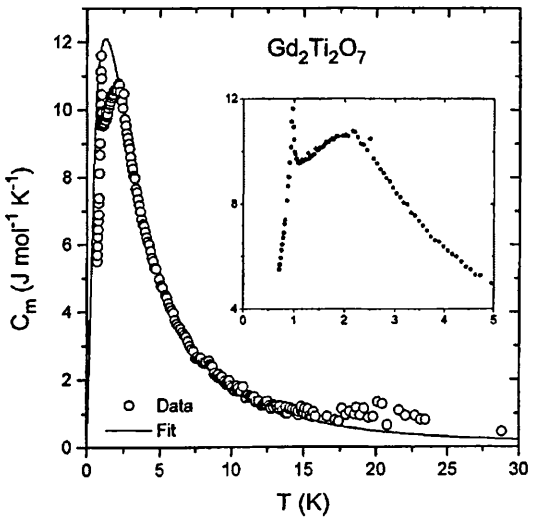

Figure 7.1: The ordering transition is evinced by a sharp peak in the magnetic specific heat C_m at $\sim 0.97\ K$ (after Raju *et al.*)

considered a Heisenberg antiferromagnet with dipolar coupling and showed that this does not completely lift the ground state degeneracy to second order in the expansion of the free energy, but rather stabilizes a degenerate set of periodic states with $h\ h\ h$ propagation vectors (where h is the Miller index). It was therefore suggested that the transition observed in $Gd_2Ti_2O_7$ might be provoked by thermal or quantum fluctuations, or alternatively by additional energy terms in the spin Hamiltonian. The second study, by Palmer and Chalker [100], in contrast, showed that the fourth order term in the free energy expansion would select, from the degenerate $h\ h\ h$ set, an ordered state with propagation vector $\mathbf{k} = 0$. These predictions are tested by the work described in this chapter.

7.2 Results of the First Experiment

Natural Gd is almost opaque to neutrons due to the high absorption cross section of ^{155}Gd and ^{157}Gd. Therefore, for neutron studies the ^{160}Gd isotope must be

used. Isotopically enriched $^{160}Gd_2Ti_2O_7$ was prepared from $^{160}Gd_2O_3$ and TiO_2 by J. Gardner. Stoichiometric quantities were mixed, ground, pressed into a pellet and fired at $\sim$ 1350 K for $\sim$ 60 hours. Powder neutron diffraction data were collected using the POLARIS high intensity diffractometer at the ISIS pulsed neutron facility (see section 5.5.1). The sample was contained in a vanadium can with a small amount of ^{4}He exchange gas. The can was mounted in an Oxford Instruments dilution refrigerator, and then placed in a cryostat. Data were collected for $\sim$ 9 hours at 1.5 K for $\sim$ 9 hours, above the ordering transition ($T_c \sim 0.97$ K), at intermediate temperatures between 1 K and 300 mK for $\sim$ 45 minutes and at 300 mK for $\sim$ 15 hours.

7.2.1 Analysis of the 1.5 K data

Refinement of the data taken at 1.5 K was performed using the GENLES routine of the GSAS Suite [93]. The optimum refined profile is shown in Fig. 7.2. The data were refined with two impurity phases: rutile (TiO_2) and Gd_2TiO_5.

TiO_2

The strongest rutile impurity peaks were observed specifically at the following *d*-spacings: 2.18, 2.30, 2.48 Å. In Figure 7.2 the nuclear reflections of the rutile phase are marked by the middle line of ticks.

Gd_2TiO_5

The strongest Gd_2TiO_5 impurity peaks were observed specifically at the following *d*-spacings: 3.37, 3.55, 4.75, 4.97, 7.63 Å. In Figure 7.2 the nuclear reflections of the Gd_2TiO_5 phase are marked by the top line of ticks.

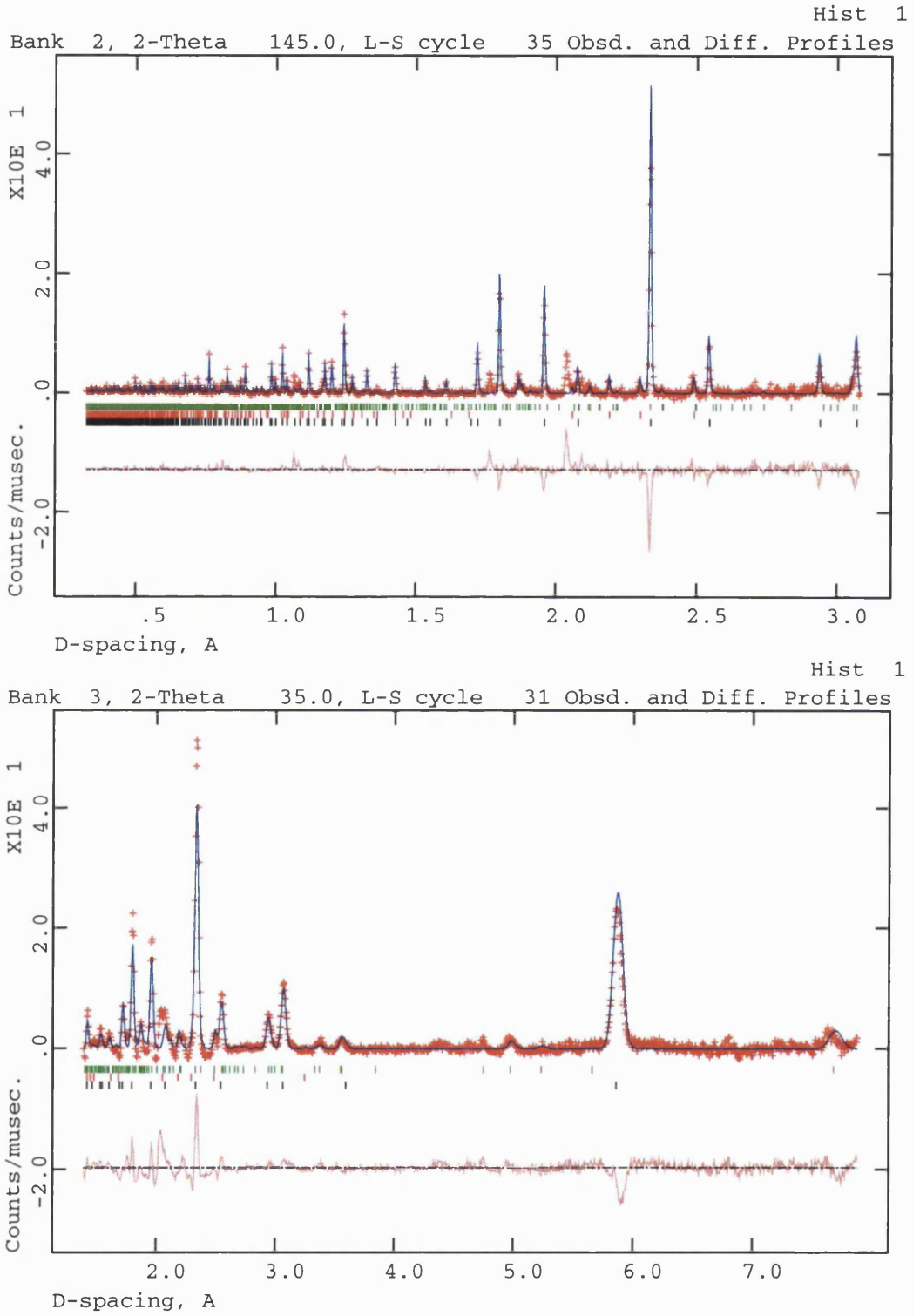

Figure 7.2: Refined profile for data collected from the C (top) and A (bottom) detector banks of the POLARIS instrument from $Gd_2Ti_2O_7$ at 1.5 K, before the sample was re-annealed (TiO_2 - middle row of ticks, Gd_2TiO_5 - top row of ticks).

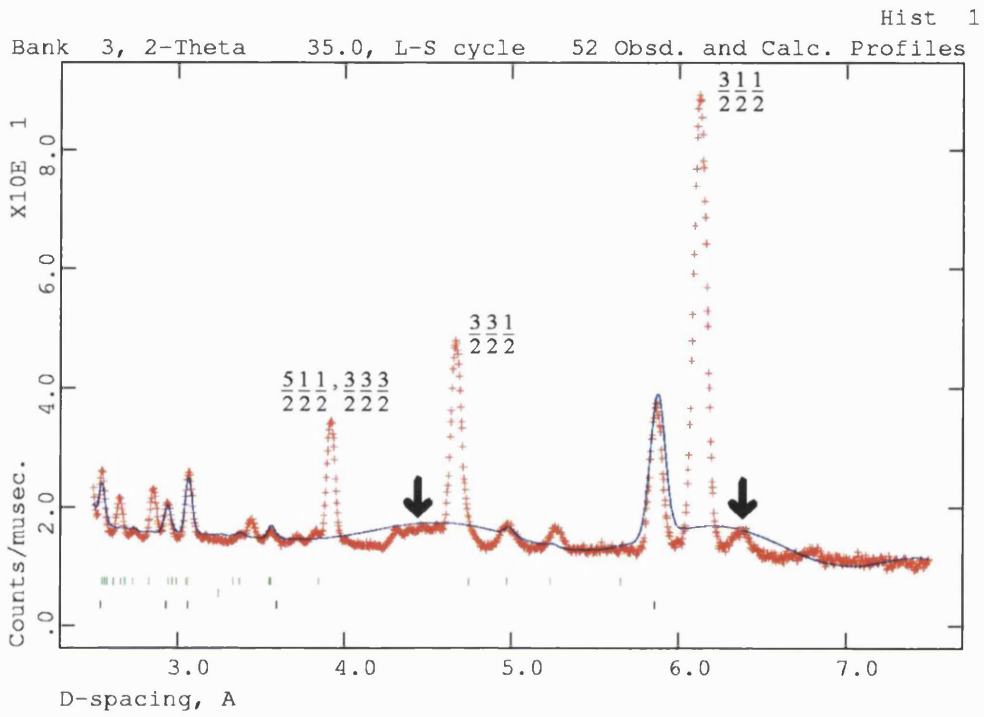

Figure 7.3: Diffraction pattern of $Gd_2Ti_2O_7$, taken at 300 mK from detector bank A. The low wave vector magnetic Bragg peaks are indexed accordingly and the black arrows show the magnetic impurity peaks.

7.2.2 Analysis of the 300 mK data

The low temperature data could still be utilised to good effect. New reflections were observed below T_c and the diffraction pattern is shown in Figure 7.3. This figure shows a section of data taken from detector bank A to illustrate the new reflections at d = 2.66, 2.86, 3.92, 4.67, 6.12 Å. These reflections can be indexed with a magnetic propagation vector of $\mathbf{k} = \frac{1}{2}\frac{1}{2}\frac{1}{2}$. Full refinement of these data proved to be difficult due to the impurities in the sample. Figure 7.3 also illustrates magnetic impurity peaks such as those at d = 4.3-4.6, 6.37 Å. These peaks impaired proper refinement of the ordered magnetic structure.

7.3 Experimental Results: Re-annealed Sample

In view of the above results, it was decided to re-anneal the sample for another $\sim$ 48 hours at 1350 K. This was carried out by T. Fennell. The conditions of the neutron experiment with the annealed sample were slightly different from those described in section 7.2. Data were collected for 17 hours above and below the ordering transition at 5 K, 500 mK and 50 mK.

The sample was contained in a vanadium can with a small amount of ^{4}He exchange gas. The can was mounted in an Oxford Instruments dilution refrigerator, and then placed in a cryostat. ^{3}He exchange gas was introduced into the Inner Vacuum Chamber (IVC) of the cryostat to maintain stability of the dilution refrigerator.

7.3.1 Analysis of the 5 K data

In this experiment, the nuclear pattern of the re-annealed sample did not contain any of the impurity peaks described in section 7.2.1. The pattern could be easily refined and the fits are shown in Fig. 7.4. Details of the refinement results are shown in Table 7.1.

7.3.2 Representational Analysis

The new peaks appearing below 1 K could again be indexed with a $\mathbf{k} = \frac{1}{2}\frac{1}{2}\frac{1}{2}$ propagation vector. In section 5.3 the theoretical basis of group theory applied to magnetic structures was outlined. In this section it is applied to the case of $\mathbf{k} = \frac{1}{2}\frac{1}{2}\frac{1}{2}$ propagation vector, for the spins on the 16*c* sites of the $Fd\bar{3}m$ space group.

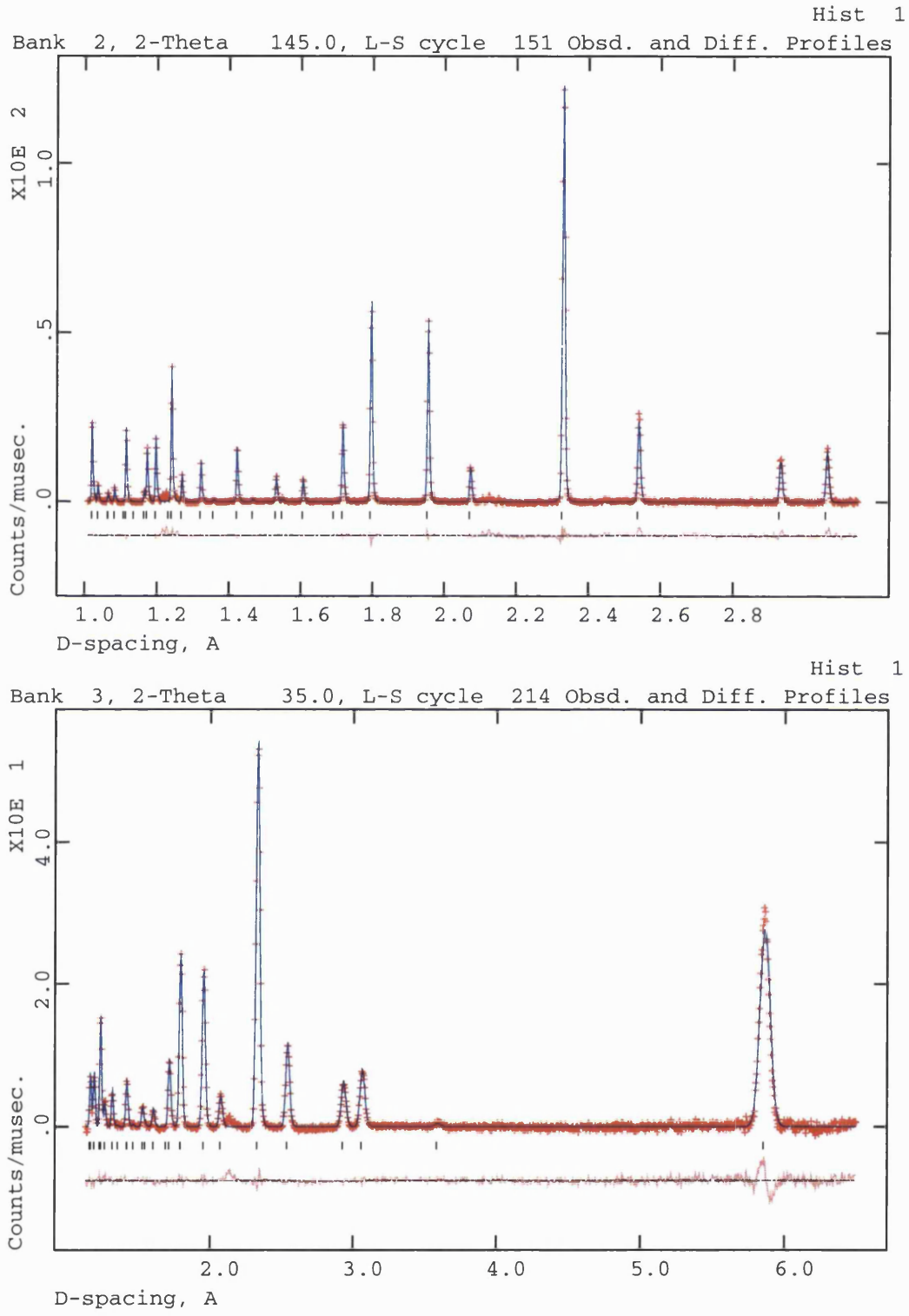

Figure 7.4: Refined profile for data collected from the C and A detector banks of the POLARIS instrument from $Gd_2Ti_2O_7$ at 4.85 K

	A Bank	C Bank
a_o	10.15185	10.15185(4)
$x(O_2)$	0.422078(73)	0.422555(79)
U_{iso}(Gd)	0.00172(38)	0.0008(28)
U_{iso}	0.00154(77)	0.00014(51)
U_{iso}(O)	0.00158(30)	0.00102(26)
Abs. Coeff.	0.08174(375)	0.18083(253)
R_{wp}	0.0181	0.0191
χ^2	2.072	7.195

Table 7.1: Refinement parameters of $Gd_2Ti_2O_7$ at 4.85 K. A linear absorption correction was used [93] and the thermal parameters of the oxygen atoms were restricted to be the same. The lattice parameter for the A Bank was constrained to be the same as that of the C Bank (due to the C Bank's higher resolution). For the structural parameters see Appendix C.

Decomposition of the magnetic representation and the basis vectors

The non-zero Irreducible Representations (IRs) in the decomposition of the magnetic representation Γ_{Gd}, and their associated basis vectors ψ_ν are given in Table 7.2. The labeling of the propagation vectors and the IRs follows the scheme used by Kovalev in his tabulated works [103].

$G_{\mathbf{k}}$ is defined as the little group of symmetry elements that leave the propagation vector $\mathbf{k}$ invariant. The magnetic representation, Γ_{Gd}, of the Gd site (16*c* in $Fd\bar{3}m$), can be decomposed in terms of the irreducible representations (IRs) of $G_{\mathbf{k}}$. These are listed in Table 7.2 along with their associated basis vectors. The application of $G_{\mathbf{k}}$ to the four Gd positions of the tetrahedron of the asymmetric unit results in two orbits. When applied to $0,0,0$ it generates only the position $0,0,0$ — orbit 1. When applied to another seed position, say $\frac{3}{4},\frac{1}{4},\frac{1}{2}$, it generates the remaining 16*c* sites: $\frac{3}{4},\frac{1}{4},\frac{1}{2}$ $\frac{1}{4},\frac{1}{2},\frac{3}{4}$ and $\frac{1}{2},\frac{3}{4},\frac{1}{4}$ — orbit 2.

These two orbits can be understood in terms of a description of the pyrochlore lattice as a set of two dimensional kagomé lattice sheets (the (1 1 1) planes) decorated by interstitial spins which serve to link the sheets. These form 'up' and 'down' pointing corner-sharing tetrahedra. If the lattice is described in this way, then orbit 2 describes the three atoms that make up the triangular motif of a particular kagomé sheet and orbit 1 is the unique atom present in the interstitial site. The decomposition of the magnetic representation Γ_{Gd} for orbits 1 and 2 are:

$$\begin{aligned}\Gamma_{Gd}^{orbit1} &= 0\Gamma_1^{(1)} + 0\Gamma_2^{(1)} + 1\Gamma_3^{(1)} + 0\Gamma_4^{(1)} + 1\Gamma_5^{(2)} + 0\Gamma_6^{(2)} \\ \Gamma_{Gd}^{orbit2} &= 0\Gamma_1^{(1)} + 2\Gamma_2^{(1)} + 0\Gamma_3^{(1)} + 1\Gamma_4^{(1)} + 0\Gamma_5^{(2)} + 3\Gamma_6^{(2)}. \end{aligned} \quad (7.1)$$

Landau theory states that the magnetic ordering transition in a system with only terms of order 2 in the Hamiltonian can involve only one IR becoming critical. Therefore, the basis vectors involved in the resulting structure are limited to those associated with a single IR. This allows all the degrees of freedom of a magnetic structure to be split into distinct symmetry-allowed models, with in general only a

Orbit 1:					Orbit 2:										
IR	BV	Atom 1			IR	BV	Atom 2			Atom 3			Atom 4		
		m_x	m_y	m_z			m_x	m_y	m_z	m_x	m_y	m_z	m_x	m_y	m_z
Γ_3	ψ_1	1	1	1	Γ_2	ψ_4	1	1	0	0	1	1	1	0	1
Γ_5	ψ_2	1	$\bar{1}$	0		ψ_5	0	0	1	1	0	0	0	1	0
	ψ_3	1	1	$\bar{2}$	Γ_4	ψ_6	1	$\bar{1}$	0	0	1	$\bar{1}$	$\bar{1}$	0	1
					Γ_6	ψ_7	1	1	0	0	$\bar{1}$	$\bar{1}$	$\bar{1}$	0	$\bar{1}$
						ψ_8	0	0	1	$\bar{1}$	0	0	0	$\bar{1}$	0
						ψ_9	0	0	0	0	$\bar{1}$	1	$\bar{1}$	0	1

Table 7.2: Non-zero IRs and associated basis vectors ψ_ν for the space group $Fd\bar{3}m$ with $\mathbf{k} = \frac{1}{2}\frac{1}{2}\frac{1}{2}$ calculated using the program SARA*h*-Representational Analysis. [98, 97]. The labelling of the propagation vectors and the IRs follows the scheme of Kovalev [103].

few variables involved in each. Thus, the determination of a magnetic structure is reduced to the sequential testing of the basis vectors associated with the different non-zero IRs. In the case of systems with atoms on several Bravais lattices, or when orbits are present within one Bravais lattice, Landau theory states that the same IR should be responsible for ordering of the different atoms. As the same IRs are not present in the decomposition of Γ_{Gd} on the different sites, the only restriction that symmetry affords in the present case is the constraint that each site or orbit orders under a single IR. There are therefore six possible permutations of IRs between the two orbits that need to be tested against the experimental data.

7.3.3 Analysis of the 50 mK data

The refinement of the 5 K data was used as a starting point for the 50 mK data. Only the lattice and background parameters were varied for the system at lower temperature.

Magnetic structure factors were calculated using the GENLES routine of the GSAS suite [93], while the orientations of the magnetic moments were controlled and refined separately by the simulated annealing-based program SARA*h*–Refine for GSAS [98]. The six permutations discussed in section 7.3.2 were refined sequentially and the χ^2 and R_{wp} values for each refinement are shown in Table 7.3.

7.3.4 Possible Magnetic Structures

It is clear that, among the six possibilities, there are only two candidates for the magnetic structure; all the other combinations can be immediately discarded. These candidate structures are referred to as (i) and (ii), see Table 7.3.

While both involve the basis vector ψ_6 for orbit 2, they differ in that, for orbit 1, structure (i) involves ψ_1 while structure (ii) involves the two basis vectors ψ_2 and ψ_3. The basis vector ψ_6, which refers to the kagomé planes, in fact corresponds to

Label	Orbit		A Bank		C Bank	
	1	2	χ^2	R_{wp}	χ^2	R_{wp}
	Γ_3	Γ_2	43.44	0.0876	11.68	0.0424
(i)	Γ_3	Γ_4	3.844	0.0261	2.720	0.0205
	Γ_3	Γ_6	13.17	0.0483	5.168	0.0282
	Γ_5	Γ_2	40.76	0.0849	11.62	0.0423
(ii)	Γ_5	Γ_4	2.838	0.0224	2.494	0.0196
	Γ_5	Γ_6	11.66	0.0454	4.957	0.0276
(iii)	0	Γ_4	2.977	0.0229	2.186	0.0184

Table 7.3: Goodness of fit parameters χ^2 and R_{wp} for each of the six alternative combinations of IRs, for the data measured on the A and C detector banks of POLARIS. The last line indicates the fit that considers ordering only in orbit 2. The IRs corresponding to models (i), (ii) and (iii) are indicated.

the 'q=0' spin structure observed in ordered kagomé antiferromagnets [109] (see also section 1.2.7). For the interstitial site, structure (i), with the basis vector ψ_1, corresponds to a spin pointing parallel to the [111] direction which is perpendicular to the kagomé plane. Structure (ii), with basis vectors ψ_2 and ψ_3, corresponds to a spin lying with any orientation in a plane parallel to the kagomé sheet. It is noted that powder neutron diffraction cannot distinguish the absolute orientation of the spins in this plane. Three dimensional visualizations of the two possible structures are shown in Fig. 7.5. In both cases (i) and (ii) the interstitial spins are ferromagnetically aligned within their planes, and alternating planes are antiferromagnetically aligned.

Both structures (i) and (ii) fit well to the data, but there is an important difference at $d \approx 3.1$ Å (see Fig. 7.5). Here, structure (i) predicts more intensity than structure (ii), while experiment suggests that the reflections at this d-spacing

(for example $\frac{3}{2}, \frac{3}{2}, \frac{5}{2}$) are systematically absent. Thus neither structures (i) nor (ii) are satisfactory. A further fit was made which assigned zero moment to the interstitial site, structure (iii). This is plausible, since a planar antiferromagnetic structure on the kagomé sheets gives a zero mean field at the interstitial site.

Structure (iii), with zero interstitial moment was found to improve the fit to experiment by, most importantly, removing the peak at 3.1 Å (see Fig. 7.5). It is therefore concluded that structure (iii), with zero interstitial moment, is fully consistent with the experimental data. It should be noted that the current diffraction experiment cannot shed any light on whether the fourth moment is zero as a result of static or fluctuating disorder. The final refined profile is shown in Fig. 7.6 and goodness of fit parameters are listed in Table 7.3.

7.4 Discussion

In high symmetry crystals powder neutron diffraction does not give an unambiguous determination of the magnetic structure, because there is always the possibility of a multi-k structure. In the present case, multi-k structures can be formed by contributions from any of the four equivalent arms of the star of $\mathbf{k}$. However, recent investigations of $Gd_2Ti_2O_7$ by Mössbauer spectroscopy [110] suggest that all the magnetic spins lie in planes perpendicular to the [111] direction below the ordering temperature. ESR measurements on the system above T_c have also indicated that the spins lie preferentially in the (111) plane [111]. These observations rule out a multi-k structure as the latter would always have a finite spin component parallel to [111].

The result that $\mathbf{k} = \frac{1}{2}\frac{1}{2}\frac{1}{2}$ agrees with the prediction of Raju *et al.* [37]. These authors considered a dipolar Heisenberg Hamiltonian with coupling parameters appropriate to $Gd_2Ti_2O_7$. They showed that, to quadratic order in the Landau expansion of the free energy, the ground state consisted of a degenerate manifold of

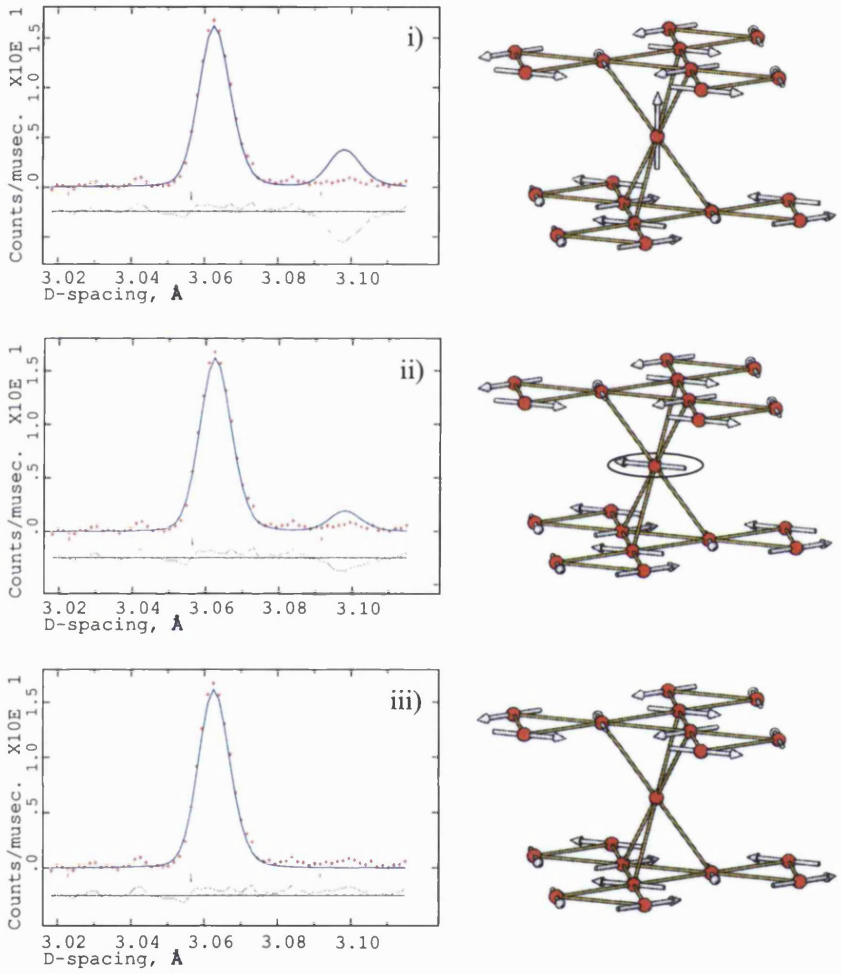

Figure 7.5: The intensity of the magnetic reflection as a function of the different structural models (i), (ii), (iii) defined in the text, for the spin at position $(0, 0, 0)$.

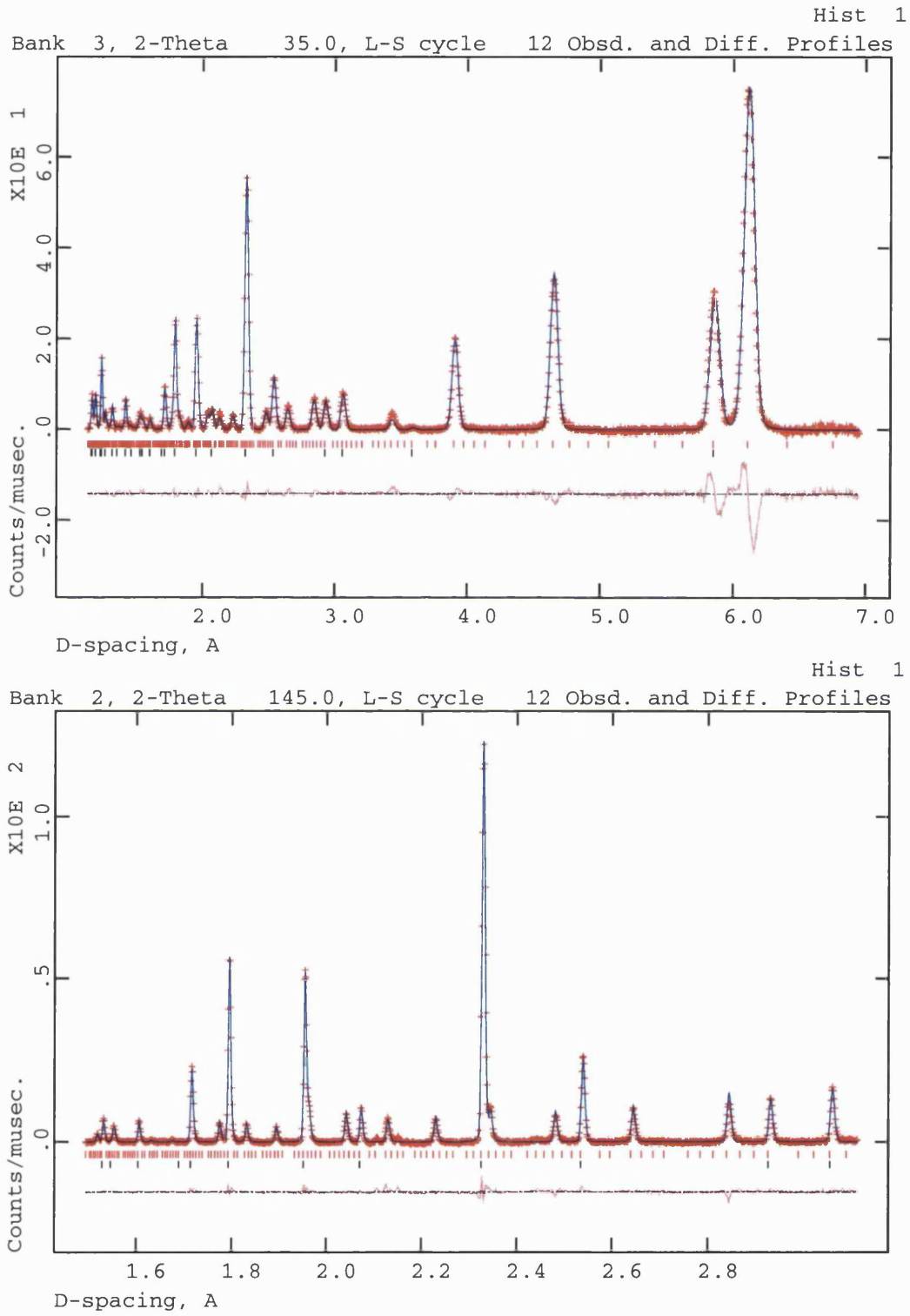

Figure 7.6: The final refined magnetic profiles for data collected from the A and C detector banks of the POLARIS instrument from $Gd_2Ti_2O_7$ at 50 mK (nuclear reflections are marked by the lower line of ticks)

magnetic structures with $h\ h\ h$ propagation vectors. It was therefore suggested that thermal or quantum fluctuations, or additional terms in the Hamiltonian, might operate to select a single ordered state in the real material, with one particular value of h. Palmer and Chalker extended this calculation to the fourth order term, and found it to be minimised by setting moments of equal magnitudes on each site of the elementary tetrahedron. A general state was constructed by combining three basis vectors of the type ψ_6 (in our notation). Each of these basis vectors has three coplanar and one zero moment, as described above, but differ in the choice of $\langle 1\ 1\ 1 \rangle$ plane. The condition of equal moments was found to restrict the possibilities to a single ground state with $h = 0$, with the four spins in a $\langle 1\ 0\ 0 \rangle$ plane, contrary to the findings presented here.

There are two possible explanations for the disagreement between experiment and theory. The first is that the real material has additional terms in the spin Hamiltonian, such as further neighbour exchange, that overcome the fourth order terms in the free energy expansion. The influence of such terms was considered in a rather general sense by Reimers *et al.* [23] and it would be interesting to develop the latter study in the present context. From an experimental perspective, the Hamiltonian could be investigated by studying relatives of $Gd_2Ti_2O_7$ such as $Gd_2Sn_2O_7$ and Gd_2SbGaO_7, where additional energy terms might have a different weighting. The second, and perhaps more intriguing explanation, is that quantum fluctuations, neglected in the classical theory, play a role in determining the ordering pattern. However, the refined value of the ordered moment of $Gd_2Ti_2O_7$ is $6.73 \pm 0.05\,\mu_B$, which is comparable with the maximum expected value of $7.0\,\mu_B$ [104]. This suggests that quantum mechanical fluctuations out of the ground state are not very important in this spin $S = \frac{7}{2}$ system.

Chapter 8

Single Crystal Neutron Scattering Studies

This chapter describes further experiments on $Ho_2Ti_2O_7$ and $Dy_2Ti_2O_7$. They are presented only for completeness, since this work is not the main focus of the thesis. The results are nonetheless important, and have been included to present a fuller picture of the understanding of spin ice materials.

These investigations described here were performed in collaboration with the following people: T. Fennell, S. T. Bramwell, M. J. Harris, B. C. den Hertog, M. J. P. Gingras, J. S. Gardner, D. F. McMorrow, A. R. Wildes, A. L. Cornelius, R. G. Melko, B. Fåk and O.Petrenko, who also performed the majority of the data analysis.

Single crystal neutron scattering studies have been performed on two of the rare-earth titanates: $Ho_2Ti_2O_7$ and $Dy_2Ti_2O_7$. In both cases neutron scattering was carried out at the ISIS facility on the indirect geometry spectrometer PRISMA (see section 5.5.2). The spectrometer was configured in the diffraction mode so that sixteen ^3He tube detectors were used simultaneously. Rotation of the crystal in question allowed a rapid mapping of a large section of reciprocal space.

8.1 Scattering Picture of $Ho_2Ti_2O_7$

The diffuse magnetic scattering from a flux grown single crystal of $Ho_2Ti_2O_7$ was measured. The crystal was oriented with $[1\bar{1}0]$ vertical such that the (hhl) scattering plane included the three principal symmetry axes [100], [110] and [111]. Figure 8.1(a) shows the scattering pattern at $T \sim 50$ mK.

One of the main features of these data is the intense scattering around $0, 0, 0$. Diffuse scattering is also observed around $0, 0, 3$ with a broader region of slightly weaker scattering around $\frac{3}{2}, \frac{3}{2}, \frac{3}{2}$. The width of the intense regions indicates short-range correlations on the order of one lattice spacing. Qualitative agreement with the scattering of ice is observed [112].

The nearest neighbour model of spin ice has been shown to be a relatively good model of $Ho_2Ti_2O_7$ through comparison of the inverse susceptibility, and field-induced ordered states [11, 15] (see section 1.1). Figure 8.1(b) shows the calculated neutron scattering $S(\mathbf{q})$ of the nearest neighbour spin ice model defined:

$$S(\mathbf{q}) \propto |f(q)|^2 \frac{1}{N} \sum_{ij} e^{i\mathbf{q}\cdot(\mathbf{r_i}-\mathbf{r_j})} \langle \mathbf{S}^{z_i}_{i,\perp} \cdot \mathbf{S}^{z_j}_{j,\perp} \rangle. \tag{8.1}$$

$z_i = \langle 111 \rangle$ denotes the associated easy-axis of each ith spin, $\langle \ldots \rangle$ denotes a thermal average and $\mathbf{S}^{z_i}_{i,\perp}$ is the spin component at site i perpendicular to $\mathbf{q}$.

Figure 8.1(b) successfully reproduces the main features of Figure 8.1(a), the main differences being in the extension of the scattering along $[hhh]$ from $0, 0, 0$ absent in Figure 8.1(a). The scattering at $\frac{3}{2}, \frac{3}{2}, \frac{3}{2}$ is more localised than Figure 8.1(a) which is spread out more along the diagonal directions.

It has been suggested that a better model for $Ho_2Ti_2O_7$ is one with dipolar interactions [42, 43, 44] (see also section 1.3.2) with the Hamiltonian:

$$\begin{aligned} H &= -J \sum_{\langle ij \rangle} \mathbf{S}^{z_i}_i \cdot \mathbf{S}^{z_j}_j \\ &+ D r^3_{\mathrm{nn}} \sum_{i>j} \frac{\mathbf{S}^{z_i}_i \cdot \mathbf{S}^{z_j}_j}{|\mathbf{r}_{ij}|^3} - \frac{3(\mathbf{S}^{z_i}_i \cdot \mathbf{r}_{ij})(\mathbf{S}^{z_j}_j \cdot \mathbf{r}_{ij})}{|\mathbf{r}_{ij}|^5}, \end{aligned} \tag{8.2}$$

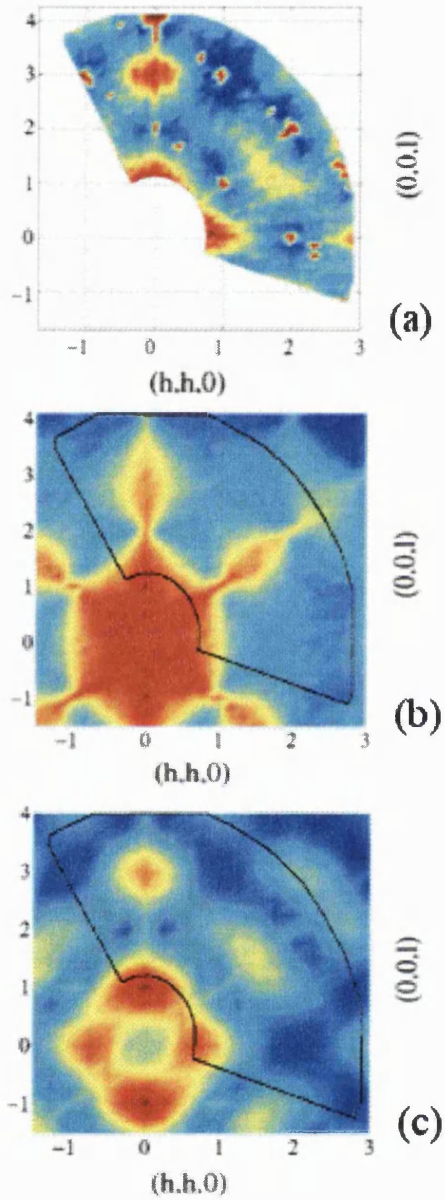

Figure 8.1: (a) Experimental neutron scattering pattern of $Ho_2Ti_2O_7$ in the (hhl) plane of reciprocal space at $T \sim 50$ mK. Dark blue shows the lowest intensity level, red-brown the highest. Temperature dependent measurements have shown that the sharp diffraction spots in the experimental pattern are nuclear Bragg peaks with no magnetic component. (b) $S(\mathbf{q})$ for the nearest neighbor spin ice model at $T = 0.15J$. (c) $S(\mathbf{q})$ for the dipolar spin ice model at $T = 0.6$ K. The areas defined by the solid lines denote the experimental data region of (a).

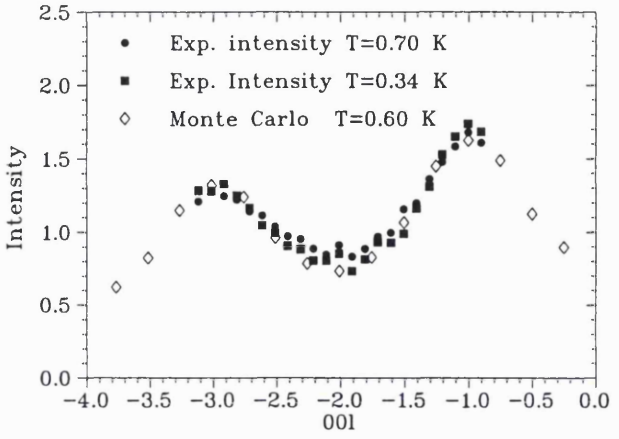

Figure 8.2: Experimental neutron scattering intensity of $Ho_2Ti_2O_7$ (filled symbols) along the (00l) direction of reciprocal space. For quantitative comparison is the intensity (open symbols) obtained from Monte Carlo simulation of the dipolar spin ice model with $J_{nn} = -0.52$ K and $D_{nn} = 2.35$ K.

where Ising spins $\mathbf{S}_i^{z_i}$ of unit length are constrained to their local $z_i = \langle 111 \rangle$ axes; J is a near neighbour exchange coupling and D the dipolar coupling. Because of the local Ising axes the effective nearest neighbour energy scales are $J_{nn} \equiv J/3$ and $D_{nn} \equiv 5D/3$ [44].

Specific heat measurements had previously only been used to compare the dipolar model with experiment. Figure 8.1(c) shows the calculated neutron scattering for the dipolar model (Eqn. (8.1)) with single spin-flip dynamics. The agreement between the theoretical and experimental results is striking, particularly in the shape of the four intense regions around $0, 0, 0$ and the spread of the broad features along the diagonal.

Quantitative comparisons of the measured scattering intensity have also been made with theoretical simulations of the dipolar spin ice model [17] (see Fig. 8.2). Again the agreement is remarkable confirming the applicability of the dipolar spin ice model to the properties of $Ho_2Ti_2O_7$.

All the experimental and theoretical results referred to in this section have been

published in Ref. [17].

8.2 Scattering Picture of $Dy_2Ti_2O_7$

The absorption cross section of natural Dysprosium is $\sigma_a = 994$ barn, the large value being due mainly to the presence of ^{164}Dy. Isotopically enriched Dy_2O_3 with composition ^{156}Dy< 0.01%, ^{158}Dy< 0.01%,^{160}Dy= 0.02%, ^{161}Dy= 0.47%, ^{162}Dy= 96.8%,^{163}Dy= 2.21% and ^{164}Dy= 0.5% was prepared by Goss Scientific Instruments Ltd. Enrichment in ^{162}Dy was considered optimum as it has a high abundance and the dominant impurity is ^{163}Dy which has a slightly lower absorption cross section. Enrichment in ^{163}Dy would have led to ^{164}Dy as the dominant impurity. Through enrichment, the absorption cross section was reduced by a factor of five to 208 ± 13 barn.

A single crystal of $Dy_2Ti_2O_7$ was prepared from the isotopically enriched Dy_2O_3 and TiO_2 by the floating zone technique [113].

Diffuse magnetic scattering was measured at 270 mK in a zero field on the PRISMA spectrometer at ISIS. The scattering map of the (*hhl*) plane was again recorded (see Fig. 8.3). All areas of diffuse scattering seem to be connected, with predominantly less scattering around the structural Bragg peaks.

There is qualitative agreement of Figure 8.3 with Figure 8.1(a), with common areas of diffuse scattering, but the diffuse scattering in Figure 8.3 seems to be more connected.

When a field was applied along the [100] direction all diffuse scattering disappeared and magnetic Bragg peaks were observed in the q=0 positions such as $2,0,0$ $1,1,1$ and $2,2,0$ [11].

When the field was applied along the $[1\bar{1}0]$ direction, magnetic Bragg peaks were again observed consistent with a q=0 structure. In this case the diffuse scattering of Fig. 8.3 developed into localised features at points such as $3,3,0$ and

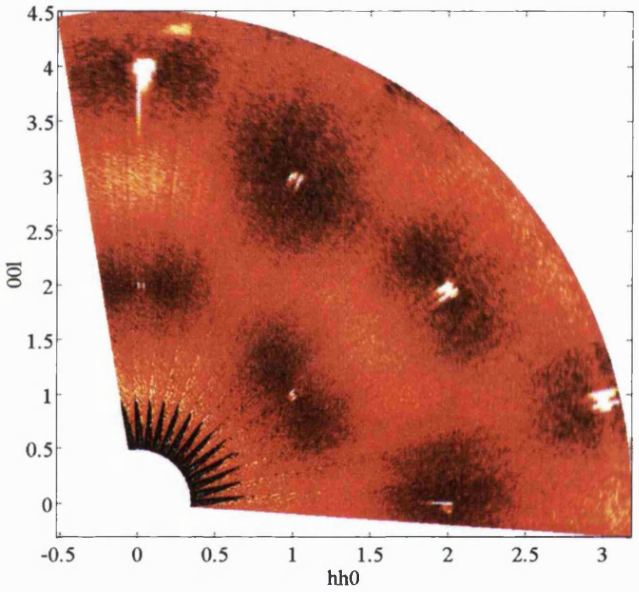

Figure 8.3: Diffuse scattering of $Dy_2Ti_2O_7$ in the (hhl) plane. In zero field at 270 mK no magnetic Bragg peaks are observed. All resolution limited intense features are of nuclear origin. Black shows the lowest intensity level, white the highest. Diffuse scattering is shown in red.

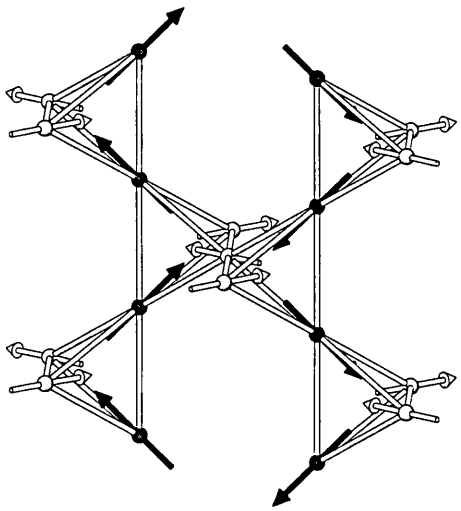

Figure 8.4: A fragment of the pyrochlore lattice illustrating the q=X structure.

1, 1, 2 , consistent with a q=X structure [11] (see Figure 8.5).

A graphical representation of the q=X structure is shown in Figure 8.4. The applied field is projected into the plane of the page and pins the unshaded spins into ferromagnetic chains. The shaded spins in the vertical rods are not coupled to the field but *are* governed by the 'ice-rules'. The shaded spins may form two structures, either q=0 with all shaded spin chains parallel or q=X with shaded spin chains anti-parallel. This degeneracy is not raised by the field. This explains the coexistence of the q=0 structure and the q=X structure in the applied field. When the field is applied along the [100] direction all the spins are coupled with the magnetic field and only the q=0 structure is formed [40].

All the experimental results in this section are taken from Ref. [114].

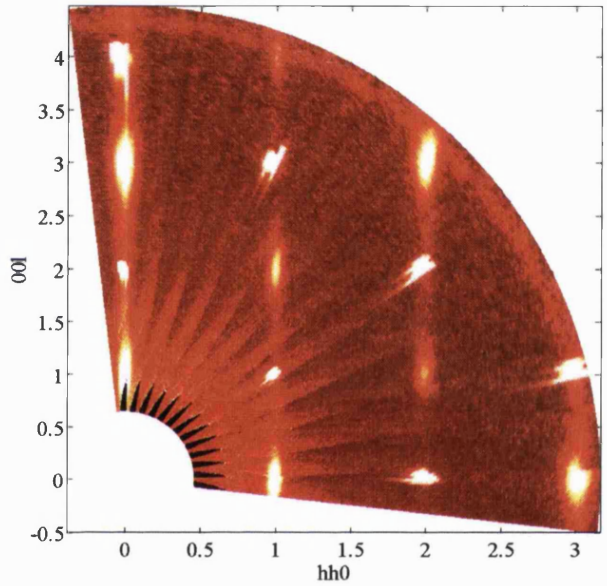

Figure 8.5: Diffuse scattering of $Dy_2Ti_2O_7$ in the (hhl) plane with a field of 1.5T applied on $[1\bar{1}0]$ at $\approx$ 60mK. q=0 magnetic Bragg peaks have appeared at positions such as 2,2,0 and the diffuse features observed in zero field at positions such as 3,3,0 and 1,1,2 have sharpened into features elongated on $[00l]$. Black shows the lowest intensity level, white the highest.

Chapter 9

Conclusions and Further Work

In this chapter, it is aimed to extend the conclusions presented in previous chapters. The main results are summarised and more general conclusions are put forward. In particular, various elements of the thesis have been brought together and it has been endeavoured to show the importance of the work.

9.1 The Easy-Axis Ferromagnet

In Chapter 3 the continuous spin ice model was shown to have q=0 order. The transition to the long-range ordered state was either first-order or second-order, depending on the strength of the local easy-axis anisotropy. The tricritical point was observed for $D_{tc}/J \approx 5$.

When a magnetic field was applied along the [100] direction a magnetic phase diagram was revealed similar to that found in some ferroelectrics [61]. If the magnetic field h is replaced by the electric field E and magnetization M by polarisation P a remarkably similar phase diagram is observed for $D_{tc}/J < D/J < \infty$.

9.1.1 Comparison with Ferroelectrics

The phase diagram shown in Figure 9.1 was mapped out and can be discussed in terms of Landau theory. In section 1.7 the Landau free energy $\mathcal{L}$ was introduced. When a magnetic field is applied to the system it can be rationalised as such [59]:

$$\mathcal{L} = \mathcal{L}_0 + \alpha_2\eta^2 + \alpha_4\eta^4 + \alpha_6\eta^6 + \ldots - N\eta h \tag{9.1}$$

Here, η and h are the order parameter and conjugate applied field and the α_n's are constants related to the n-th order susceptibilities.

As mentioned in section 1.7 if $\alpha_4 > 0$ then the zero-field transition is second-order and if $\alpha_4 < 0$ it is first-order, with the characteristic 'winged' phase diagram (see Fig. 9.1). The slopes of the wings are approximately $\sim \sqrt{\frac{\alpha_4}{\alpha_2}}$ [61]. The edge of the 'wing' represents the termination of the existence of field-induced first-order phase transitions for finite $D/J > D_{tc}/J$. In general, the termination points of first-order lines need not be associated with critical fiuctuations, in which case they should be termed 'first-order critical points'. This analysis also agrees with the results of Harris *et al.* [40], where no critical fluctuations were observed at the termination of the line of first-order phase transitions.

One such point is known to occur on the zero-field axis of the phase diagram of the one dimensional Ising ferromagnet with additional inverse square interaction [115]. In fact it has been suggested [60] that the end-point of a line of symmetry sustaining transitions is usually first-order, the liquid gas transition being a special case. In general, at a first-order critical point, the susceptibility will diverge, but there may or may not be critical fluctuations [60, 116]. A detailed analysis of this question with regard to the current system would be an interesting topic of future study.

It is plausible that ice itself would exhibit a phase diagram such as that in Figure 9.1. But in the case of ice the dynamics are immeasurably slow at temperatures well above the triple point [5]. However ice is not proton ordered in the

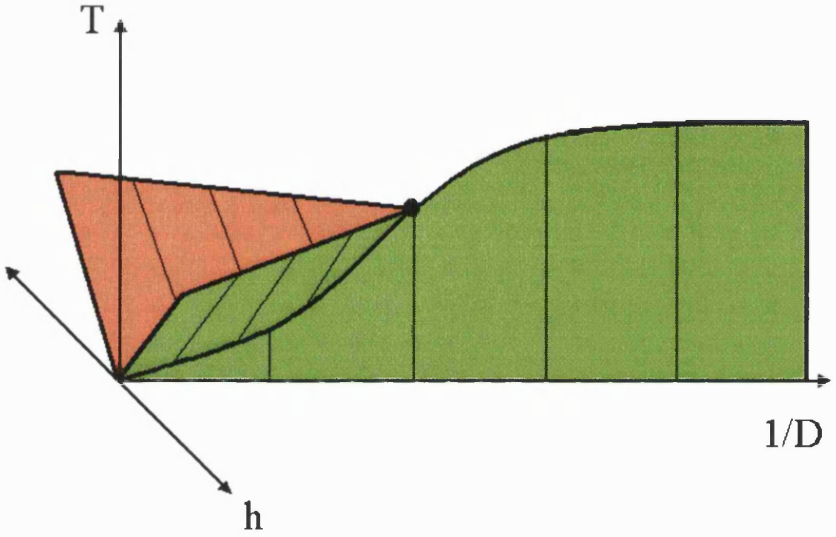

Figure 9.1: Schematic magnetic phase diagram for the continuous spin-ice model.

absence of defects or stabilizing surfaces and there is much debate concerning the true nature of its ground state [117, 118, 119, 120, 121].

9.1.2 Comparison of $Ho_2Ti_2O_7$ and $Dy_2Ti_2O_7$ with Dipolar Spin Ice

When the dipolar spin ice model is simulated with single spin-flip dynamics it has been shown to be a very good model for the experimental observations of $Ho_2Ti_2O_7$ [42, 17](see also section 8.1).

Recently a $Ho_2Ti_2O_7$ sample has been cooled in zero field to 50 mK and the magnetic field applied along the [110] direction, q=0 and q=X magnetic Bragg peaks formed as expected. The system was heated up slowly until q=X features were at maximum intensity [11]. The system was then cooled back down to base temperature and the field removed. The q=0 peaks were heavily reduced but the q=X features remained, and were stable.

The results in sections 8.2, and 8.1 suggest that $Dy_2Ti_2O_7$ has very similar

behaviour to that of $Ho_2Ti_2O_7$. The existence of q=X features is common to both compounds and the neutron scattering maps were also very similar, with common areas of diffuse scattering.

What this means exactly with respect to the ground state of $Ho_2Ti_2O_7$ and $Dy_2Ti_2O_7$ is not clear. The stability of the q=X in $Ho_2Ti_2O_7$ features and the agreement with the dipolar spin-ice simulation suggest that the *true* ground state of $Ho_2Ti_2O_7$ and $Dy_2Ti_2O_7$ might be the q=X structure. However, no zero-field ordering is seen in either of the compounds at base temperature. It is possible that the q=X structure is dynamically inhibited from being accessed on experimental timescales [43].

Further experiments on the dynamics of the experimental systems are necessary to shed light on the problem. In view of the results presented in this thesis, it might be that the ordered state favoured by the long-range part of the dipolar coupling competes with that favoured by continuous spins. A real system has continuous spins in the classical approximation, but a real system is also necessarily a quantum mechanical one. A continuous model is closer to a real system with respect to the classical approximation, but note that a real system also necessarily contains dipolar interactions.

9.2 The Magnetic structure of $Gd_2Ti_2O_7$

In Chapter 7, the Heisenberg antiferromagnet $^{160}Gd_2Ti_2O_7$ was shown to have long-range magnetic order at 50 mK, with a magnetic phase transition at $\sim$ 1 K. The best fit of the powder neutron diffraction pattern showed a partially ordered magnetic structure. The structure is one with q=0 order of the spins on the kagomé planes, and zero moment on the interstitial spins. The precise dynamics of the ordering of the spins is unclear. It is possible that the moment on the interstitial site has a freezing transition at a finite temperature above 50 mK. Further neutron

experiments are proceeding to determine the magnetic structure as a function of temperature.

The partial order of chemically pure $Gd_2Ti_2O_7$ contrasts with the behaviour of Heisenberg antiferromagnets with small amounts of quenched chemical disorder, such as $CsNiCrF_6$ [108] and $Y(Sc)Mn_2$ [122]. These materials show spin freezing transitions in the absence of long range order and spin correlations characteristic of the pure Heisenberg system [36, 108, 122]. Thus the results presented in Chapter 7 support the idea that quenched chemical disorder is a strongly relevant perturbation in the pyrochlore system that is responsible for the glassy ground states often observed [22].

The system selected $\mathbf{k} = \frac{1}{2}\frac{1}{2}\frac{1}{2}$ as an ordering wave vector. This result is valid with respect to the results of Raju *et al.* [37] where a general propagation vector of $h\ h\ h$ was predicted. In symmetry terms $h\ h\ h$ is an equivalence line in the Brillouin zone, such that all possible ordering wave vectors share the IRs and basis vectors that are enumerated in Table 7.2. It is possible that $h = \frac{1}{2}$ is specific to ordering in $Gd_2Ti_2O_7$ or might be more general; this question remains to be answered.

The higher order theory of Palmer and Chalker [100] predict a value of $h = 0$ which does not agree with the results of Chapter 7. The disagreement between experiment and theory in this case is very puzzling. It will remain an interesting challenge, both experimental and theoretical to ascertain the origin of this disagreement.

9.3 $Er_2Ti_2O_7$ and the Easy-Plane Antiferromagnet

The easy-plane antiferromagnet and the real $Er_2Ti_2O_7$ systems have some common properties. This section addresses these similarities and speculates on some of the consequences.

9.3.1 Degeneracy and Order of the Easy-plane Antiferromagnet

Section 4.3 illustrated the possible q=0 ground state configurations possible for the system. There is one degree of freedom in the system, for example the x-component of spin 1. Once this is fixed, there is a set of eight different solutions with the same x-component on spin 1. For special values of the degree of freedom there are only six solutions, since two pairs of solutions become coincident with one another. The set of solutions is fully connected and one ground state can be easily deformed into another with no increase in the internal energy.

A representative set of ground states was studied, labelled **I** to **IV**. Sections 4.4.3, 4.4.1 and 4.4.2 showed that some of the states, such as state **I** were 'rigid' with little thermal entropy whereas others, such as state **III**, had much more freedom of existence. These properties were formally confirmed after analytical calculation of the normal modes for excitations out of the different states. State **III** was shown to have zero modes which contributed $k_BT/4$ to the specific heat. These analytical calculations were confirmed by Monte Carlo simulation. The mechanism of the 'order by disorder' transition reported in Ref. [84] was therefore established with certainty.

Order by disorder and the infinite line defect

Section 4.2.2 showed that an infinite line defect sometimes formed in the lattice for $T < T_N$. The defect coexisted in a 'sea' of q=0 ordered states, and the total energy of the system was at a minimum. There are of the order L^2 independent rods in the lattice which could support the defect. In some cases microscopic examination of the spin configurations showed two defects coexisting within a q=0 ordered system. These line defects seem somewhat analogous to weathervane defects in the kagomé lattice. Their observation is consistent with the spin wave calculation

and $O(L^2)$ modes.

Weathervane defects are formed by six spins on a hexagon rotating simultaneously out of the plane [24, 123]. This rotation is at zero cost to the internal energy. It has not been possible to determine the microscopic process of the formation of the defects in the easy-plane system in the same way. It is clear that the instantaneous cooperative movement of all the spins on each rod is required. It seems unlikely that the defect is topological (where the defect cannot be removed by small movements of spins), since the system is observed to escape from defected states (see section 4.2.2).

9.3.2 The Free Energy Surface

The Gibbs free energy of a system is defined:

$$G = U - TS - Mh. \tag{9.2}$$

As discussed in section 1.2.6, a degenerate system which has order by disorder fluctuates in a special part of phase space where it can gain entropy and thus lower its free energy. A system will order into a state where its Gibbs free energy G is at a minimum with respect to its magnetization.

In section 4.4.3 the system was placed in particular ordered states and allowed to relax out of them. It might be expected that the system would *always* relax into the ground state with the lowest free energy (*i.e.* state **III**). The results of these tests suggested otherwise. This suggests that there exists a free energy surface with local maxima and minima. A schematic diagram of such a surface is shown in Figure 9.2.

When the system was placed in defect state **IV** it relaxed directly into the local free energy minimum of defect state **I**. In the same way, the symmetric state **II** relaxed into ground state **III** which *does* have the lowest free energy. It would be interesting to do a more complete mapping of the free energy surface. More

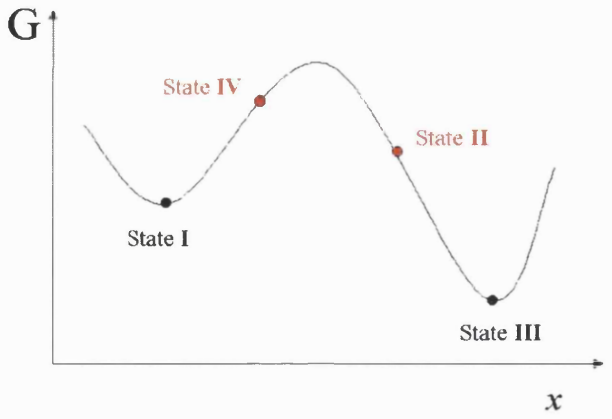

Figure 9.2: Local easy-plane antiferromagnet: Free energy versus phase space parameter x (schematic).

insights into the dynamics of the system might be revealed as well as the particular positions of the local free energy maxima and minima.

9.3.3 Similarities with $Er_2Ti_2O_7$

In Chapter 6 $Er_2Ti_2O_7$ was confirmed (using powder neutron diffraction) to be an easy-plane antiferromagnet and not an easy-axis system. The system was shown to have q=0 ordering within the two dimensional representation Γ_5

In section 4.3 the symmetric solution to the model system was described using the positions of the spins in states **II** and **III** as basis vectors. The directions of ψ_2 and ψ_3, the basis vectors of Γ_5, are identical to the spin configurations of states **II** and **III** respectively. It is remarkable that both experimental and model systems order into states described by the same set of basis vectors. The necessary domain averaging of a powder experiment precluded the isolation of the precise ordering pattern of $Er_2Ti_2O_7$. Further single crystal experiments on $Er_2Ti_2O_7$ are in progress. Preliminary results suggest the ordered magnetic structure to be state **III** [124].

It would be interesting to extrapolate the properties of the Monte Carlo system to the real one. The degeneracy of ground states must certainly be applicable. The main difference is that the real system orders with a second and not a first-order transition.

The model system does not include any dipolar interactions which are ubiquitous in real materials. Palmer and Chalker calculated the ground state of an Heisenberg antiferromagnet with dipolar interactions [100]. They found the ground state to be state **I** and other symmetry related structures. As state **I** is a ground state for the local XY model, this means that state **I** is the energetic ground state for the XY model with additional dipolar interactions. However, $Er_2Ti_2O_7$ certainly does not order in this way. Dipole interactions may, however, affect the order of the transition.

$Er_2Ti_2O_7$ can be described as an effective $S = \frac{1}{2}$ system due to the crystal field interaction. The specific moment reduction observed for $Er_2Ti_2O_7$ suggests that quantum fluctuations are of importance in this system [105, 106]. It is probable that the classical spin wave calculation correctly captures the effect of these fluctuations [105]. Hence should the system order only with basis vector ψ_3 (as seems so [124]), it is prescient to suggest that $Er_2Ti_2O_7$ is a spectacular example of a real system with quantum order by disorder.

9.4 Investigation of the Easy-Plane Ferromagnet and the Easy-Axis Antiferromagnet

This section discusses the last two combinations of exchange and anisotropy mentioned in section 2.4. Both these systems are described by the Hamiltonian below:

$$\mathbb{H} = -J \sum_{<i,j>} \mathbf{S}_i \cdot \mathbf{S}_j - D \sum_{i=1}^{N} (\boldsymbol{\delta}_i \cdot \mathbf{S}_i)^2$$

Very brief details are given of each investigation and the results obtained.

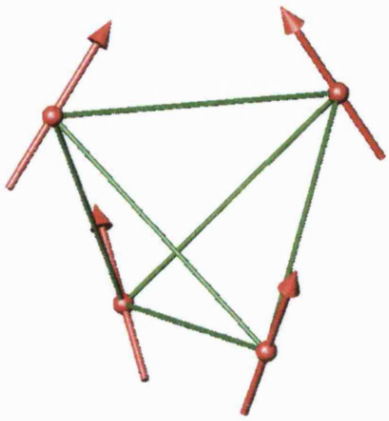

Figure 9.3: Ground state of the easy-plane ferromagnet.

9.4.1 The Easy-Plane Ferromagnet

This system consists of spins which have a competition between lying in the local easy-planes and ferromagnetic alignment. For finite easy-plane anisotropy the spins can cant off the easy-planes and lower their internal energy at the expense of anisotropy energy. This happens in much the same way as the continuous spin-ice model (see section 3.6.2). Unlike the spin-ice model for $|D/J| = \infty$ there is a single non-degenerate q=0 ground state observed in the system. The spins can form a non-collinear ferromagnetic ground state with the spins fixed in the local easy-planes, which has a saturated magnetization $M = \frac{2}{\sqrt{6}}$ (see Fig. 9.3).

Figure 9.4 shows the results of the investigation. For all values of anisotropy there is a phase transition to the long-range ordered state described above. As $D/J \to 0$ the system becomes more like a simple ferromagnet, the spins cant off the local easy-planes and $M \to 1$.

9.4.2 The Easy-Axis Antiferromagnet

The easy-axis pyrochlore antiferromagnet has already been studied theoretically [50, 125]. The system undergoes a phase transition into a long-range ordered ground

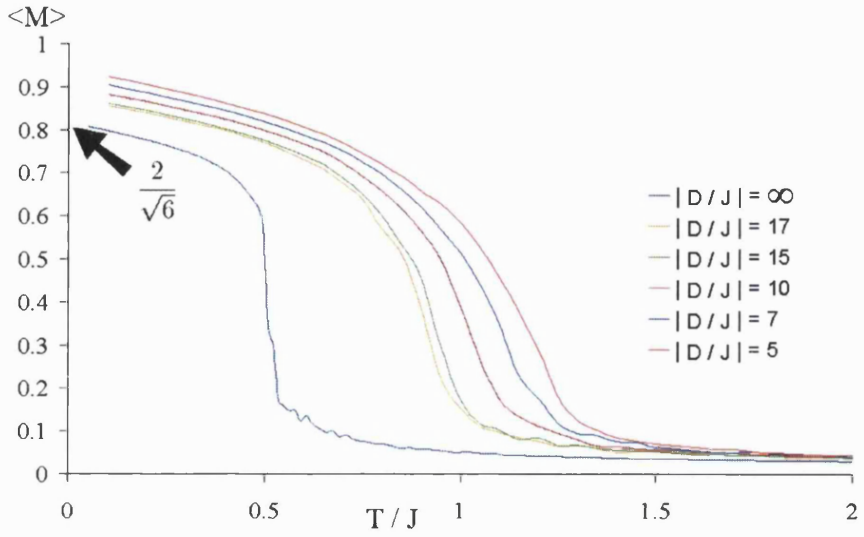

Figure 9.4: Plot of magnetization vs T/J for the easy-plane ferromagnet. Simulations were performed for a system with $J = 1, L = 5$ and a range of $D/J < 0$, with 10,000 MCS/S and 3000 equilibration steps.

state with either all four spins pointing into or out of every tetrahedron (see Fig. 9.5). FeF_3 was shown to be an experimental realisation of a system with these magnetic properties and ordered ground state [49].

Figure 9.6 shows the results of the investigation. For every value of finite anisotropy D, as well as the Ising case when $D = \infty$, there is long-range sublattice order into the same q=0 ordered state. In this case the anisotropy energy and the exchange energy can both be minimised, and there is no degeneracy present. As $D/J \to 0$ the transition temperature decreases since the system is becoming more like the fully frustrated Heisenberg pyrochlore antiferromagnet, and the exchange energy becomes more important.

These results agree with the previous work of Reimers *et al.* [50] and Moessner [125].

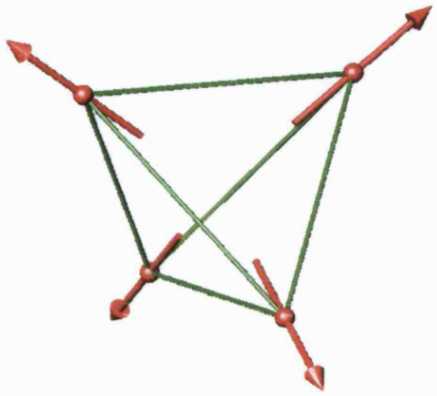

Figure 9.5: Ground state of the easy-axis antiferromagnet.

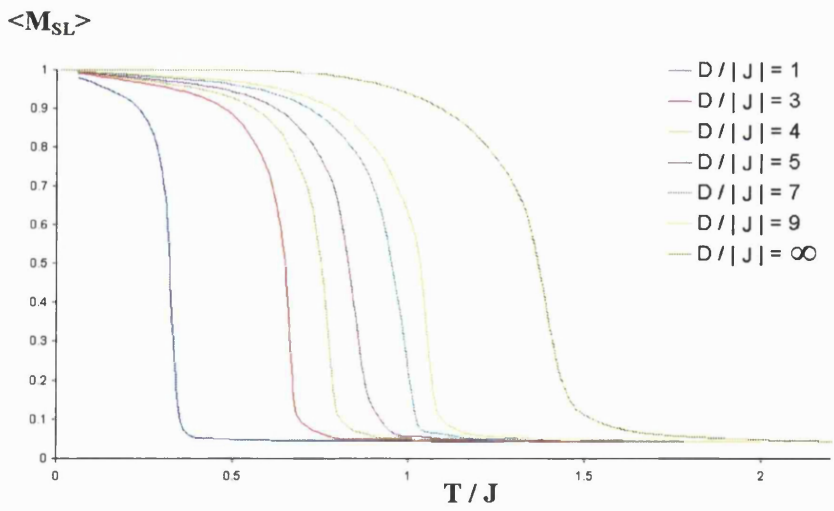

Figure 9.6: Plot of M_{SL} vs T/J for the easy-axis antiferromagnet. Simulations were performed for a system with $J = -1, L = 8$ and a range of $D/J > 0$, with 20,000 MCS/S and 6000 equilibration steps.

9.4.3 A General Relation between the Ground States

There is a remarkable parallel between the ferromagnetic and antiferromagnetic ground states of each of the two types of anisotropy (easy-axis and easy-plane). In each case the ferromagnetic and antiferromagnetic ground states are related by the flipping of a pair of spins. Considering the variety of properties shown by these models, this simple relationship is quite a fundamental observation.

9.5 Perspectives

This thesis describes an investigation of four simple combinations of exchange and anisotropy for a simple Hamiltonian expression. While these simple models have limited application to real materials, this study has shown that they can be used as an excellent starting point for the study of more complex phenomena. The rare-earth titanate series shows a wide range of complex properties. Models are required to enhance the understanding of these complex systems.

The local easy-plane antiferromagnet model has been shown in this work to be in excellent agreement with the experimental results for $Er_2Ti_2O_7$. The easy-axis antiferromagnet has long been known to be applicable to the ordering of FeF_3.

The Ising ferromagnet (the spin ice model) has been shown to be relevant to $Ho_2Ti_2O_7$ [11, 40, 15, 114] and $Dy_2Ti_2O_7$ [20, 41]. The addition of dipolar interactions to this model was able to improve the understanding of the properties shown by [42, 44, 17]. It is possible that the easy-plane ferromagnet is applicable to the $Yb_2Ti_2O_7$ system [126].

The investigation of $Gd_2Ti_2O_7$ showed that there are some systems which are less easy to explain with simple models. $Tb_2Ti_2O_7$ is another example of a system with more complicated properties [127].

Figure 9.7 shows a summary of the results in this thesis, with their application to real systems.

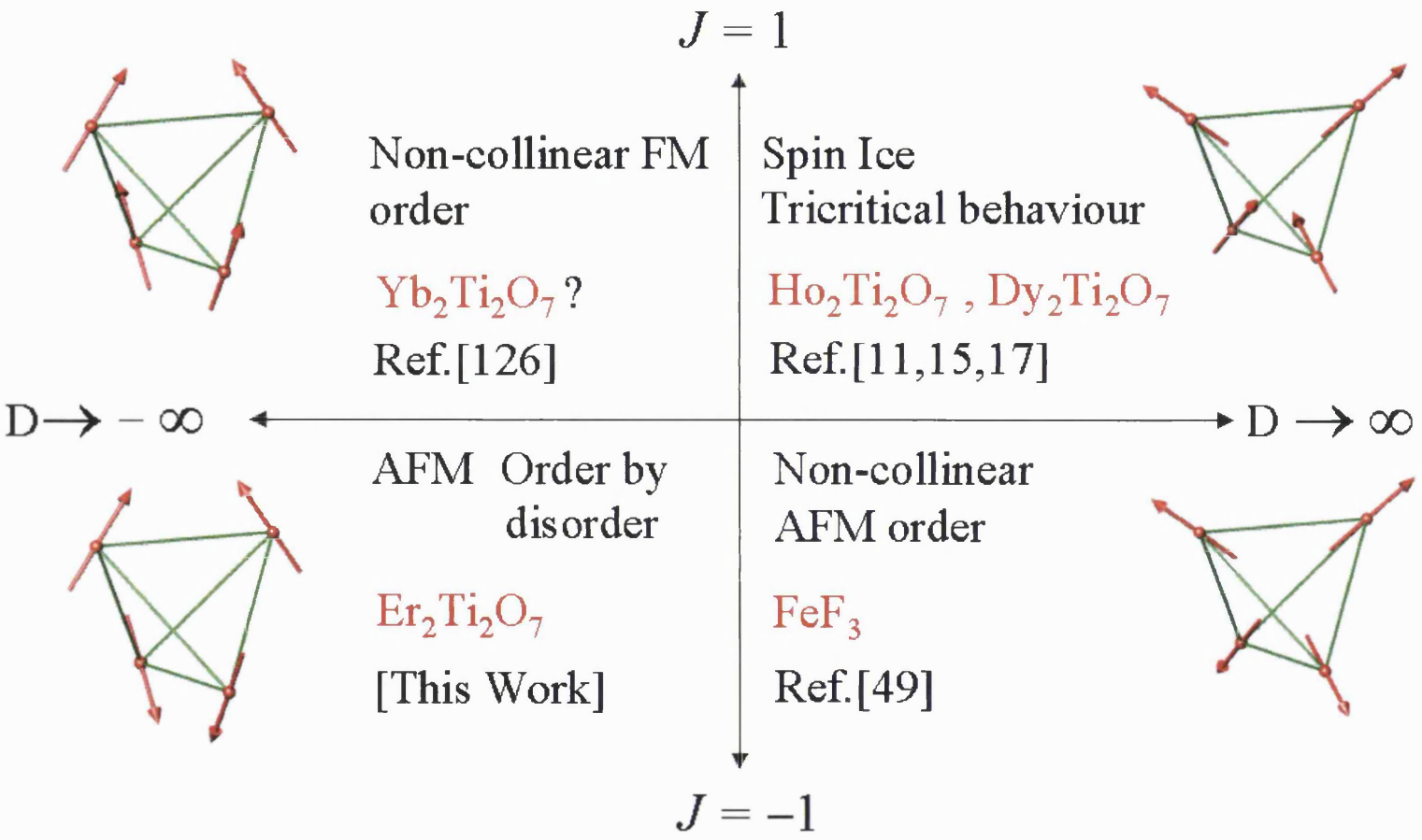

Figure 9.7: Exchange-anisotropy phase diagram. The q=0 ordering patterns are shown for the ferromagnetic systems with $D = \infty$. The q=0 ordering patterns shown for the antiferromagnetic systems are valid for all anisotropies.

Appendix A

Statistical Mechanical Definitions

A.1 Fluctuations of the Energy and Magnetization

A.1.1 Specific Heat

Eqn. (2.6) can easily be derived from Eqn. (2.5) and the thermodynamic definition of specific heat.

$$C_p = \left(\frac{\partial H}{\partial T}\right)_p = \left(\frac{\partial \langle E \rangle}{\partial T}\right)_p = -\frac{\partial}{\partial T}\left[\frac{\partial}{\partial \beta}(\ln Z)\right] \tag{A.1}$$

$$\frac{\partial}{\partial T} = \frac{\partial \beta}{\partial T}\frac{\partial}{\partial \beta} \qquad \beta = \frac{1}{k_B T} \qquad \frac{\partial \beta}{\partial T} = -\frac{\beta}{T} \tag{A.2}$$

$$C_p = \frac{\beta}{T}\frac{\partial^2}{\partial \beta^2}(\ln Z) = \frac{\beta}{T}\frac{-\partial}{\partial \beta}\left[\frac{-\partial}{\partial \beta}(\ln Z)\right] = \frac{\beta}{T}\frac{-\partial \langle E \rangle}{\partial \beta} \tag{A.3}$$

$$C_p = \frac{\beta}{T}\frac{-\partial}{\partial\beta}\left[\frac{\sum_r E_r \exp\left(-\beta E_r\right)}{\sum_r \exp\left(-\beta E_r\right)}\right] \tag{A.4}$$

$$C_p = \frac{\beta}{T}\left(\frac{\sum_r E_r^2 \exp(-\beta E_r)}{\sum_r \exp\left(-\beta E_r\right)} - \frac{\left[\sum_r E_r \exp\left(-\beta E_r\right)\right]^2}{\left[\sum_r \exp\left(-\beta E_r\right)\right]^2}\right) \tag{A.5}$$

$$\therefore C_p = \frac{\beta}{T}\left[\langle E^2\rangle - \langle E\rangle^2\right] \tag{A.6}$$

A.1.2 Magnetic Susceptibility

The expression for the magnetic susceptibility in Eqn. (2.12) is derived in a similar way. When a magnetic field is applied to the system the Hamiltonian $\mathbb{H}$ is expressed as a function of the applied field h and the partition function is thus [128]:

$$Z = \sum_r \exp(-\beta\mathbb{H}(h)) \tag{A.7}$$

Using Eqn. 2.1 and Eqn. (A.7) the average magnetization of the system is defined:

$$\langle M\rangle = \frac{\sum_r M_r \exp(-\beta\mathbb{H}(h))}{Z} \tag{A.8}$$

We differentiate Eqn. (A.7) with respect to h:

$$\frac{\partial \ln Z}{\partial h} = \frac{1}{Z}\frac{\partial Z}{\partial h} = \frac{1}{Z}\beta \sum_r M_r \exp(-\beta \mathbb{H}(h)) = \beta \langle M \rangle$$

$$\chi = \frac{\partial \langle M \rangle}{\partial h} = \frac{1}{\beta}\frac{\partial^2 \ln(Z)}{\partial h^2}$$

$$\frac{\partial^2 \ln(Z)}{\partial h^2} = \frac{1}{Z}\left(\beta^2 \sum_r M_r^2 \exp(-\beta \mathbb{H})\right) - \frac{1}{Z^2}\frac{\partial Z}{\partial h}\left(\beta \sum_r M_r \exp(-\beta \mathbb{H})\right)$$

$$\frac{\partial^2 \ln(Z)}{\partial h^2} = \beta^2 \left(\frac{\sum_r M_r^2 \exp(-\beta \mathbb{H})}{Z}\right) - \beta^2 \left(\frac{\sum_r M_r \exp(-\beta \mathbb{H})}{Z}\right)^2$$

$$\frac{\partial^2 \ln(Z)}{\partial h^2} = \beta^2 \left(\langle M^2 \rangle - \langle M \rangle^2\right)$$

$$\therefore \chi = \beta \left(\langle M^2 \rangle - \langle M \rangle^2\right)$$

Appendix B

Expression for the Partition Function

The partition function Z can be expressed as an indefinite integral:

$$\left\{ Z = \int \exp(-\beta H(x)) dx \right\}^N \tag{B.1}$$

If $H(x) \sim x^2, x^4$ the different terms can be separated:

$$Z = \left\{ \int \exp(-\beta x^2) dx \right\}^{N_2} \left\{ \int \exp(-\beta x^4) dx \right\}^{N_4} \tag{B.2}$$

Where N_2 is the number of quadratic modes and N_4 is the number of quartic modes. By making the changes of variable $y^2 = \beta x^2$ and $y^4 = \beta x^4$, Eqn. (B.2) can be simplified:

$$Z = \left\{ \beta^{-\frac{1}{2}} \int \exp(-y^2) dy \right\}^{N_2} \left\{ \beta^{-\frac{1}{4}} \int \exp(-y^4) dy \right\}^{N_4} \tag{B.3}$$

The remaining integrals have standard solutions which are just constants of order unity. Eqn. (B.3) is then evaluated to give a simple expression for Z where $\beta = \frac{1}{kT}$ with $k = 1$:

$$Z = A(T)^{\frac{N_4}{4} + \frac{N_2}{2}}, \qquad A = a^N. \tag{B.4}$$

Appendix C

Structural data

The structural parameters for the $Fd\bar{3}m$ Space Group are shown below with respect to $R_2Ti_2O_7$. In most cases $x(O_2) \sim 0.42$.

$R_2Ti_2O_7$				
Cubic, $Fd\bar{3}m$				
	Site	x	y	z
R	16c	0	0	0
Ti	16d	$\frac{1}{2}$	$\frac{1}{2}$	$\frac{1}{2}$
O_1	8a	$\frac{1}{8}$	$\frac{1}{8}$	$\frac{1}{8}$
O_2	48f	x	$\frac{1}{8}$	$\frac{1}{8}$

Bibliography

[1] W. G. V. Rosser, *An Introduction to Statistical Physics* (Ellis Horwood Limited, Chichester, 1982).

[2] L. J. de Jongh and A. R. Miedema, *Experiments on Simple Magnetic Model Systems* (Taylor & Francis, London, 1974).

[3] W. F. Giauque and M. F. Ashley, Phys. Rev. **43**, 81 (1933).

[4] F. Simon, Handbuch der Physik **10**, 363 (1926).

[5] W. F. Giauque and J. W. Stout, J. Am. Chem. Soc. **58**, 1144 (1936).

[6] J. D. Bernal and R. H. Fowler, J. Chem. Phys. **1**, 515 (1933).

[7] L. Pauling, J. Am. Chem. Soc. **57**, 2680 (1935).

[8] E. O. Wollan, W. L. Davidson, and C. G. Schull, Phys. Rev. **75**, 1348 (1949).

[9] S. Rosenkranz, A. P. Ramirez, A. Hayashi, R. J. Cava, R. Siddharthan, and B. S. Shastry, J. Appl. Phys. **68**, 855 (1992).

[10] S. T. Bramwell, M. N. Field, M. J. Harris, and I. P. Parkin, J. Phys.: Condens. Mat. **12**, 483 (2000).

[11] M. J. Harris, S. T. Bramwell, D. F. McMorrow, T. Zeiske, and K. W. Godfrey, Phys. Rev. Lett. **79**, 2554 (1997).

[12] J. D. Cashion, A. H. Cooke, M. J. M. Leask, T. L. Thorp, and M. R. Wells, J. Mater. Sci **3**, 402 (1968).

[13] M. J. Harris, S. T. Bramwell, T. Zeiske, D. F. McMorrow, and P. J. C. King, J. Magn. Magn. Mater. **177**, 757 (1998).

[14] P. W. Anderson, Phys. Rev. **102**, 1008 (1956).

[15] S. T. Bramwell and M. J. Harris, J. Phys.: Condens. Mat. **10**, L215 (1998).

[16] A. L. Cornelius and J. S. Gardner, Phys. Rev. B **64**, 060406(R) (2001).

[17] S. T. Bramwell, M. J. Harris, B. C. den Hertog, M. J. P. Gingras, J. S. Gardner, D. F. McMorrow, A. R. Wildes, A. L. Cornelius, J. D. M. Champion, R. G. Melko, and T. Fennell, Phys. Rev. Lett. **87**, 047205 (2001).

[18] J. E. Greedan, J. Mater. Chem. **11**, 37 (2001).

[19] P. Schiffer and A. P. Ramirez, Comments Cond. Mat. Phys. **18**, 21 (1996).

[20] A. P. Ramirez, A. Hayashi, R. J. Cava, R. Siddharthan, and B. S. Shastry, Nature **399**, 333 (1999).

[21] J. Villain, Z. Phys. B **33**, 31 (1979).

[22] L. Bellier-Castella, M. J. P. Gingras, P. C. W. Holdsworth, and R. Moessner, cond-mat/0006306 .

[23] J. N. Reimers, A. J. Berlinsky, and A. C. Shi, Phys. Rev. B **43**, 865 (1991).

[24] J. T. Chalker, P. C. W. Holdsworth, and E. F. Shender, Phys. Rev. Lett. **68**, 855 (1992).

[25] E. Shender and P. C. W. Holdsworth, in *Fluctuations and Order: A New Synthesis*, edited by M. M. Millonas (Springer-Verlag, Berlin, 1996), pp. 259 – 279.

[26] J. Villain, J. Physique **41**, 1263 (1980).

[27] R. Moessner and J. T. Chalker, Phys. Rev. Lett. **80**, 2929 (1998).

[28] R. Moessner and J. T. Chalker, Phys. Rev. B **58**, 12049 (1998).

[29] R. Moessner, cond-mat/0010301 .

[30] J. N. Reimers and A. J. Berlinsky, Phys. Rev. B **48**, 9539 (1993).

[31] J. Frunzke, T. Hansen, A. Harrison, J. S. Lord, G. S. Oakley, D. Visser, and A. S. Wills, J. Mater. Chem. **11**, 179 (2001).

[32] D. A. Huse and A. D. Rutenberg, Phys. Rev. B **45**, 7536 (1992).

[33] A. B. Harris, C. Kallin, and A. J. Berlinsky, Phys. Rev. B **45**, 2899 (1992).

[34] J. N. Reimers, Phys. Rev. B **45**, 7287 (1992).

[35] B. Canals and C. Lacroix, Phys. Rev. Lett. **80**, 2933 (1998).

[36] B. Canals and C. Lacroix, Phys. Rev. B **61**, 1149 (2000).

[37] N. P. Raju, M. Dion, M. J. P. Gingras, T. E. Mason, and J. E. Greedan, Phys. Rev. B **59**, 14489 (1999).

[38] E. H. Lieb and F. Y. Wu, in *Two Dimensional Ferroelectric Models*, Vol. 1 of *Phase Transitions and Critical Phenomena*, edited by C. Domb and M. S. Green (Academic Press, London, 1972).

[39] A. S. Wills, (personal communication).

[40] M. J. Harris, S. T. Bramwell, P. C. W. Holdsworth, and J. D. M. Champion, Phys. Rev. Lett. **81**, 4496 (1998).

[41] H. Fukazawa, R. G. Melko, R. Higashinaka, Y. Maeno, and M. J. P. Gingras, cond-mat/0108129 .

[42] B. C. den Hertog and M. J. P. Gingras, Phys. Rev. Lett. **84**, 3430 (2000).

[43] R. G. Melko, B. C. den Hertog, and M. J. P. Gingras, cond-mat/0009225 .

[44] M. Gingras and B. den Hertog, cond-mat/0012275 .

[45] R. Siddharthan, B. S. Shastry, A. P.Ramirez, A. Hayashi, R. J. Cava, and S. Rosenkranz, Phys. Rev. Lett. **83**, 1854 (1999).

[46] R. Siddharthan, B. S. Shastry, and A. P.Ramirez, Phys. Rev. B **63**, 184412 (2001).

[47] P. P. Ewald, Ann. Phys. **64**, 253 (1921).

[48] Z. Wang and C. Holm, cond-mat/0107064 .

[49] G. Ferey, R. de Pape, M. Leblanc, and J. Pannetier, Rev. Chem. Miner. **23**, 474 (1986).

[50] J. N. Reimers, J. E. Greedan, and M. Björgvinsson, Phys. Rev. B **45**, 7295 (1992).

[51] E. B. Smith, *Basic Chemical Thermodynamics* (Clarendon, Oxford, 1973).

[52] H. E. Stanley, *Phase Transitions and Critical Phenomena* (Clarendon Press, Oxford, 1971).

[53] J. E. Noakes, N. E. Tornberg, and A. Arrott, J. Appl. Phys. **37**, 1264 (1966).

[54] J. M. Yeomans, *Statistical Mechanics of Phase Transitions* (Clarendon Press, Oxford, 1992).

[55] M. F. Collins, in *Magnetic Critical Scattering*, Vol. 5 of *Oxford Series on Neutron Scattering in Condensed Matter*, edited by S. W. Lovesey and E. W. J. Mitchell (Oxford University Press, Oxford, 1989).

[56] J. J. Binney, N. J. Dowrick, A. J. Fisher, and M. E. J. Newman, *The Theory of Critical Phenomena* (Oxford University Press, Oxford, 1992).

[57] E. A. Guggenheim, J. Chem. Phys. **13**, 253 (1945).

[58] L. D. Landau, Phys. Z. Sowjet. **11**, 26 (1937).

[59] N. Goldenfeld, in *Lectures on Phase Transitions and The Renormalisation Group*, Vol. 85 of *Frontiers in Physics*, edited by D. Pines (Perseus Books, Reading, Massachusetts, 1992).

[60] A. Aharony, in *Critical Phenomena*, Vol. 186 of *Lecture Notes in Physics*, edited by F. J. W. Hahne (Springer-Verlag, Berlin, Heidelberg, 1983).

[61] T. Mitsui, I. Tatsuzaki, and E. Nakamura, in *An Introduction to the Physics of Ferroelectrics, Ferroelectricity and Related Phenomena*, edited by I. Lefkowitz and G. I. Taylor (Gordon and Breach Science Publishers, London, 1986), Vol. 1.

[62] I. D. Lawrie and S. Sarbach, in *Theory of Tricritical Points*, Vol. 9 of *Phase Transitions and Critical Phenomena*, edited by C. Domb and J. L. Leibowitz (Academic Press, London, 1984).

[63] R. B. Griffiths, Phys. Rev. Lett. **24**, 715 (1970).

[64] R. B. Griffiths, Phys. Rev. B **7**, 545 (1973).

[65] P. M. Chaikin and T. C. Lubensky, *Principles of Condensed Matter Physics* (Cambridge University Press, Cambridge, 1994).

[66] K. Binder, Rep. Progr. Phys. **60**, 487 (1997).

[67] N. Metropolis, A. Rosenbluth, M. Rosenbluth, A. Teller, and E. Teller, J. Chem. Phys. **21**, 1087 (1953).

[68] The program 'GLMAG' was written by Andrew Richardson. It utilizes the OPEN-GL capability of the DEC 433au computer.

[69] D. P. Landau, J. Appl. Phys. **42**, 1284 (1971).

[70] D. P. Landau, Phys. Rev. Lett. **28**, 449 (1972).

[71] J. L. Alonso, A. Tarancón, H. G. Ballesteros, L. A. Fernández, V. Martín-Mayor, and A. M. Sudupe, Phys. Rev. B **53**, 2537 (1996).

[72] E. H. Boubcheur, R. Quartu, H. T. Diep, and O. Nagai, Phys. Rev. B **58**, 400 (1998).

[73] J. L. Cardy, *Scaling and Renormalisation Group* (Cambridge University Press, Cambridge, 1996).

[74] K. Binder and D. P. Landau, Phys. Rev. B **30**, 1477 (1984).

[75] E. F. Shender and P. C. W. Holdsworth, Phys. Rev. Lett. **76**, 2583 (1996).

[76] R. J. Birgeneau, G. Shirane, M. Blume, and W. C. Koehler, Phys. Rev. Lett. **33**, 1098 (1974).

[77] E. Stryjewski and N. Giordano, Adv. Phys. **26**, 487 (1977).

[78] M. Blume, L. M. Corliss, J. M. Hastings, and E. Schiller, Phys. Rev. Lett. **32**, 544 (1974).

[79] E. K. Riedel and F. J. Wegner, Phys. Rev. Lett. **29**, 349 (1972).

[80] J. M. Kincaid and E. G. D. Cohen, Phys. Lett. **50A**, 317 (1974).

[81] D. P. Landau, Phys. Rev. B **14**, 4054 (1976).

[82] H. J. Herrmann and D. P. Landau, Phys. Rev. B **48**, 239 (1993).

[83] L. Hernández, H. T. Diep, and D. Bertrand, Phys. Rev. B **47**, 2602 (1993).

[84] S. T. Bramwell, M. J. P. Gingras, and J. N. Reimers, J. Appl. Phys. **75**, 5523 (1994).

[85] M. L. Boas, *Mathematical Methods in the Physical Sciences* (Wiley, New York, Chichester, 1983).

[86] J. Barker and M. L. Roberts, (personal communication).

[87] The XMAPLE software from Waterloo Maple Inc. was used.

[88] C. Kittel, *Elementary Solid State Physics* (Wiley, New York, 1996).

[89] The Mathematica software from Wolfram was used.

[90] The calculation for state **II** was performed. The results were much the same as those for state **I**.

[91] The material in this section follows the lecture course given by Dr. Andrew Boothroyd at the 1999 Neutron School (Oxford).

[92] R. A. Young, *The Rietveld Method* (Oxford University Press, Oxford, 1993).

[93] A.C. Larsen and R.B. von Dreele, General Structure Analysis System (Lansce, Los Alamos National Laboratory, Los Alamos, 1994).

[94] J. Rossat-Mignod, in *Magnetic Structures*, Vol. 23 of *Methods of Experimental Physics*, edited by K. Sköld and D. L. Price (Academic Press, New York, 1986).

[95] V. E. N. Yu. A. Izymov and R. P. Ozerov, *Neutron Diffraction of Magnetic Materials* (Consultants Bureau, New York, 1991).

[96] E. F. Bertaut, J. Magn. Magn. Mat. **24**, 267 (1981).

[97] A. S. Wills, Phys. Rev. B **63**, 064430 (2001).

[98] A. S. Wills, Physica B **680**, 276 (2000), program available from ftp://ftp.ill.fr/pub/dif/sarah/.

[99] U. Steigenberger, M. Hagen, R. Caciuffo, C. Petrillo, F. Cilloco, and F. Sacchetti, Nucl. Instrum. Meth. **B 53**, 87 (1991).

[100] S. E. Palmer and J. T. Chalker, Phys. Rev. B **62**, 488 (2000).

[101] O. Knop, F. Brisse, L. Castelliz, and Sutarno, Can. J. Chem. **43**, 2812 (1965).

[102] H. W. J. Blöte, R. F. Weilinga, and H. Huiskamp, Physica **43**, 549 (1969).

[103] O. V. Kovalev, *Representations of the Crystallographic Space Groups*, 2 ed. (Gordon and Breach Science Publishers, Switzerland, 1993).

[104] G. E. Bacon, *Neutron Diffraction* (Clarendon Press, Oxford, 1975).

[105] P. W. Anderson, Phys. Rev. **102**, 1008 (1956).

[106] R. M. White, *Quantum Theory of Magnetism* (McGraw-Hill, New York, 1970).

[107] J. D. M. Champion, A. S. Wills, T. Fennell, S. T. Bramwell, J. S. Gardner, and M. A. Green, Phys. Rev. B **64**, 140407(R) (2001).

[108] M. P. Zinkin, M. J. Harris, and T. Zeiske, Phys. Rev. B **56**, 11786 (1997).

[109] J. N. Reimers and A. J. Berlinsky, Phys. Rev. B **48**, 9539 (1993).

[110] J. Hodges and J. P. Sanchez, (private communication).

[111] A. Hassan, Abstract $Z\,24\,7$, APS March Meeting Bulletin (2001).

[112] J. C. Li, V. M. Nield, and D. K. Ross, Philos. Mag. B **69**, 1173 (1994).

[113] G. Balakrishnan, O. A. Petrenko, M. R. Lees, and D. M. Paul, J. Phys.: Condens. Mat. **10**, L723 (1998).

[114] T. Fennell, O. A. Petrenko, G. Balakrishnan, S. T. Bramwell, J. D. Champion, B. Fåk, M. J. Harris, and D. M. Paul, cond-mat/0107414 .

[115] D. J. Thouless, Phys. Rev. B **187**, 732 (1969).

[116] M. E. Fisher and A. N. Berker, Phys. Rev. B **26**, 2507 (1982).

[117] G. Barkema and J. Deboer, J. Chem. Phys. **99**, 2059 (1993).

[118] E. R. Davidson and K. Morokuma, J. Chem. Phys. **81**, 3741 (1984).

[119] S. M. Jackson, V. M. Nield, and R. W. Whitworth, J. Phys. Chem. B **101**, 6142 (1997).

[120] J. Lekner, Physica B **252**, 149 (1998).

[121] V. Buch, P. Sandler, and J. Sadlej, J. Phys. Chem. B **101**, 6142 (1997).

[122] R. Ballou, E. Lelièvre-Berna, and B. Fåk, Phys. Rev. Lett. **76**, 2125 (1996).

[123] E. F. Shender, V. B. Cherepanov, P. C. W. Holdsworth, and A. J. Berlinsky, Phys. Rev. Lett. **70**, 3812 (1993).

[124] M. J. Harris, (personal communication).

[125] R. Moessner, Phys. Rev. B **57**, R5587 (1998).

[126] J. Hodges, (personal communication).

[127] J. S. Gardner, S. Dunsiger, B. D. Gaulin, R. Kiefl, M. D. Lumsden, Z. Tun, N. Raju, I. Swainson, and J. E. Greedan, Phys. Rev. Lett. **82**, 1012 (1999).

[128] O. Mouritsen, *Computer Studies of Phase Transitions and Critical Phenomena* (Springer-Verlag, Berlin, 1984).